

## ABSTRACT

Brocato, Brett Chandler. Micromachining Using Elliptical Vibration Assisted Machining (EVAM). (Under the direction of Thomas A. Dow, Ph.D.)

The goal of this research is to demonstrate Elliptical Vibration Assisted Machining (EVAM) as a multi-level planar microstructuring tool for MEMS applications. While many MEMS (Micro Electro Mechanical Systems) devices are fabricated using silicon etching techniques developed for the microelectronics industry, micromachining is an attractive alternative because of its low start-up cost, applicability to a wide range of materials, high flexibility of feature geometry, and low prototyping cost. Vibration assisted diamond turning is proposed as an alternative method of fabricating 3D MEMS devices. To demonstrate the capabilities of this technique, a diamond tool holder that moves in an elliptical path at 1000 Hz (the Ultramill) was attached to a 3-axis diamond turning machine (DTM). Using this system, structured surfaces with high accuracy and surface finish were created. Multi-level structures with 15  $\mu\text{m}$  plan-view features, 500 nm elevation features, and 20 nm RMS surface finish have been achieved on a 200  $\mu\text{m}$  part scale. In addition, the limits of the fabrication technique in its current form were identified by machining specific features and relating them to the tool, the process and the DTM. Limitations of the current process include a sub-Hertz drift error in the air-bearing third axis, temperature control of the Ultramill, and natural frequencies of the DTM axes in the range of measured error frequencies in machined parts.

**MICROMACHINING USING ELLIPTICAL VIBRATION ASSISTED  
MACHINING (EVAM)**

**BRETT C. BROCATO**

A thesis submitted to the graduate faculty of  
North Carolina State University  
in partial fulfillment of the  
requirements for the degree of  
Master of Science

**MECHANICAL AND AEROSPACE ENGINEERING  
NORTH CAROLINA STATE UNIVERSITY**

Raleigh, NC  
2005

**APPROVED BY:**

---

---

## BIOGRAPHY

Brett Brocato, born July 11, 1975, grew up in Brandon, Mississippi. He is a graduate of Jackson Academy in Jackson, Mississippi. Brett attended the University of Alabama on a Presidential Scholarship. At Alabama, he earned a bachelor's degree in mechanical engineering with a minor in the Computer Based Honors Program, an undergraduate computer science research curriculum. Brett's engineering education was enhanced by several semesters of co-op education with James River Corporation and TRW Vehicle Safety Systems. After graduation from Alabama, Brett worked with Bell Helicopter in Fort Worth, Texas, and Corning Optical Fiber in Wilmington, North Carolina. He entered the master's program in mechanical engineering at North Carolina State University in 2003. Upon completion of his MSME in spring 2005, Brett will move to San Diego, California, to accept a position with General Atomics as an Engineer IV, Micromachining, in the Inertial Confinement Fusion Group.

## ACKNOWLEDGEMENTS

I would like to thank everyone who has given me guidance and instruction during my time at NC State University. The whole team at the Precision Engineering Center has provided invaluable help, and I can't imagine a research environment with more possibilities for learning in such a wide variety of disciplines. The following people deserve a personal thank-you:

- Dr. Thomas Dow, my advisor, for giving me the chance to learn so much at the PEC, sharing his great knowledge, and the recommendation to General Atomics.
- Drs. Greg Buckner and Ron Scattergood, my committee members.
- Alex Sohn and Ken Garrard, Research Engineers at the PEC, for an extraordinary amount of help, knowledge, and support.
- Dr. Dow, Alex, Matthew Cerniway, and Nobu Negishi, for their work on the Ultramill.
- Dave Brehl, Ph.D. candidate at the PEC, for help with the temperature experiments and access to the SEM.
- The rest of the graduate student team at the PEC: Karl Freitag, Witoon Panusittikorn, Karalyn Folkert, and Nathan Buescher – thanks for all your help. Congratulations on your degrees and jobs, Karl and Witoon. Nathan and Kara: good luck on The Race to 100!
- Karl Falter, PEC MS '89, for his expertise with the Nanoform and the y-axis.

- Lara Masters for the 5:00 P.M. purchase orders and for keeping the PEC running smoothly.
- Drs. Paul Ro, Jay Tu, Jeffrey Eischen, Thomas Dow, and Ron Scattergood for my most-challenging graduate classes.
- Dr. Gould and Dr. Zikry, for their support early in my time at NC State.
- Dr. Joey Parker at the University of Alabama, for encouraging me to give graduate school a shot.
- Zygo Technical Support for the `dat_to_xyz.exe` utility.
- Acappology 101 *a cappella* group, for the sanity break before quite a few all-nighters.

Thanks especially to Mom and Dad, for all their love, support, and advice since day one.

This project was sponsored by the National Science Foundation.

NSF contract # DMI-0115175, Monitor: George Hazelrigg

# TABLE OF CONTENTS

<b>List of Tables .....</b>	<b>viii</b>
<b>List of Figures.....</b>	<b>ix</b>
<b>1 Introduction.....</b>	<b>1</b>
1.1 Precision Manufacturing Techniques .....	1
1.2 3-D Micromachining and MEMS Overview .....	1
1.3 Vibration Assisted Machining .....	16
1.4 History of EVAM at NC State.....	16
1.4.1 UMLS .....	16
1.4.2 UMHS design .....	17
1.4.3 UMHS development .....	18
1.4.4 Problem Statement: Micromachining with EVAM .....	19
1.5 Terminology .....	19
<b>2 Experimental Apparatus .....</b>	<b>19</b>
2.1 Ultramill Structure.....	19
2.2 Cooling System .....	21
2.3 Nanoform/Ultramill Integration .....	22
<b>3 Experimental Process .....</b>	<b>24</b>
3.1 Workpiece Preparation .....	24
3.2 Touch-off.....	25
3.3 Rastering Sequence .....	28
<b>4 Micromachining Experiments .....</b>	<b>30</b>
4.1 Ultramill Motion Planning .....	30
4.1.1 Ultramill Elliptical Tool Path .....	30

4.1.2	Ultramilled Surface Features .....	32
4.1.3	Surface Finish .....	36
4.1.4	Ultramill Motion Programming .....	37
4.2	Micromachining Results.....	40
4.2.1	Large Angstrom Symbol.....	44
4.2.2	Small Angstrom Symbol.....	48
4.2.3	Flats .....	57
<b>5</b>	<b>Characterization of Possible Sources of Error .....</b>	<b>66</b>
5.1	Nanoform Diamond Turning Machine Axes.....	66
5.1.1	Z-axis .....	68
5.1.2	X-axis .....	80
5.1.3	Y-axis .....	84
5.1.4	Spindle.....	106
5.2	Temperature Effects .....	109
5.2.1	Thermal Effect on Depth of Cut .....	111
5.2.2	Thermal Effects on Tool Holder Position.....	116
5.2.3	Thermal Effects at Equilibrium .....	125
5.3	Piezoelectric or Amplifier Effects .....	126
5.4	Diagnosis of Surface Features .....	127
5.4.1	Crossfeed Spatial Frequencies .....	127
5.4.2	Upfeed Spatial Frequencies .....	128
<b>6</b>	<b>Conclusions.....</b>	<b>134</b>
<b>7</b>	<b>References.....</b>	<b>136</b>
7.1	Appendix A: Data-gathering Methods .....	140
7.1.1	Method for Importing Zygo NewView Surface Topology Data to Matlab .....	140
7.1.2	Method for Gathering High-Frequency Axis-Position Data In Delta Tau PEWinPro32 .....	143
7.2	Appendix B: Matlab Functions .....	147

7.2.1	Loading Zygo Surface Topology Data into Matlab: xyzread.m .....	147
7.2.2	Analyzing Rastered Crossfeed Features: crossfeed.m .....	147
7.2.3	Analyzing Rastered Upfeed Features: upfeed_line.m.....	153
7.2.4	Analyzing nanometer spatial frequency signals: freq_nm.m, plot_freq_nm.m .....	157
7.2.5	Loading Nanoform Axis Position Data into Matlab: process_flat.m, processxyz.m, read_umac_data.m .....	162
7.2.6	Analyzing Nanoform Axis Upfeed Data: axis_upfeed_pickline.m .....	168
7.3	Appendix C: Ultramill PMAC Sample Part Program.....	171
7.4	Appendix D: Y-axis Regap Procedure .....	186

## LIST OF TABLES

TABLE 1.2-1. MATERIAL AND FEATURE SIZE GUIDELINES BY PROCESS TYPE [1].....	2
TABLE 4.2-1. SUMMARY OF ABSOLUTE AND RELATIVE TILT AND SAG DATA, 200 $\mu\text{M}$ ANGSTROM. ....	56
TABLE 4.2-2. FINISH ERROR SUMMARY FOR 1.67 $\mu\text{M}$ UFPC, 1.67 $\mu\text{M}$ CROSSFEED INCREMENT FLAT. ....	60
TABLE 4.2-3. SAG AND TILT RESULTS FOR EVAM FLAT. ....	65
TABLE 5.1-1. NANOFORM SHAKER-TEST AXIS VIBRATION SUMMARY.....	68
TABLE 5.1-2. THREE PEAK FREQUENCIES FROM FIGURE 5.1-25 DATA WITH ACCELERATION AMPLITUDES AND PREDICTED DISPLACEMENT AMPLITUDES (SUPPORTING EQUATIONS: SECTION 5.1.1) .....	87
TABLE 5.1-3. EXAMPLES OF MEASURED PERFORMANCE IN TWO DIFFERENT PART PROGRAMS. .....	100
TABLE 5.1-4. Y-AXIS ACCURACY STATISTICS OF EACH PASS.....	105
TABLE 5.2-1. TEMPERATURE CHANGES FROM FIGURE 5.2 – 3 (MEASURED AND PREDICTED). 115	
TABLE 5.2-2. CHANGES IN TEMPERATURE AND TOOL HOLDER POSITION, LONG-TERM EXCURSIONS. ....	121

## LIST OF FIGURES

FIGURE 1.2-1. CUSTOM-GROUND CARBIDE TOOL AND GROOVES MACHINED IN BRASS .....	5
FIGURE 1.2-2. PSEUDO BALL-END DIAMOND MILL. [6].....	6
FIGURE 1.2-3. DIAMOND-MILLED MICROSTRUCTURES. [7].....	6
FIGURE 1.2-4. DIAMOND-MILLED MICROSTRUCTURES. [7].....	7
FIGURE 1.2-5. ROUNDED CUTTING TOOL [8] .....	8
FIGURE 1.2-6. MICROMILLED SPIRAL STRUCTURE WITH DETAILS IN FIGURE 1.2-7. [8] .....	8
FIGURE 1.2-7. INTERSECTION DETAIL OF SPIRAL STRUCTURE [8].....	9
FIGURE 1.2-8. EXCIMER-LASER STRUCTURED POLYMERIC OPTICAL WAVEGUIDE: INTERFEROGRAM SURFACE PROFILE, BOTTOM RIGHT [9]. .....	10
FIGURE 1.2-9. LASER-MACHINED FLATS IN CARBIDE, $R_A$ 0.93 $\mu$ M. [13] .....	11
FIGURE 1.2-10. PARTIAL SPHERE IN PHOTORESIST MACHINED BY THE HIGH-SPEED MASKLESS GRAYSCALE LITHOGRAPHY [HMSGL] PROCESS [15]. .....	12
FIGURE 1.2-11. (A) CIRCULAR RINGS OF $\sim 20$ $\mu$ M WIDTH WITH A DEPTH OF 10-20 MICRONS; (B ) 10-20 MICRON DEEP DOUGHNUT FEATURE WITH 20 $\mu$ M DIAMETER PEDESTAL IN CENTER [16].....	13
FIGURE 1.2-12. $1/8^{\text{TH}}$ SPHERE IN SQUARE CAVITY. [17] .....	13
FIGURE 1.2-13. SEM MICROGRAPH OF 65 $\mu$ M DIAMETER DIFFRACTIVE OPTICAL ELEMENT MACHINED BY FIB MILLING IN DIAMOND FILM [3] .....	14
FIGURE 1.2-14. CONTOUR ACCURACY OF PMMA STRUCTURES PROCESSED BY LIGA TECHNOLOGY [18]. .....	15
FIGURE 1.4-1. ULTRAMILL LOW SPEED [22, § 1.3.4].....	17
FIGURE 1.4-2. UMHS (LEFT), UMLS (RIGHT) [22, § 2.0] .....	18
FIGURE 2.1-1. ULTRAMILL PRELOAD SYSTEM [22, § 2.1].....	20
FIGURE 2.1-2. ULTRAMILL COOLING CHAMBER AND PRELOAD SYSTEM [22, § 2.1.2].....	20
FIGURE 2.2-1 ULTRAMILL COOLING CHAMBER CUT-AWAY [22].....	21
FIGURE 2.2-2 ULTRAMILL COOLING SYSTEM [22, § 2.2.3] .....	22
FIGURE 2.3-1. NANOFORM 600 SETUP (DIAGRAM).....	23
FIGURE 3.1-1. DETAILS OF EXPERIMENTAL SETUP.....	24
FIGURE 3.2-1. TOUCH-OFF VIEW, 50 $\mu$ M RADIUS TOOL AND REFLECTION, 130X VIDEO MICROSCOPE .....	26
FIGURE 3.2-2. IDENTIFICATION OF A PHANTOM CHIP.....	27
FIGURE 3.3-1 RASTERING SEQUENCE .....	29
FIGURE 4.1-1. ELLIPTICAL TOOL PATH.....	31
FIGURE 4.1-2 THREE ULTRAMILL UPFEED CYCLES .....	32
FIGURE 4.1-3. CROSSFEED-DIRECTION CHARACTERISTIC FEATURE SIZE.....	33
FIGURE 4.1-4. UPFEED-DIRECTION CHARACTERISTIC FEATURE SIZE (DOC < B).....	34
FIGURE 4.1-5. CHARACTERISTIC FEATURE SIZES VS. DOC .....	35
FIGURE 4.1-6. CHARACTERISTIC SURFACE FEATURE (DOC < B).....	36

FIGURE 4.1-7. ULTRAMILL FEATURES .....	38
FIGURE 4.1-8. ELLIPTICAL APPROACH TO CORNER. ....	40
FIGURE 4.2-1. WHILE LIGHT INTERFEROGRAMS OF 1 MM-SCALE ANGSTROM SYMBOL, 200 UM SYMBOL (TOP LEFT) .....	41
FIGURE 4.2-2. 1 MM-SCALE AND 200 μM ANGSTROM SYMBOLS; COMPARATIVE DIMENSIONS.42	
FIGURE 4.2-3. 200 μM ANGSTROM SYMBOL TOP SECTION FLATNESS (*) ~ 82 NM.....	43
FIGURE 4.2-4. 200 μM ANGSTROM SYMBOL DOC ~ 500 NM (DESIGN VALUE = 500 NM).....	44
FIGURE 4.2-5. PEC 1 MM-SCALE ANGSTROM LOGO(WHITE LIGHT INTERFEROGRAM).....	45
FIGURE 4.2-6. 1MM-SCALE ANGSTROM SYMBOL CROSSFEED CHECK DIMENSION (394 μM MEASURED, 487 μM DESIGN).....	45
FIGURE 4.2-7. ANGSTROM BACKGROUND UPFEED PROFILE (WHILE LIGHT INTERFEROGRAM) .....	47
FIGURE 4.2-8. ANGSTROM BACKGROUND CROSSFEED PROFILE (WHITE LIGHT INTERFEROGRAM) .....	47
FIGURE 4.2-9. WHITE LIGHT INTERFEROGRAM OF 200 μM PEC LOGO.....	48
FIGURE 4.2-10. ANGSTROM SYMBOL EXAMPLE DESIGN DIMENSIONS.....	50
FIGURE 4.2-11. MEASURED UPFEED DISTANCE FOR COMPARISON TO EXPECTED DISTANCE $D_E$ = 27.2 μM (WHITE LIGHT INTERFEROGRAM, 20X).....	51
FIGURE 4.2-12. 200 μM ANGSTROM SYMBOL TOTAL FOREGROUND WIDTH, FOR COMPARISON TO 145.6 μM INTENDED DIMENSION. ....	51
FIGURE 4.2-13 ANGSTROM SYMBOL FEATURE DETAIL (WHITE LIGHT INTERFEROGRAM) .....	52
FIGURE 4.2-14. 200 μM SYMBOL ISOMETRIC: INTERFEROMETRY ARTIFACTS AND SEM INSETS. .....	52
FIGURE 4.2-15. CROSSFEED MEASURED SIZE SHOWN FOR COMPARISON WITH EXPECTED SIZE OF 22 μM (WHITE LIGHT INTERFEROGRAM, 20X).....	53
FIGURE 4.2-16. 200 μM ANGSTROM SYMBOL BACKGROUND UPFEED, APPROXIMATELY 112 UPFEEDS AT 1 NM PEAK-PEAK SHOULD BE VISIBLE (WHITE LIGHT INTERFEROGRAM). ...	54
FIGURE 4.2-17. 200 μM ANGSTROM SYMBOL BACKGROUND CROSSFEED, APPROXIMATELY 85 CROSSFEED MARKS AT 2.5 NM PEAK-PEAK SHOULD BE VISIBLE (WHITE LIGHT INTERFEROGRAM) .....	54
FIGURE 4.2-18. MASKS USED FOR DT FLAT, BACKGROUND, AND FOREGROUND TILT AND SAG STATISTICS (LEFT TO RIGHT).....	56
FIGURE 4.2-19 UPFEED PROFILE SHOWING 10 ULTRAMILL CYCLES AT 1.67 μM PER CYCLE.....	58
FIGURE 4.2-20 UPFEED PROFILE: LOW FREQUENCY, 1.67 MM/S UPFEED .....	59
FIGURE 4.2-21. UNFILTERED (TOP) AND LOW-PASS FILTERED (BOTTOM, < 599/MM) LOW- FREQUENCY FINISH ERROR FOR 1.67 μM UFPC, 1.67 μM CROSSFEED INCREMENT FLAT. ...	61
FIGURE 4.2-22. UNFILTERED (LEFT), BAND-PASS FILTERED (RIGHT, 6-299 WAVES/MM) MEDIUM-FREQUENCY FINISH ERROR FOR 1.67 μM UFPC, 1.67 μM CROSSFEED INCREMENT FLAT. ....	62

FIGURE 4.2-23. UNFILTERED (LEFT), BAND-REJECT FILTERED (6/MM-299/MM) FINISH ERROR FOR 1.67 $\mu$ M UFPC, 1.67 $\mu$ M CROSSFEED INCREMENT FLAT.....	62
FIGURE 4.2-24. UNFILTERED (LEFT), LOW-PASS FILTERED (RIGHT, < 584 WAVES/MM) FINISH ERROR FOR 1.67 $\mu$ M UFPC, 1.67 $\mu$ M CROSSFEED INCREMENT FLAT.....	63
FIGURE 4.2-25. UNFILTERED (LEFT), HIGH-PASS FILTERED (RIGHT, > 584 WAVES/MM) FINISH ERROR FOR 1.67 $\mu$ M UFPC, 1.67 $\mu$ M CROSSFEED INCREMENT FLAT.....	64
FIGURE 4.2-26. MASKING SCHEME FOR DT FLAT (LEFT) AND EVAM FLAT (RIGHT).....	65
FIGURE 5.1-1. NANOFORM DTM AND ULTRAMILL DIAGRAM. ....	67
FIGURE 5.1-2. Z-AXIS SHAKER TEST EXPERIMENTAL SETUP. ....	70
FIGURE 5.1-3. Z-AXIS ACCELEROMETER SIGNAL, EXCITATION FREQUENCY = 102 HZ. ....	70
FIGURE 5.1-4. Z-AXIS DISPLACEMENT MEASURED BY THE LASER INTERFEROMETER, EXCITATION FREQUENCY = 102 HZ. ....	71
FIGURE 5.1-5. FFT OF ACCELEROMETER SIGNAL SHOWN IN FIGURE 5.1-3. ....	72
FIGURE 5.1-6. Z-AXIS VIBRATION AMPLITUDES AT SEVERAL FREQUENCIES: MEASURED ACCELERATION (LEFT), MEASURED OR PREDICTED DISPLACEMENT (RIGHT).....	73
FIGURE 5.1-7. TEN 1.5 $\mu$ M CROSSFEED PASSES (ULTRAMILL ACTUATED AT 400 VPP / 1000 HZ) .	74
FIGURE 5.1-8. PASS #1: Z-AXIS POSITION VS. TIME.....	74
FIGURE 5.1-9. FFT OF PASS #1.....	75
FIGURE 5.1-10. DIAGRAM OF Z-AXIS PITCH EXPERIMENT.....	76
FIGURE 5.1-11. FFT OF $\Theta$ IN RADIANS.....	77
FIGURE 5.1-12. FFT OF SIGNAL A.....	77
FIGURE 5.1-13. FFT OF SIGNAL B.....	77
FIGURE 5.1-14. TRANSFER FUNCTION OF CAPACITANCE GAGE STAND B INSTRUMENTED-HAMMER IMPACT TEST.....	78
FIGURE 5.1-15. Z-AXIS Y-DIRECTION STIFFNESS DATA MEASURED AT CAP GAGE A.....	79
FIGURE 5.1-16. Z-AXIS Y-DIRECTION STIFFNESS DATA MEASURED AT CAP GAGE B.....	79
FIGURE 5.1-17. X-AXIS, Z-DIRECTION SHAKER TEST SETUP.....	81
FIGURE 5.1-18. X-AXIS, Z-DIRECTION ACCELEROMETER SIGNAL AT $F_1 \sim 275$ HZ.....	82
FIGURE 5.1-19. X-AXIS, X-DIRECTION SHAKER TEST SETUP.....	83
FIGURE 5.1-20. X-AXIS, X-DIRECTION ACCELEROMETER SIGNAL AT $F_1 \sim 120$ HZ.....	83
FIGURE 5.1-21. Y-AXIS Z-DIRECTION SHAKER TEST.....	85
FIGURE 5.1-22. Y-AXIS VIBRATION FREQUENCY VS. EXCITATION FREQUENCY.....	85
FIGURE 5.1-23. Y-AXIS ACCELERATION AMPLITUDE VS. VIBRATION FREQUENCY.....	86
FIGURE 5.1-24. Y-AXIS VIBRATION AT 25 HZ EXCITATION FREQUENCY.....	87
FIGURE 5.1-25. FFT OF FIGURE 5.1-24 DATA (25 HZ EXCITATION FREQUENCY).....	87
FIGURE 5.1-26. Y-AXIS AND ULTRAMILL VIBRATION TEST SETUP, REMOVED FROM THE NANOFORM DTM.....	89
FIGURE 5.1-27. Y-AXIS AND ULTRAMILL VIBRATION TEST SETUP DIAGRAM.....	90

FIGURE 5.1-28. Y-AXIS DISPLACEMENT: BEARING AIR SUPPLY 75 PSI, ULTRAMILL OFF, COOLING PUMP OFF. 20 MV/DIVISION, 5 NM/MV, 10 SECONDS PER DIVISION, SUB-HERTZ SIGNAL VISIBLE.....	91
FIGURE 5.1-29. Y-AXIS DISPLACEMENT: BEARING AIR SUPPLY ZERO PSI, ULTRAMILL OFF, COOLING PUMP OFF. 20 MV/DIVISION, 5 NM/MV, 10 SECONDS PER DIVISION, NO SUB- HERTZ SIGNAL VISIBLE.....	91
FIGURE 5.1-30. Y-AXIS DISPLACEMENT: BEARING AIR SUPPLY 75 PSI, ULTRAMILL OFF, COOLING PUMP OFF, SUB-HERTZ SIGNAL VISIBLE.....	92
FIGURE 5.1-31. FFT OF Y-AXIS DISPLACEMENT, AIR BEARING SUPPLIED AT 75 PSI.....	92
FIGURE 5.1-32. Y-AXIS VIBRATION: ULTRAMILL 1000 HZ, 400 VPP.....	93
FIGURE 5.1-33. Y-AXIS VIBRATION: ULTRAMILL 1000 HZ, 400 VPP, SUB-HERTZ SIGNAL VISIBLE. .....	94
FIGURE 5.1-34. FFT: FULL FREQUENCY RANGE.....	94
FIGURE 5.1-35. FFT: LOW FREQUENCY RANGE.....	95
FIGURE 5.1-36. FFT: MIDDLE FREQUENCY RANGE.....	95
FIGURE 5.1-37. Y-AXIS DISPLACEMENT: AIR BEARING SUPPLIED AT 75 PSI, COOLING PUMP ON, ULTRAMILL NOT RUNNING. SUB-HERTZ SIGNAL IS VISIBLE.....	96
FIGURE 5.1-38. FFT OF Y-AXIS DISPLACEMENT: AIR BEARING SUPPLIED AT 75 PSI, COOLING PUMP ON, ULTRAMILL OFF.....	97
FIGURE 5.1-39. AIR BEARING DRIFT INTERACTION WITH UPFEED PASS FREQUENCY: 100 SECONDS ELAPSED TIME.....	98
FIGURE 5.1-40. AIR BEARING DRIFT INTERACTION WITH 1 $\mu$ M DEPTH OF CUT: 500 SECONDS ELAPSED TIME.....	99
FIGURE 5.1-41. EXAMPLES OF PREDICTED LONG-WAVELENGTH SURFACE FREQUENCIES AND PROBABLE CLIPPING.....	100
FIGURE 5.1-42. Y-AXIS YAW AND COSINE ERROR ILLUSTRATION.....	101
FIGURE 5.1-43. COSINE AND SINE ERROR DIAGRAM.....	101
FIGURE 5.1-44. CROSSFEED PROFILE: 2 $\mu$ M CROSSFEED, 1.91 MM/S UPFEED, 1000 HZ.....	102
FIGURE 5.1-45. CROSSFEED PASS #1.....	103
FIGURE 5.1-46. PLACING CROSSFEED PASS #1 AND LOCATION ZERO. 50 $\mu$ M RADIUS TOOL 49.955 $\mu$ M OUT OF PART, ZYGO Y-COORDINATE 47.8.....	103
FIGURE 5.1-47. CROSSFEED PASS #2 LOCATION.....	104
FIGURE 5.1-48. PLACING PASS #2 AT 44.5 $\mu$ M.....	104
FIGURE 5.1-49. SPINDLE Z-DIRECTION SHAKER TEST SETUP.....	107
FIGURE 5.1-50. SPINDLE Z-DIRECTION ACCELEROMETER SIGNAL AT $F_1 \sim 190$ HZ.....	107
FIGURE 5.1-51. SPINDLE X-DIRECTION SHAKER TEST SETUP WITH TWO ACCELEROMETER POSITIONS.....	108
FIGURE 5.1-52. SPINDLE X-DIRECTION ACCELEROMETER SIGNAL IN TWO POSITIONS, $F_1 \sim 300$ HZ.....	109

FIGURE 5.2-1. PREDICTED TEMPERATURE VS. POSITION IN PIEZO STACK LENGTH: ULTRAMILL ACTUATION 400 V <sub>pp</sub> - 1000 HZ. ....	111
FIGURE 5.2-2 TEMPERATURE EXCURSION VS. CROSSFEED. ....	112
FIGURE 5.2-3 CHANGES IN PIEZO STACK TEMPERATURE AND IN DEPTH OF CUT. ....	113
FIGURE 5.2-4. LOCATION OF RTD PROBE .....	115
FIGURE 5.2-5. PRELOAD ADJUSTMENT NUT SHOWN WITH COOLING CHAMBER AND ASSOCIATED PARTS [22]. ....	116
FIGURE 5.2-6. CAPACITANCE AND FEDERAL GAGES POSITIONED TO MEASURE THERMAL EXPANSION .....	117
FIGURE 5.2-7 THREE DEGREE TEMPERATURE EXCURSION, 10 MINUTES DURATION .....	119
FIGURE 5.2-8 THREE DEGREE TEMPERATURE EXCURSION, 20 MINUTES DURATION .....	120
FIGURE 5.2-9 THREE DEGREE TEMPERATURE EXCURSION, 25 MINUTES DURATION .....	121
FIGURE 5.2-10. DIAGRAM OF COOLING CHAMBER WALL HEAT CONDUCTION. ....	122
FIGURE 5.2-11 CYCLICAL TEMPERATURE VARIATIONS .....	124
FIGURE 5.2-12 DEFLECTION AT THERMAL EQUILIBRIUM .....	126
FIGURE 5.4-1. 20 PASS, 2 μM CROSSFEED FLAT (LEFT), HIGHLIGHTED PROFILE (RIGHT).....	127
FIGURE 5.4-2. FFT OF SPATIAL PROFILE IN NANOMETERS AMPLITUDE .....	128
FIGURE 5.4-3 ACTUAL UPFEED SPEED VS. POSITION, PROGRAMMED VALUE 2 MM/S.....	129
FIGURE 5.4-4. TROUGH UPFEED LINE .....	130
FIGURE 5.4-5. SPATIAL PROFILE AT LINE OF INTEREST .....	130
FIGURE 5.4-6. FFT OF SPATIAL PROFILE AT LINE OF INTEREST .....	131
FIGURE 5.4-7. PEAK UPFEED LINE .....	132
FIGURE 5.4-8. PEAK UPFEED LINE SPATIAL PROFILE .....	132
FIGURE 5.4-9. PEAK UPFEED LINE FFT .....	133
FIGURE 7.1-1. PIXEL SCALING IN METERS PER PIXEL .....	140
FIGURE 7.1-2. JMP FORMULA CONVERTING TEXT “NO” TO TEXT “NAN” WHILE PRESERVING FLOATING POINT VALUES. ....	141
FIGURE 7.4-1. BOLT LABELS, GAGE AND CLAMP LOCATIONS. ....	186
FIGURE 7.4-2. PROPER FEDERAL GAGE LOCATIONS (NOT NECESSARY TO DEMOUNT SLIDE FROM AXIS).....	189
FIGURE 7.4-3. PROPER CLAMP LOCATIONS SHOWN, CLAMP FINGER THUMBSCREW HIGHLIGHTED (IGNORE FEDERAL GAGE AT BOLT #3) .....	189
FIGURE 7.4-4. GAGE STAND: CHECK INTERFERENCE WITH TABLE. PAPER ON TABLE SHOULD MOVE FREELY .....	190
FIGURE 7.4-5. Y-AXIS BASE CLAMPING SHOULD NOT INTERFERE WITH GAGE HEADS.....	190
FIGURE 7.4-6. IF EITHER FEDERAL GAGE BASE WOBBLER, SHIM THE LOOSE CORNER. ....	191
FIGURE 7.4-7. ENSURE THAT FEDERAL GAGE INVOLUTE TIP CONTACTS IN THE CURVED SECTION.....	191
FIGURE 7.4-8. CLAMPS REVERSED AS SPREADERS, GROOVED FINGER SHOWN IN INSET.....	192

# **1 INTRODUCTION**

## **1.1 PRECISION MANUFACTURING TECHNIQUES**

Precision fabrication techniques play an increasingly important role in industries ranging from optics to biological sensors. High-precision manufacturing is made up of traditional methods, such as diamond turning and milling, and newer techniques like focused ion beam (FIB) milling. Diamond turning is the standard for fabricating optical systems. The precision capabilities of milling are gradually being improved, but accuracy is limited by spindle runout and by the deflection of thin milling tools. Elliptical vibration assisted machining (EVAM) will be shown to be an alternative to both traditional and newer techniques of precision fabrication.

## **1.2 3-D MICROMACHINING AND MEMS OVERVIEW**

Micro electromechanical systems (MEMS) offer designers the ability to create miniature mechanical oscillators, optical network components and biological labs on a chip. Most MEMS devices use VLSI techniques developed for microprocessors using silicon. Although manufacturers are introducing a wide range of MEMS-based products, developers have found that guiding MEMS devices from the laboratory to the marketplace is a costly and time-consuming venture. For example, it is not unusual for a single MEMS prototyping run to take three months. The high cost of a MEMS fabrication facility forces companies to use existing foundries such as Sandia, MCNC or Berkeley with long lead times. The problem lies not with the MEMS devices themselves, but with the semiconductor-based manufacturing techniques employed to build them. Semiconductor wafer fabs excel at

producing high-volume integrated circuits using Complementary Metal Oxide Semiconductor (CMOS) processing, but many MEMS devices are manufactured in lower volumes with more complex structures such as moving three-dimensional micromirror arrays.

There are also non-semiconductor processes for making MEMS-scale devices that include mechanical turning and milling, laser processing, micro-electrical discharge machining, focused ion beam machining, and LIGA. Each of these techniques can be classified in terms of minimum feature size, position tolerance, maximum material removal rate and material compatibility as shown in Table 1.2-1 [1].

<b>Technology / Feature Geometry</b>	<b>Min. Feature size / tolerance</b>	<b>Feature Positional Tolerance</b>	<b>Material Removal Rate</b>	<b>Materials</b>	<b>Equipment Cost (\$USD)</b>
Micro Milling or Turning / 2D or 3D	25 $\mu\text{m}$ / 2 $\mu\text{m}$	3 $\mu\text{m}$	10,400 $\mu\text{m}^3/\text{sec}$	Polymers, Al, Brass, Nickel, SS and Titanium	
Excimer Laser / 2D or 3D	6 $\mu\text{m}$ / < 1 $\mu\text{m}$	< 1 $\mu\text{m}$	40,000 $\mu\text{m}^3/\text{sec}$	Polymers, Ceramics and some metals	\$1M [2]
Femtosecond Laser / 2D or 3D	1 $\mu\text{m}$ / <1 $\mu\text{m}$	< 1 $\mu\text{m}$	13,000 $\mu\text{m}^3/\text{sec}$	Any	\$1 - 10M [3]
Micro-EDM(Sinker or Wire) / 2D or 3D	25 $\mu\text{m}$ / 3 $\mu\text{m}$	3 $\mu\text{m}$	25x10 <sup>6</sup> $\mu\text{m}^3/\text{sec}$	Conductive materials	
Focused Ion Beam / 2D & 3D	200 nm / 20 nm	100 nm	0.5 $\mu\text{m}^3/\text{sec}$	Any	\$0.5 – 2M [4]
LIGA / 2D	< 1 $\mu\text{m}$ / 20-500 nm	~ 300 nm across 75 mm	N/A	Copper, Nickel, Permalloy	\$10M [2]

**Table 1.2-1.** Material and Feature Size Guidelines by Process Type [1]

Turning and milling are common material-removal processes in macro-scale manufacturing. The lower dimensional limits of these processes are being expanded by current research.

Diamond turning is capable of nanometer surface finishes and is the standard in optical component fabrication. Its use is limited to rotationally-symmetric part designs or to parts that may be decomposed into a rotationally-symmetric component and deviations created by a Fast Tool Servo (FTS) axis. The flexible, asymmetric three-dimensional profiling of micromilling and other micromachining techniques is not possible with diamond turning. Diamond turning is also generally unsuitable for ferrous and silicon carbide workpieces. Such limitations led to work on new approaches, among them vibration assisted machining (VAM).

Micromilling is the process of chip removal by means of a spindle and an end mill in the diameter range of 200  $\mu\text{m}$  or less. Part features are on the order of 25  $\mu\text{m}$ . Carbide milling tools are commercially available in 100  $\mu\text{m}$  size. Custom diamond tools as small as 22  $\mu\text{m}$  have been created by researchers. Feature aspect ratios of 40:1 have been achieved on machined parts. Micromilling has the advantage of greater material and geometry flexibility than that of lithography and most other micromachining processes. However, current micromilling techniques using a high-speed spindle are plagued with tool runout that limits the feature size and tolerance. Also, as milling tool diameter decreases, stiffness is reduced and errors due to tool bending become worse.

Excimer lasers and femtosecond lasers have comparable material removal rates to micromilling. The achieved tolerances are superior to micromilling. Excimer lasers have less material flexibility than micromilling. Femtosecond lasers, although highly flexible in terms of workpiece materials, have high startup costs. Micro-Electrical Discharge

Machining (Micro-EDM) has an extremely high MRR and comparable accuracy to micromilling, but only works on conductive materials. Focused Ion Beam (FIB) machining is a process in which the kinetic energy of accelerated ions is converted to thermal energy and used to vaporize very small amounts of material from a workpiece. It is a 3-D process with extremely high tolerances that can be used on any material. The main disadvantages are slow material removal rate (MRR) and high equipment costs. LIGA is a German acronym which translates to lithography, electroforming, and molding. This process is capable of high accuracy, high aspect ratios, and good surface quality, but equipment is very expensive. The following literature review examines the current state of the art in various micromachining techniques.

## **RECENT RESEARCH IN MICROMACHINING TECHNIQUES**

Schaller [5] illustrated the capability to mill small grooves with custom-made 35-120  $\mu\text{m}$  tools. The left side of Figure 1.2-1 shows one of the tools, and the right side shows milled grooves in brass. The tools were manufactured with diamond grinding wheels from tungsten carbide rods. With a non-CNC grinding machine, a tool break rate of up to 50% and tolerances of  $\pm 5 \mu\text{m}$  were reported during manufacture. Channel-cutting parameters of 19,000 rpm spindle speed and a feed rate of 35  $\mu\text{m/s}$  were used. This resulted in a feed per tooth in the range of the cutting edge radii, 1 to 2  $\mu\text{m}$ . A maximum depth of cut of 20  $\mu\text{m}$  was tested. Run-out of the tool was minimized to 10  $\mu\text{m}$ .

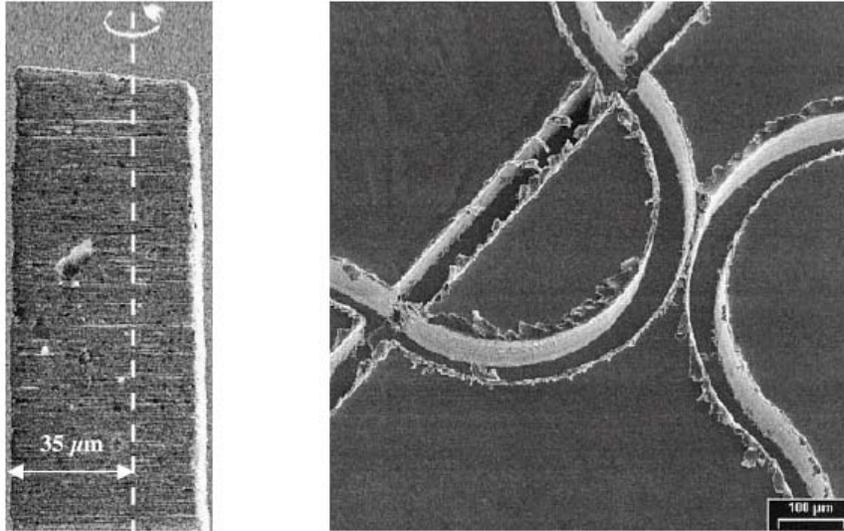


**Figure 1.2-1.** Custom-ground Carbide Tool and Grooves Machined in Brass

(note burrs at edges of grooves). [5]

Burr creation occurred with both brass and steel workpieces when cutting with carbide tools (Figure 1.2-1, right). Burrs were not seen when cutting brass with diamond tools. Diamond tools were not used for making channels due to the lack of very small-diameter sizes, but were valuable for deburring (milling the surface of the grooved part) after channels were cut with carbide tools.

Takeuchi [6] used a CNC 3-axis lathe with a spindle in place of the tool holder to confirm that ultra-precision sculptured metal workpieces could be made. Rough cuts were made with a 200  $\mu\text{m}$  diameter tungsten carbide ball-endmill. Custom diamond pseudo-ball-endmills (Figure 1.2-2) were used for finishing passes. A 3-mm diameter sculpture of a face similar to that in Figure 1.2 – 4 was made. Cutting parameters were 50,000 rpm, feed rate 50 mm/min,

and depth of cut  $1\ \mu\text{m}$  (for finishing with the diamond tool). Tool path resolution was  $2\ \mu\text{m} \times 5\ \mu\text{m}$ , and the machining took 6 hours.

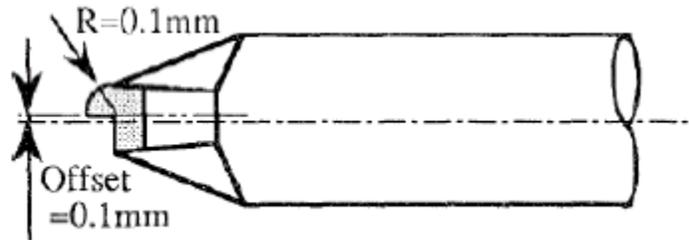


**Figure 1.2-2.** Pseudo Ball-end Diamond Mill. [6]

Kawai [7] continued the research of Takeuchi [6]. Figure 1.2-3 shows (counter-clockwise from top left) high-density grooves milled in Ni-P plated steel, high aspect ratio trapezoidal grooves milled in brass, and a milled mold for a  $25\ \mu\text{m}$  pitch encoder disk.

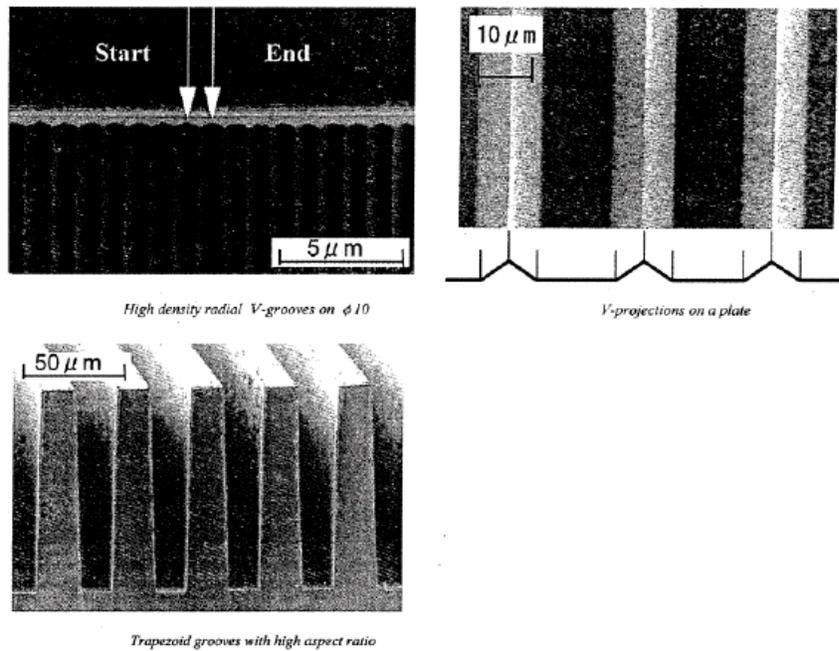


**Figure 1.2-3.** Diamond-milled microstructures. [7]

The array of lenses in Figure 1.2-4 was milled using tools that are approximately the same diameter as the lenses, about 230  $\mu\text{m}$ . The wavy shape was milled by a single-crystal diamond endmill of radius 25  $\mu\text{m}$ . The face in Figure 1.2-4 is smaller than that created in the previous study and was created with a diamond pseudo-ball-endmill of radius 30  $\mu\text{m}$ . Kawai also machined a 25  $\mu\text{m}$  square by 1 mm tall column from brass.

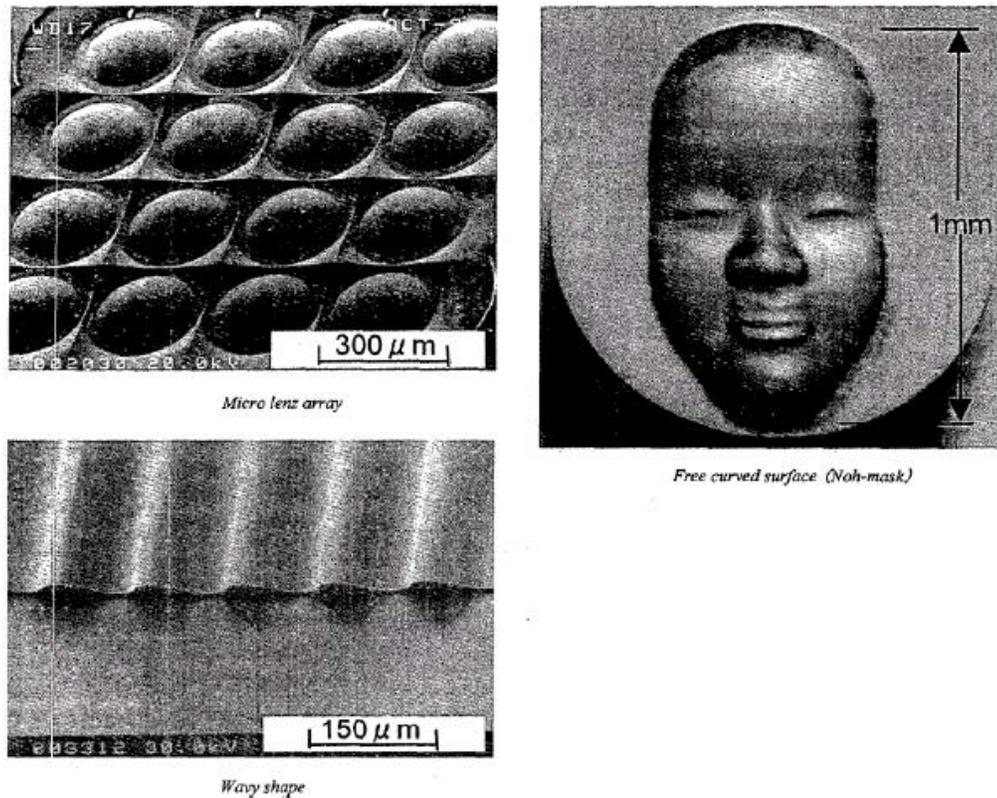


**Figure 1.2-4.** Diamond-milled microstructures. [7]

Friedrich [8] used custom milling tools that were created using Focused Ion Beam (FIB) micromachining of steel or tungsten carbide blanks. The tool shown in Figure 1.2-5 has an effective cutting diameter of 22  $\mu\text{m}$  and a cutter length of 77  $\mu\text{m}$ . Friedrich used these tools to manufacture the spiral pattern 1.5 mm in diameter, shown in Figure 1.2-6. The workpiece

is PMMA and the trench depth is 62  $\mu\text{m}$ . Minimum wall thickness was investigated at the center of the pattern where the spirals converge (Figure 1.2-7, left). The radial trench allowed the investigation of groove intersections (Figure 1.2-7, right) Depth of cut was 4  $\mu\text{m}$  per pass for 15 passes and machining time was 3 hours.

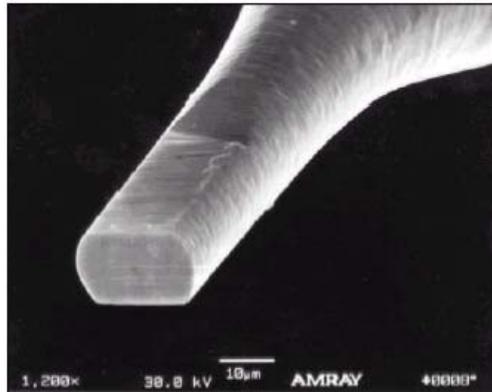


**Figure 1.2-5.** Rounded Cutting Tool [8]

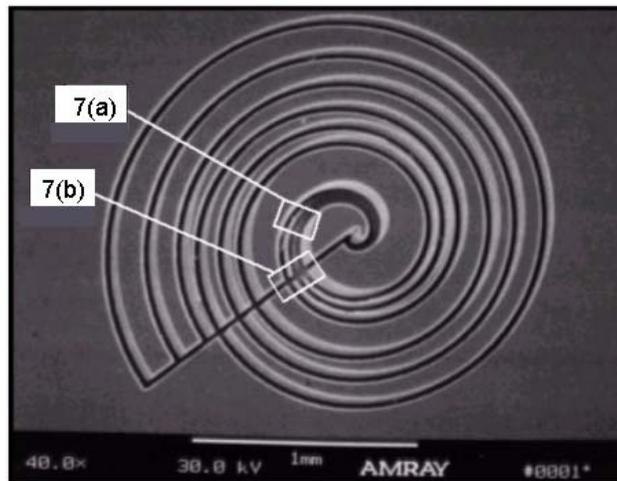


**Figure 1.2-6.** Micromilled Spiral Structure with details in **Figure 1.2-7**. [8]

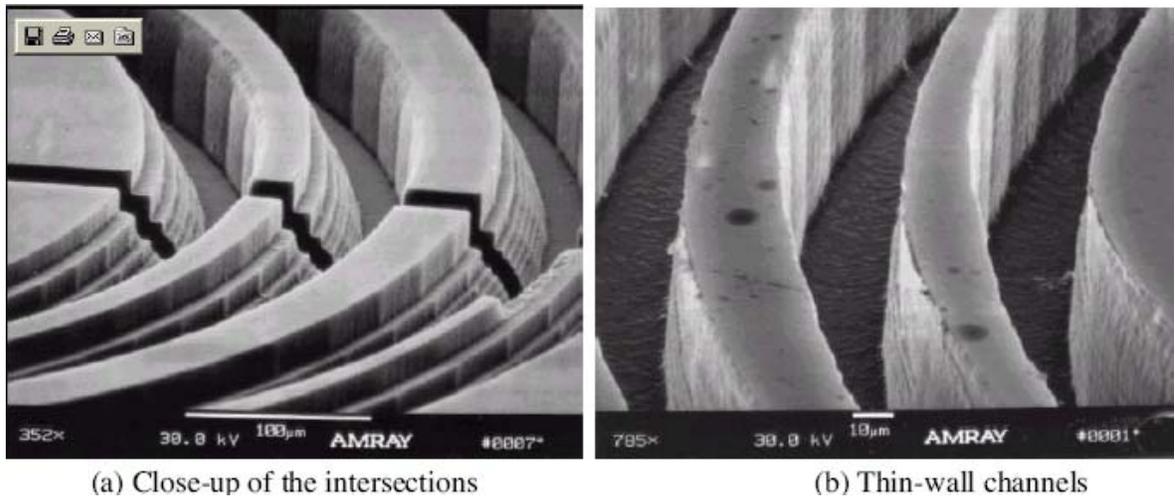


**Figure 1.2-7.** Intersection Detail of Spiral Structure [8]

Berden [9] used pulsed KrF-excimer laser radiation to generate optical waveguides on a spin-coated polymer multilayer. The KrF-excimer laser is a 248 nm wavelength laser used in photolithography; suitable for exposing 180 nm geometries [10]. One limitation of polymeric waveguides is high absorption losses caused by the formation of debris on the surface during structuring. Berden tested various processing gasses and pressures in an effort to minimize the formation of debris. Microscopic and interferometric views of a waveguide with reduced surface debris are shown in Figure 1.2-8. It can be seen from the white light interferogram surface profile on the bottom right that remaining surface imperfections are significant on a micrometer scale.

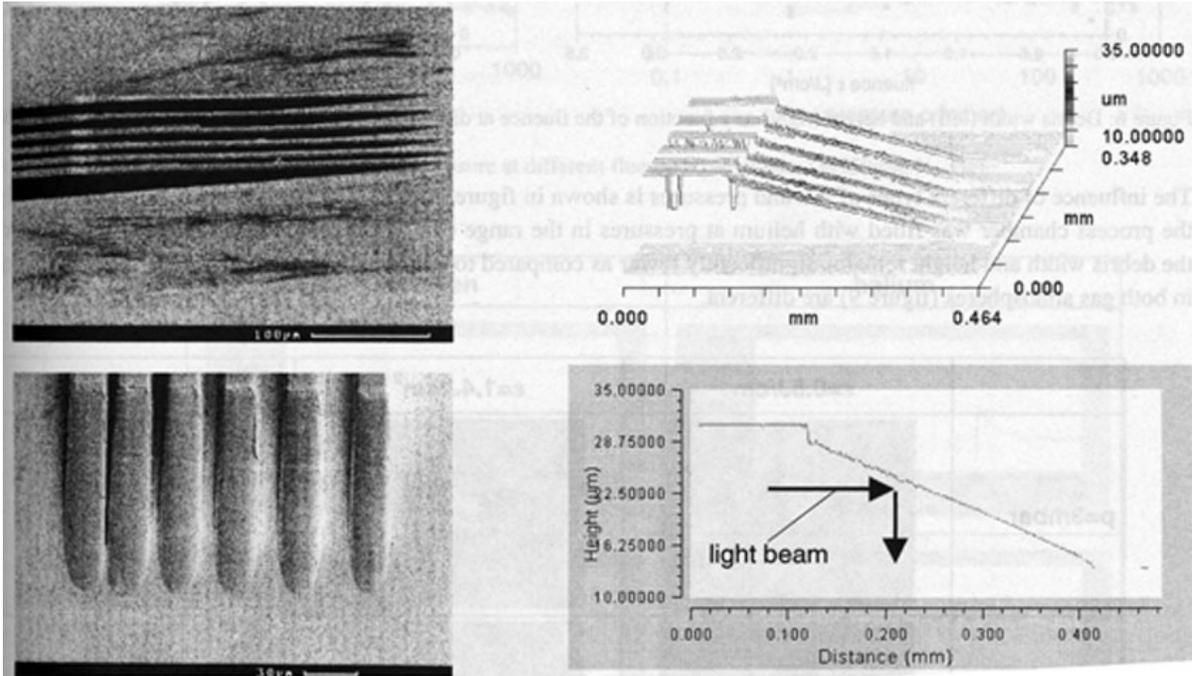


**Figure 1.2-8.** Excimer-laser structured polymeric optical waveguide: interferogram surface profile, bottom right [9].

Pfleging [11] used KrF-excimer and Nd:YAG lasers in the manufacture of microcomponent mold inserts for the light-induced reaction injection molding (UV-RIM) process.. Nd:YAG is a flashlamp-pumped solid-state laser of Neodymium:Yttrium-Aluminum Garnet, similar to the Nd:glass laser [12]. Light-induced reaction injection molding (UV-RIM) uses light to produce polymer macromer gelation and avoids the elevated temperatures and slow polymerization of traditional RIM processes [13]. Laser-ablated flats in carbide WC6Co are shown in Figure 1.2-9. The surface roughness achieved for these features is an Ra of 0.93  $\mu\text{m}$ .

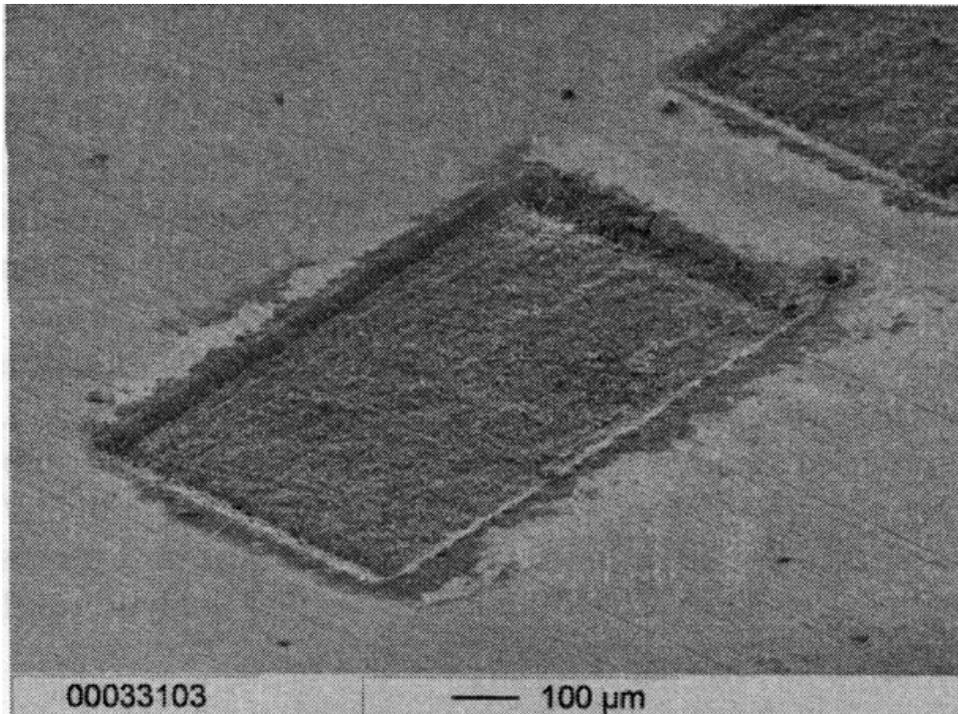
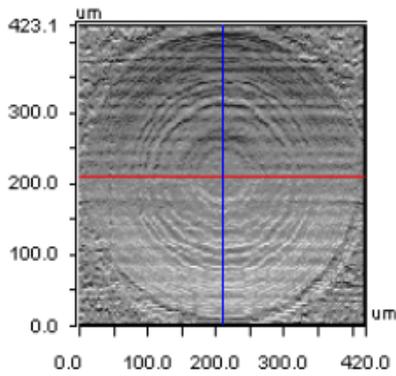


**Figure 1.2-9.** Laser-machined flats in carbide,  $R_a$  0.93  $\mu\text{m}$ . [13]

The high cost and difficulty of pattern modification inherent in printed circuit board (PCB) technology UV laser mask generators motivated Tamkin to pursue High-Speed Maskless Grayscale Lithography (HSMGL) as a tool for the manufacture of diffractive and micro-optics in photosensitive materials, such as photoresist and solgels [14, 15]. He cites examples of binary-surface UV laser direct write tools with 50  $\mu\text{m}$  resolution that cost about \$750K and 8" wafer mask pattern generators with 0.25  $\mu\text{m}$  resolution that cost \$10 million. The HSMGL process is capable of printing 1  $\mu\text{m}$  pixels with 8-bit depth control over a 30 mm x 30 mm area in less than one minute. Figure 1.2-10 shows a 400  $\mu\text{m}$  partial sphere in photoresist. Form error on the order of 100 nm is visible in the x- and y-direction profiles.



X	210.00	-	-	um
Y	208.69	-	-	um
Ht	1.02	-	-	um
Dist		-	-	um
Angle		-	-	°

Title: Subregion

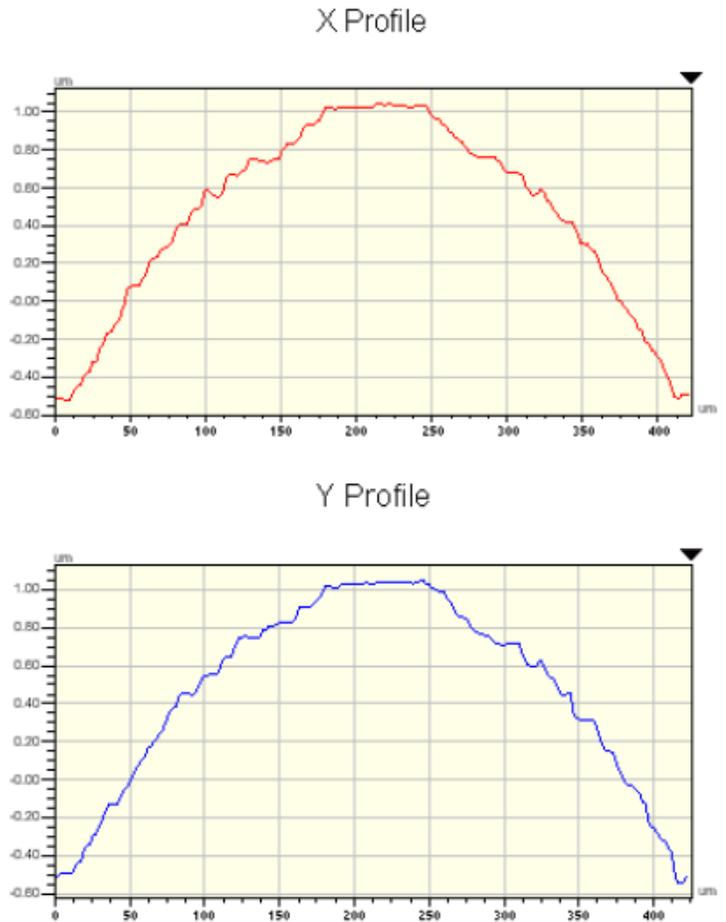


**Figure 1.2-10.** Partial sphere in photoresist machined by the High-Speed Maskless Grayscale Lithography [HMSGL] process [15].

Stock used the GX Pulsar laser system, based on an Ytterbium-doped fiber amplifier, to machine silicon [16]. The amplifier was designed for femtosecond pulses, but experimental results were obtained with 6-nanosecond pulse duration. Groove features machined with this system are shown in Figure 1.2-11. Thermal damage in the workpiece surface plane was found to be nearly negligible, but a molten “sludge” remained at the bottom of the ablated features, suggesting a depth limit of 20  $\mu\text{m}$  or less for this laser system in silicon.

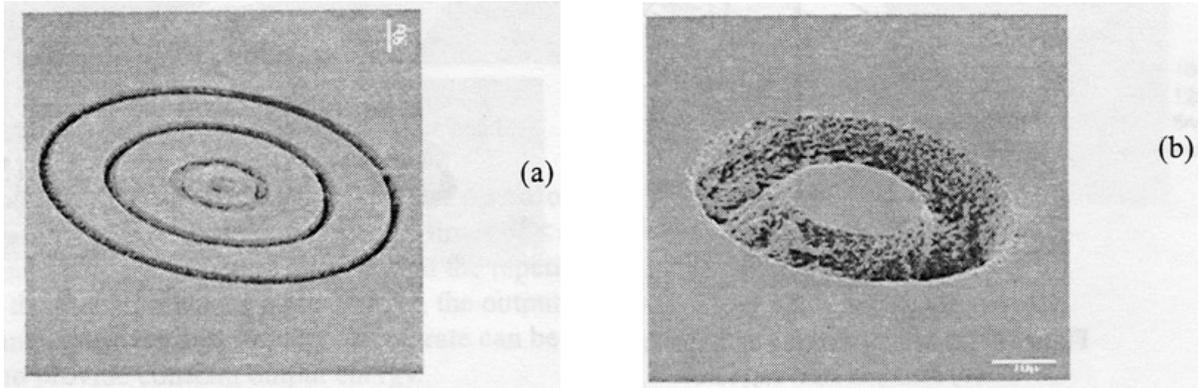


**Figure 1.2-11.** (a) Circular rings of  $\sim 20 \mu\text{m}$  width with a depth of 10-20 microns; (b) 10-20 micron deep doughnut feature with  $20 \mu\text{m}$  diameter pedestal in center [16]

One aspect of micro-electrical discharge machining (micro-EDM) which affects accuracy is electrode wear. Narasimhan used a theoretical model of tool wear to generate tool paths that take wear into account [17]. Figure 1.2-12 shows a partial sphere machined in a square cavity using micro-EDM. Surface accuracy is  $1 \mu\text{m}$ .

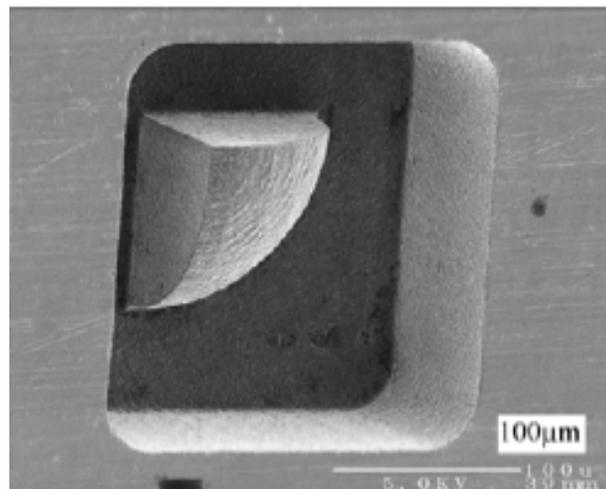


**Figure 1.2-12.**  $1/8^{\text{th}}$  sphere in square cavity. [17]

Focused Ion Beam (FIB) milling is capable of very high accuracy and surface finish on small workpieces, but it is a slow process and the cost of the equipment is very high. Fused silica (Fu) manufactured micro-optical elements with FIB milling, shown in Figure 1.2-13 [3]. Profile accuracy is less than 100 nm and surface roughness  $\leq 2$  nm over a  $1 \mu\text{m} \times 1 \mu\text{m}$  area. FIB milling equipment cost is \$0.5 - \$2 million.

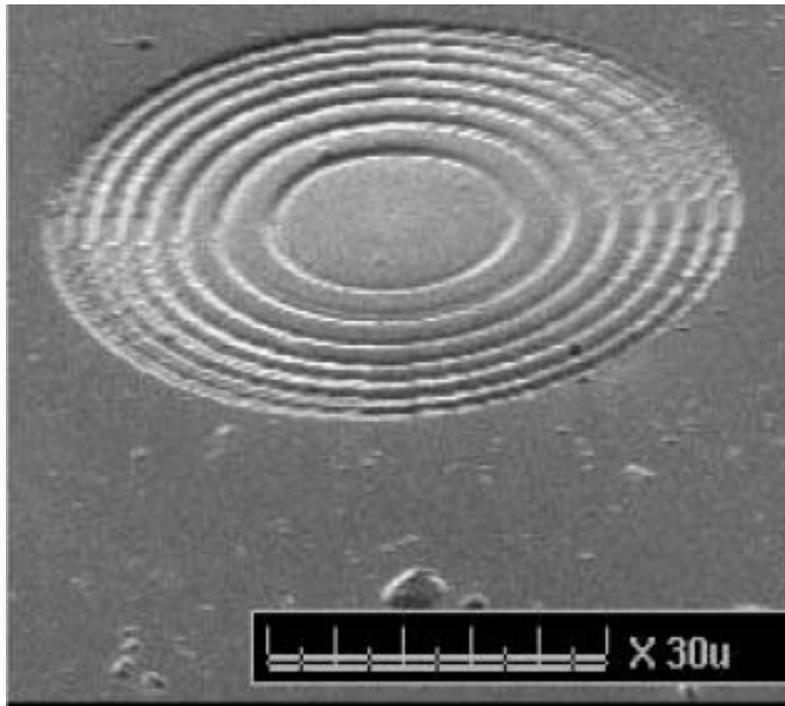


**Figure 1.2-13.** SEM micrograph of 65  $\mu\text{m}$  diameter diffractive optical element machined by FIB milling in diamond film [3]

Frese investigated LIGA as a technology for the manufacture of micro-optics [18]. His work achieved form error of  $\pm 5 \mu\text{m}$  over  $130 \mu\text{m}$  and typical surface roughness of 30 nm. A cylindrical lens in photoresist is shown in Figure 1.2-14.

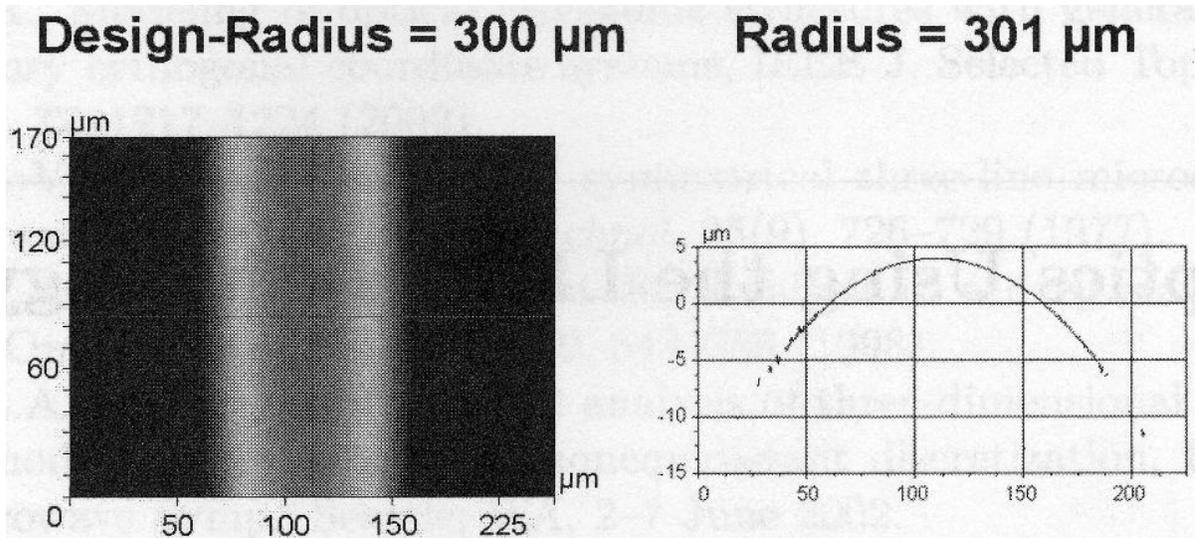


**Figure 1.2-14.** Contour Accuracy of PMMA structures processed by LIGA technology [18].

A proposed alternative to both traditional mechanical machining and to newer non-traditional machining techniques is EVAM. It replaces the high-speed spindle used in milling with a piezoelectrically driven tool holder that can move the diamond tool tip in an elliptical motion at frequencies up to 5000 Hz - the equivalent of 300,000 rpm. The two actuators are driven independently to create a tool path that can be changed from linear to elliptical to circular by changing the amplitude, frequency and phase of the excitation voltages. The widespread use of this process would have a profound influence on fabrication techniques for micro-mechanical, micro-optical and micro-fluidic devices. Its key features are:

- Optical surface finish
- Extremely low cutting forces
- No burring at the edge of a cut
- Applicable to a wide range of materials – metals, plastics and ceramics

### **1.3 VIBRATION ASSISTED MACHINING**

Several types of vibrating tool actuators are found in the literature. The earliest iterations had a one-dimensional vibrating tool path and operated at a single, resonant frequency [19]. A non-resonant, quasi-elliptical-path 2-D servo was developed at Pusan University, South Korea [20] and used in micromachining. Moriwaki [21] focused on turning hardened steel with a resonant, 2-D elliptical path device. A common finding by these researchers was reduced tool force or tool wear in comparison to conventional diamond turning. The PEC's approach to VAM is unique in that it combines a non-resonant structure, variable actuation frequency, and an elliptical tool path.

### **1.4 HISTORY OF EVAM AT NC STATE**

#### **1.4.1 UMLS**

The Ultramill Low Speed (UMLS) was fabricated using available components in the PEC to demonstrate the concept of Elliptical Vibration Assisted Machining (EVAM). The UMLS bandwidth was 400 Hz and the maximum voltage was 800V, yielding an elliptical tool path  $47.5 \times 7.3 \mu\text{m}$  [22, § 6.2.2]. The structure of the UMLS is shown in Figure 1.4-1.

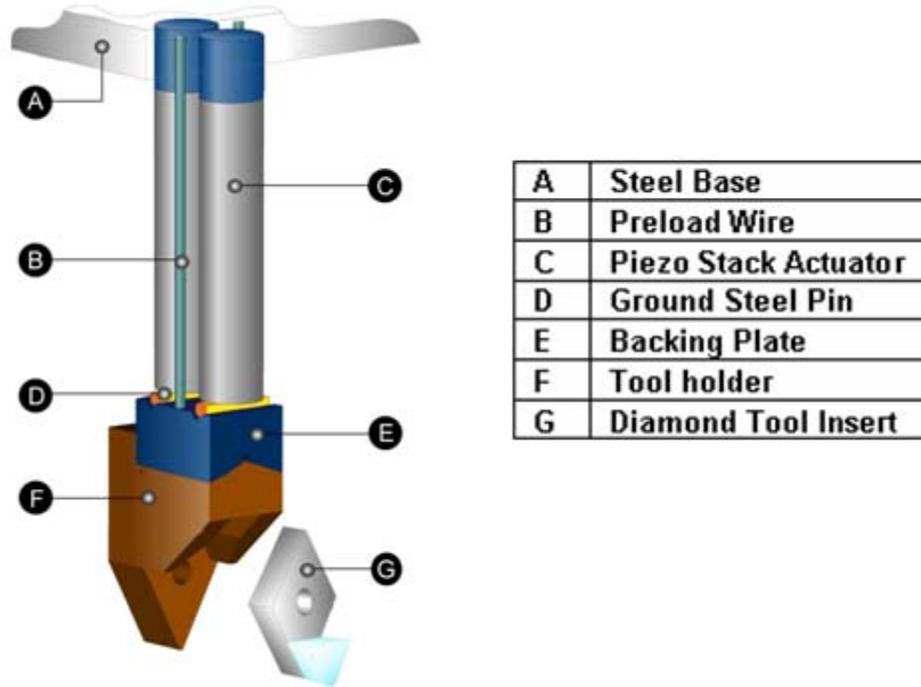


**Figure 1.4-1.** Ultramill low speed [22, § 1.3.4].

Cerniway [23, § 4.3.3] demonstrated that this iteration of the design performed better than conventional diamond turning in machining steel. The UMLS had feedrate limitations due to its low operating frequency. Another disadvantage of the design was failure of the preload wires. The Ultramill High Speed was designed to remedy these issues.

### 1.4.2 UMHS design

Cerniway designed the Ultramill High Speed (UMHS) with 4 kHz bandwidth. Its elliptical tool path is  $40.1 \mu\text{m} \times 8.5 \mu\text{m}$  at 600 Vpp (Volts peak-peak). A picture of both the old and new designs is shown in Figure 1.4-2.

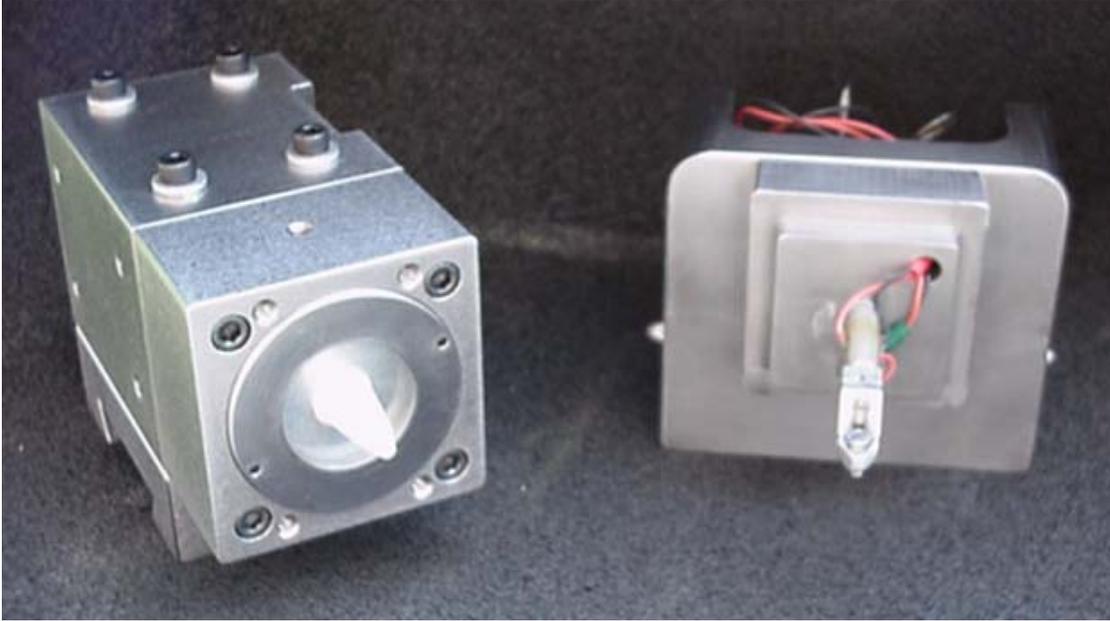


**Figure 1.4-2.** UMHS (left), UMLS (right) [22, § 2.0]

The UMLS used passive air cooling to keep the piezo stacks at operating temperature. Increased heating of the UMHS piezo stacks, due to the higher operating frequency, required liquid cooling. UMHS details will be discussed further in Section 2.

### **1.4.3 UMHS development**

Negishi [22] further developed the UMHS design and demonstrated its capabilities in turning applications. This work included design changes in the diamond tool holder, cooling system development and characterization, tool path measurement, and tool forces measurement. The UMHS, when used as a turning tool, demonstrated surface finishes of 7 nm RMS in acrylic and 8 nm RMS in SiC. Reduced tool forces and tool wear were also demonstrated when compared to conventional diamond turning for difficult-to-machine materials.

#### **1.4.4 Problem Statement: Micromachining with EVAM**

This research seeks to apply the UMHS to multi-level planar, non-rotationally symmetric micromachining. The following key questions were investigated:

- Is the Ultramill capable of multi-level microstructuring on a micrometer scale?
- What form and finish accuracy are attainable with the current experimental setup?
- How are the deviations from theoretical surfaces related to the limitations of the Nanoform 3-axis diamond turning machine (DTM) arrangement?

### **1.5 TERMINOLOGY**

The Ultramill High Speed is generally referred to as the Ultramill or UMHS in the rest of this thesis. A convention will be used throughout this thesis to differentiate between the vibrating elliptical motion of the Ultramill diamond tool and the overall motion of the Ultramill as a unit during machining operations. The Ultramill's diamond tool motion with respect to the Ultramill body will be referred to as the tool path. The motion of the Ultramill body with respect to the workpiece will be referred to as a motion plan or motion program.

## **2 EXPERIMENTAL APPARATUS**

### **2.1 ULTRAMILL STRUCTURE**

The Ultramill tool holder, preload diaphragm, and piezo stack actuators are pictured in Figure 2.1-1. The actuators are manufactured by Kinetic Ceramics. The cooling chamber doubles as the support structure for the preload system. The elements of the preload system

are shown in Figure 2.1-2. The Ultramill elliptical tool path will be discussed in Section 4.1.1.

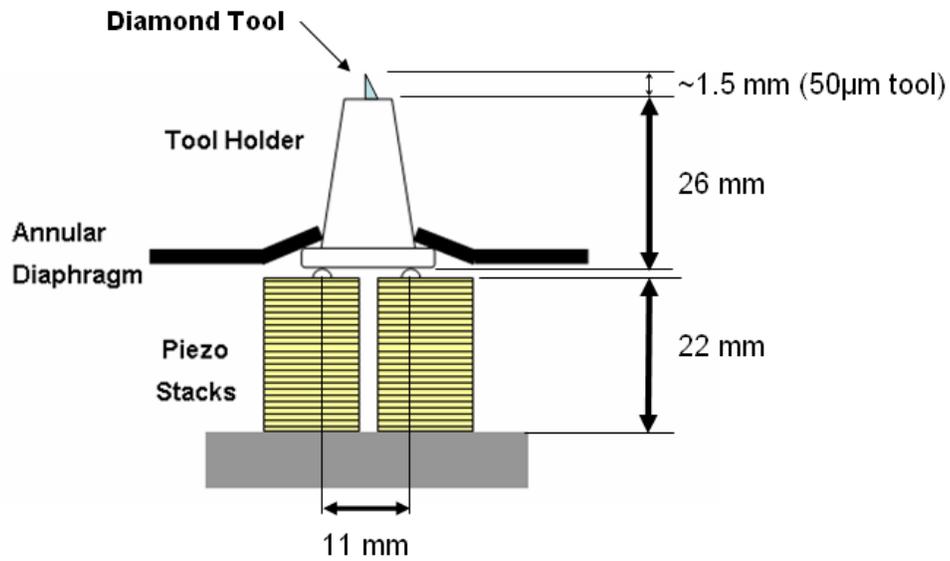


**Figure 2.1-1.** Ultramill preload system [22, § 2.1]

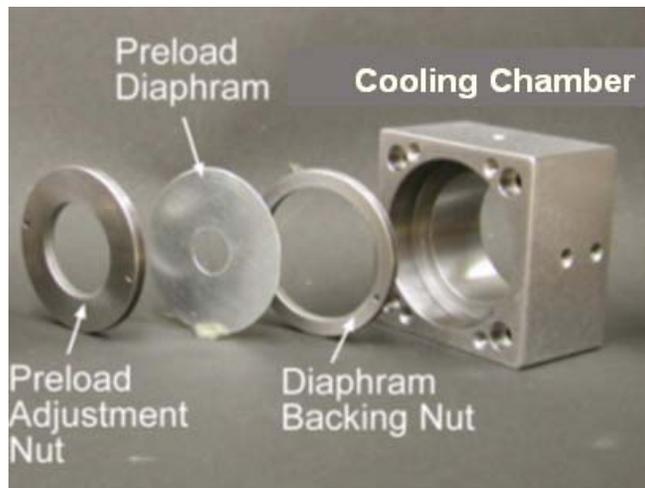


**Figure 2.1-2.** Ultramill cooling chamber and preload system [22, § 2.1.2]

## 2.2 COOLING SYSTEM

A photograph of the Ultramill with part of the cooling chamber cut away is shown in Figure 2.2-1 [22, § 2.1]. A diagram of the Ultramill cooling system is shown in Figure 2.2-2 [22, § 2.2.3].

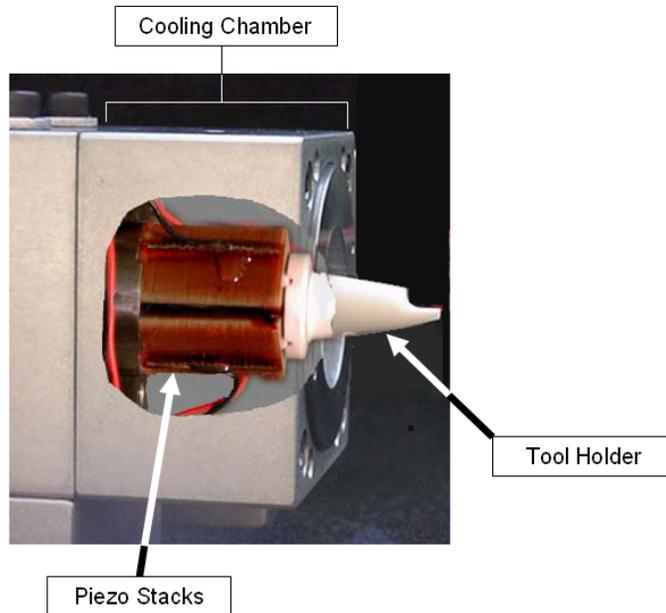


**Figure 2.2-1** Ultramill cooling chamber cut-away [22].

The reservoir, chiller, pump, and controller are contained within a Thermocube thermoelectric cooler. The controller maintains a constant temperature of the fluid returning to the reservoir from the Ultramill cooling chamber. This temperature is the setpoint of the Thermocube controller. The fluid used is 3M Fluoroinert 3283. It is a dielectric, extremely low viscosity coolant chosen to be compatible with the piezoceramic actuators and to promote turbulent convection [22, § 2.2.3]. The Thermocube is equipped with a 30 Hz diaphragm pump. A centrifugal pump is available for the Thermocube but the seals in this pump are not compatible with the Fluoroinert coolant. Pump vibration transmission to the

Ultramill was minimized by eliminating any connections between the pump and cooling chamber. A gravity feed is used to transfer coolant from the Thermocube output line to the Ultramill coolant chamber.

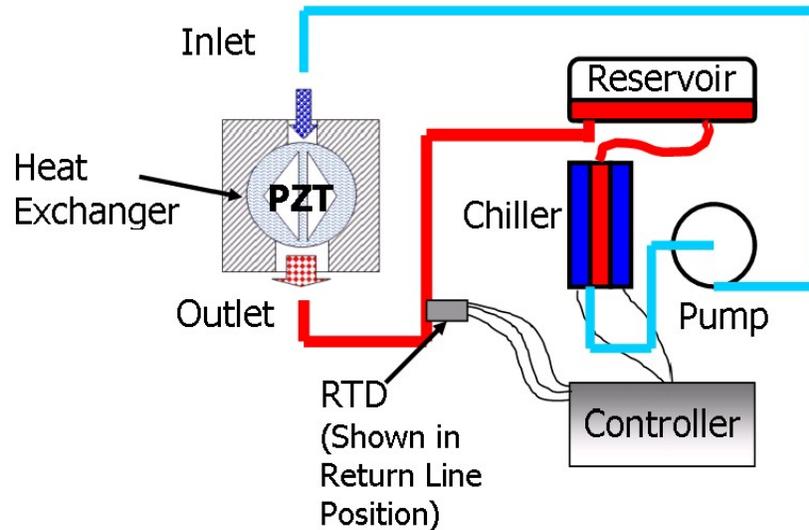
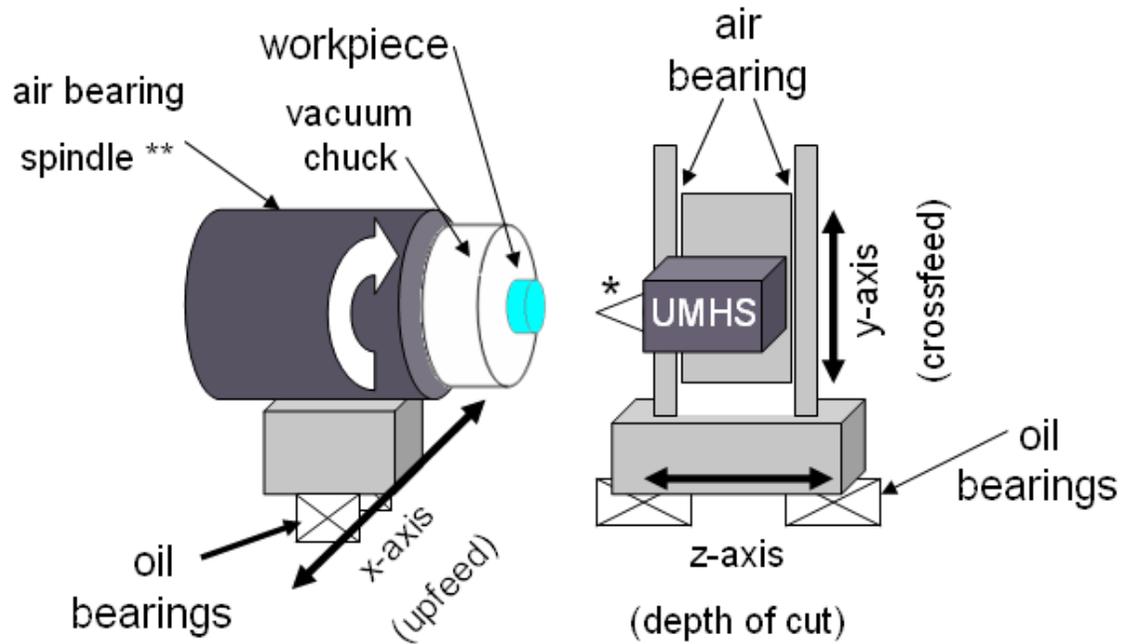


**Figure 2.2-2** Ultramill cooling system [22, § 2.2.3]

### 2.3 NANOFORM/ULTRAMILL INTEGRATION

The foundation of this research was the idea of replacing a high-speed milling spindle with the Ultramill. The Ultramill was adapted to the multi-level microstructuring application by mounting it on a Nanoform 600 3-axis DTM, as shown in Figure 2.3-1. The Zygo laser interferometers on the x- and z-axes allow the workpiece (x-axis) and the Ultramill (z-axis) to be moved in those directions with nanometer resolution. The x- and z-axis ride on oil-hydrostatic bearings. The Ultramill is mounted on the y-axis, guided by an air bearing, and a Heidenhain encoder provides 40-nm resolution in that direction. Upfeed motion for the

Ultramill is accomplished by motion of the x-axis and workpiece with respect to the Ultramill. Crossfeed motion is in the y-direction. Depth of cut is controlled by the z-axis. In standard diamond turning operations, parts are mounted on the DTM by means of a vacuum-operated chuck. This method was retained for the Ultramill.



\* elliptical tool path: in the x-z plane

\*\* rotates when using static diamond tool; locked when using Ultramill

**Figure 2.3-1.** Nanoform 600 setup (diagram).

### 3 EXPERIMENTAL PROCESS

#### 3.1 WORKPIECE PREPARATION

Parts to be machined are placed on the Nanoform vacuum chuck. Figure 3.1-1 shows a close-up of the vacuum chuck and Ultramill and shows the 130x video microscope used for Ultramill touch-off and process monitoring. The inset shows the rake face of the 1 mm radius Ultramill diamond tool and a side view of the static diamond tool (also mounted on the y-axis) used to turn parts flat before using the Ultramill. The workpiece is vacuumed to the rotating chuck, and the static tool is fed across the surface to make it flat and produce optical quality finish. After a blank is surfaced, the spindle is locked to prevent rotation during micromachining with the Ultramill. In the inset of Figure 3.1-1, the major axis (a) of Ultramill tool motion is in the x-direction and the minor axis (b) is in the z-direction.

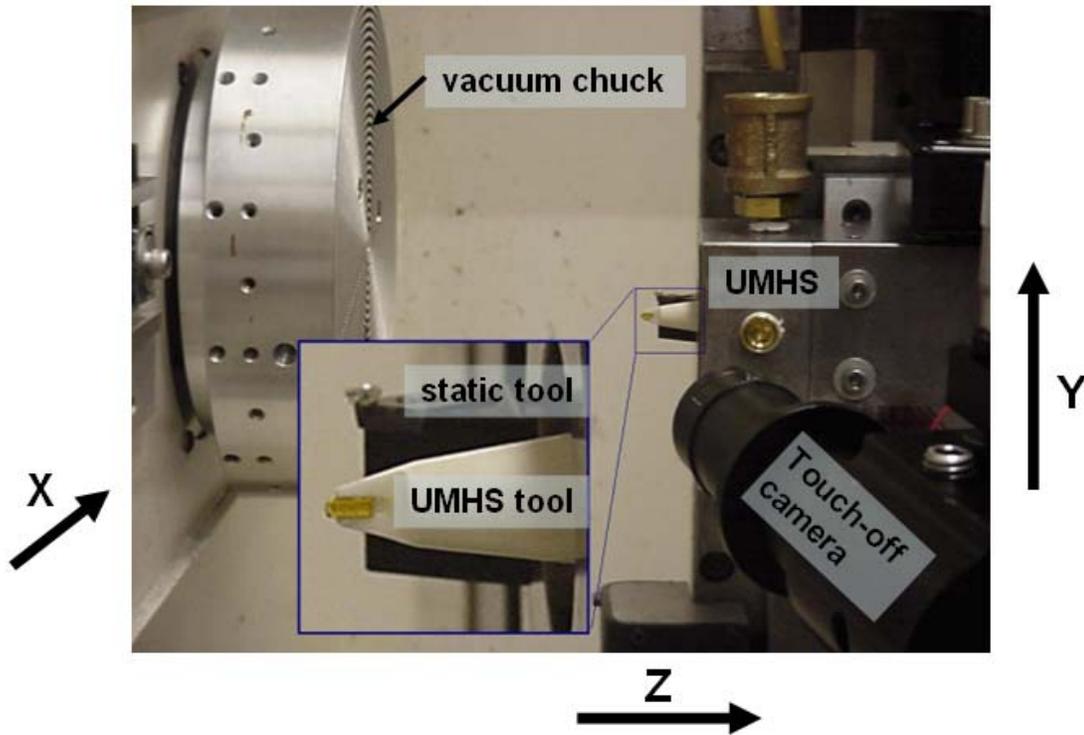


**Figure 3.1-1.** Details of experimental setup.

Flatness of the workpiece is important for Ultramill touch-off viability and for consistent Ultramill depth of cut (DOC), which influences tool forces. However, part sizes in the micromachining industry are sub-millimeter, and flatness at that length scale is not difficult to achieve with diamond turning. A form error of 25 nm RMS over several millimeters was found to be sufficient for the application.

### **3.2 TOUCH-OFF**

Touch-off is a standard procedure in diamond turning that has been modified for use with the Ultramill. In general, touch-off occurs when the smallest chip visible to the operator (under some magnification) is observed at the point where the tool touches the workpiece. When this occurs, the coordinate of the axis that controls depth of cut is set to zero. The small size of the microstructuring tools makes touch-off a challenging part of the process. The blank's optical surface finish on the order of 25 nm RMS is important in reflecting the image of the diamond tool. This reflection is used in the touch-off procedure. The workpiece must be cleaned of any cutting oil before Ultramill touch-off. A 130x video microscope, partially shown in Figure 3.1-1, is used to view the diamond tool and its reflection on the workpiece. Touch-off is performed with the Ultramill running. The vibrating tool motion in the DOC direction at 400 Vpp is about 4  $\mu\text{m}$  peak-to-peak<sup>1</sup>. At the minimum amplifier operating frequency of 1000 Hz, this motion is not visible. The approximate separation of the tool average position and its reflection, if greater than about 10  $\mu\text{m}$ , may be gauged by the video

---

<sup>1</sup> Negishi [22, Appendix L (column labels “a” and “b” should read “2a” and “2b”)]

image. The tool is half this distance from the workpiece. An image of the 50  $\mu\text{m}$  tool and its reflection in the workpiece is shown in Figure 3.2-1. The 0.45 mm distance illustrated is twice the actual distance from the tool tip to the surface. The Nanoform z-axis is zeroed when a chip is seen to form at the common edge of the tool and its reflection.

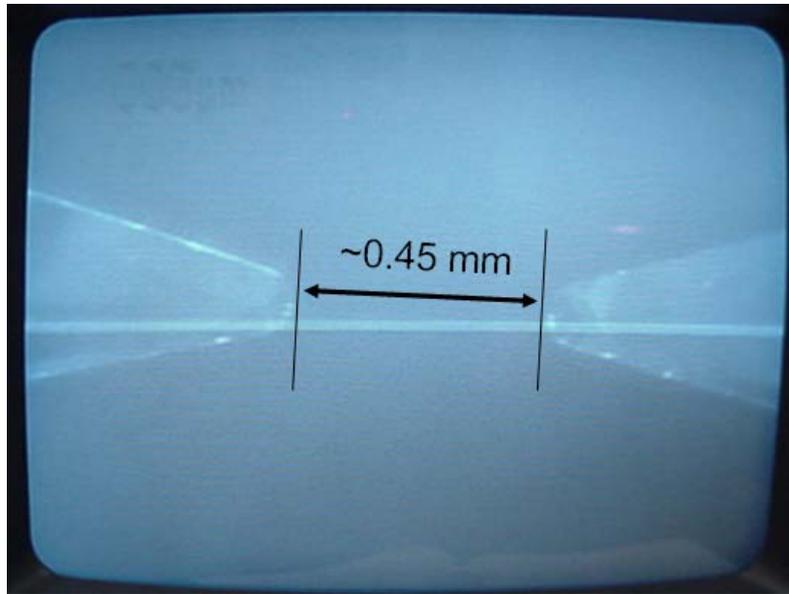


**Figure 3.2-1.** Touch-off view, 50  $\mu\text{m}$  radius tool and reflection, 130x video microscope

Cleaning of both the diamond tool and workpiece are important for the touch-off procedure. Cleaning procedures may be influenced by several factors. If the workpiece has been diamond-turned during the current setup of the DTM, and workpiece flatness is critical to the part program, the part should not be removed for ultrasonic cleaning. The operator should clean the workpiece while on the machine with an acetone-soaked optical wipe. If the workpiece may be removed from the vacuum chuck before the next attempt at touch-off, it

should be ultrasonically cleaned<sup>2</sup>. The Ultramill diamond tool may be cleaned while the piezo stacks are running by repeated flushing with acetone and near-zero-force wiping with an optical wipe. Shop-grade compressed air blow-off should be avoided after cleaning, because oil or water in the air may be deposited on the workpiece or the tool.

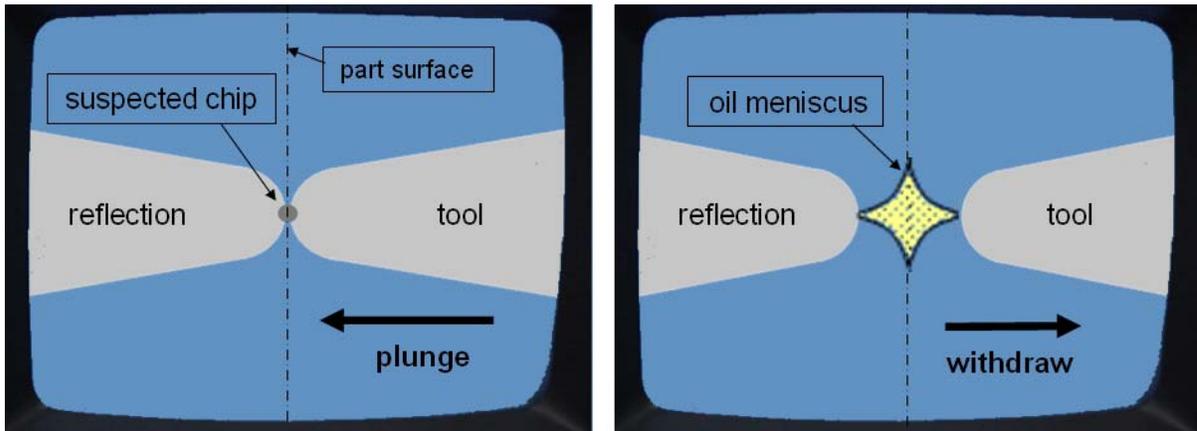


**Figure 3.2-2.** Identification of a phantom chip.

A “phantom chip” of oil meniscus has been observed above the surface of the workpiece in cases where either the tool or the workpiece was dirty before touch-off. Figure 3.2-2 shows the process for identifying a phantom chip. As apparent distance between tool and tool reflection goes to zero, a suspected chip (Figure 3.2-2, left) will be seen at the common edge. The z-axis coordinate on the DTM should be either noted or set to zero at this time. If the suspected chip grows almost instantly to tens of micrometers in size after a very shallow (<1  $\mu\text{m}$ ) plunge toward the workpiece, it may not be a machined chip. To check, the tool should be withdrawn from the part. If a “liquid-like” feature such as that seen in Figure 3.2-2 (right)

---

<sup>2</sup> workpieces ultrasonically cleaned with Alconox Liqui-Nox detergent and deionized water

is observed at 1  $\mu\text{m}$  or more from the previous plunge depth (while lengthening the withdrawal distance), an operator may conclude that the workpiece or tool was dirty and that the workpiece surface has not been penetrated by the tool. Both should be cleaned thoroughly before the next attempt at touch-off.

If the check procedure for a phantom chip produces no oil meniscus, the tool may be plunged deeper into the workpiece by single 20 to 200 nm steps in an attempt to confirm a solid chip. If the Ultramill tool is plunged further into the part, and a possible chip appears to grow slowly but remains solid in appearance, confidence in the touch-off is increased. After touch-off and the addition of a few drops of cutting oil<sup>3</sup> from a wash bottle or medicine dropper, the video microscope should be zoomed out to increase the depth of field and field of view in preparation for machining. As the Ultramill traverses through an upfeed pass, chip flow may be seen in the oil meniscus around the tool, confirming that machining is actually taking place. At a medium light level chips will be seen as rapidly-moving “stars” in the cutting oil.

### **3.3 RASTERING SEQUENCE**

Micromachining is accomplished by rastering the Ultramill across the face of the part. Figure 3.3-1 shows an example machining sequence of five raster passes for a flat with no depth changes. In this example the upfeed distance is 2 mm and the crossfeed increment is 1  $\mu\text{m}$  per pass. Negative-x direction on the Nanoform 600 is the upfeed direction for the

---

<sup>3</sup> Mobilmet Omicron used in all experiments

Ultramill. At touch-off the z-axis is zeroed at the apparent surface of the part. In the Nanoform coordinate system, negative-z displacements from zero are deeper into the part, and a move from zero to a negative-z displacement constitutes the depth of cut (DOC) plunge. In Figure 3.3-1, the programmed depth of cut is 3  $\mu\text{m}$  and clearance from the part during x-axis backfeed is 1.5  $\mu\text{m}$ .

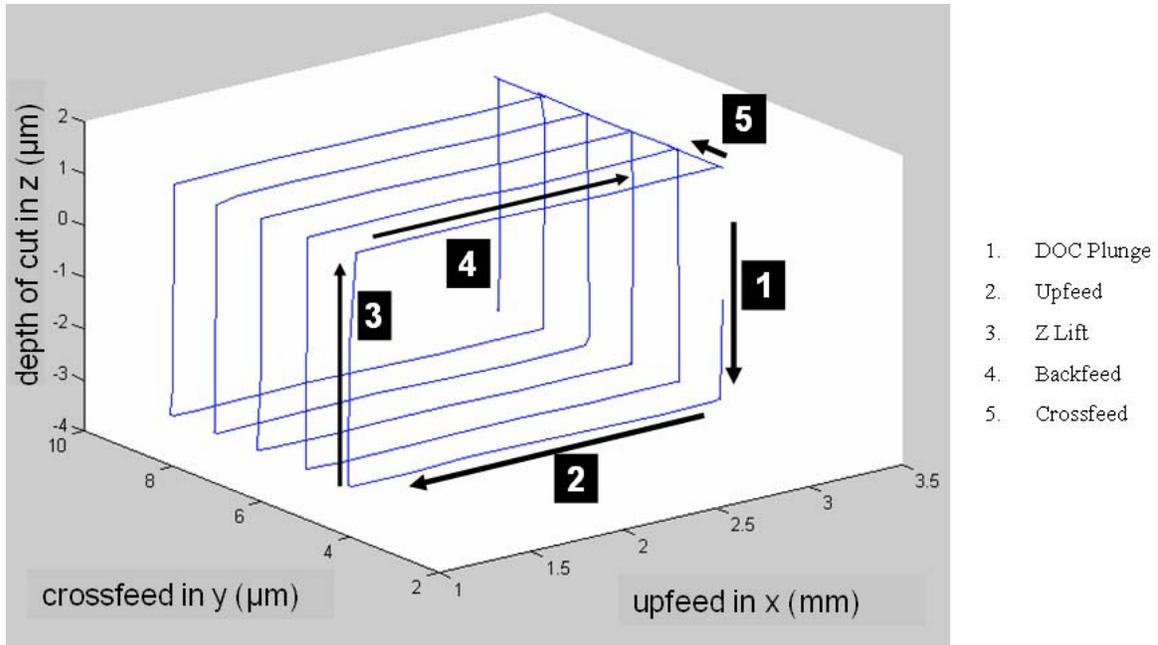


**Figure 3.3-1** Rastering sequence

Between part programs, it is useful to blow off the cutting oil with compressed air to clear most of the chips. Contamination by the oil and water in shop-grade compressed air are not problematic after touch-off. After fresh cutting oil is added and a new part program started, a similar amount of chip flow should be observed in the cutting oil meniscus.

## **4 MICROMACHINING EXPERIMENTS**

### **4.1 ULTRAMILL MOTION PLANNING**

Traditional milling motion programs require that the tool center path be offset from the desired surface by the tool radius. The elliptical motion of the Ultramill diamond tool means that the effective tool shape is an ellipse and therefore the offset distance will be a function of the relative orientation of the Ultramill and the desired structure. This section discusses how Ultramilled surface features affect the motion program path and methods of Ultramill motion planning.

#### **4.1.1 Ultramill Elliptical Tool Path**

The Ultramill linkage consists of two parallel piezoceramic actuators with a tilting tool holder and diamond tool (see Figure 2.1-1). The elliptical tool path is generated by actuating the piezo stacks with out-of-phase sinusoidal voltages. The structure and tool path is shown in Figure 4.1-1.

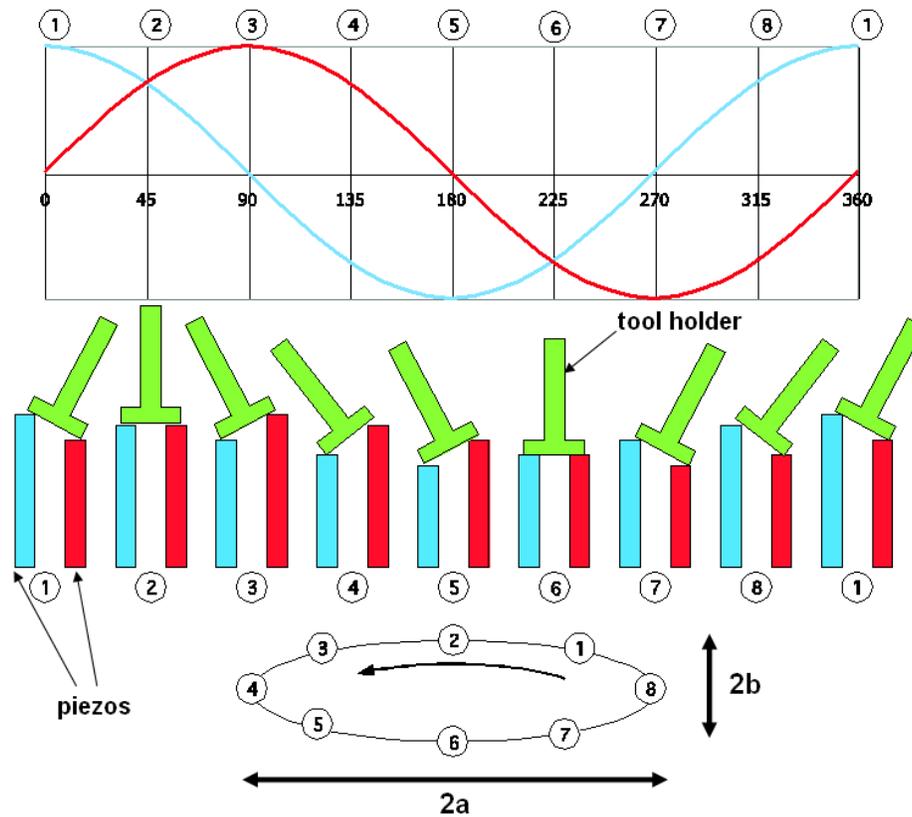


**Figure 4.1-1.** Elliptical tool path.

The graph at the top of Figure 4.1-1 shows the  $\cos(t)$  voltage signal applied to the left-hand piezo stack and the  $\sin(t)$  actuation applied to the right-hand stack. The changes in length of the piezo stacks and resulting position of the tool holder are illustrated in the bottom of the Figure 4.1-1. Kinetic Ceramics' specification for the change in length of one piezo stack for a 400 volt peak-to-peak ( $V_{pp}$ ) sine wave is  $9 \mu\text{m}$ . The measured tool path ellipse is  $21.4 \mu\text{m}$  in the major direction ( $2a$ ) and  $4.0 \mu\text{m}$  in the minor direction ( $2b$ ) for a 400  $V_{pp}$  sine wave at  $1000 \text{ Hz}$ <sup>4</sup>. In the case of 1000 Hz voltage signals, the elapsed time of this cycle would be

---

<sup>4</sup> Negishi [22, Appendix L (column labels "a" and "b" should read "2a" and "2b")]

one millisecond. An illustration of successive Ultramill upfeed cycles is shown in Figure 4.1-2 [22, § 3.2].

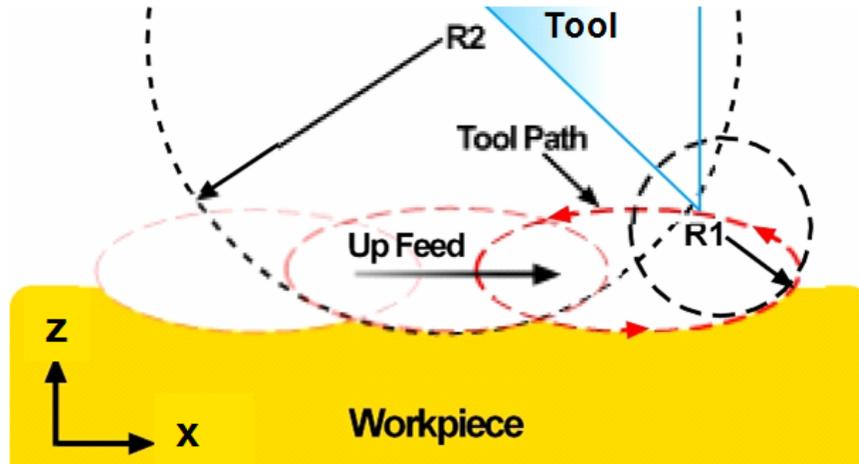


**Figure 4.1-2** Three Ultramill upfeed cycles

$R_2$  is the approximate surface radius at the bottom of a single cycle, assuming an elliptical tool path, and is defined in Equation 1 [22, § 3.2].

$$R_2 = \frac{a^2}{b} \quad (1)$$

$R_1$  is a transient chip radius that is not seen on a finished part because it is eliminated by a subsequent upfeed cycle.

### 4.1.2 Ultramilled Surface Features

Microstructured features on Ultramilled parts depend on elliptical tool path size, tool radius, feed speed or increment of the Nanoform axes, and depth of cut. A characteristic Ultramilled

surface feature created by a plunge into the part may be described by the terms depth of cut (DOC), characteristic feature size in crossfeed ( $c_{\text{cross}}$ ), and characteristic feature size in upfeed ( $c_{\text{up}}$ ). The characteristic feature size in crossfeed is equal to the chord of the tool radius at a given depth of cut and is illustrated in Figure 4.1-3.

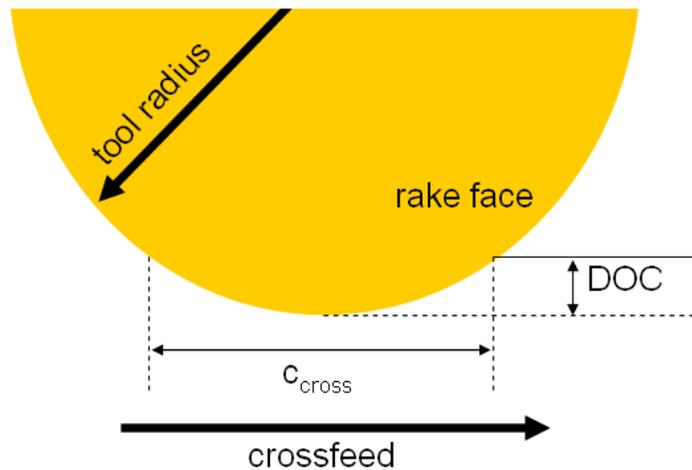


**Figure 4.1-3.** Crossfeed-direction characteristic feature size

The characteristic feature size in the upfeed direction is equal to the chord of the tool path at the depth of cut. It is illustrated in Figure 4.1-4.

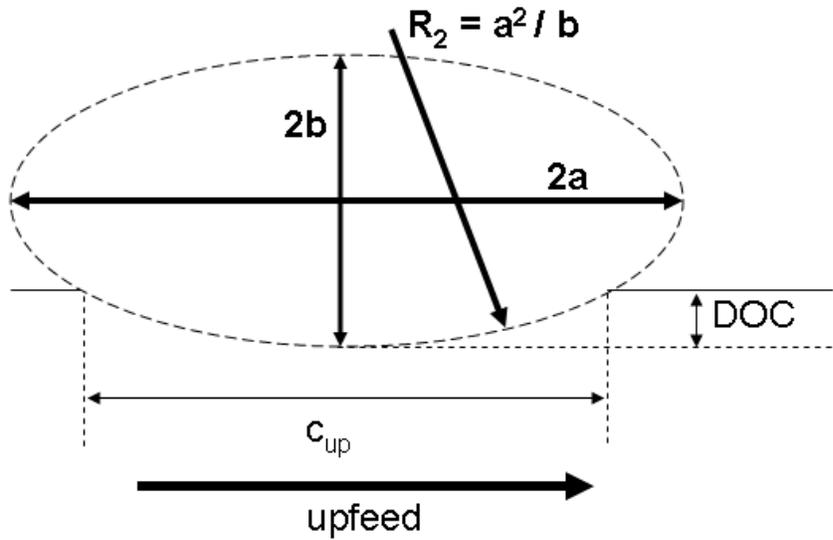


**Figure 4.1-4.** Upfeed-direction characteristic feature size ( $DOC < b$ )

$R_2$  is the approximate workpiece surface radius at the bottom of an Ultramill cycle. The size of the characteristic feature in the upfeed direction may be calculated with Equation 2:

$$c_{up} = \frac{2 \sqrt{2 b DOC - DOC^2} a}{b}, \quad (DOC < b) \quad (2)$$

The relationship between  $c_{cross}$  and  $c_{up}$  as a function of DOC, for the 50  $\mu\text{m}$  and 1 mm radius tools used in this research, is shown in Figure 4.1-5. The graph uses a constant 400 Vpp, elliptical tool path; varies the depth of cut, and shows different traces for the two tool radii. The characteristic feature size in upfeed ( $c_{up}$ ) does not vary with tool radius (only with elliptical tool path size), and is constant at a given DOC. The characteristic feature size in crossfeed ( $c_{cross}$ ) does not vary with elliptical path size, but does vary with tool radius and DOC. The characteristic surface feature created on the workpiece for  $DOC < b$  is shown in

Figure 4.1-6. The relative DOC between all multi-level machined surfaces in this research is less than b.

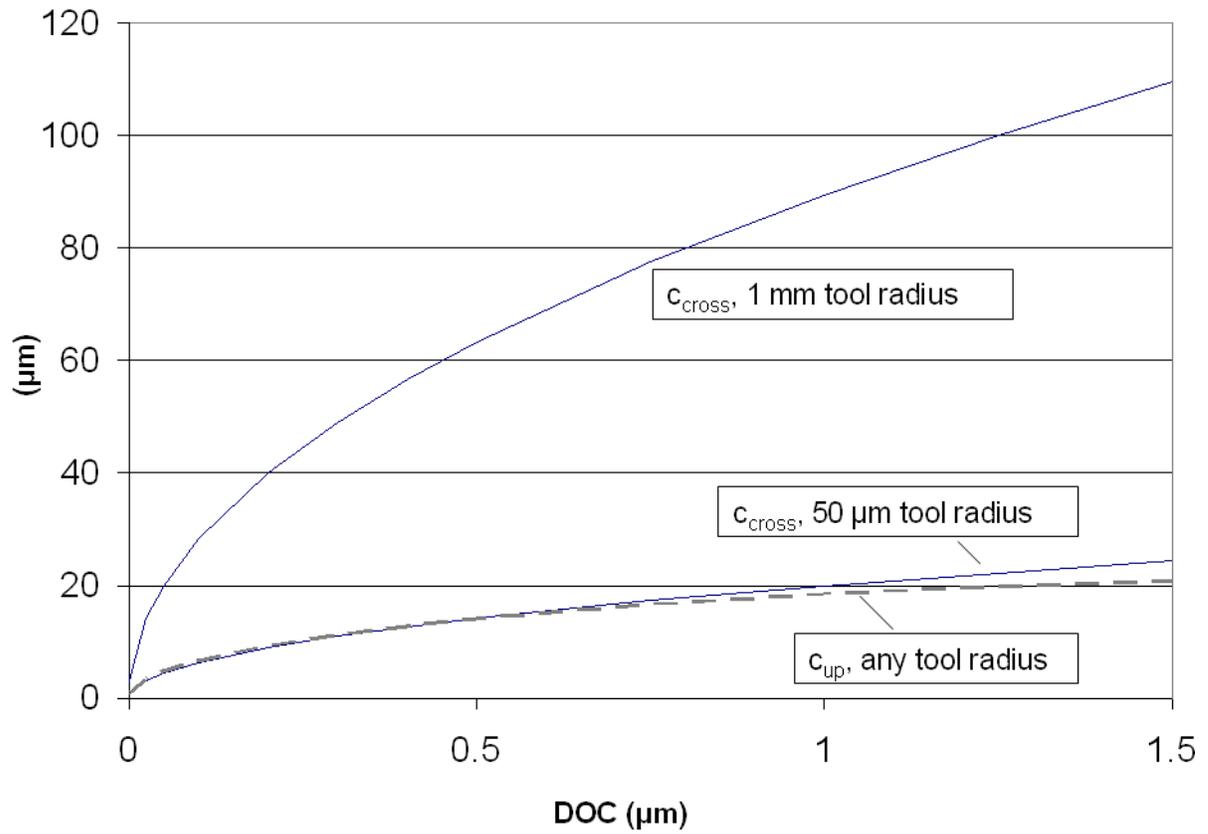


**Figure 4.1-5.** Characteristic feature sizes vs. DOC

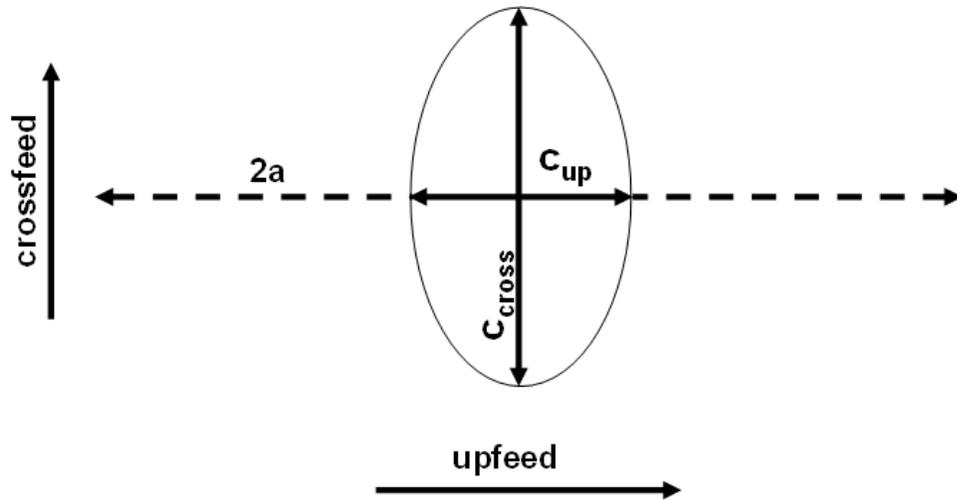


**Figure 4.1-6.** Characteristic surface feature ( $DOC < b$ ).

This feature is elliptical ( $c_{cross} > c_{up}$ ) when the tool radius is much greater than  $R_2$ , as with the 1 mm radius diamond tool. It is roughly circular ( $c_{cross} \sim c_{up}$ ) when the tool radius is approximately equal to  $R_2$ , as with the 50  $\mu\text{m}$  radius diamond tool. This characteristic surface feature must be taken into account when programming Ultramill tool motion to produce a multi-level microstructure. If a feature is to remain on the part, the Ultramill may approach it no closer than  $c_{up} / 2$  in the upfeed direction or  $c_{cross} / 2$  in the crossfeed direction during the machining process.

### 4.1.3 Surface Finish

The theoretical surface finish of a raster-cut flat surface is affected by Ultramill actuation frequency, elliptical tool path, tool radius, upfeed speed and crossfeed pass increment. The peak-to-valley (PV) surface finish in the upfeed direction, using a parabolic approximation of the elliptical tool path, is given by Equation 3 [22, § 3.2.3]:

$$PV = \frac{ufpc^2}{8(R_2)} \quad (3)$$

where  $ufpc$  is the upfeed per cycle, and is defined by Equation 4 [22, § 3.2.1]:

$$ufpc = \frac{V_{Workpiece}}{f_{UM}} \quad (4)$$

where  $f_{UM}$  is the Ultramill actuation frequency.  $R_2$  in Equation 3 is the surface radius of the workpiece at the bottom of an Ultramill cycle, assuming an elliptical tool path, given in Equation 1 (Section 4.1.1).  $PV$  surface finish in the crossfeed direction is defined by Equation 5 [22, § 5.1.1]:

$$PV = \frac{f^2}{8(R_t)} \quad (5)$$

where  $R_t$  is the tool radius and  $f$  is the crossfeed increment per pass.

#### 4.1.4 Ultramill Motion Programming

An Ultramill motion program path must be planned using varying approach distances between the Ultramill characteristic feature centroid and a desired structure. These approach distances depend on the relative orientation of the Ultramill tool with respect to the microstructure. As discussed in the previous section, a minimum-size characteristic surface feature created by the Ultramill is characterized by the length of cut in the upfeed direction

and by the width of cut in the crossfeed direction. If a desired microstructure is comprised of features orthogonal to the tool rake face and to the tool path major and minor dimensions, raised features may be preserved by limiting the motion program approach distance to either  $c_{up}/2$  in the upfeed direction or  $c_{cross}/2$  in the crossfeed direction. Desired microstructure features not parallel to either feed direction require graphical planning of the motion program approach distance.

This requirement is illustrated in Figure 4.1-7. The drawing shows a section of a 1mm x 1mm angstrom symbol with Ultramill characteristic features placed at critical points in the shape to be machined.

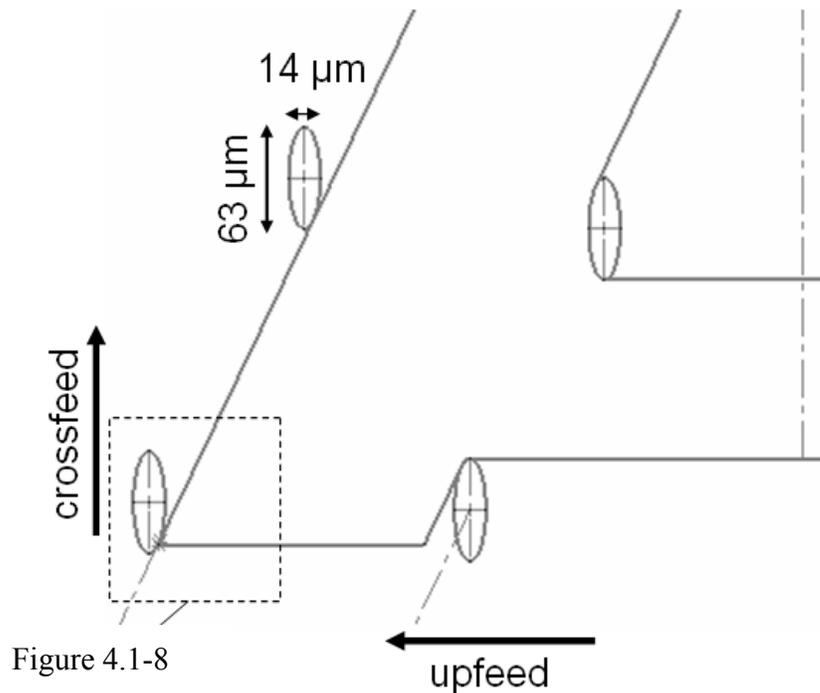


**Figure 4.1-7.** Ultramill features

The angstrom symbol, the logo of the Precision Engineering Center, was used as a proof-of-concept microstructure design for Ultramill motion planning. A 1 mm-scale angstrom symbol was designed to be machined with the 1 mm radius diamond tool mounted on the Ultramill. In this example, the letter was raised over the background and the change in height is 500 nm. At that change in DOC and with ellipse parameters  $a = 11 \mu\text{m}$  and  $b = 2 \mu\text{m}$ , the characteristic feature cut by the Ultramill is an ellipse  $63 \mu\text{m}$  wide in the crossfeed direction by  $14 \mu\text{m}$  long in the upfeed direction. If a raised feature is to be preserved, tool motion must be offset so that the raised feature has no interference with the Ultramill elliptical tool path at the planned depth of cut. In the case of the diagonal sides of the A, that amount is equal to the distance from the ellipse centroid to the ellipse's point of tangency with the diagonal feature.

Figure 4.1-8 shows the detail of a corner of the angstrom symbol. Upfeed motion of a given pass must be stopped before the Ultramill characteristic surface feature collides with the desired geometry. The location shown for each pass in Figure 4.1-8 is the pause in upfeed motion prior to a change in depth of cut before a raised feature. The elliptical approach to this corner results in a different coordinate for this pause in each subsequent pass. Calculation of these points for the angstrom symbol program was done using CAD software to model each pass. The program for the  $200 \mu\text{m}$  angstrom symbol is included in Appendix C.

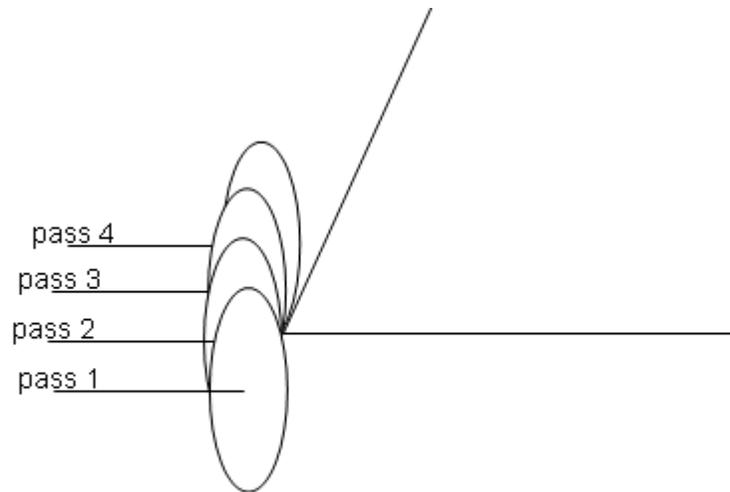


**Figure 4.1-8.** Elliptical approach to corner.

## **4.2 MICROMACHINING RESULTS**

A number of different features were machined using the Ultramill on the DTM. Some made use of the Ultramill characteristic feature to define binary-level microstructures while others were used to find the limits of form and finish possible with the system. Two sizes of binary structures and multiple Ultramilled flats were machined. Of the binary microstructure type, the first was a 1 mm-scale version of the Precision Engineering Center angstrom logo. The second was a 200  $\mu\text{m}$  x 200  $\mu\text{m}$  version of the logo. The comparative size of the structures is shown in Figure 4.2-1. Upfeed and crossfeed directions in the rastering sequence are shown for reference.

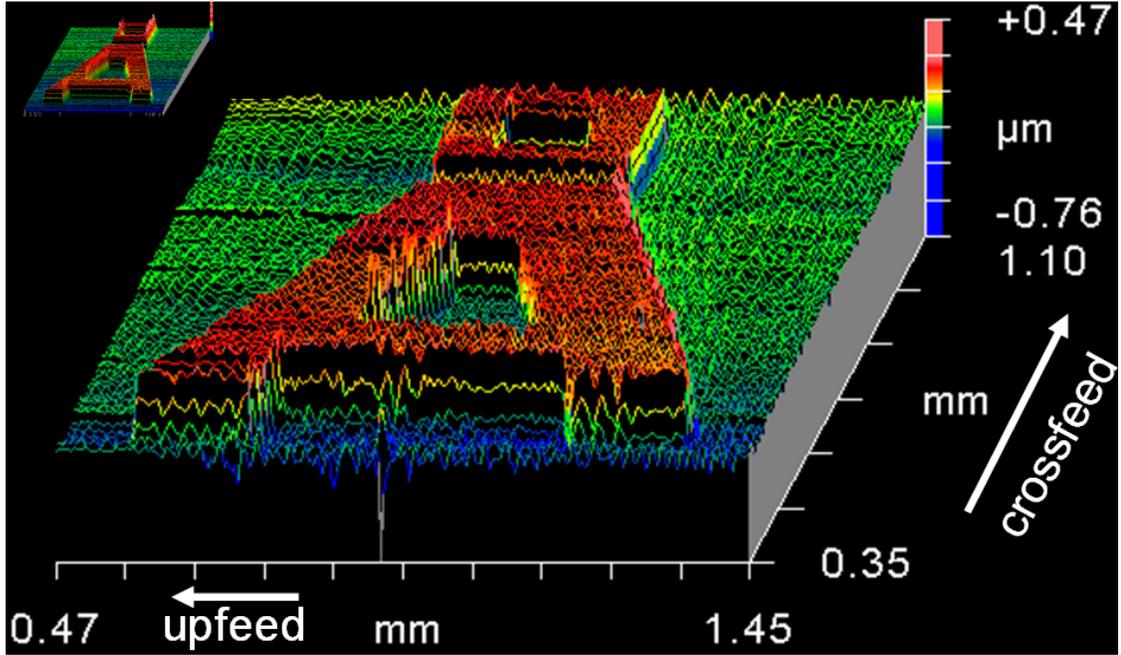
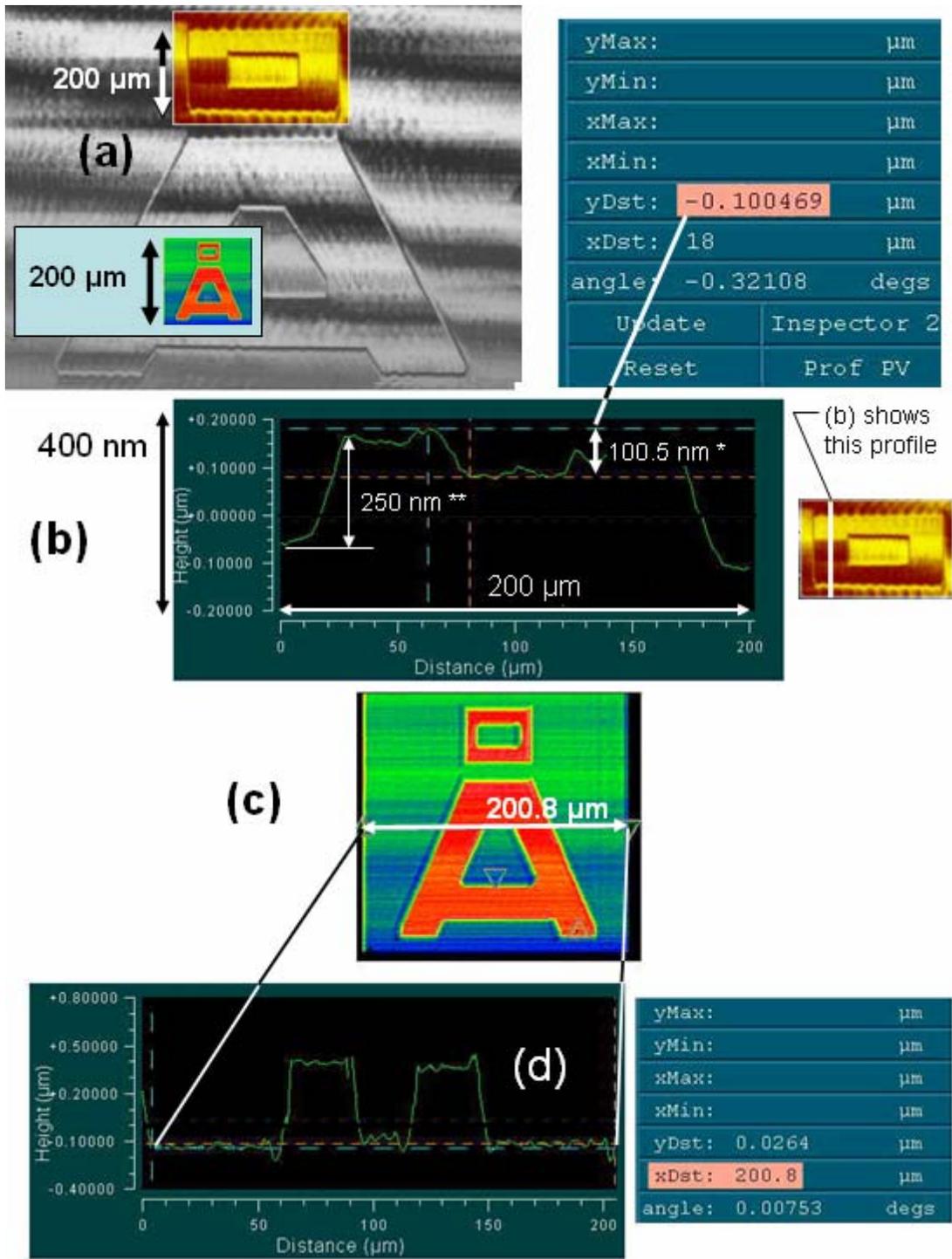


**Figure 4.2-1.** While light interferograms of 1 mm-scale angstrom symbol, 200  $\mu\text{m}$  symbol (top left)

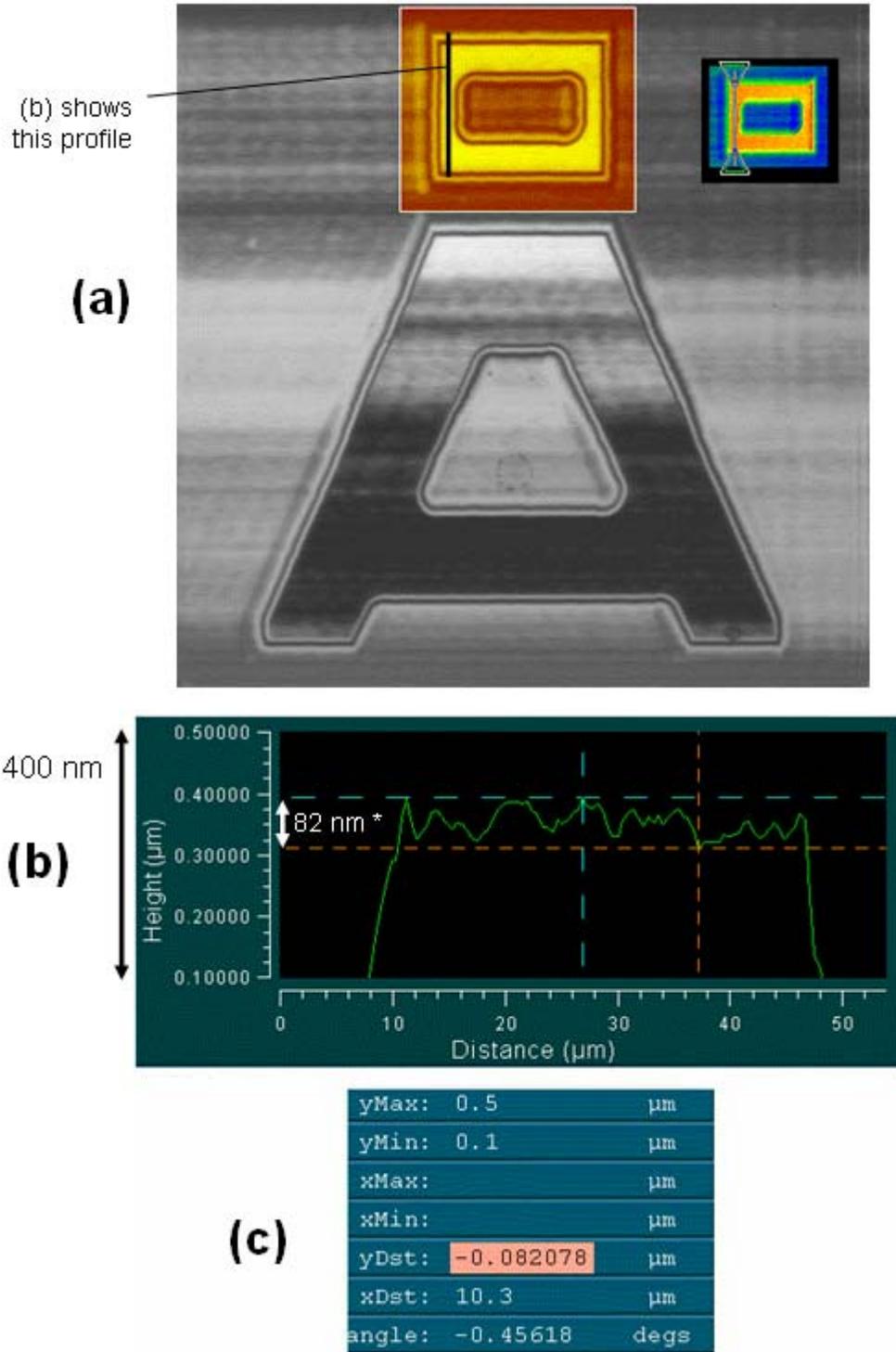
The smaller angstrom symbol is approximately the size of the “topknot” feature in the larger angstrom symbol. Figure 4.2-2 (a) again shows the comparative sizes of the two symbols. Figure 4.2-2 (b) illustrates the  $\sim 150 \mu\text{m}$  crossfeed-direction size of the topknot in the larger angstrom symbol, the  $\sim 100 \text{ nm}$  flatness of the topknot feature, and the 250 nm DOC (depth of cut) change between the foreground and background. The design change in DOC was 500 nm. Figure 4.2-2 (c) and (d) show the 200  $\mu\text{m}$  upfeed-direction dimension of the smaller angstrom symbol.



- \* 1 mm-scale angstrom symbol top section finish error  $\sim 100$  nm
- \*\* 1mm-scale angstrom DOC  $\sim 250$ -300 nm (design value = 500 nm)

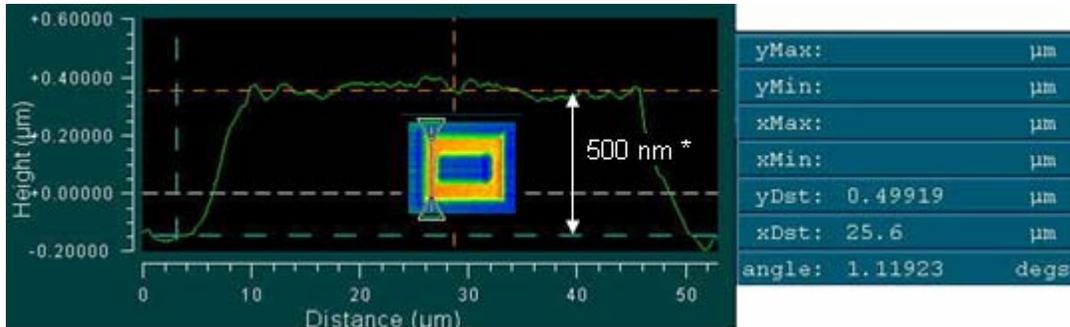
**Figure 4.2-2.** 1 mm-scale and 200  $\mu\text{m}$  angstrom symbols; comparative dimensions

Figure 4.2-3 (b) and (c) show the dimensions of the profile highlighted in Figure 4.2-3 (a).  
 The flatness of the topknot in this symbol is 82 nm.



**Figure 4.2-3.** 200  $\mu\text{m}$  angstrom symbol top section flatness (\*) ~ 82 nm.

Figure 4.2-4 shows the change in depth of cut between the foreground and background of the topknot feature on the 200  $\mu\text{m}$  angstrom symbol. This dimension is 500 nm, equal to the design value. Further details on the features and errors in both symbols are given in the following sections.



**Figure 4.2-4.** 200  $\mu\text{m}$  angstrom symbol DOC  $\sim$  500 nm (design value = 500 nm).

### 4.2.1 Large Angstrom Symbol

Figure 4.2-5 shows a 1mm x 0.77 mm area machined with the PEC angstrom logo. The design change in depth of cut between foreground and background is 500 nm. The design dimensions of the flat area in the background of this symbol were 1 mm x 1 mm. The machined area is 1 mm wide  $\pm$  5  $\mu\text{m}$  in the upfeed (Nanoform x-axis) direction but only 0.77 mm tall in the crossfeed (y-axis) direction. Another check dimension is shown in Figure 4.2-6, with a value of 394  $\mu\text{m}$ . The design value for this dimension was 487  $\mu\text{m}$ .

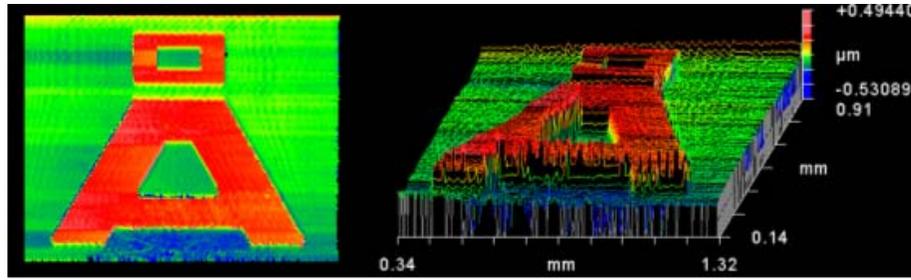


**Figure 4.2-5.** PEC 1 mm-scale angstrom logo(white light interferogram).

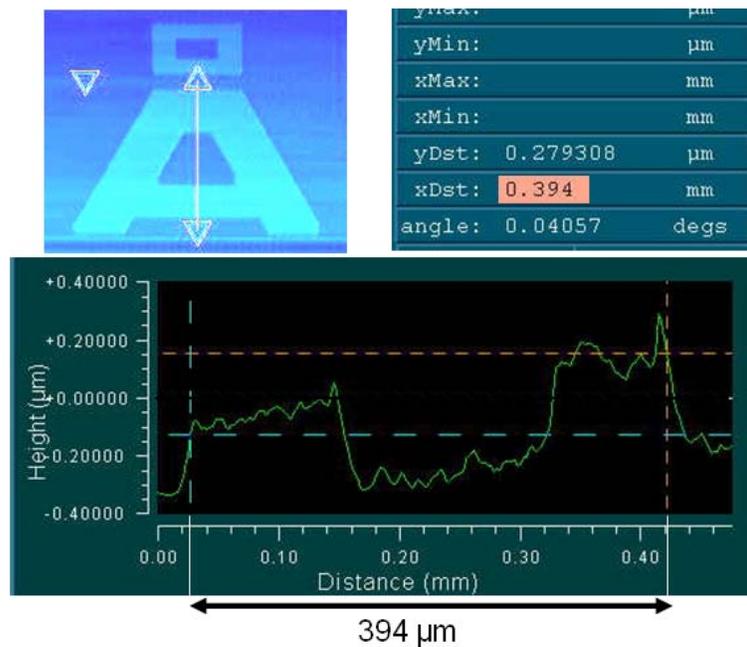


**Figure 4.2-6.** 1mm-scale angstrom symbol crossfeed check dimension (394 μm measured, 487 μm design)

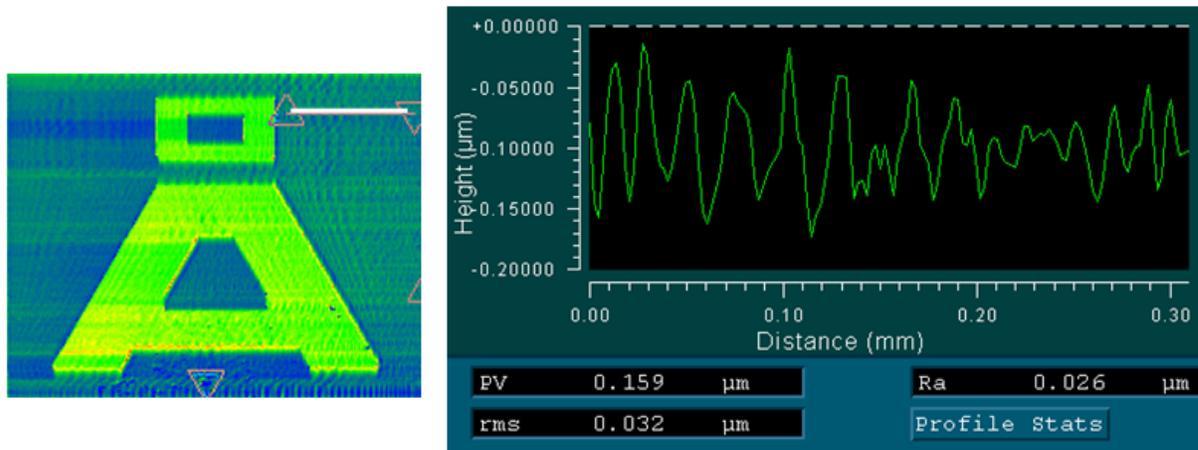
While the design difference in depth of cut between the two levels was 500 nm, a difference of only 200-300 nm was achieved. This change affects the expected size of plan-view features. The design of the 1 mm-scale angstrom symbol used an Ultramilled characteristic feature size of 63 μm in the crossfeed direction at 500 nm depth of cut. The feature size is reduced to about 45 μm in the crossfeed direction at 200-300 nm depth of cut. For a crossfeed-direction foreground feature on the size scale (500 μm) of the check dimension in

Figure 4.2-6, this reduction in Ultramilled characteristic feature size would be expected to cause an 18  $\mu\text{m}$  (4%) expected increase in the dimension. The observed error in the check dimension in Figure 4.2-6 is higher than this value, and the measured value is smaller than designed, as opposed to larger. The 394  $\mu\text{m}$  measured value of the check dimension is 81% of the design value. This deviation shows agreement with that of the overall crossfeed dimension of the symbol, which was 77% of the design value. Electrical noise caused by the DTM axis motor amplifiers was found to cause errors in the interface between the y-axis encoder and the Nanoform control system. This source of error was corrected before the 200  $\mu\text{m}$ -scale angstrom symbols were made (see Section 4.2.3).

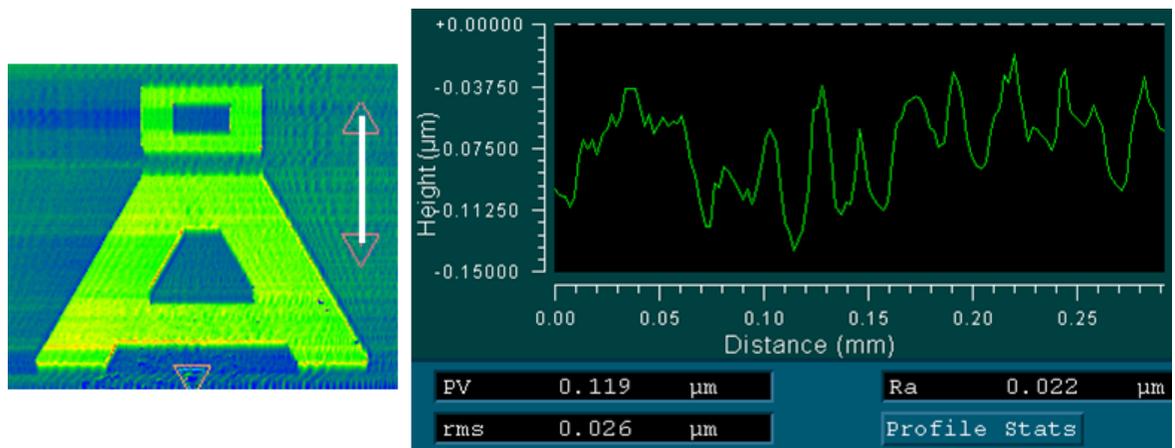
### **Surface Finish**

Figure 4.2-7 shows a background upfeed direction profile of the 1 mm-scale angstrom symbol. The x-axis controls upfeed, but x-axis speed is zero at all depth-change points for the z-axis. The small upfeed distances between depth changes, ranging from a few tens of micrometers to the full part width of 1 mm, were insufficient distances for the x-axis to reach the programmed upfeed speed. Because the x-axis was accelerating to reach the programmed speed or decelerating before a depth change over the entire surface of the part, upfeed speed was not constant at any point. Surface frequencies and prediction of surface features can only be averaged over distance. The average upfeed speed in this upper section of the symbol was about 2.4 mm/sec. The expected surface finish in this profile was about 12 nm, and the expected surface frequency was 416 cycles/mm. This upfeed profile demonstrates much higher error than expected, and has visible surface frequencies lower than the Ultramill

operating frequency. A background crossfeed profile is shown in Figure 4.2-8. The expected PV error in this profile was 3.1 nm, with a spatial frequency equal to the crossfeed spatial frequency of 200/mm. The crossfeed profile also shows much higher error and lower spatial frequency than expected.



**Figure 4.2-7.** Angstrom background upfeed profile (white light interferogram)



**Figure 4.2-8.** Angstrom background crossfeed profile (white light interferogram)

## 4.2.2 Small Angstrom Symbol

A smaller diamond tool was installed on the Ultramill tool holder to reduce feature size capability. The radius of the smaller tool is 50  $\mu\text{m}$  and the included angle is 58 degrees. As shown in Section 4.1.2, the characteristic Ultramilled surface feature with this diamond tool is 14  $\mu\text{m}$  wide (in crossfeed) at a DOC of 500 nm. This is a 78% reduction in characteristic feature width from the size used to design the 1 mm-scale angstrom symbol. The characteristic feature is unchanged in the upfeed direction, and is now nearly circular at 14.1  $\mu\text{m}$  x 14.1  $\mu\text{m}$ . A 200  $\mu\text{m}$  x 200  $\mu\text{m}$  angstrom symbol motion program was based on a reduction of the design dimensions of the 1mm-scale angstrom symbol. The resulting structure is shown in Figure 4.2-9. This microstructure was evaluated for tolerance in feature placement and for surface finish.

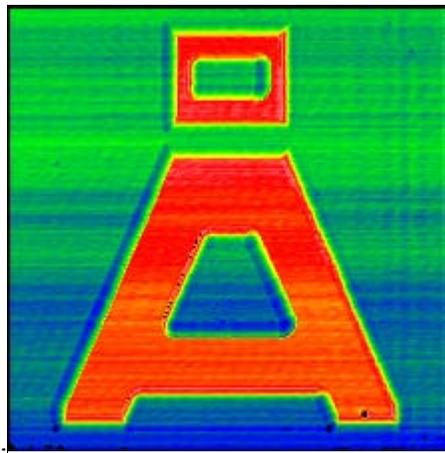


**Figure 4.2-9.** White light interferogram of 200  $\mu\text{m}$  PEC logo

The measured size of the background flat is 200.5  $\mu\text{m}$  in the upfeed (x-axis) direction by 201.5  $\mu\text{m}$  in the crossfeed (y-axis) direction. As mentioned in the previous section, crossfeed inaccuracies due to electrical interference with y-axis encoder signals had been remedied

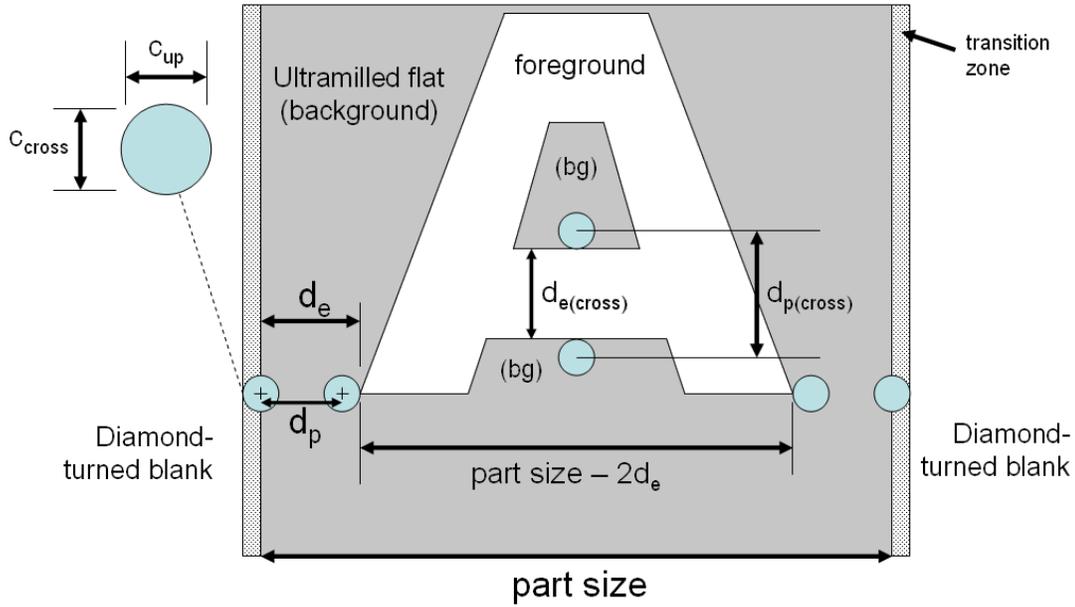
prior to the machining of this part. An evaluation of expected vs. actual feature placement can be performed using the dimensions shown in Figure 4.2-10. In this figure,

- $d_p$  is a programmed upfeed distance
- $d_e$  is the expected size of the marked section of background in the upfeed direction
- $d_{p(\text{cross})}$  is a programmed distance in crossfeed between two sections of the background level
- $d_{e(\text{cross})}$  is the expected size of the marked section of foreground in the crossfeed direction
- $c_{\text{up}}$  is the size of the Ultramill characteristic surface feature in the upfeed direction at the programmed DOC
- $c_{\text{cross}}$  is the size of the Ultramill characteristic surface feature in the upfeed direction at the programmed DOC

In the case of the 50  $\mu\text{m}$  radius tool, 500 nm DOC, and 400 Vpp; the characteristic feature is nearly circular at about 14.1  $\mu\text{m}$  x 14.1  $\mu\text{m}$ <sup>5</sup>. Part size is 200  $\mu\text{m}$  for the workpiece discussed in this section.

---

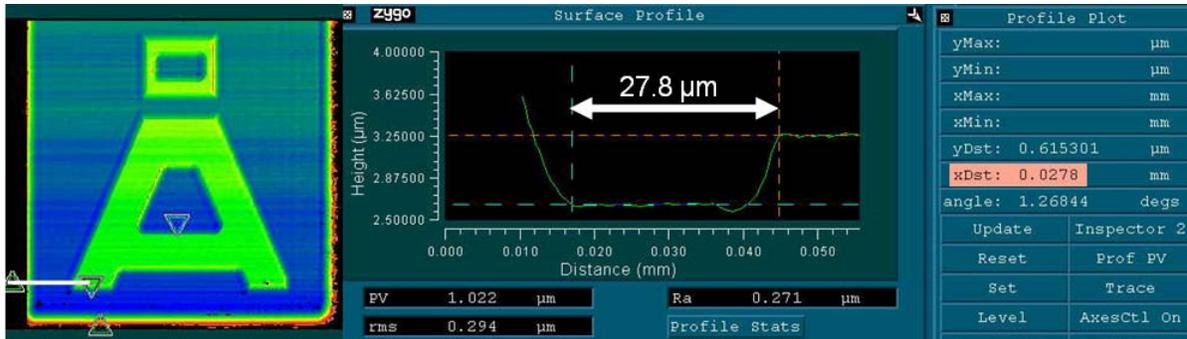
<sup>5</sup> based on Negishi's tool path measurements [22, Appendix L (column labels "a" and "b" should read "2a" and "2b")]



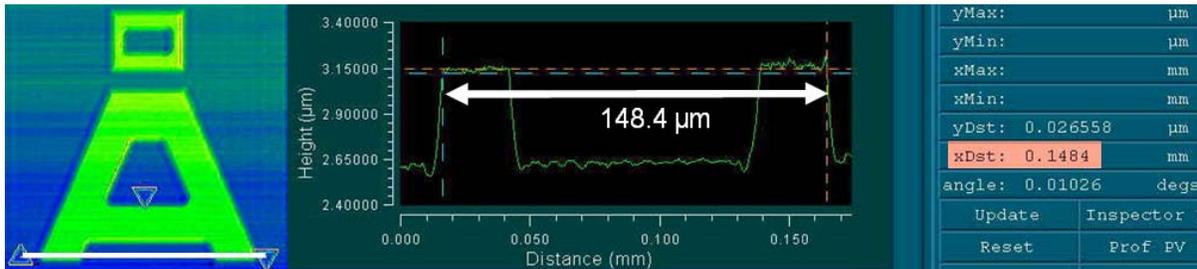
**Figure 4.2-10.** Angstrom symbol example design dimensions.

### UPFEED FEATURE ACCURACY

The programmed upfeed distance,  $d_p$ , at the bottom left corner of the “A” is 20.1  $\mu\text{m}$ . The expected distance  $d_e$  from the edge of the diamond-turned blank to the corner of the “A” is  $d_p + c_{up}/2 = 27.2 \mu\text{m}$ . The measured distance is shown in Figure 4.2-11. Resolution of the Zygo Newview white light interferometer is 560 nm at 20X magnification, so measured distance is  $27.8 \mu\text{m} \pm 0.3 \text{ mm}$ , and the deviation from the expected distance is 1-3%. The expected total width of the “A” foreground is equal to  $200 \mu\text{m} - 2d_e = 145.6 \mu\text{m}$ . The measured width, shown in Figure 4.2-12, is  $148.4 \mu\text{m} \pm 0.3 \text{ mm}$ , and the deviation from the expected width is 1-2%.

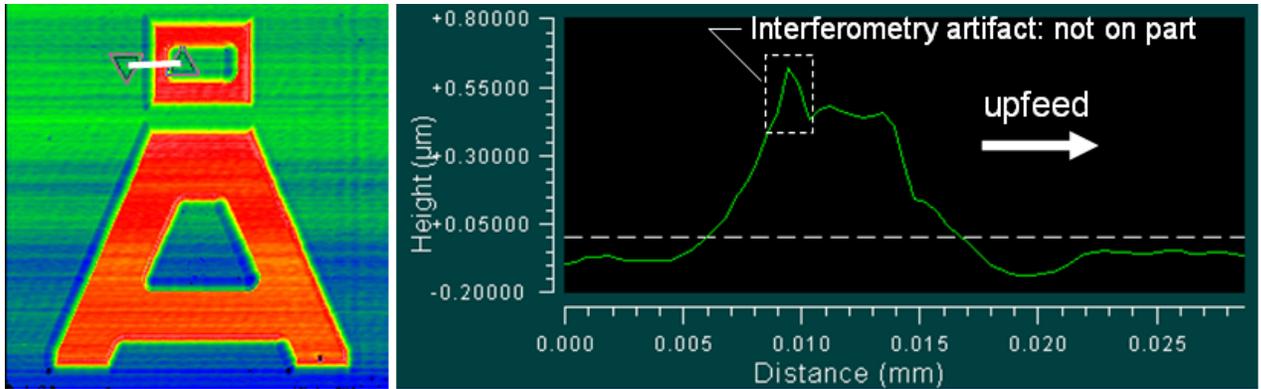


**Figure 4.2-11.** Measured upfeed distance for comparison to expected distance  $d_e = 27.2 \mu\text{m}$  (white light interferogram, 20X).



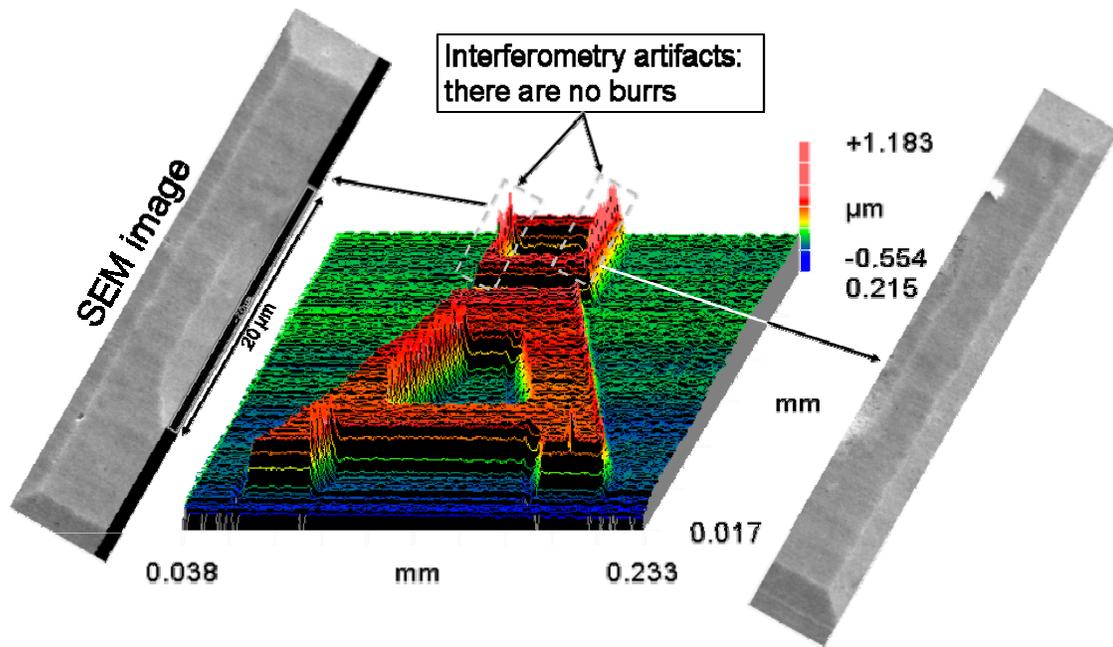
**Figure 4.2-12.** 200 μm angstrom symbol total foreground width, for comparison to 145.6 μm intended dimension.

Figure 4.2-13 shows the smallest feature achieved with the Ultramill to date. This section of the symbol is 15 μm wide in the upfeed direction. The flat foreground of the 15 μm feature in Figure 4.2-13 is 5 μm in the upfeed direction and the transitions from background to foreground are also 5 μm in upfeed.



**Figure 4.2-13** Angstrom symbol feature detail (white light interferogram)

The height ambiguity seen as a spike or burr in Figure 4.2-13 is due to the slope limitations of white light interferometry [24]. Similar artifacts are visible in the isometric view of this part in Figure 4.2-14, which includes scanning electron microscope (SEM) insets of the area in question. The SEM image shows that the “burrs” in the interferogram are not on the part.



**Figure 4.2-14.** 200 µm symbol isometric: interferometry artifacts and SEM insets.

## CROSSFEED FEATURE SIZE ACCURACY

The expected distance in crossfeed  $d_{e(\text{cross})}$ , shown in Figure 4.2-10, is 22  $\mu\text{m}$ . The measured distance, 24.2  $\mu\text{m} \pm 0.3 \mu\text{m}$ , is shown in Figure 4.2-15. This represents a 7-11% deviation from the expected value.

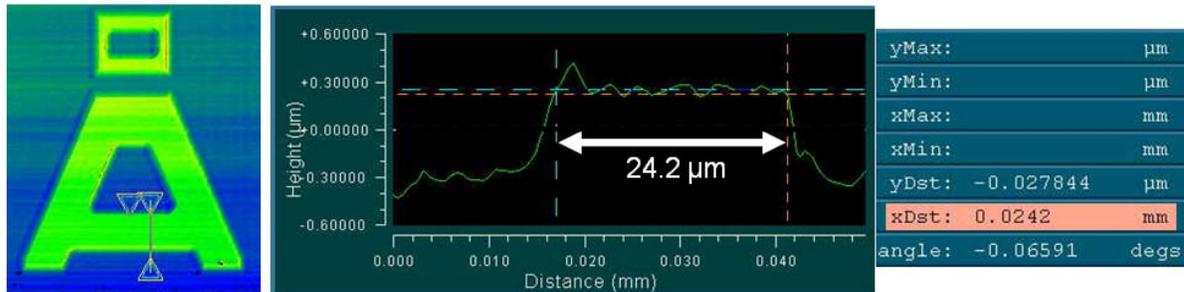


**Figure 4.2-15.** Crossfeed measured size shown for comparison with expected size of 22  $\mu\text{m}$  (white light interferogram, 20X).

## SURFACE FINISH

Figure 4.2-16 shows a background upfeed profile of this part. Actual upfeed speed for this section of the symbol averaged 0.5 mm/sec, as measured by the Nanoform x-axis interferometer and gathered with Delta Tau PlotPro32. The part was machined with the Ultramill running at 1000 Hz. The upfeed per cycle is 500 nm at that speed. The theoretical PV error in the upfeed direction is about 1 nm. Figure 4.2-17 shows a crossfeed profile of this part. The area of interest in the interferogram is masked so that the raised sections of the angstrom symbol will not dominate the Zygo NewView's best-fit plane calculation. The crossfeed increment for this part was 1  $\mu\text{m}$ . The theoretical PV error in the crossfeed direction with the 50  $\mu\text{m}$  radius tool is 2.5 nm. Over the 85  $\mu\text{m}$  length of this profile, 85 crossfeed marks of 2.5 nm height were expected, and some are visible but larger features are also present. The PV error in this profile is 91 nm, and the RMS error is 19 nm.

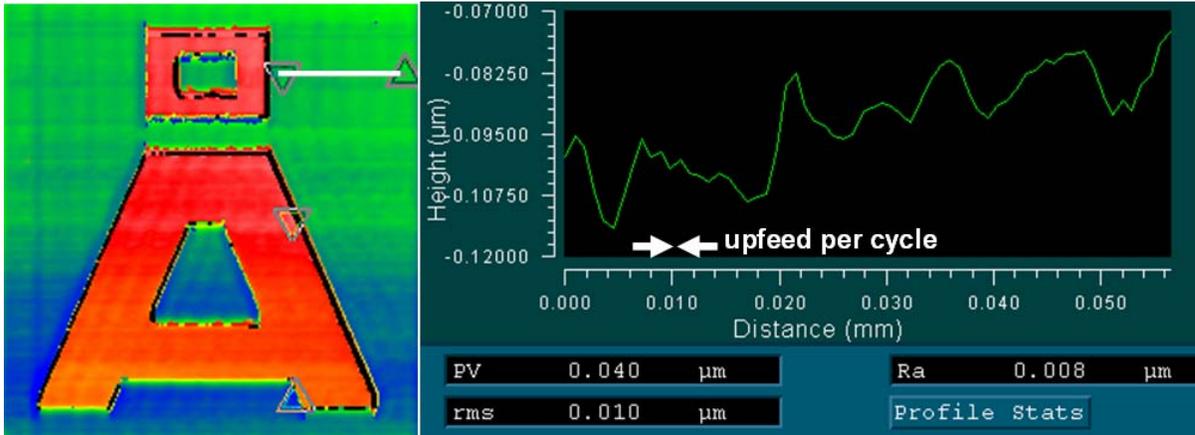


**Figure 4.2-16.** 200  $\mu\text{m}$  angstrom symbol background upfeed, approximately 112 upfeeds at 1 nm peak-peak should be visible (white light interferogram).

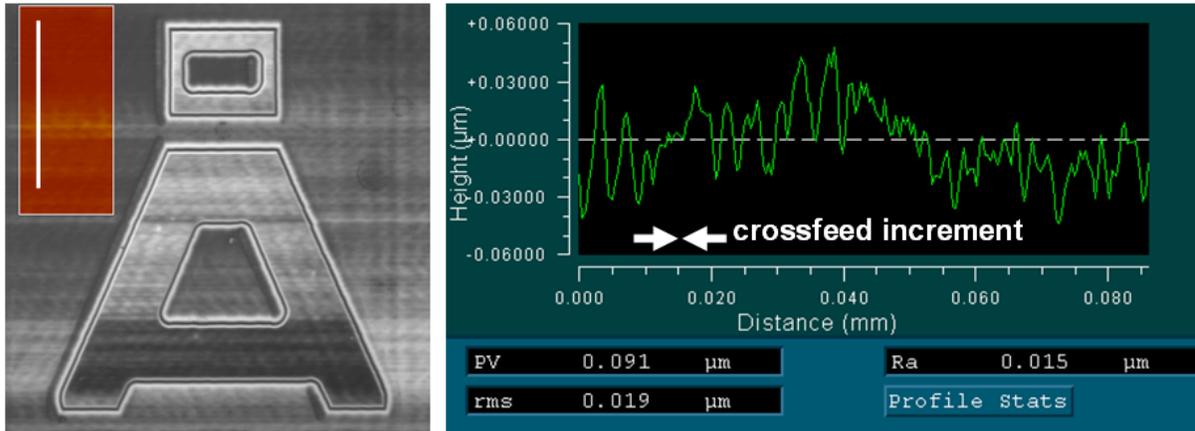


**Figure 4.2-17.** 200  $\mu\text{m}$  angstrom symbol background crossfeed, approximately 85 crossfeed marks at 2.5 nm peak-peak should be visible (white light interferogram)

### Surface Form

The overall slopes of Ultramilled parts will be compared to the “zero” slope of the surrounding diamond-turned blank to determine form error. Tilt error over the measured length of an area in question is defined by Equation 6, valid for both the upfeed and crossfeed directions.

$$e_t = \theta * length \quad (6)$$

because  $\sin\theta$  is equal to  $\theta$  at small angles. However, this method has limitations. The diamond-turned blank was flat relative to the Nanoform x-z plane after its initial preparation. It was not flat relative to the y-axis. Also, the blank was removed and replaced from the vacuum chuck several times during the course this research, and it was not re-surfaced after those replacements. Due to these circumstances, the following errors will be included in tilt-derived form calculations:

1. Tilt between the y-axis and diamond-turned blank prior to microstructuring.
2. Tilt caused by removal and replacement of the diamond-turned blank through rotation relative to the vacuum chuck or by debris between the vacuum chuck and the blank.

Because of these limitations, sag<sup>6</sup> will be used as an alternate characterization of form error. Figure 4.2-18 shows the masks used on the Zygo NewView white light interferometer for tilt and sag calculations. The Zygo MetroPro software's Sag X and Tilt X results were used as upfeed tilt and sag; Sag Y and Tilt Y were used for crossfeed tilt and sag. Table 4.2-1 gives a summary of tilt and sag data for the 200  $\mu\text{m}$  angstrom symbol.

---

<sup>6</sup> Sag is a measure of the curvature of the surface or wavefront without distinguishing between the X and Y dimensions. It is equivalent to the height difference between the center point and the point farthest from the center. The Sag result is derived from a best fit cylindrical surface. Sag X is a measure of the curvature of the surface or wavefront in the X dimension only [25].



**Figure 4.2-18.** Masks used for DT flat, background, and foreground tilt and sag statistics (left to right)

	upfeed				crossfeed			
	tilt	length	tilt*length	sag	tilt	length	tilt*length	sag
	$\mu\text{rad}$	$\mu\text{m}$	nm	nm	$\mu\text{rad}$	$\mu\text{m}$	nm	nm
DT blank	-100	533	-53.3	16.1	544.5	400	217.8	-22.8
background	98	195	19.1	-8.0	-945	196	-185.2	-3.5
difference			72.4				-403.0	
DT blank	-100	533	-53.3	16.1	544.5	400	217.8	-22.8
foreground	-65.6	137	-9.0	6.5	-1403.9	100	-140.4	-30.0
difference			44.3				-358.2	
background	98	195	19.1	-8.0	-945	196	-185.2	-3.5
foreground	-65.6	137	-9.0	6.5	-1403.9	100	-140.4	-30.0
difference			-28.1				44.8	

**Table 4.2-1.** Summary of absolute and relative tilt and sag data, 200  $\mu\text{m}$  angstrom.

It is not unexpected that tilt-derived results in the crossfeed direction (on the order of 400 nm) should be higher than those in the upfeed direction (44-72 nm). The blank was diamond-turned by traversing the x-axis and would be expected to align with it more closely than with the y-axis. Sag results for the background and foreground of the angstrom are 30 nm or less. The background and foreground have a maximum relative tilt error of 45 nm.

Notably, the sag of the angstrom background on a 200  $\mu\text{m}$  length scale is 15% of the sag of the diamond-turned blank on a 400  $\mu\text{m}$  length scale.

### 4.2.3 Flats

Rastered flats were machined with the Ultramill to assess best-case form and finish capability. Because no depth of cut change is required during an upfeed pass, upfeed speed is constant over a significant portion of the part. Constant surface frequencies in the upfeed direction allow comparison of expected frequencies in the machining process (and unexpected frequencies characterized in later sections) with those measured on the part. The part in Figures Figure 4.2-19 and Figure 4.2-20 was machined with the 50  $\mu\text{m}$  radius Ultramill tool. The upfeed speed was 100 mm/min upfeed speed and the crossfeed increment was 1.67  $\mu\text{m}$ . At 1000 Hz, the upfeed speed of 1.67 mm/sec yields a 1.67  $\mu\text{m}$  ufpc. An upfeed profile white light interferogram at 100x is shown in Figure 4.2-19. Over the 16.7  $\mu\text{m}$  length of the profile, the 10 expected Ultramill cycles are visible. The expected PV height of these cycles is 6 nm. Each peak shown is about 10 nm above the section of the profile on which it is centered. Figure 4.2-19, a 100x white light interferogram, should be compared to the upfeed profile of the small angstrom symbol shown in Figure 4.2-16, a 20x white light interferogram. The average upfeed speed achieved with the angstrom motion program was 0.5 mm/s. At this speed, the Ultramill ufpc is 500 nm. The 20x interferogram in Figure 4.2-16 has a resolution of 560 nm, so the upfeed marks are not visible. Lower frequencies are discussed next.

A longer profile of the same flat is shown in Figure 4.2-20. The 31 Ultramill cycles expected in this 52  $\mu\text{m}$  profile are visible, but 3 lower-frequency waves are also visible, with a surface frequency of about 58 waves/mm. At the programmed upfeed speed of 1.67 mm/s, this translates to a time-domain frequency of 97 Hz. Frequencies in this range are supported by the Nanoform axes' natural frequencies, discussed in the next section. The upfeed profile of the 200  $\mu\text{m}$  angstrom symbol in Figure 4.2-16 shows 6-8 low-frequency peaks in 55  $\mu\text{m}$ . At an average upfeed speed of 0.5 mm/s, this translates to 55-73 Hz time-domain frequency. Possible explanations for this difference include:

1. Varying acceleration in the upfeed direction during the angstrom motion program would make an average surface frequency calculation insufficient to describe the surface.
2. Interaction of vibrations in multiple axes or direction (such as upfeed and depth of cut), perhaps combined with upfeed acceleration (and therefore changing upfeed spatial frequencies), could cause unexpected or inconstant surface frequencies on the finished part.

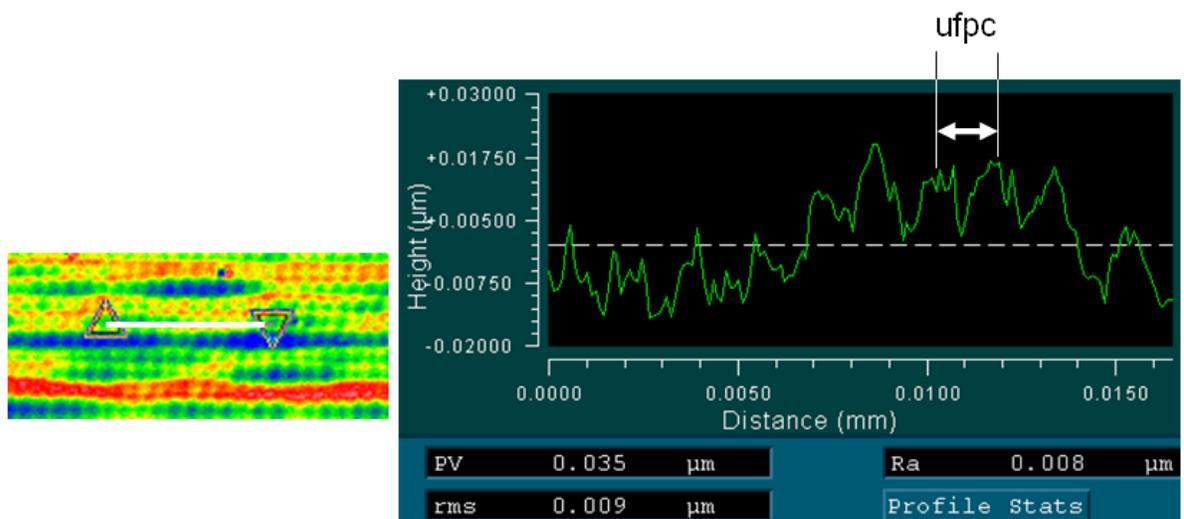


**Figure 4.2-19** Upfeed profile showing 10 Ultramill cycles at 1.67  $\mu\text{m}$  per cycle

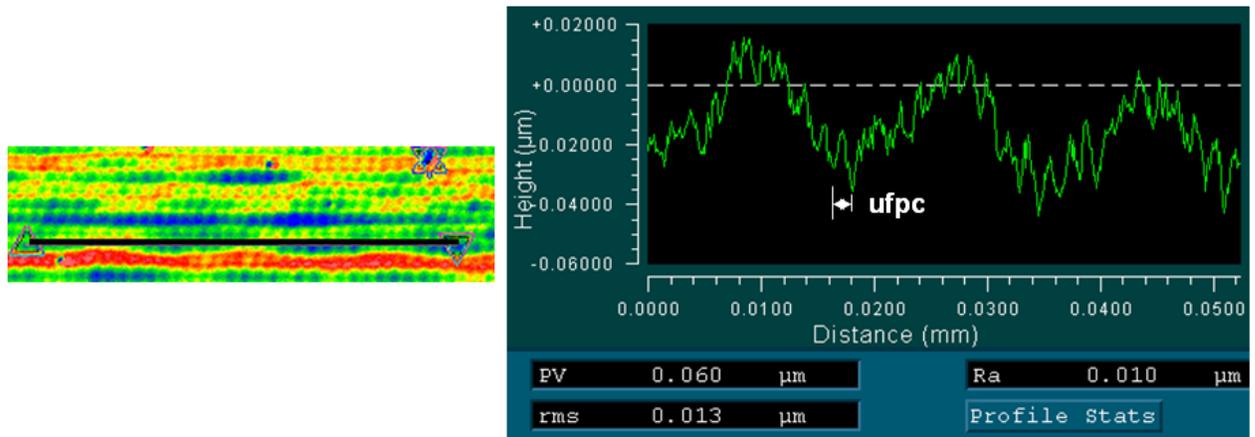


**Figure 4.2-20** Upfeed profile: low frequency, 1.67 mm/s upfeed

### Finish Frequency Ranges

The scale of micromachined parts and the rastering sequence of Ultramill motion make it a challenge to define finish error for these experiments. The time scale of a single 200 µm- to 3mm-long upfeed pass is 0.5 to 3 seconds of cutting time and 10 to 15 seconds between passes. The elapsed time of the 40 to 3000 passes that would cover a similar distance in the crossfeed direction is measured in minutes. Errors have been found in three categories of time-domain frequencies. Errors at the Ultramill actuation frequency (usually 1000 Hz) are expected and comprise the high-frequency finish error. Medium-frequency errors have been found along upfeed passes in the 100 Hz range. This medium-frequency range of finish error will be defined as 10-500 Hz. Lower spatial frequencies than expected in the crossfeed direction have also been identified. The range of time-domain frequencies in the crossfeed direction for low-frequency error will be defined as less than one elapsed time of a crossfeed

pass, or below about 0.1 Hz. The equivalent spatial frequency range is below the spatial frequency of the crossfeed increment. The spatial frequency of the crossfeed increment is 200 waves/mm at 5  $\mu\text{m}$  crossfeed increment and 1000 waves/mm at 1  $\mu\text{m}$  crossfeed increment.

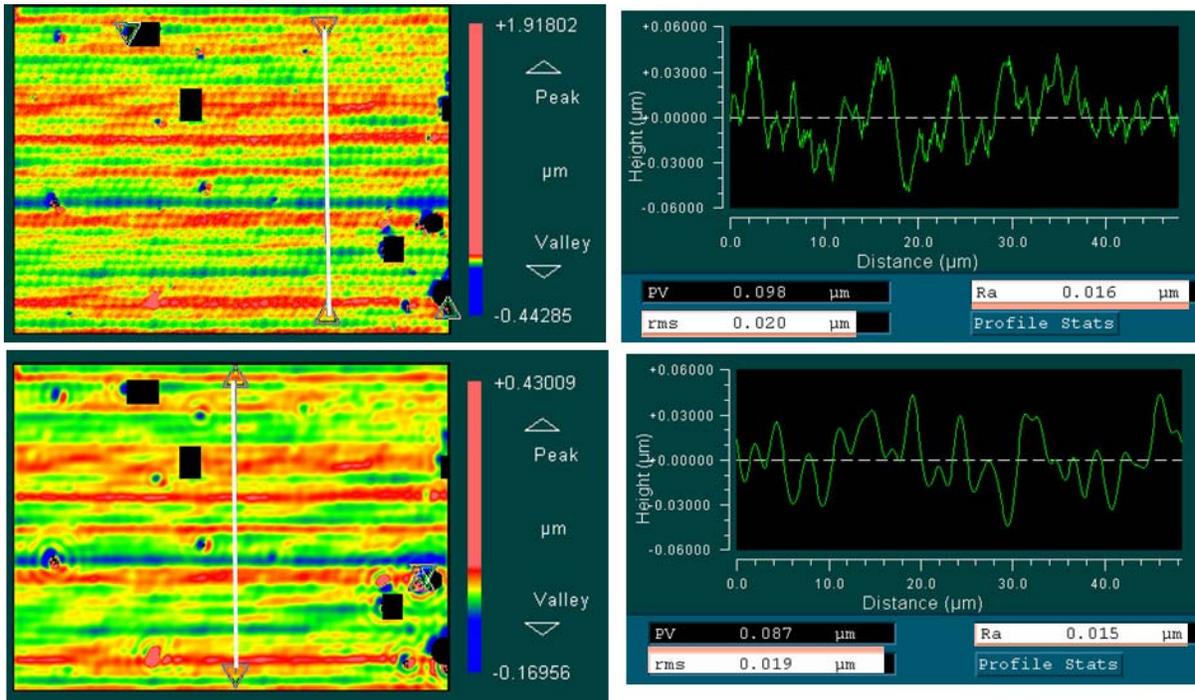
In the case of a rastered flat machined with 1.67  $\mu\text{m}$  crossfeed increment and 1.67  $\mu\text{m}$  ufpc (upfeed per Ultramill cycle), a summary of the error ranges and results is shown in Table 4.2-2. These results were obtained with the filter functions of the Zygo MetroPro software on the NewView white light interferometer.

frequency ranges included	filter type	filter ranges				unfiltered errors		filtered errors		change in RMS
		min	max	min	max	Ra	RMS	Ra	RMS	
		Hz	Hz	1/mm	1/mm	nm	nm	nm	nm	
low	low-pass	n/a	~ 0.15	n/a	599	14-16	19-20	14-16	19	-3%
medium	band-pass	10	500	6	299	15-28	31-36	9	14	-58%
low + high	band-reject	10	500	6	299	15-28	31-36	16	21	-36%
low + med	low-pass	975	n/a	584	n/a	15-28	31-36	15	22	-33%
high	high-pass	975	n/a	584	n/a	15-28	31-36	11	26	-21%

**Table 4.2-2.** Finish error summary for 1.67  $\mu\text{m}$  ufpc, 1.67  $\mu\text{m}$  crossfeed increment flat.

Figure 4.2-21 shows examples of filtered and unfiltered crossfeed profiles used to determine low-frequency finish error. The figures are 100x interferogram with 110 nm resolution. The spatial frequency range visible to the instrument is approximately 14-9090 waves/mm. This range is based on the size of the flat (maximum wavelength visible) and the resolution (minimum wavelength visible). The largest debris or corrosion peaks are masked from the analysis and appear as black squares or circles. The values in Table 4.2-2 were determined by comparing 4-5 randomly-chosen crossfeed profiles in both the filtered and unfiltered cases. Although the filtered profiles were noticeably smoother, the RMS and Ra values for

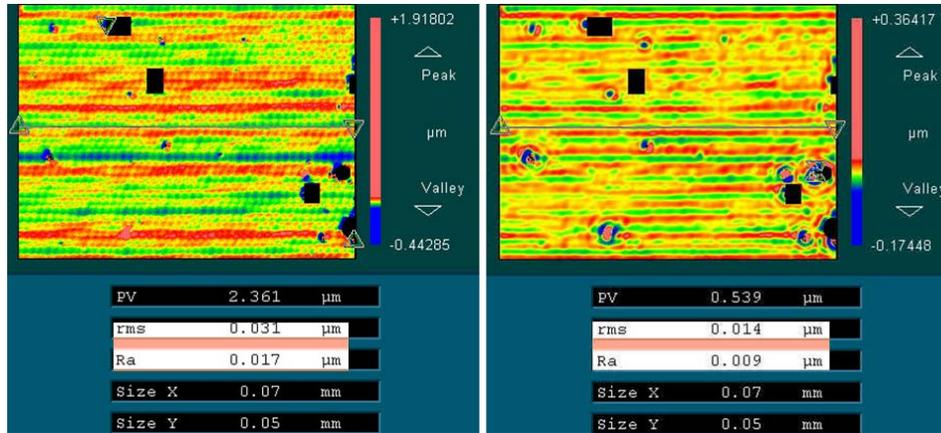
the profiles showed little sensitivity to filtering at this frequency. This indicates that errors below above one crossfeed increment ( $1.67 \mu\text{m}$ ) in wavelength, or below 0.15 Hz in time-domain frequency, are responsible for most of the error in the crossfeed direction.



**Figure 4.2-21.** Unfiltered (top) and low-pass filtered (bottom,  $< 599/\text{mm}$ ) low-frequency finish error for  $1.67 \mu\text{m}$  ufdc,  $1.67 \mu\text{m}$  crossfeed increment flat.

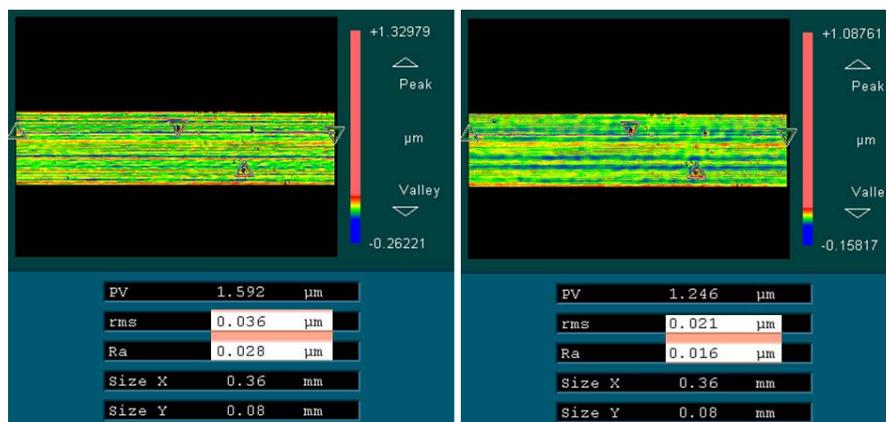
Figure 4.2-22 shows the results for the medium range of frequency error. The band-pass filter used a frequency range of 6 to 299 waves/mm. The lower frequency is somewhat below the minimum frequency visible to the instrument at this magnification (about  $14/\text{mm}$ ). The minimum time-domain frequency visible to the instrument is in the 30 Hz range. The 299 waves/mm upper cutoff filters out upfeed frequencies above 500 Hz in the time domain. However, it also filters out crossfeed features with a wavelength shorter than  $3.34 \mu\text{m}$ , or

twice the crossfeed increment wavelength. This filter setting results in a 58% reduction in RMS surface error.



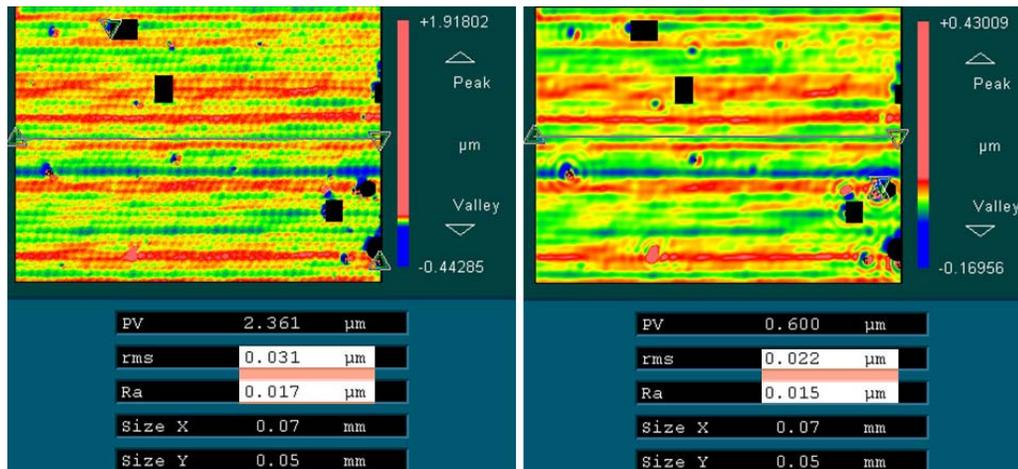
**Figure 4.2-22.** Unfiltered (left), band-pass filtered (right, 6-299 waves/mm) medium-frequency finish error for 1.67 μm ufpc, 1.67 μm crossfeed increment flat.

Figure 4.2-23 shows the unfiltered (left) and band-reject filtered (right) finish error for the “low + high” frequency range of finish error for this flat. This interferogram was taken at 20X with a resolution of 560 nm, so the frequency range visible to the instrument is 2.7 waves/mm to 1785 waves/mm. This filter produced a 36% reduction in RMS error.



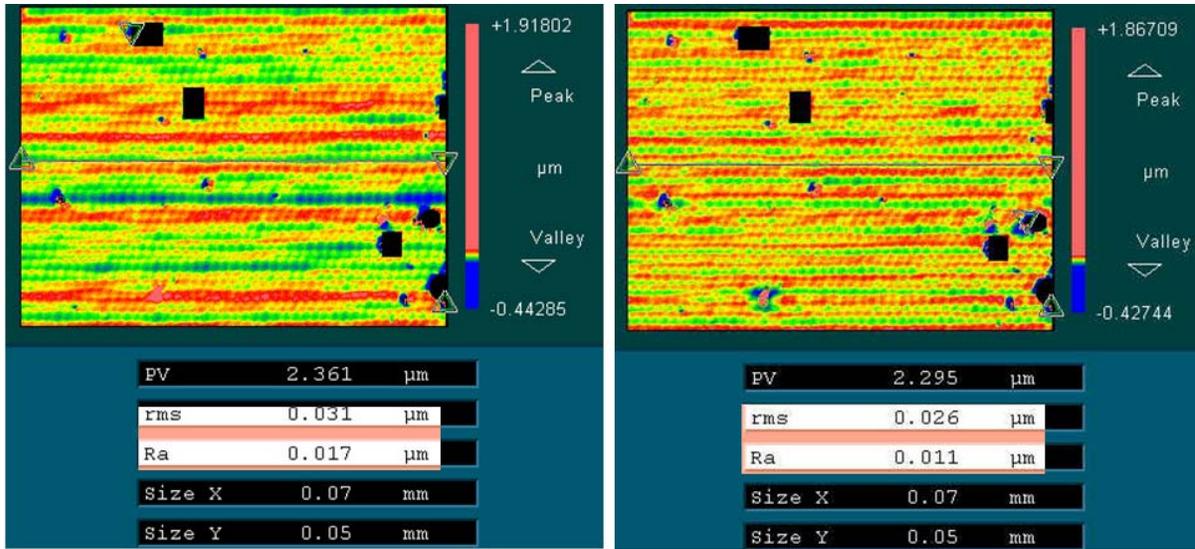
**Figure 4.2-23.** Unfiltered (left), band-reject filtered (6/mm-299/mm) finish error for 1.67 μm ufpc, 1.67 μm crossfeed increment flat.

Figure 4.2-24 shows the unfiltered (left) and filtered (low-pass < 584 waves/mm) “low + medium” finish error results for this flat. Although the cutoff is less than that used for the low-frequency error filter (599/mm), this filter should have little affect on low-frequency error because the smallest wavelength eliminated is only 103% of the crossfeed increment. This filter caused a 33% reduction in RMS finish error.



**Figure 4.2-24.** Unfiltered (left), low-pass filtered (right, < 584 waves/mm) finish error for 1.67  $\mu\text{m}$  ufpc, 1.67  $\mu\text{m}$  crossfeed increment flat.

Figure 4.2-25 shows the unfiltered (left) and high-pass filtered (> 584/mm) results for the high-frequency finish error. This filter setting resulted in a 21% reduction in RMS finish error.



**Figure 4.2-25.** Unfiltered (left), high-pass filtered (right, > 584 waves/mm) finish error for 1.67 μm ufpc, 1.67 μm crossfeed increment flat.

## Form

Figure 4.2-26 shows the masking scheme used on the Zygo NewView white light interferometer to obtain tilt and sag statistics for both the diamond-turned blank and the EVAM flat. Table 4.2-3 shows a summary of results for form error. As seen in the 200 μm angstrom symbol results in Section 4.2.2, crossfeed direction tilt errors are much larger than upfeed-direction tilt errors. This is likely due to the fact that the blank was diamond-turned by traversing the x-axis. The y-axis (crossfeed direction) would not be expected to align as well with the blank. The sag results for the EVAM flat are on the order of 10 nm in both directions.

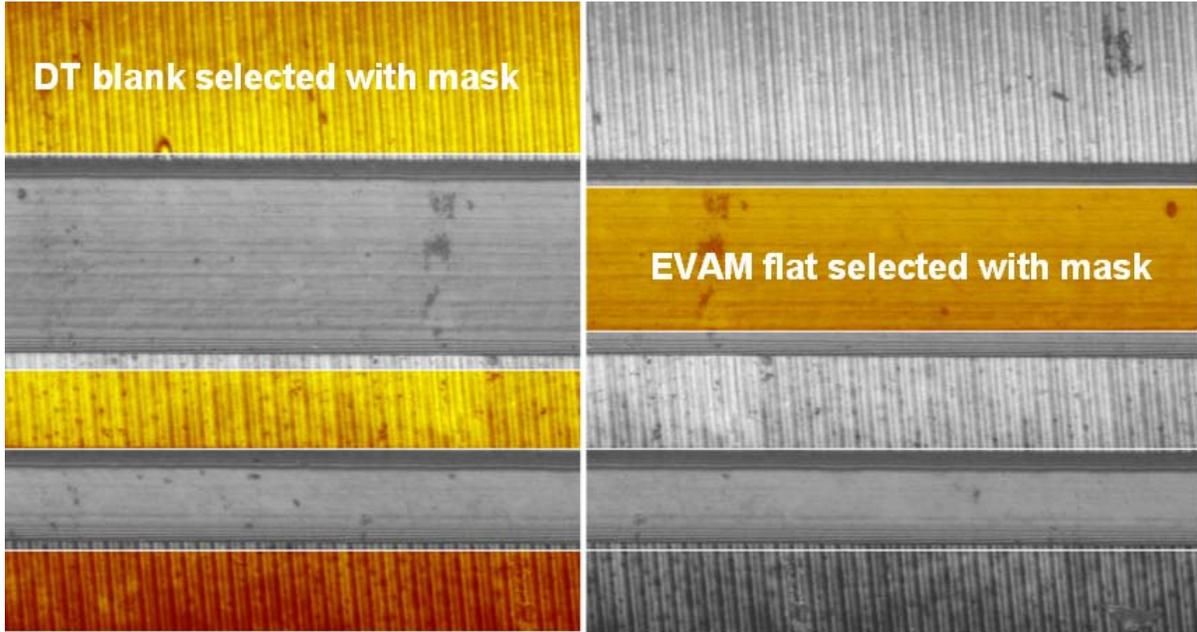


**Figure 4.2-26.** Masking scheme for DT flat (left) and EVAM flat (right).

	upfeed				crossfeed			
	tilt	length	tilt*length	sag	tilt	length	tilt*length	sag
	$\mu\text{rad}$	$\mu\text{m}$	nm	nm	$\mu\text{rad}$	$\mu\text{m}$	nm	nm
DT blank	-11.3	356	-4.0	-0.7	850	356	302.6	5.5
EVAM flat	-117	354	-41.7	3.7	-2187	50	-109.4	10.2
difference			-37.6				-412.0	

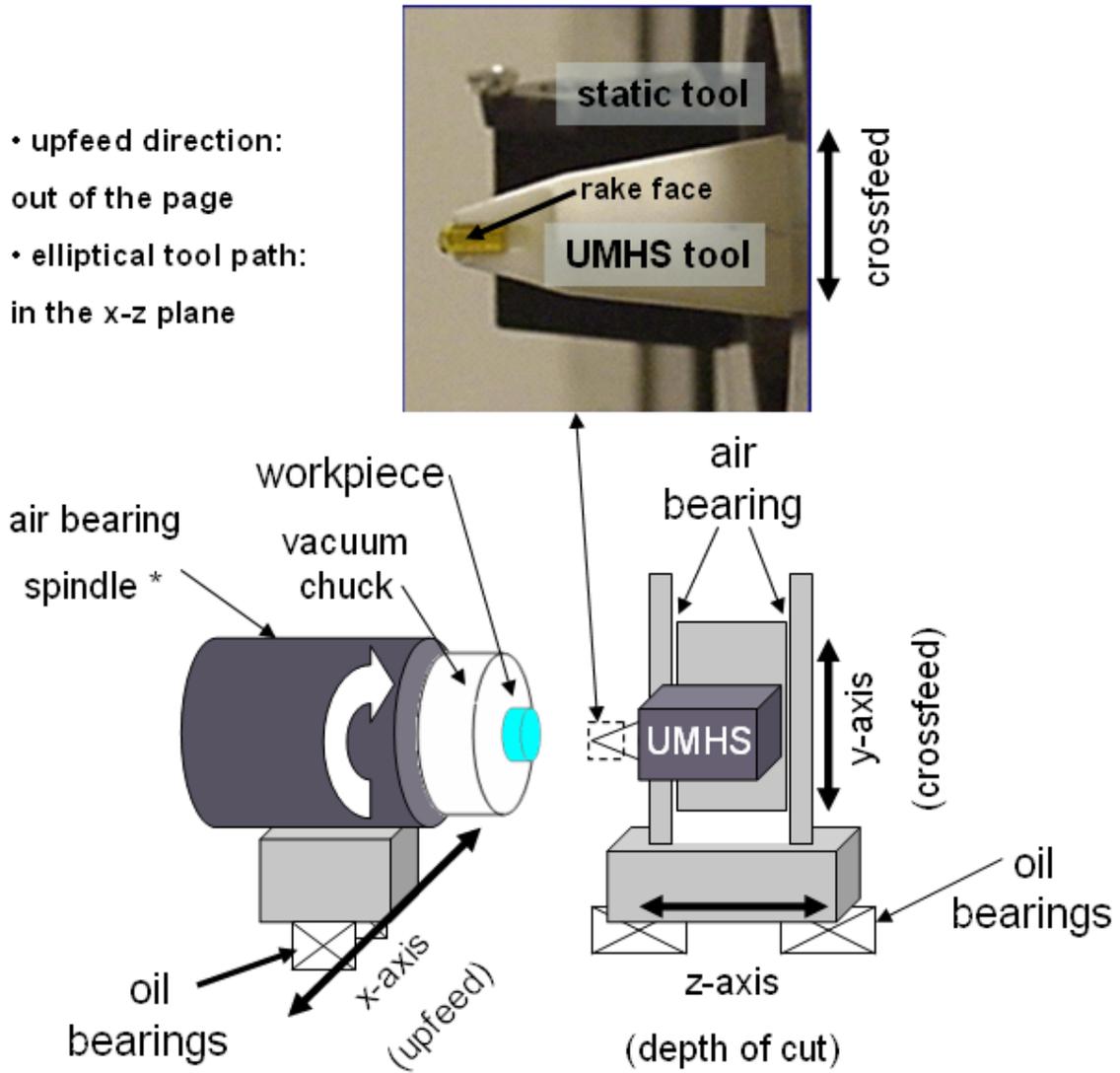
**Table 4.2-3.** Sag and tilt results for EVAM flat.

## **5 CHARACTERIZATION OF POSSIBLE SOURCES OF ERROR**

In this chapter, the axes of the Nanoform DTM and specific features of the Ultramill EVAM tool are examined to determine their potential effect on machined surface features.

### **5.1 NANOFORM DIAMOND TURNING MACHINE AXES**

This Section will characterize the Nanoform DTM components, shown in Figure 5.1-1, in terms of natural frequencies and measured vibration. Table 5.1-1 shows a summary of vibration amplitudes in acceleration and displacement. This data was gathered from shaker testing, described in Section 5.1.1. The “f,1” listed for each case is the frequency of the highest displacement amplitude found, and “f,2” is the frequency of the next-highest displacement amplitude. The largest amplitude found was for the y-axis in the z- or depth of cut-direction. The y-axis was also found to have the most inconsistent frequency content in measured vibration, as will be discussed in Section 5.1.3.



\* rotates when using static diamond tool; locked when using Ultramill

**Figure 5.1-1.** Nanoform DTM and Ultramill diagram.

		f,1	acceleration amplitude	displacement amplitude	f,2	acceleration amplitude	displacement amplitude
axis	direction	(Hz)	mm/s <sup>2</sup>	μm	(Hz)	mm/s <sup>2</sup>	μm
x	x	120	60	0.1			
	z	275	1730	0.01			
y	z	<b>95</b>	2920	<b>8.2</b>	<b>50</b>	183	<b>1.9</b>
z	z	102	750	1.8	70	64	0.33
spindle	x	300	320	0.1			
	z	190	18	0.01			

**Table 5.1-1.** Nanoform shaker-test axis vibration summary.

### 5.1.1 Z-axis

Vibration of the z-axis in either the depth of cut (z) direction is an important possible source of error in Ultramilled surfaces. Shaker<sup>7</sup> tests were performed to determine the natural frequency of the z-axis, high-frequency z-axis position data was gathered during Ultramill machining, and pitching of the z-axis was examined as a possible source of error.

#### Depth of Cut Direction Shaker Test

The experimental setup is shown in Figure 5.1-2. The y-axis was excited at various frequencies from 10-120 Hz and vibration of the z-axis was measured by an accelerometer. In addition, it was possible to measure the displacement amplitude of z-axis vibration with the Nanoform DTM laser interferometer. Comparison of the z-axis amplitudes of vibration in both acceleration and displacement under the same excitation conditions allowed the estimation of displacement vibration for other excitation conditions on both the z-axis and on

---

<sup>7</sup> shaker: A device which produces controlled and reproducible mechanical vibration for the vibration testing of mechanical systems, components and structures [25]. Equipment for all

the other axes. Figure 5.1-3 shows the accelerometer signal captured at 102 Hz excitation of the y-axis with the accelerometer mounted on the z-axis. Figure 5.1-4 shows the laser interferometer measurement of z-axis displacement under the same conditions. The displacement data may be related to acceleration by Equation 7

$$a(t) := \frac{d^2}{dt^2} x(t) \quad (7)$$

If the displacement data in Figure 5.1-4 is differentiated twice to yield acceleration, and this acceleration amplitude in mm/s<sup>2</sup> is compared to the accelerometer voltage amplitude in Figure 5.1-3, a relation for acceleration in SI units per accelerometer signal voltage may be derived and used to predict acceleration in SI units for shaker tests on all the Nanoform axes. The amplitude of acceleration derived from the interferometer data in Figure 5.1-4 is 715 mm/s<sup>2</sup>, and the acceleration per voltage found by comparing this with the data in Figure 5.1-3 is 458 mm/s<sup>2</sup> per Volt.

---

shaker tests: Labworks, Inc. shaker; driven by Kepco BOP 15-20M power supply; Kistler 8612B5 accelerometer; driven by Kistler 5004 dual-mode amplifier.

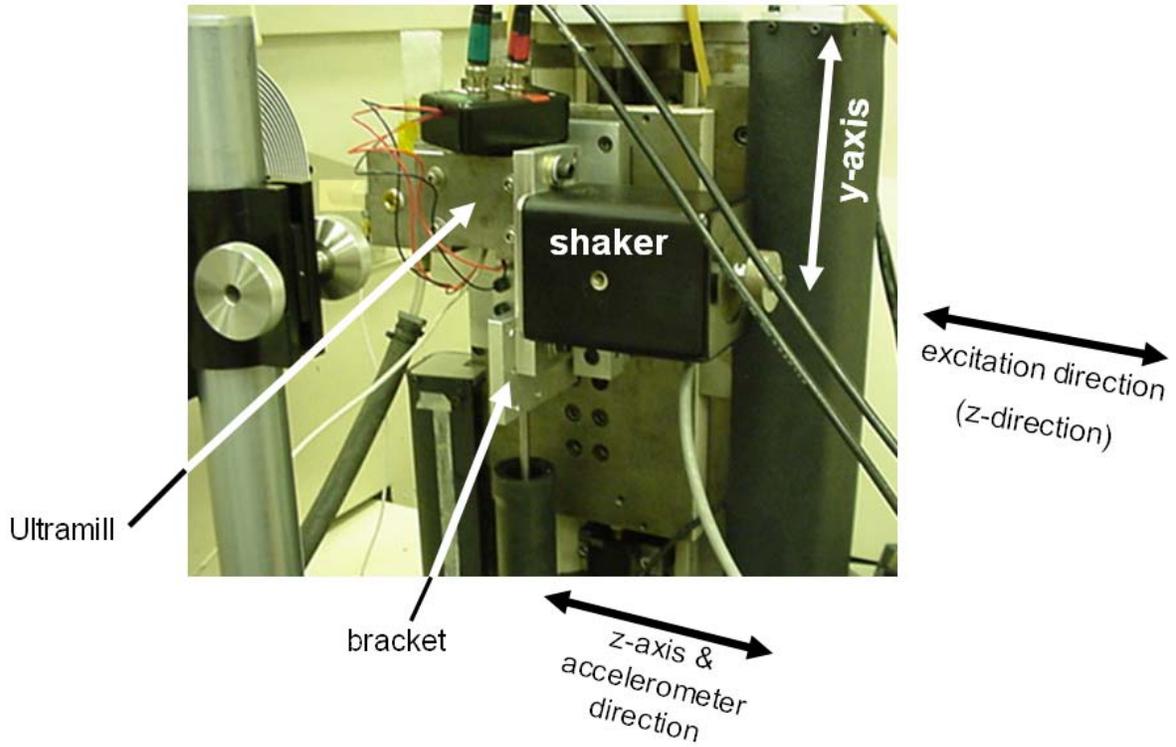


**Figure 5.1-2.** Z-axis shaker test experimental setup.

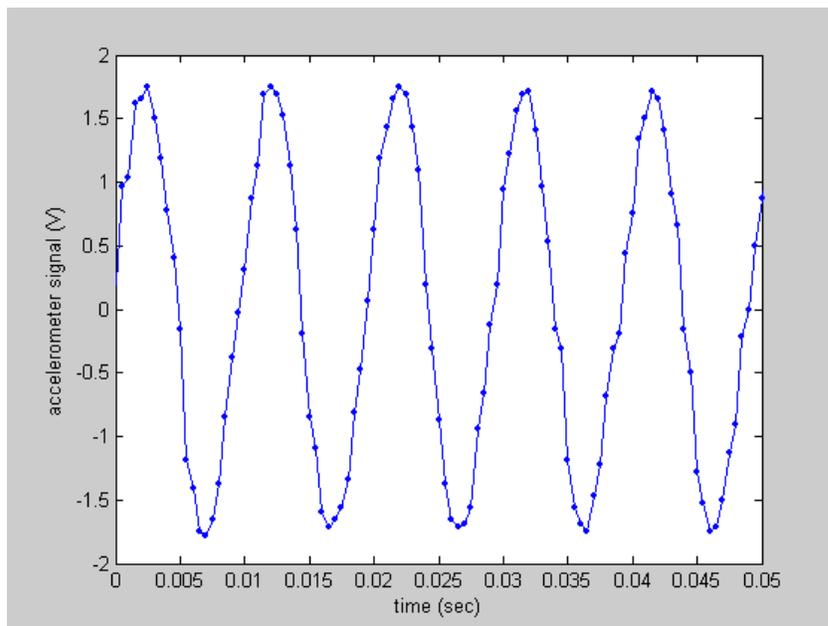


**Figure 5.1-3.** Z-axis accelerometer signal, excitation frequency = 102 Hz.

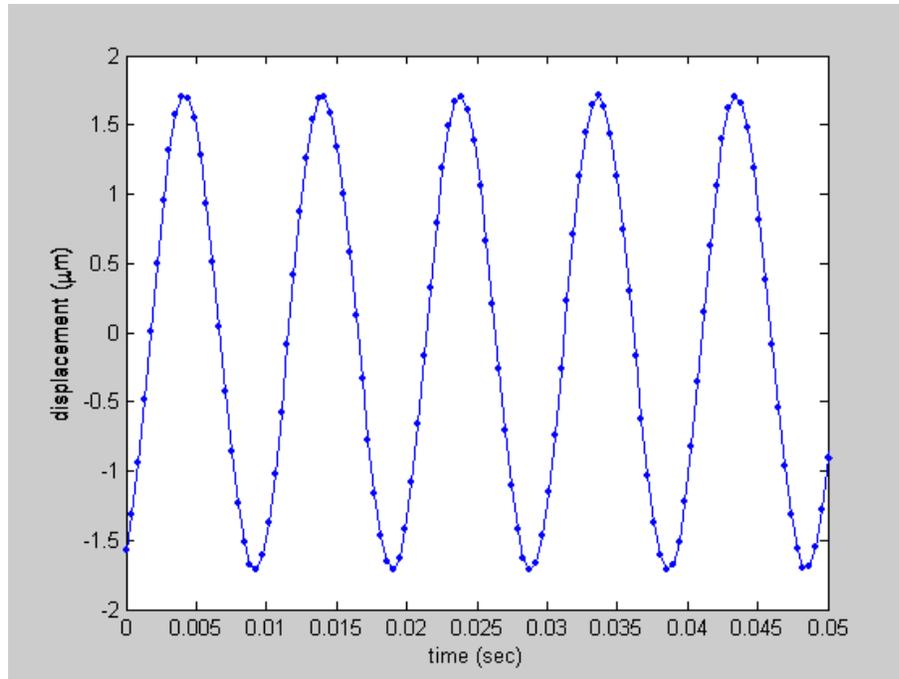


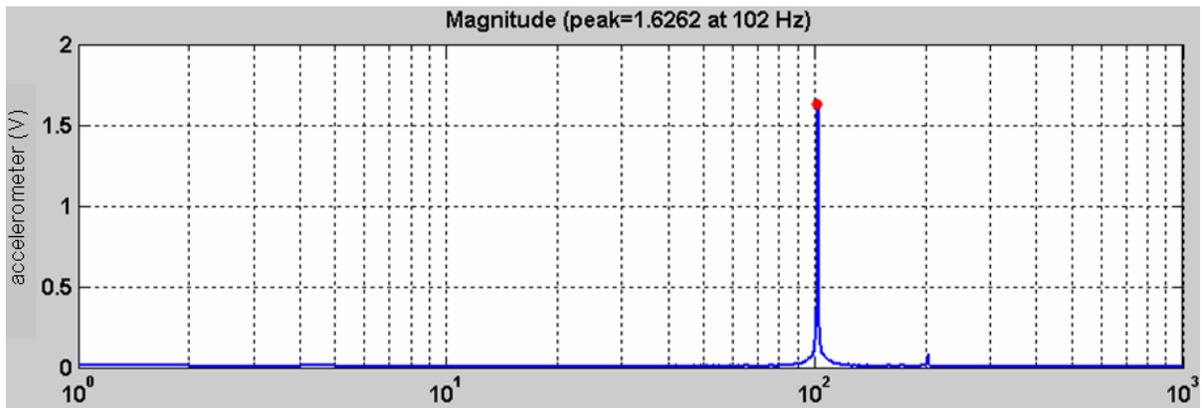
**Figure 5.1-4.** Z-axis displacement measured by the laser interferometer, excitation frequency = 102 Hz.

Furthermore, acceleration results from tests in which displacement data was not collected may be integrated to yield predicted displacement amplitudes of vibration from measured accelerometer voltage. For a cosine acceleration signal with amplitude  $A$  and frequency  $\omega$ , displacement is given by Equation 8 and the displacement amplitude  $X$  is given by Equation 9.

$$x(t) = -\frac{A \cos(\omega t)}{\omega^2} \tag{8}$$

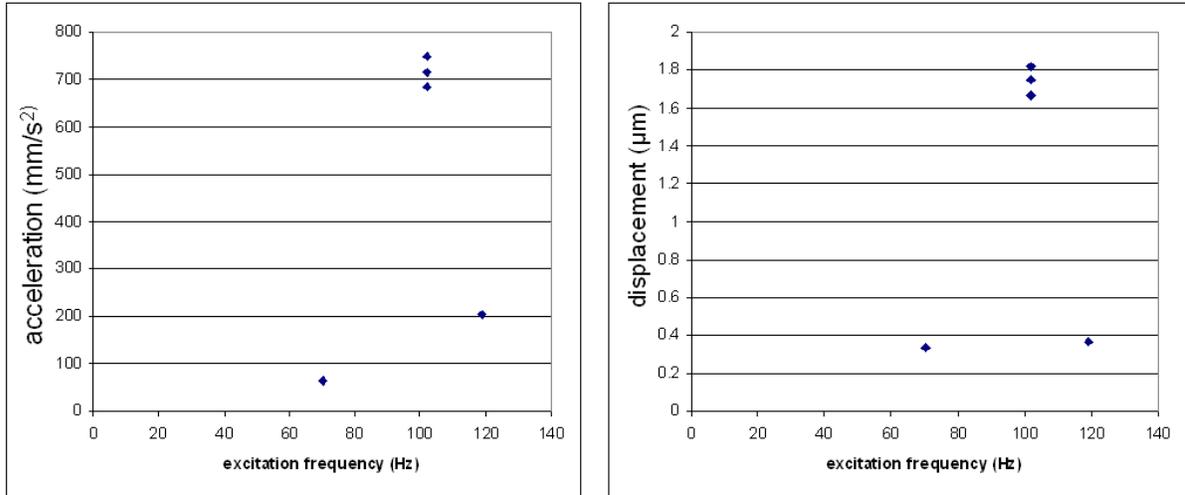
$$X = \frac{A}{\omega^2} \tag{9}$$

Figure 5.1-5 shows an FFT of the accelerometer signal in Figure 5.1-3. Application of the acceleration per voltage relation yields an acceleration amplitude of  $742 \text{ mm/s}^2$  at the excitation frequency of 102 Hz and Equation 9 predicts a displacement amplitude of  $1.8 \text{ }\mu\text{m}$ . This compares favorably with the  $1.7 \text{ }\mu\text{m}$  amplitude of vibration measured at the laser interferometer under the same conditions and shown in Figure 5.1-4.



**Figure 5.1-5.** FFT of accelerometer signal shown in **Figure 5.1-3**.

Figure 5.1-6 shows vibration amplitudes of the z-axis in acceleration (left) and displacement (right) for several excitation frequencies. All acceleration results were measured by the accelerometer. One of the three displacement peaks at 100 Hz was measured at the laser interferometer. The other two 100 Hz displacement peaks and the two lower-amplitude values were predicted by accelerometer data. The natural frequency of the z-axis was identified as 102 Hz.



**Figure 5.1-6.** Z-axis vibration amplitudes at several frequencies: measured acceleration (left), measured or predicted displacement (right).

### Z-axis Position Data Collected During Machining

Nanoform DTM z-axis position data collected during machining was examined to determine possible contributions of this axis to workpiece surface errors. Figure 5.1-7 shows 450 Hz data of ten consecutive passes in a rastered flat program with 2 mm upfeed distance and 1.5 µm crossfeed increment. The Ultramill is operating at 1000 Hz during this data collection. The data was gathered as a flat was being cut. Figure 5.1-8 shows the z-axis position in the first pass as a function of time.

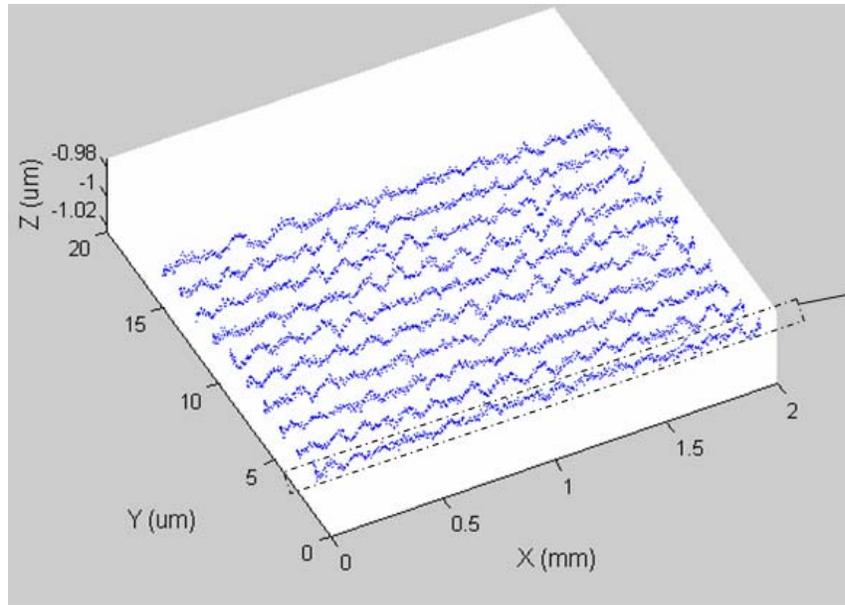


**Figure 5.1-7** Ten 1.5  $\mu\text{m}$  crossfeed passes (Ultramill actuated at 400 Vpp / 1000 Hz)

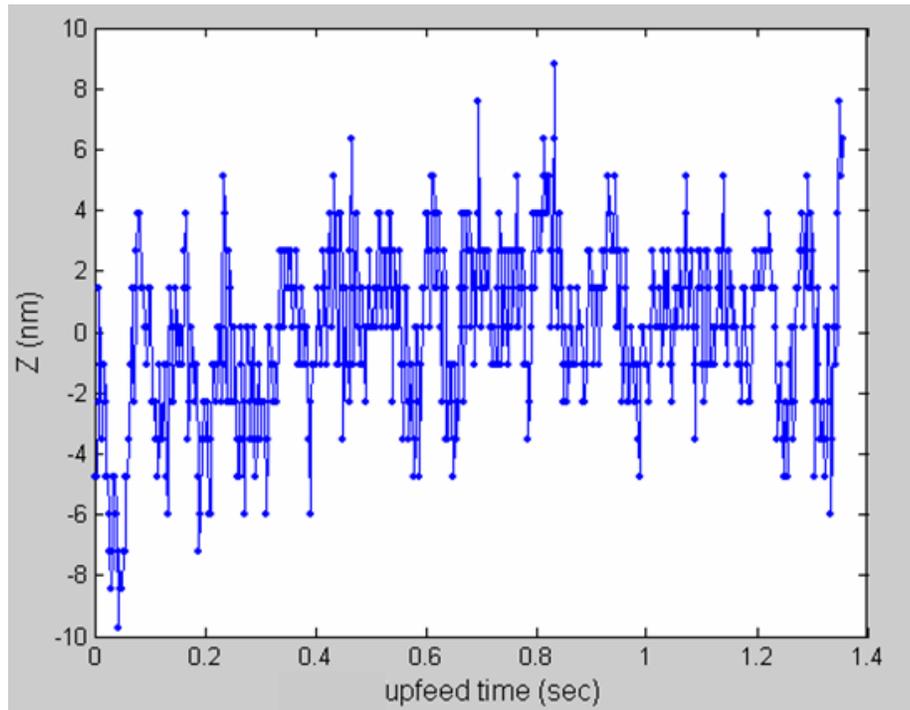


**Figure 5.1-8** Pass #1: z-axis position vs. time

A peak-to-peak position error of 19 nm is visible over this upfeed pass. Figure 5.1-9 shows an FFT of Pass #1.

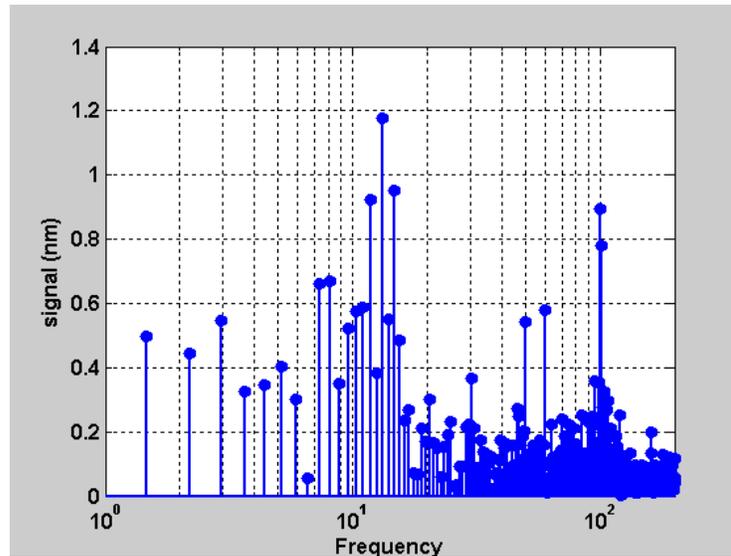


**Figure 5.1-9** FFT of pass #1

The highest amplitude, 1.2 nm, in this FFT is at 13 Hz. This amplitude is equal to the resolution of the z-axis laser interferometer and is not significant when compared to surface errors observed in Ultramilled parts. However, the Abbé offset [27] between the z-axis interferometer and the Ultramill is on the order of 400 mm. The Abbé offset is a fundamental concept of precision metrology. This concept states that angular errors between a measurement scale and the object or motion being measured cause increasing errors in distance measurement with increasing Abbé offset [27]. In order to investigate the possible contribution of this Abbé offset to depth-of-cut direction errors, z-axis pitch was examined.

## Z-axis Pitch

Two capacitance gages were used to measure the pitch angle of the z-axis, which affects the position of the y-axis and the Ultramill. Figure 5.1-10 shows the experimental setup.

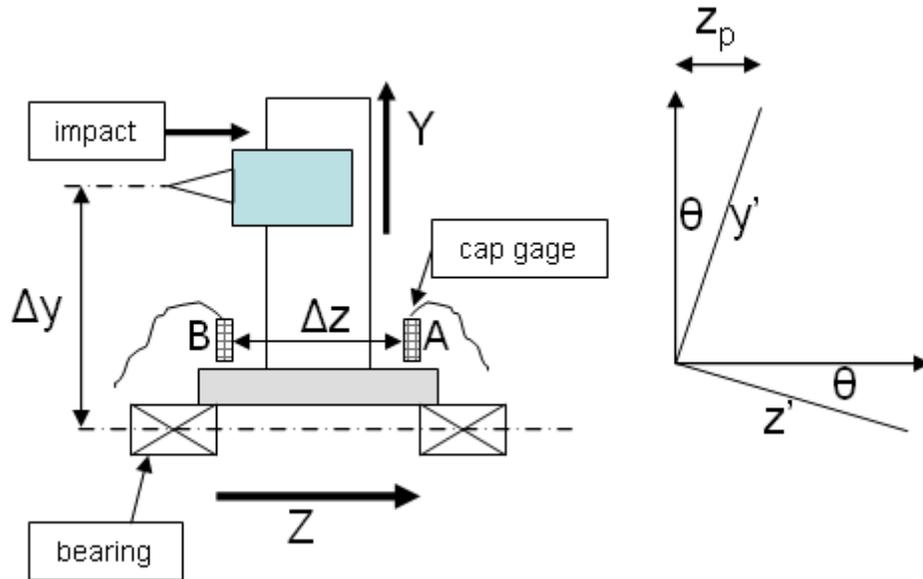


**Figure 5.1-10.** Diagram of z-axis pitch experiment

The z-axis pitch angle, assuming small angles, is defined by Equation 10.

$$\theta = \frac{(A - B)}{\Delta z} \quad (10)$$

The z-axis pitch error at the Ultramill is defined by Equation 11.

$$z_p = \Delta y \theta \quad (11)$$

An impact on the y-axis at the location of the Ultramill was used to excite the z-axis. Figure 5.1-11 shows an FFT of the pitch angle as calculated from the capacitance gages A and B.

Figure 5.1-12 and Figure 5.1-13 show FFT's of the signals from each gage.

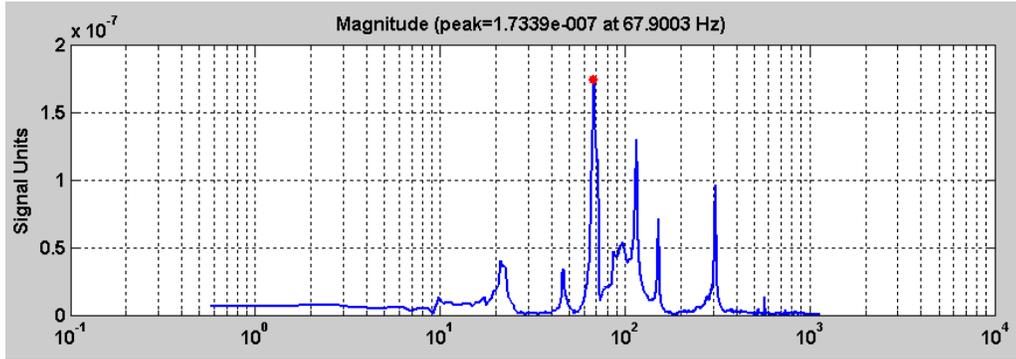


**Figure 5.1-11.** FFT of  $\theta$  in radians.

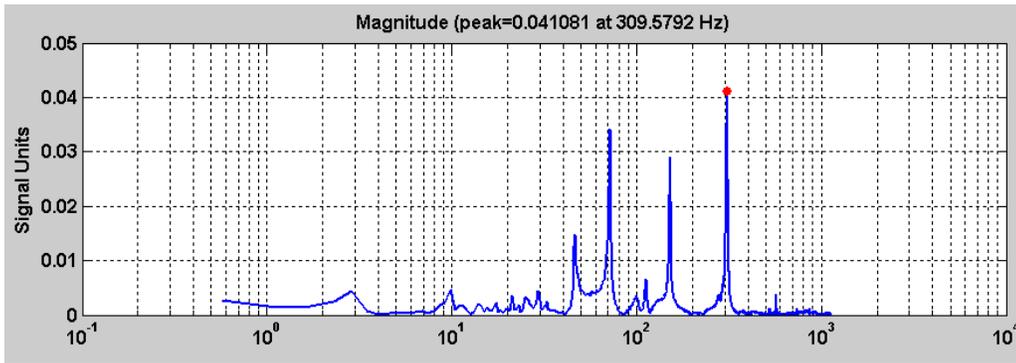


**Figure 5.1-12.** FFT of signal A.

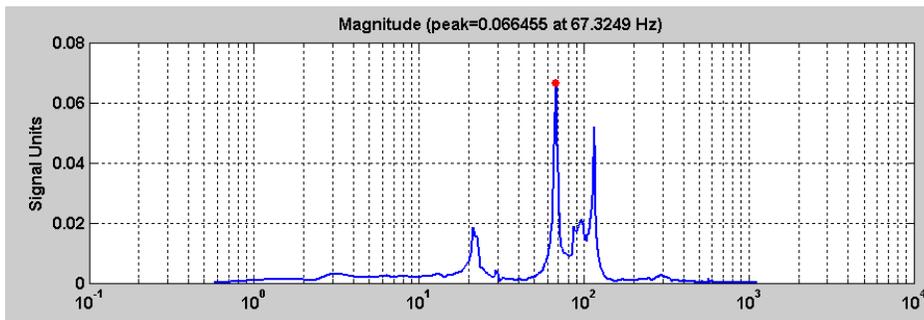


**Figure 5.1-13.** FFT of signal B.

Figure 5.1-11 shows pitch vibration at a frequency of 68 Hz. Capacitance gage mounting stand vibration was not expected to be an issue in this test because the cap gage stands were

mounted on the vibration-isolated granite base of the Nanoform DTM. However, to validate the pitch data, impact tests of the capacitance gage mounting stands were performed. An instrumented hammer was used to excite the gage stands. Capacitance displacement data was differentiated twice to yield an acceleration signal. The instrumented hammer signal was used as input and the acceleration at the cap gage was used as output to find a transfer function, an example of which is shown in Figure 5.1-14. The first natural frequency of the stand on which cap gage B was mounted was found to be 70-75 Hz in three different impact tests. The first natural frequency of cap gage stand A was found to be 150 Hz.

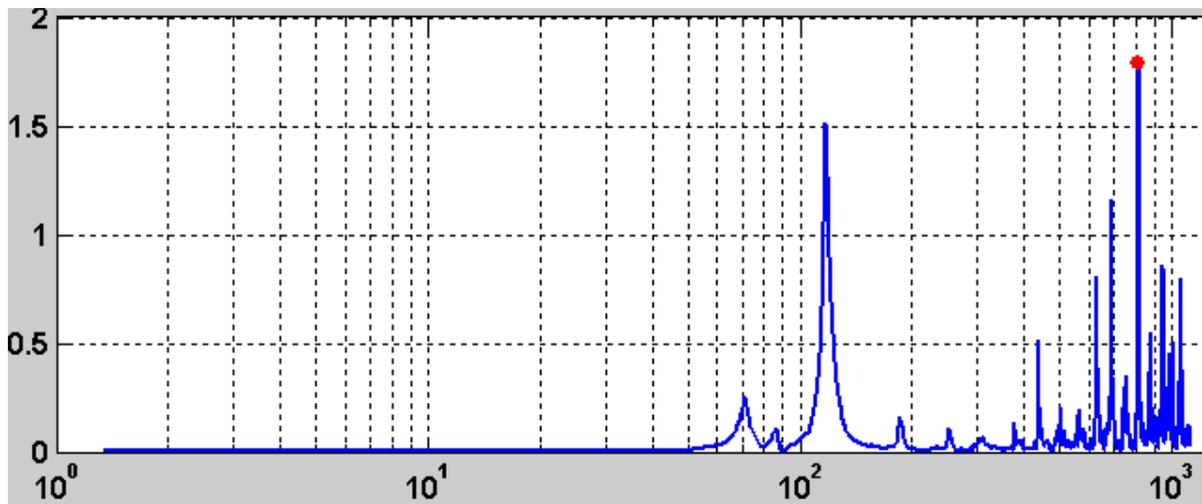


**Figure 5.1-14.** Transfer function of capacitance gage stand B instrumented-hammer impact test

A y-direction stiffness test of the z-axis was performed to determine the likelihood of z-axis vibration in the 70-Hz frequency. The stiffness data as measured at cap gage A is shown in Figure 5.1-15. The same data measured at gage B is shown in Figure 5.1-16.

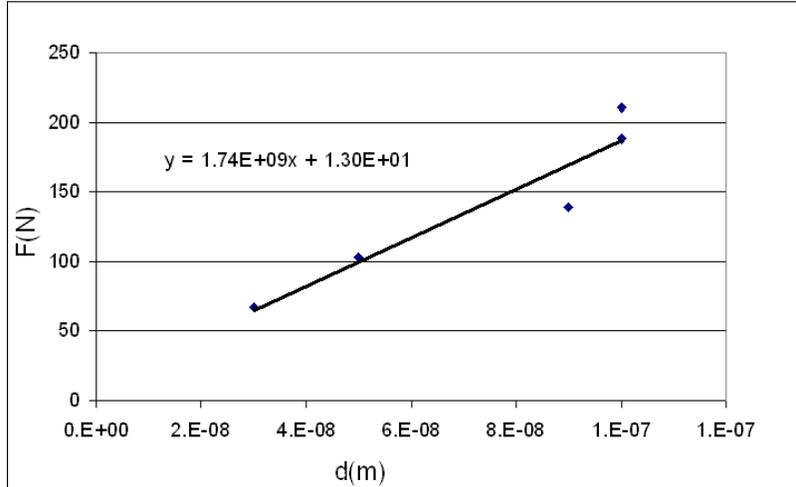


**Figure 5.1-15.** Z-axis y-direction stiffness data measured at cap gage A.

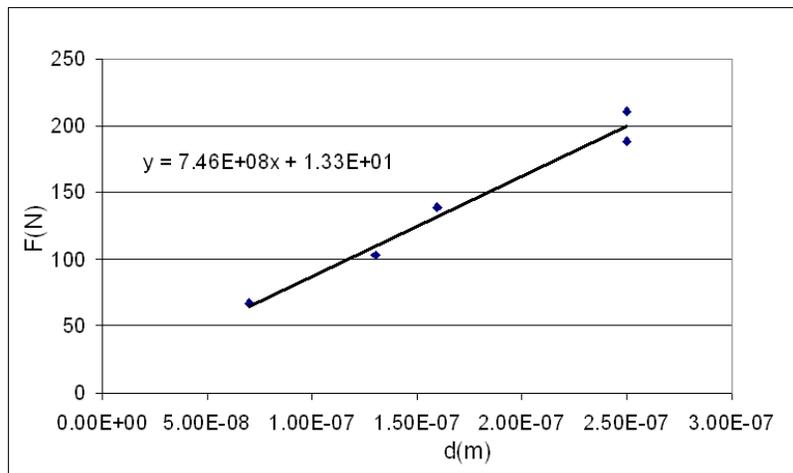


**Figure 5.1-16.** Z-axis y-direction stiffness data measured at cap gage B.

The stiffness of the z-axis in the y-direction was measured as approximately  $1 \times 10^9$  N/m. The first natural frequency of any system in radians per second is given by Equation 12.

$$\omega = \sqrt{\frac{k}{m}} \quad (12)$$

A first natural frequency of 70 Hz = 440 radians/second for the z-axis would require a mass of 5000 Kg. This and the transfer function obtained for cap gage stand B leads the authors to believe that the low-frequency vibration measured was due to capacitance gage stand vibration. For this reason, the z-axis pitch testing in this research has been discounted.

### **5.1.2 X-axis**

Vibration of the x-axis in either the depth of cut (z) direction or upfeed (x) direction is an important possible source of error in Ultramilled surfaces. A shaker<sup>8</sup> test was performed in both cases. Vibration of the x-axis in the crossfeed (y) direction was not examined in this research because neither Ultramill excitation nor x-axis motion exerts significant forces in the y-direction.

#### **Z-direction (depth of cut)**

The z-direction setup is shown in Figure 5.1-17. The excitation frequency of the shaker was adjusted slowly from 10 Hz upward to a significant peak in acceleration amplitude as measured by the accelerometer. The shaker is clamped securely to the x-axis and the accelerometer is mounted on a cast-iron strut attached to the x-axis to prevent vibration of the test equipment. In the case of the x-axis, z-direction shaker test, resonances were visible at about 180-200 and at ~275 Hz. The signal-to-noise ratio at the lower frequencies (180-200 Hz) was less than 5:1, and the amplitude at those frequencies was less than 25% of the

---

<sup>8</sup> The shaker test procedure was discussed in more detail in Section 5.1.1. Relations for accelerometer voltage, acceleration, and displacement amplitudes were also provided

amplitude at  $\sim 275$  Hz. The resonance in the 180-200 Hz range is likely caused by vibration of the spindle rotating mass in the z-direction at  $\sim 190$  Hz (see Section 5.1.4). The most-significant acceleration signal of the x-axis in the z-direction occurred at  $\sim 275$  Hz. This is the measured first natural frequency of the x-axis in the depth of cut (z) direction. The acceleration amplitude in Figure 5.1-18 may be used with the voltage and displacement relations from Section 5.1.1 to predict the displacement of the x-axis in the z-direction at this natural frequency. The acceleration amplitude is  $27.5 \text{ mm/s}^2$  at 1730 rad/s, and the predicted displacement amplitude from Equation 9 is 9 nm.

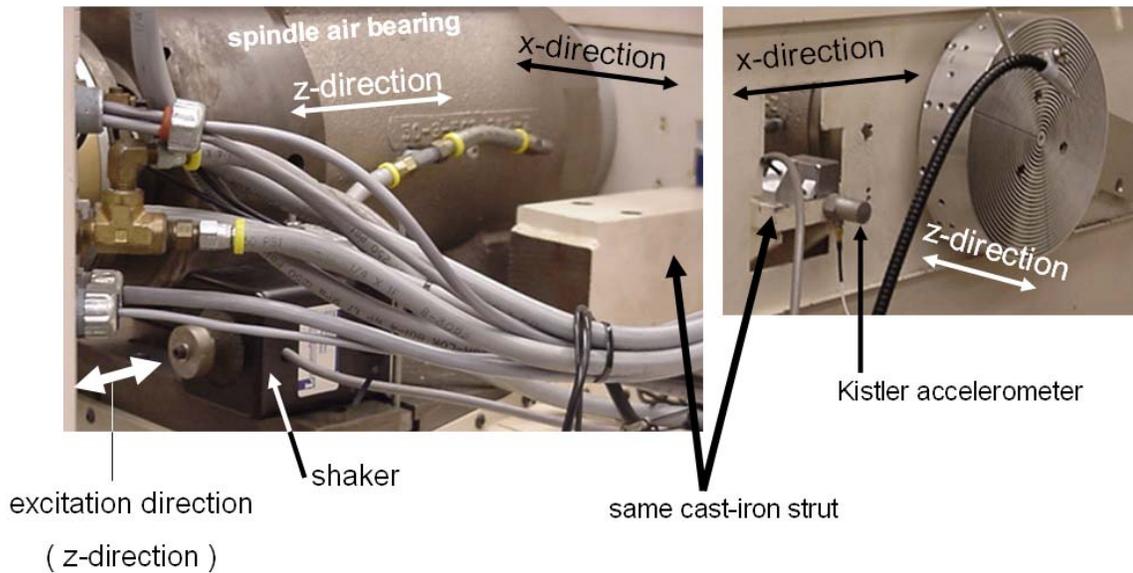


**Figure 5.1-17.** X-axis, z-direction shaker test setup.

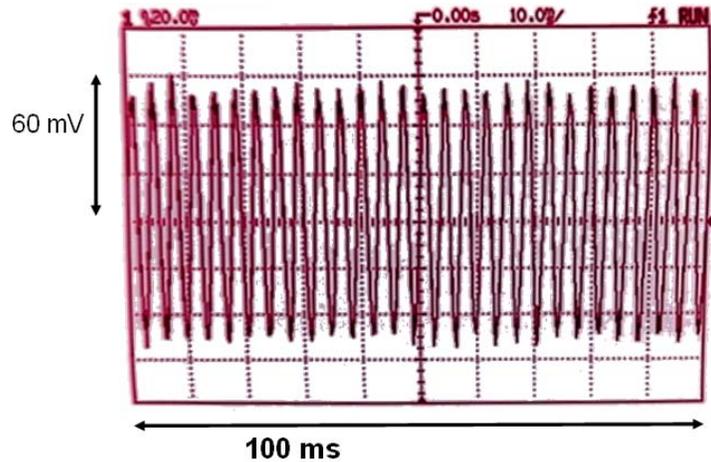


**Figure 5.1-18.** X-axis, z-direction accelerometer signal at  $f_1 \sim 275$  Hz.

### **X-direction (upfeed)**

The x-axis, x-direction shaker test setup is shown in Figure 5.1-19. The measured first natural frequency in the x-direction is  $\sim 120$  Hz, shown in Figure 5.1-20. Vibration at this frequency was also observed at lower excitation frequencies. No other significant vibration frequencies were observed at lower excitation frequencies. Using the voltage and displacement relations from Section 5.1.1, the amplitude of acceleration from Figure 5.1-20 is  $59.5 \text{ mm/s}^2$ , and the predicted displacement amplitude is 104 nm.

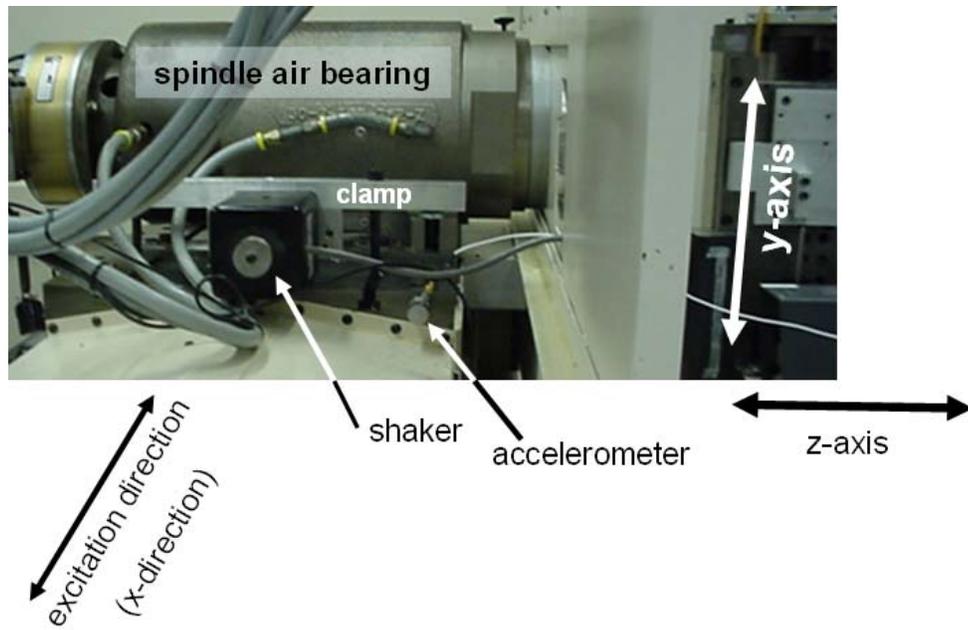


**Figure 5.1-19.** X-axis, x-direction shaker test setup.

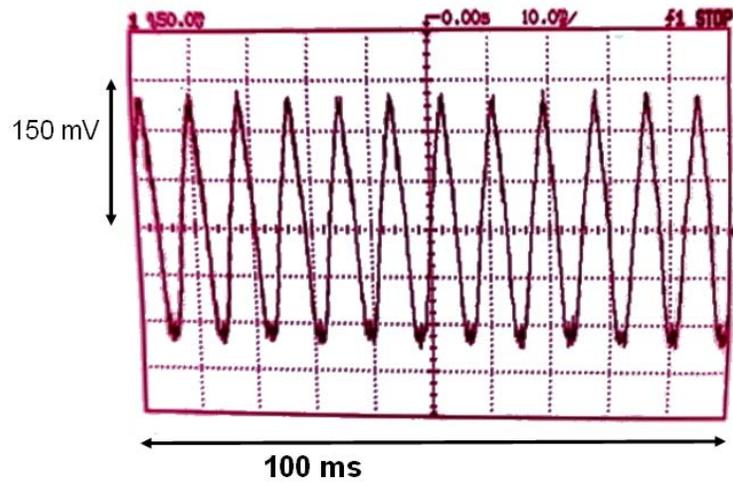


**Figure 5.1-20.** X-axis, x-direction accelerometer signal at  $f_1 \sim 120$  Hz.

### 5.1.3 Y-axis

The y-axis, unlike the oil-hydrostatic x- and z-axes, is an air bearing. The compressible nature of air makes the y-axis a likely cause of larger vibration errors relative to the other machine axes.

#### **Z-direction (depth of cut)**

A shaker test<sup>9</sup> was performed on the y-axis in the depth of cut direction. The experimental setup is shown in Figure 5.1-21. The shaker backing plate is attached by one bolt to the Ultramill and by another to a bracket which attaches to the y-axis slide. Measured vibration frequencies at various excitation frequencies are shown in Figure 5.1-22. Each vibration frequency shown is the frequency of the highest-amplitude peak in an FFT of accelerometer voltage data. Acceleration amplitudes at the highest peak in each FFT are shown in Figure 5.1-23.

---

<sup>9</sup> The shaker test procedure was discussed in more detail in Section 5.1.1. Relations for accelerometer voltage, acceleration, and displacement amplitudes were also provided

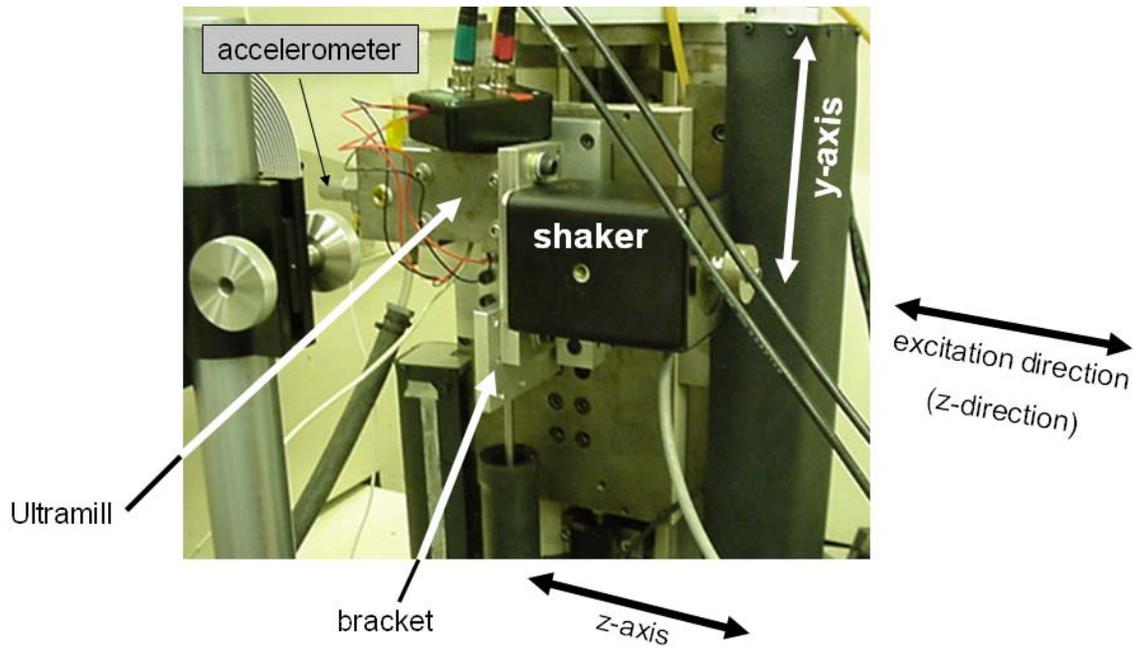


**Figure 5.1-21.** Y-axis z-direction shaker test.

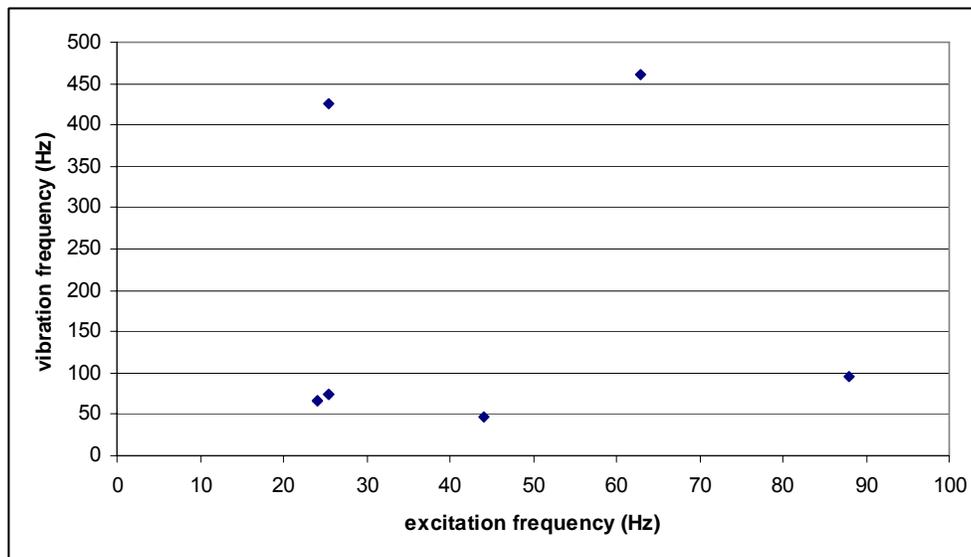


**Figure 5.1-22.** Y-axis vibration frequency vs. excitation frequency.

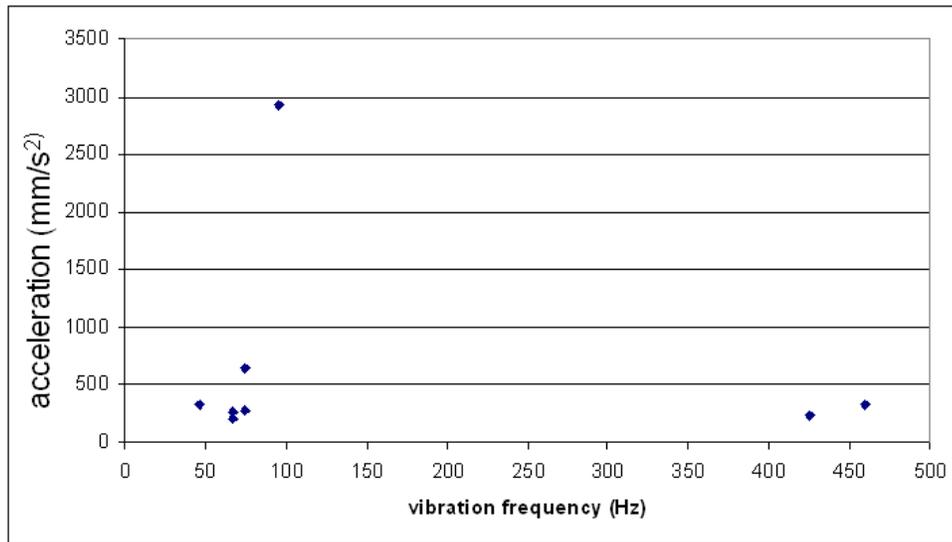


**Figure 5.1-23.** Y-axis acceleration amplitude vs. vibration frequency.

Figure 5.1-24 shows a sample of 2000 Hz accelerometer data collected at 25 Hz shaker excitation frequency. Figure 5.1-25 shows an FFT of this data. The largest amplitude in the FFT occurs at 75 Hz, the second-highest peak is at 425 Hz, and the third is at 50 Hz. Table 5.1-2 shows the acceleration and displacement amplitudes as calculated using relations from Section 5.1.1. This table demonstrates that the acceleration and displacement vibration behavior of the y-axis are not easily predictable based on excitation frequency.

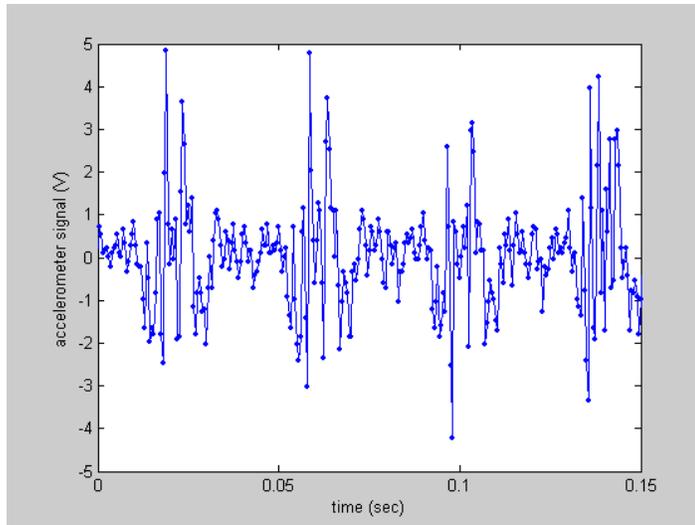


**Figure 5.1-24.** Y-axis vibration at 25 Hz excitation frequency.

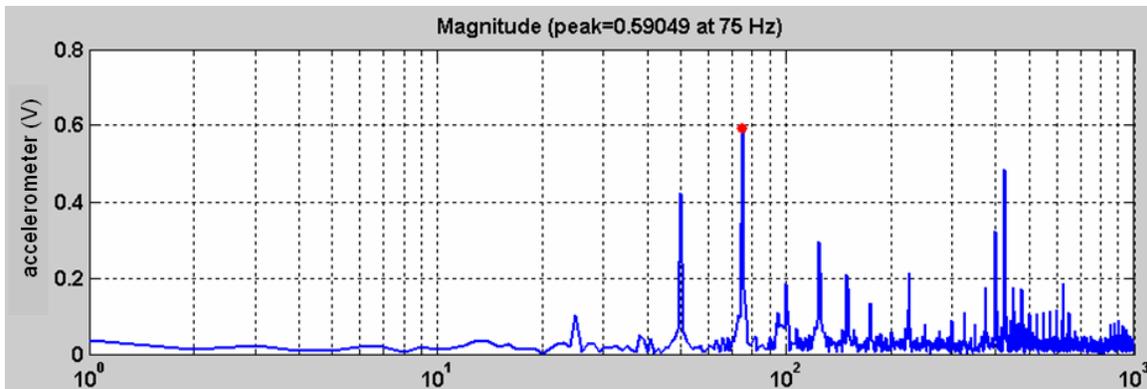


**Figure 5.1-25.** FFT of Figure 5.1-24 data (25 Hz excitation frequency)

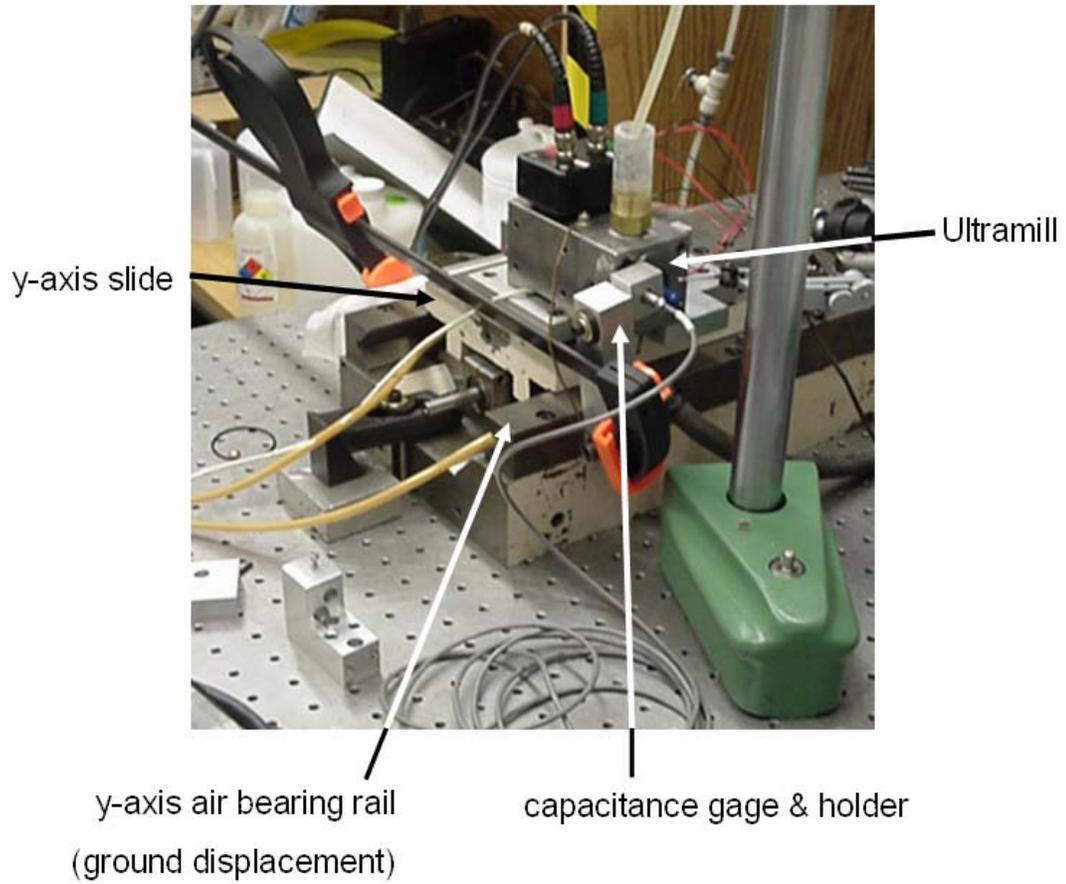
f	$\omega$	accelerometer	acceleration	displacement
(Hz)	(rad/s)	(V)	mm/s <sup>2</sup>	$\mu\text{m}$
50	314	0.4	183	1.86
75	471	0.59	270	1.22
420	2639	0.48	220	0.03

**Table 5.1-2.** Three peak frequencies from Figure 5.1-25 data with acceleration amplitudes and predicted displacement amplitudes (supporting equations: Section 5.1.1)

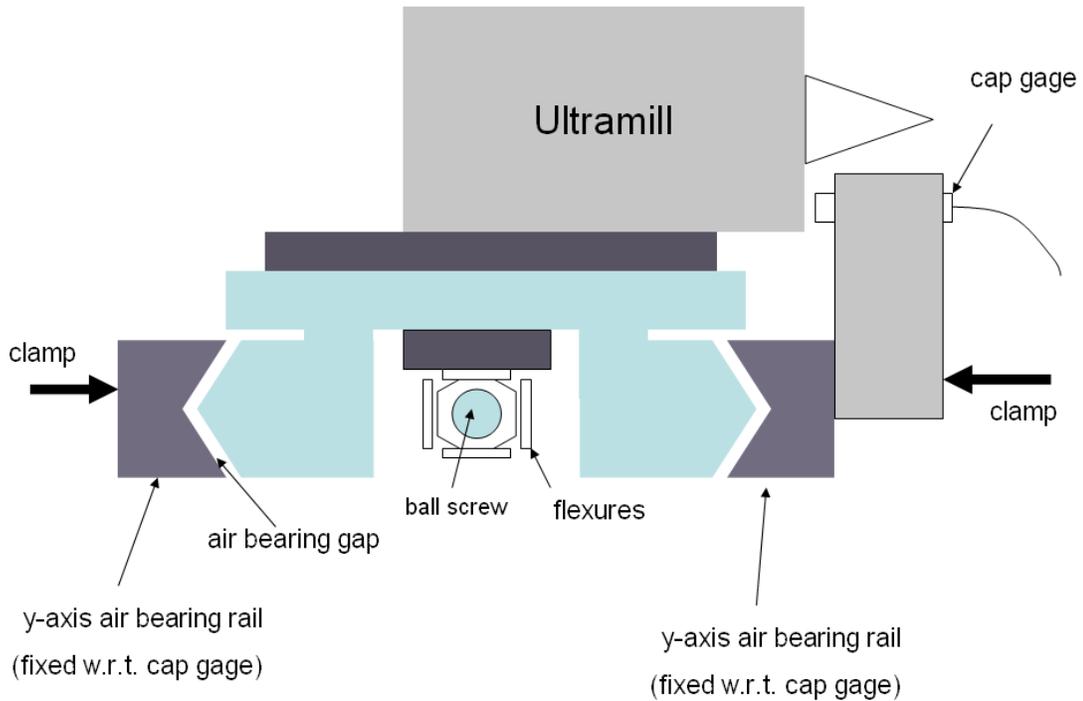
The highest acceleration peak observed in y-axis vibration is at 95 Hz (Figure 5.1-23). This acceleration occurred near the excitation frequency of 90 Hz. The displacement amplitude of vibration for an acceleration of  $2920 \text{ mm/s}^2$  at a frequency of  $95 \text{ Hz} = 596 \text{ rad/s}$  is  $8.2 \text{ }\mu\text{m}$  (from Equation 9). Although y-axis vibration performance is complex, the most significant vibration frequency appears to be at 95 Hz.

### **Sub-hertz Drift Error**

Vibration of the y-axis was examined with the axis removed from the Nanoform DTM. Y-axis slide displacement was examined with air supplied and not supplied to the air bearing. Figure 5.1-26 and Figure 5.1-27 show the experimental setup.

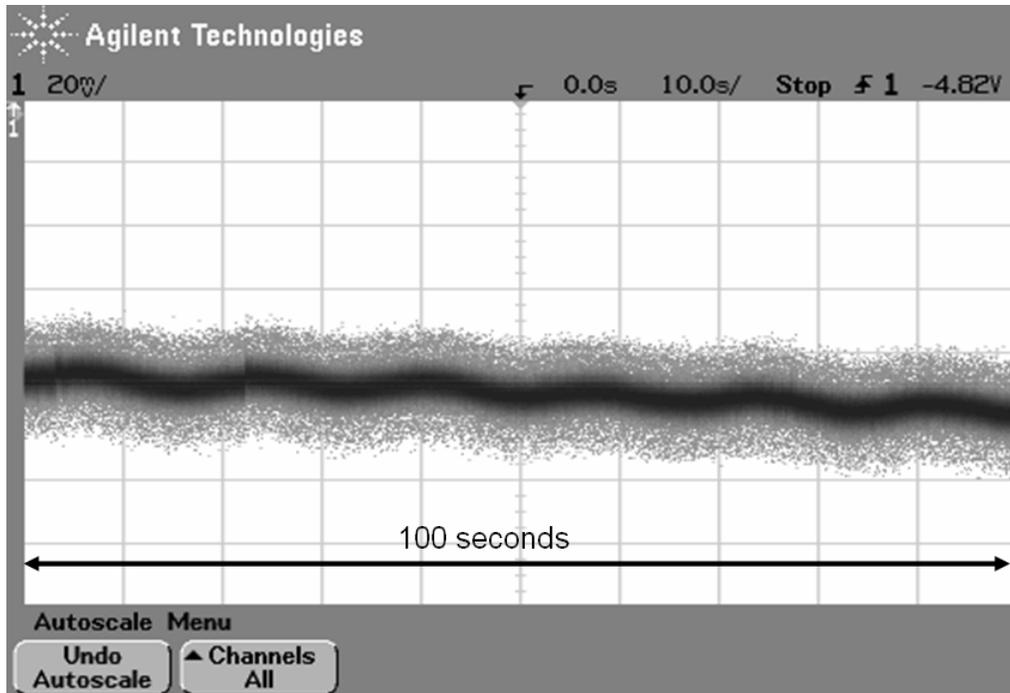


**Figure 5.1-26.** Y-axis and Ultramill vibration test setup, removed from the Nanoform DTM.

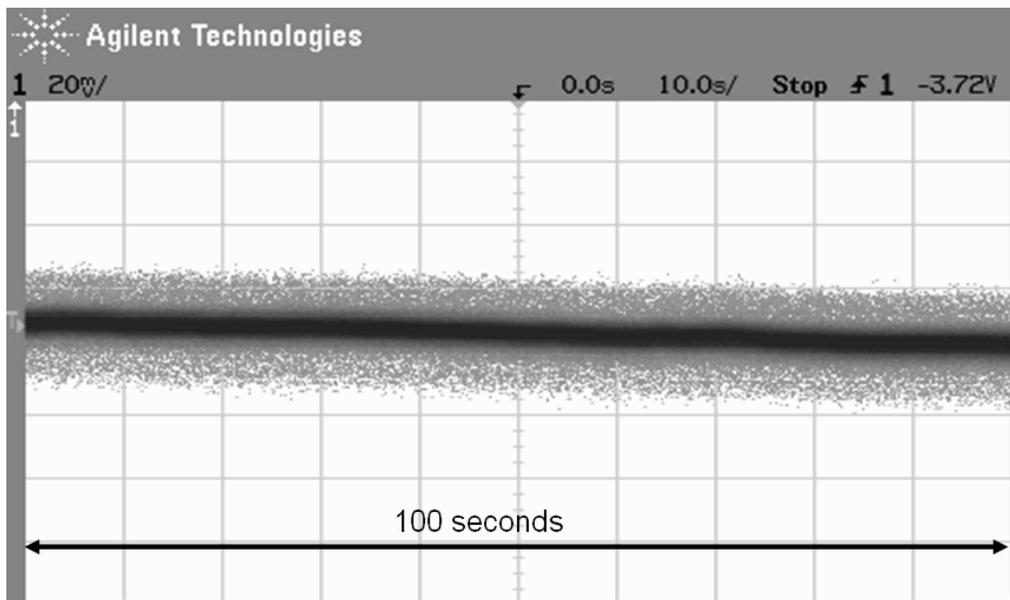


**Figure 5.1-27.** Y-axis and Ultramill vibration test setup diagram.

An extremely low-frequency displacement of the y-axis was observed when air was supplied to the axis air bearing and the Ultramill and its cooling pump were not operating. Figure 5.1-28 shows an example of this drift. The amplitude of this signal is approximately 4 mV or 20 nm. The approximate wavelength is 15 seconds, yielding a frequency of 4 cycles per minute, 0.07 Hz. This was compared with the displacement of the axis when zero pressure was supplied to the air bearing. Figure 5.1-29 shows this condition, and no sub-Hertz signal is visible.

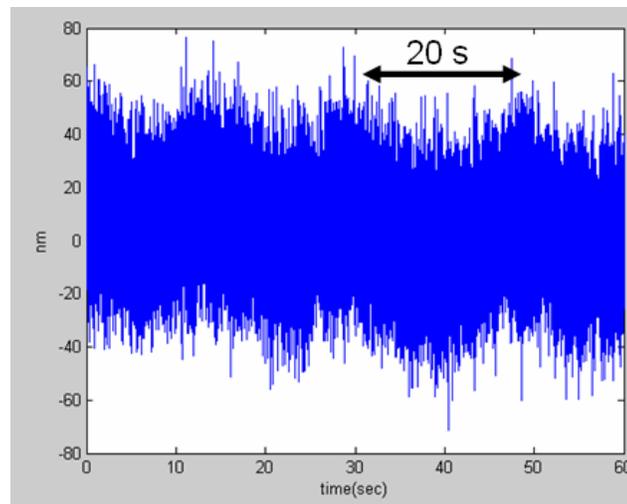


**Figure 5.1-28.** Y-axis displacement: bearing air supply 75 psi, Ultramill off, cooling pump off. 20 mV/division, 5 nm/mV, 10 seconds per division, sub-Hertz signal visible.

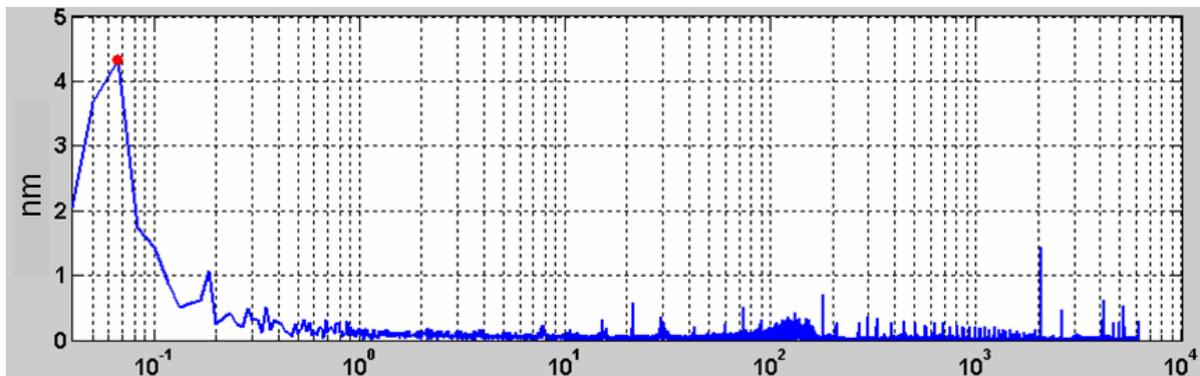


**Figure 5.1-29.** Y-axis displacement: bearing air supply zero psi, Ultramill off, cooling pump off. 20 mV/division, 5 nm/mV, 10 seconds per division, no sub-Hertz signal visible.

In order to fully characterize this drift feature, capacitance gage data was collected at 12.5 kHz for several minutes using the dSpace data acquisition system. Figure 5.1-30 shows the capacitance gage signal with the y-axis air bearing supplied at 75 psi and with the cooling pump and Ultramill not running. The sub-Hertz signal with a period of about 20 seconds is clearly visible. Figure 5.1-31 shows an FFT of this data. This FFT shows an amplitude peak of 4 nm at a frequency of .067 Hz, or 15 seconds per cycle.

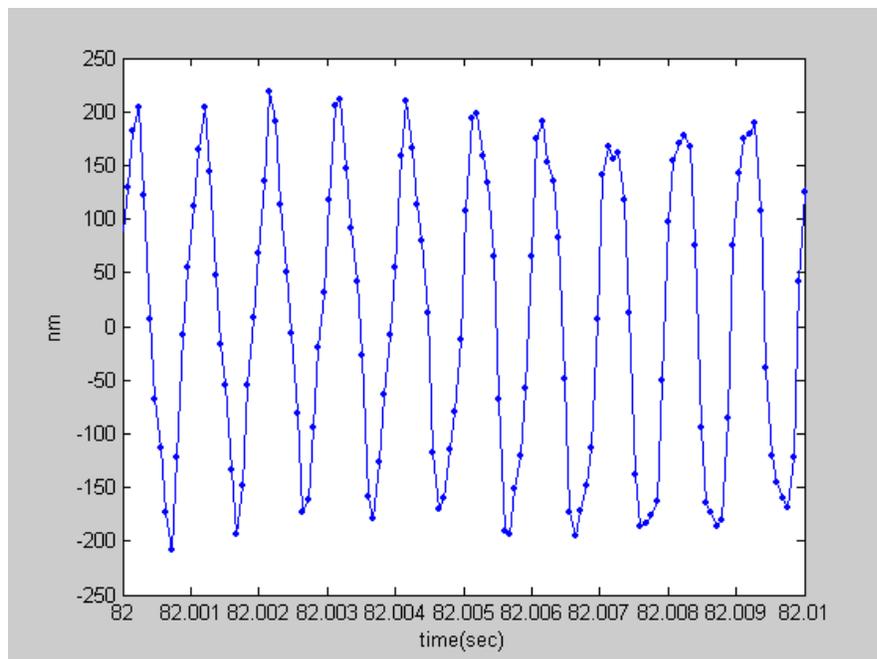


**Figure 5.1-30.** Y-axis displacement: bearing air supply 75 psi, Ultramill off, cooling pump off, sub-Hertz signal visible.

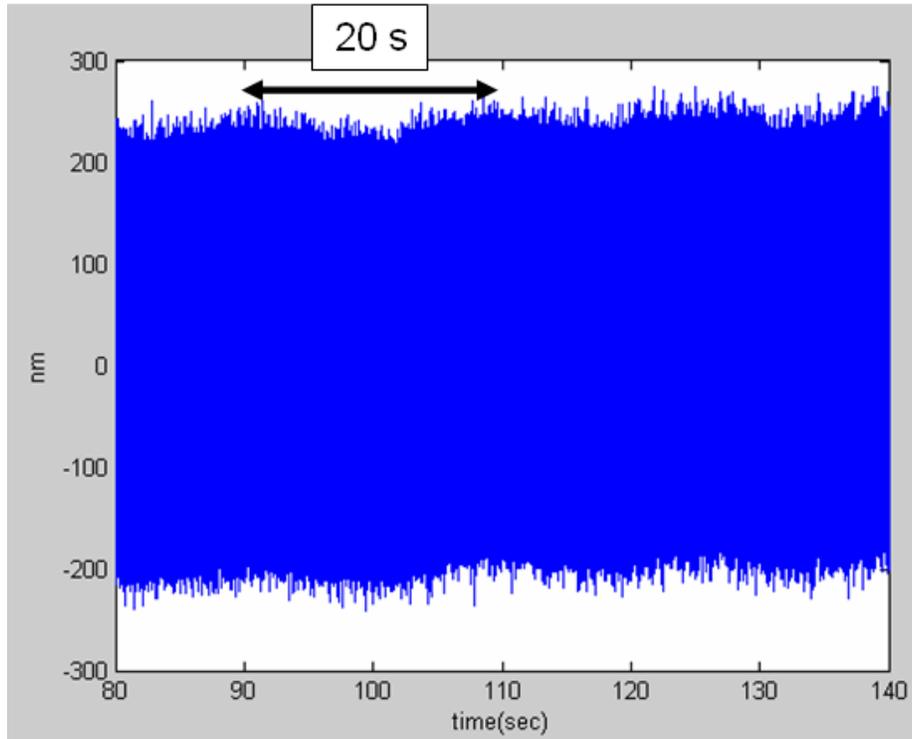


**Figure 5.1-31.** FFT of y-axis displacement, air bearing supplied at 75 psi.

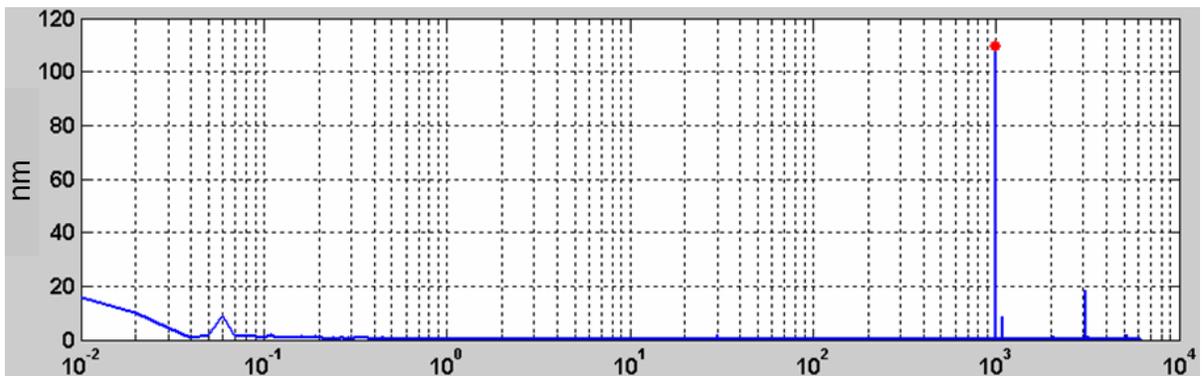
Additional data was collected to characterize this low-frequency effect when the Ultramill was running. Figure 5.1-32 shows 10 milliseconds of data in which the 1000 Hz vibration of the Ultramill is clearly visible. Figure 5.1-33 shows one minute of this data, in which a low-frequency change is visible at a frequency of about 3 cycles per minute. Figure Figure 5.1-34, Figure 5.1-35, and Figure 5.1-36 show FFT's of this data set in several frequency ranges. Figure 5.1-35 shows a 9 nm amplitude signal at a frequency of 0.6 Hz, or one cycle per 17 seconds. It is notable that the middle frequency range of this data, shown in Figure 5.1-36, reveals no vibration greater than 1 nm at 60 or 120 Hz. This demonstrates that line-frequency electrical noise in the Ultramill high-voltage amplifiers is not a significant contributor to y-axis vibration.



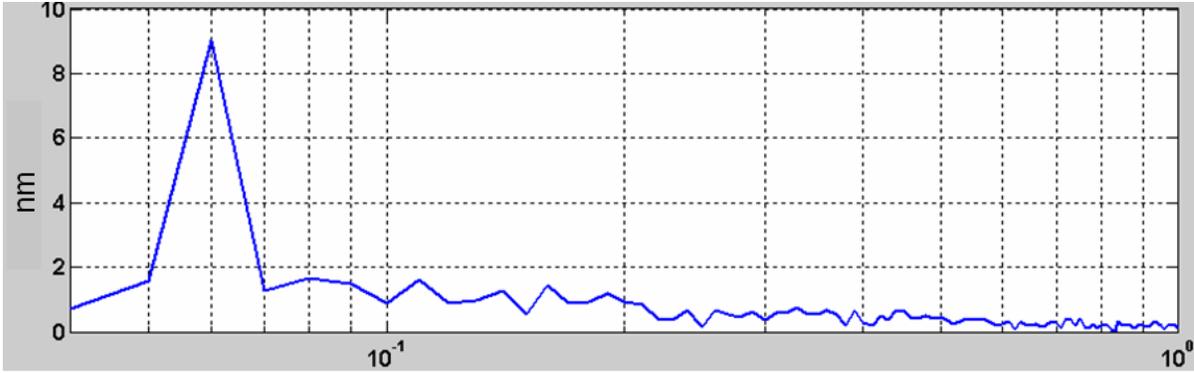
**Figure 5.1-32.** Y-axis vibration: Ultramill 1000 Hz, 400 Vpp.



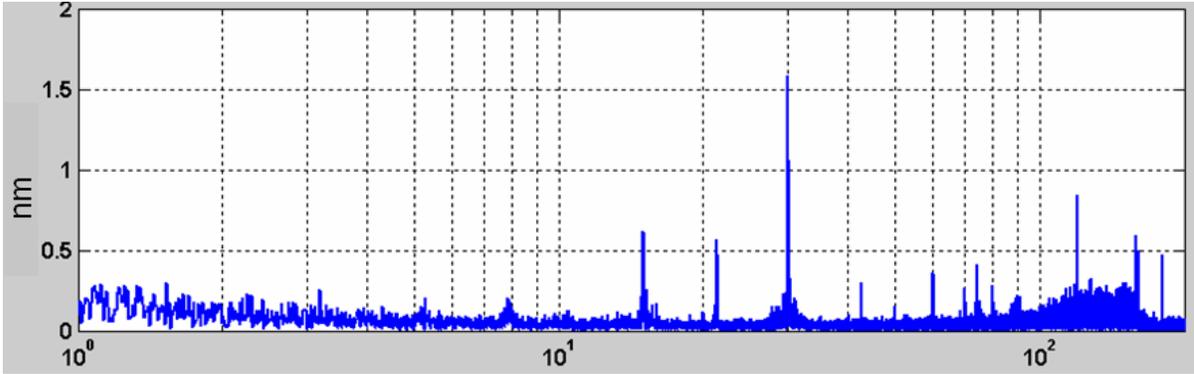
**Figure 5.1-33.** Y-axis vibration: Ultramill 1000 Hz, 400 Vpp, sub-hertz signal visible.



**Figure 5.1-34.** FFT: full frequency range.



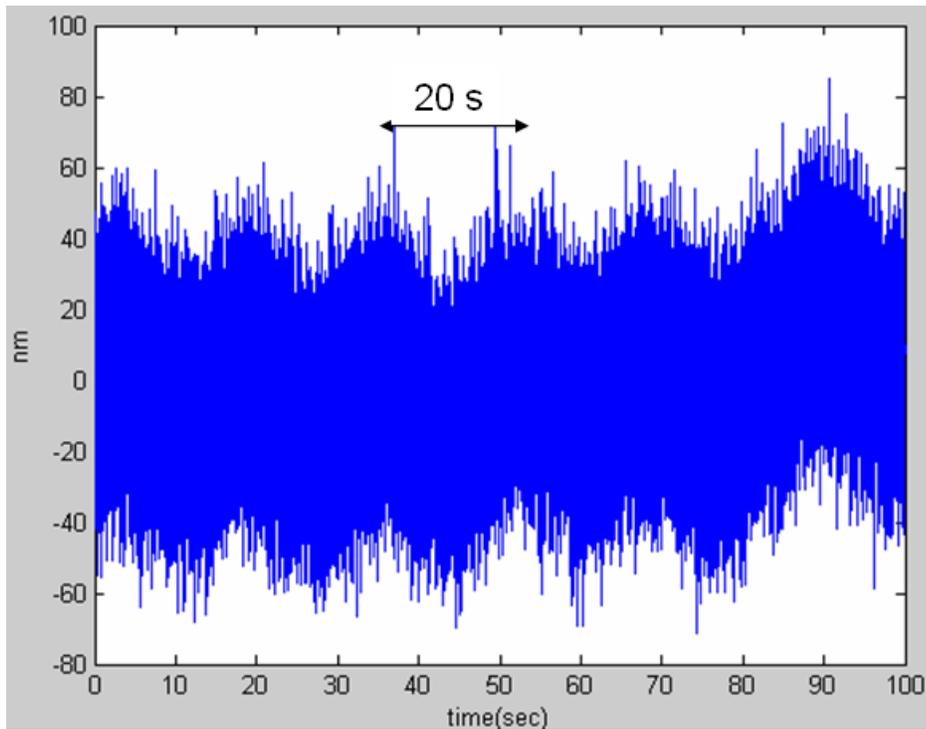
**Figure 5.1-35.** FFT: low frequency range.



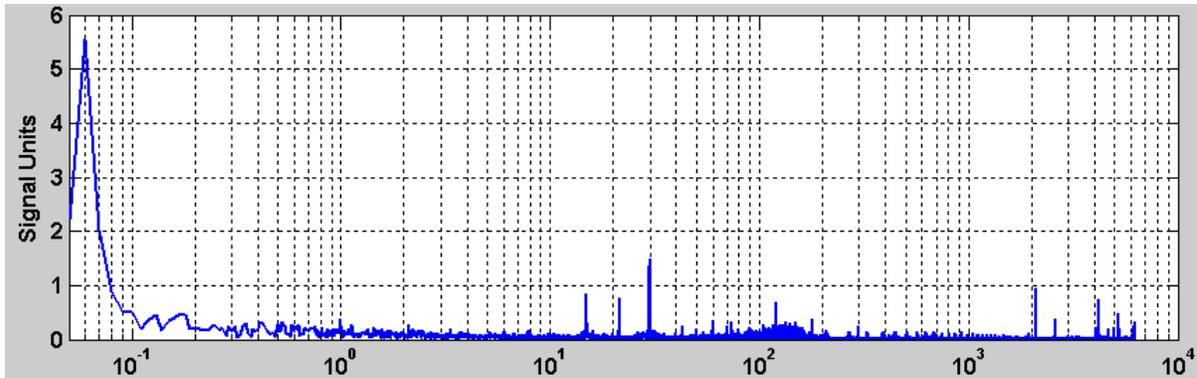
**Figure 5.1-36.** FFT: middle frequency range.

Cooling pump effects were evaluated by measuring y-axis displacement with the air bearing supplied at 75 psi, the pump on, and the Ultramill not running. Figure 5.1-37 shows the displacement signal, in which the sub-Hertz drift is again clearly visible. An FFT is shown in Figure 5.1-38. This data should be compared with the FFT in Figure 5.1-31, which shows drift due to the air bearing only. The only vibration amplitude greater than 1 nm visible in Figure 5.1-38 (with the pump running) which is not visible in Figure 5.1-31 (with the air bearing only) is at 30 Hz. This is the reciprocation frequency of the cooling pump. The data in Figure 5.1-38 (pump running, Ultramill not running) should also be compared with that in

Figure 5.1-36, the middle frequency range of vibration with the Ultramill and cooling pump both running. The amplitudes at 30 Hz, the cooling pump frequency, are both about 1.5 nm. No other amplitudes greater than 1 nm are visible in the 1 – 200 Hz frequency range of these FFT's.



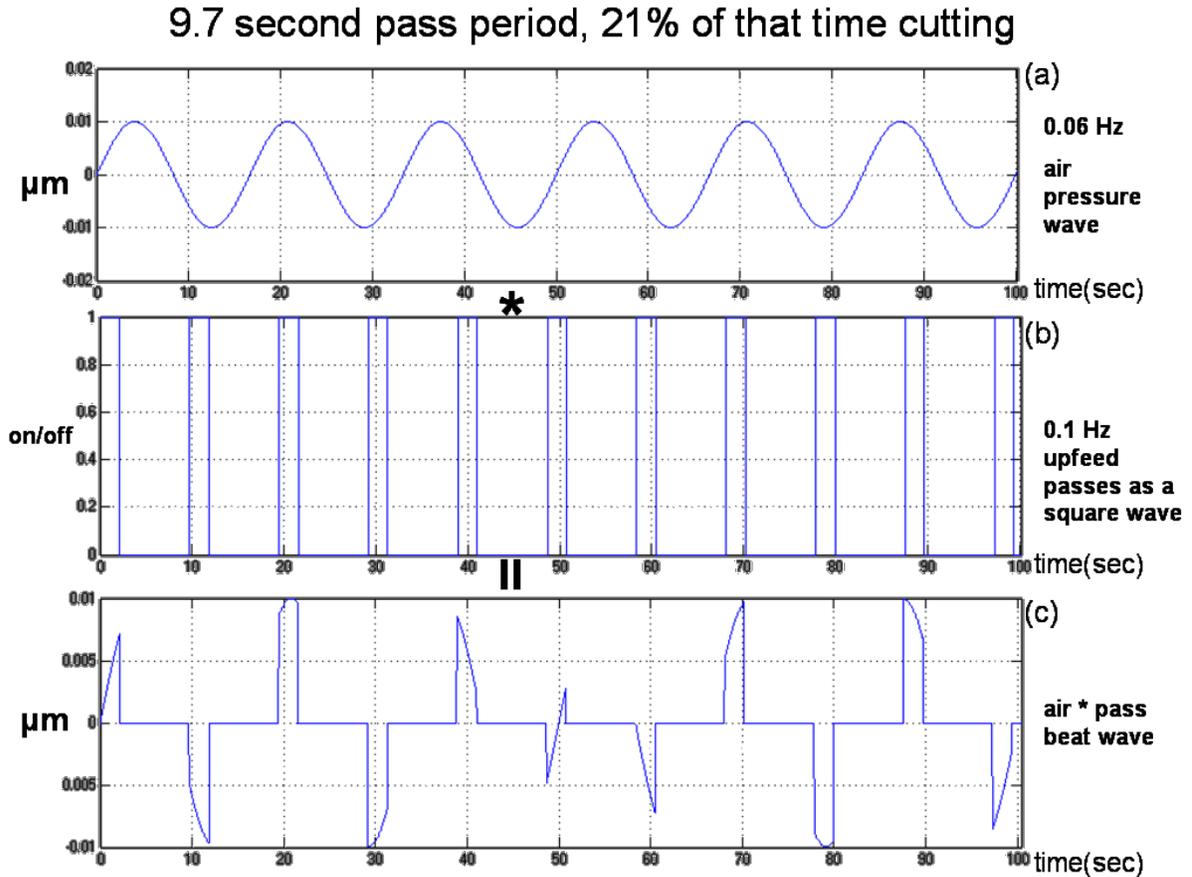
**Figure 5.1-37.** Y-axis displacement: air bearing supplied at 75 psi, cooling pump on, Ultramill not running. Sub-Hertz signal is visible.



**Figure 5.1-38.** FFT of y-axis displacement: air bearing supplied at 75 psi, cooling pump on, Ultramill off.

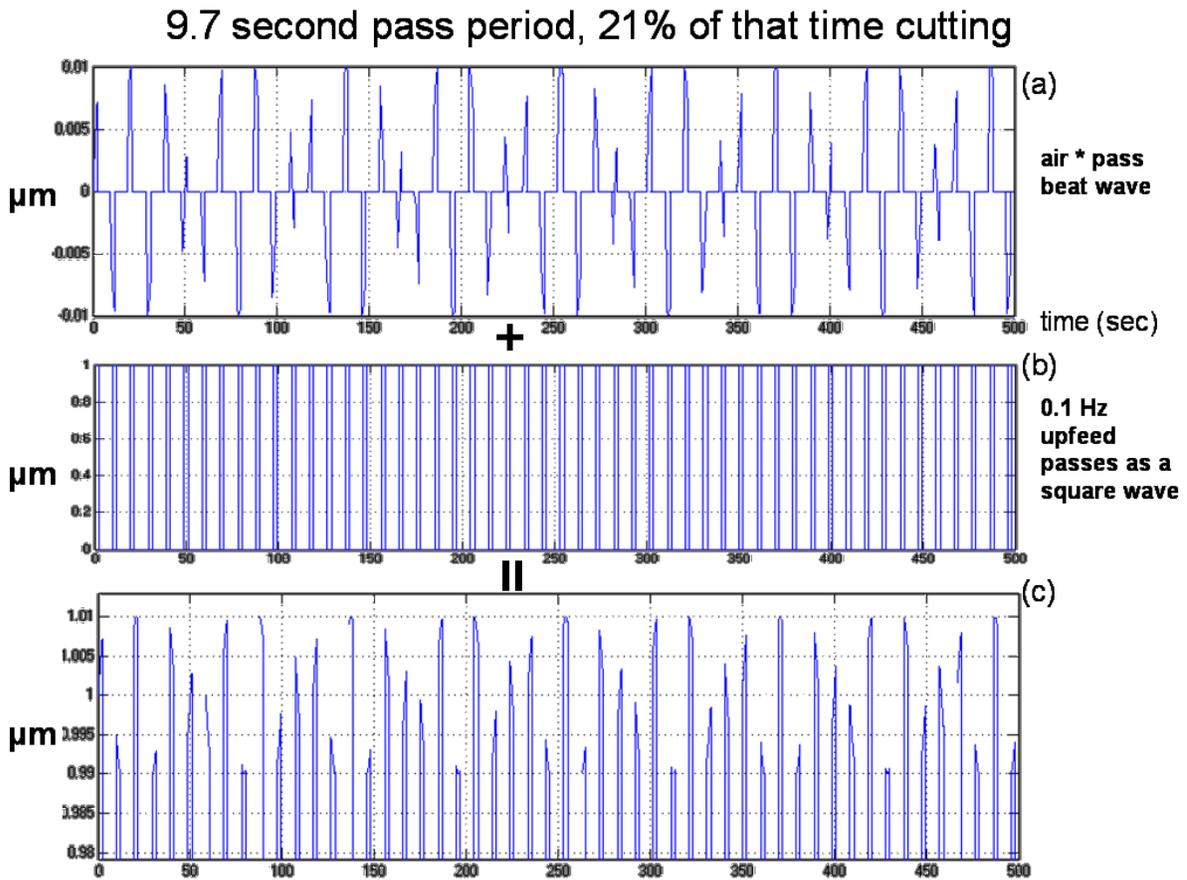
The 0.06 Hz air bearing drift frequency is similar to that of the rastering passes. The elapsed time of one upfeed pass (with backfeed and depth changes), or the time between two crossfeed passes, is 6-15 seconds, dependent on upfeed speed and the distance covered by each upfeed pass. The interaction of the frequencies of air bearing drift and rastering passes creates a complex signal. Figure 5.1-39 and Figure 5.1-40 show an example of this effect. The 0.01  $\mu\text{m}$  amplitude, 0.06 Hz air pressure wave in Figure 5.1-39 (a) is based on data from Figure 5.1-35 (low frequency range, Ultramill running, 9 nm peak @ 0.06 Hz). A part program with 1  $\mu\text{m}$  crossfeed increment, 1 mm/s upfeed speed, and 1  $\mu\text{m}$  depth of cut was measured in frequency and duration of raster passes by the Nanoform interferometers and encoder. The performance of this program was one upfeed pass every 9.7 seconds lasting 2.1 seconds. Figure 5.1-39 (b) models this measured pass frequency as a 0.1 Hz square wave with a pulse width of 21%, representing the upfeed passes as a 1- or 0-value square wave. “One” represents the Ultramill cutting and “zero” represents the Ultramill not cutting (during backfeed or a change in depth). This signal, when multiplied with a sine wave representing the 0.06 Hz air bearing drift, Figure 5.1-39 (a), yields the “air\*pass beat wave” signal in

Figure 5.1-39 (c). It can be seen by comparing Figure 5.1-39 (c) to Figure 5.1-39 (a) that the “air\*pass beat wave” in Figure 5.1-39 (c) is made up of the sections of Figure 5.1-39 (a) that are not zeroed by the on/off square wave.



**Figure 5.1-39.** Air bearing drift interaction with upfeed pass frequency: 100 seconds elapsed time.

The “air\*pass beat wave” signal, shown again in Figure 5.1-40 (a) is added to a second square wave, Figure 5.1-40 (b), to represent its effect on a hypothetical 1 μm depth of cut. The resulting surface variations in Figure 5.1-40 (c) do not vary regularly with respect to the crossfeed passes in time and would not be expected to vary regularly with respect to crossfeed in spatial frequency.



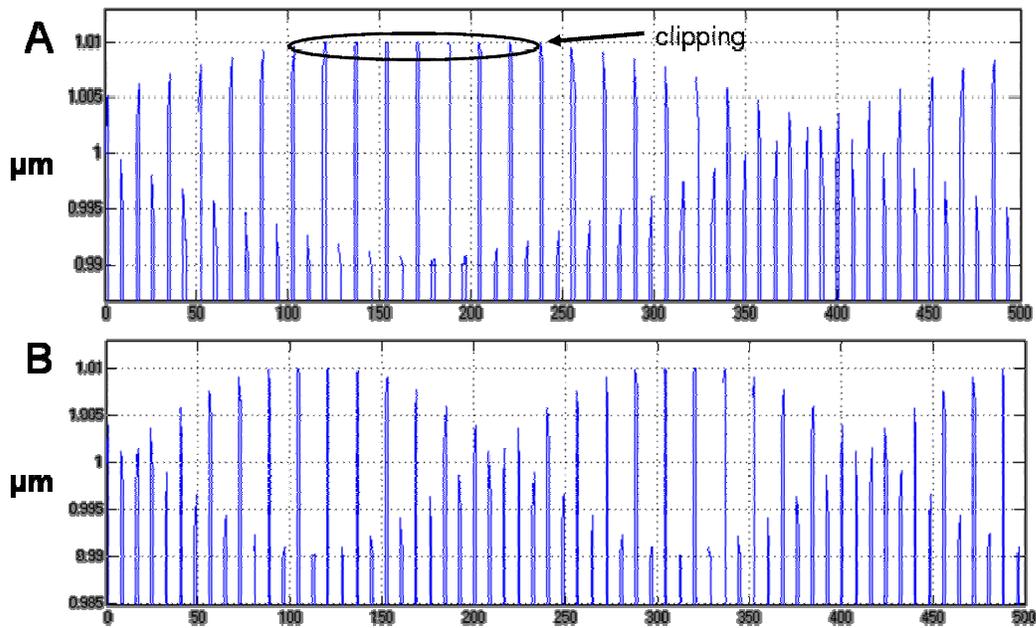
**Figure 5.1-40.** Air bearing drift interaction with 1  $\mu\text{m}$  depth of cut: 500 seconds elapsed time.

Table 5.1-3. shows two other examples of measured performance in rastered-flat part programs. With different feed speed inputs, these two programs resulted in similar elapsed times per pass and percentage of that time spent cutting. Figure 5.1-41 shows the predicted surface features versus time that would be created by the interaction of the pass frequencies of “Flat A” and “Flat B” part programs with the constant 0.06 Hz air bearing drift frequency. The long-wavelength surface frequencies are much more different (50%) than the input measured pass frequencies (<10%). Also, the maximum predicted change in DOC between

two subsequent passes of 20 nm would produce a growth in characteristic crossfeed feature size ( $c_{\text{cross}}$ ) of 1.88  $\mu\text{m}$ , equal to the difference in the chord of the 50  $\mu\text{m}$  tool radius at 1.02  $\mu\text{m}$  and 0.98  $\mu\text{m}$  DOC. The programmed crossfeed spatial increment of “Flat A” is 1.5  $\mu\text{m}$ , and a 1.88  $\mu\text{m}$  increase in the crossfeed feature size will be expected to destroy the highest isolated peaks in Figure 5.1-41-A, denoted by “clipping.” The programmed spatial crossfeed increment of “Flat B” is 2  $\mu\text{m}$ . A 1.88  $\mu\text{m}$  change in crossfeed feature size would not be expected to destroy any of the peaks in Figure 5.1-41-B.

	programmed			measured		
	DOC ( $\mu\text{m}$ )	upfeed length (mm)	upfeed speed (mm/s)	crossfeed increment ( $\mu\text{m}$ )	crossfeed elapsed time (s)	fraction cutting (%)
Flat A	1	2	1.5	1.5	8.5	17.6
Flat B	1	2	2	2	8	13.75

**Table 5.1-3.** Examples of measured performance in two different part programs.



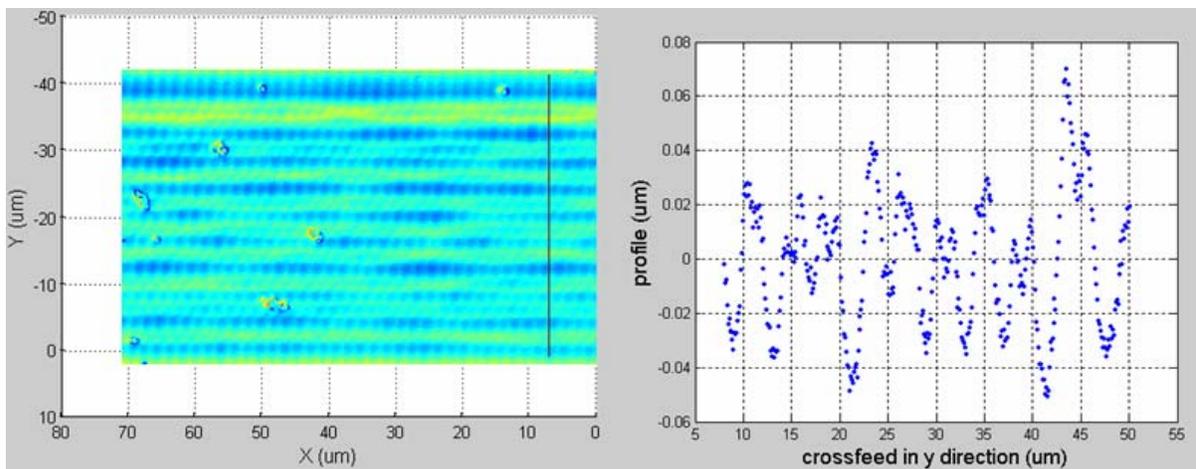
**Figure 5.1-41.** Examples of predicted long-wavelength surface frequencies and probable clipping.



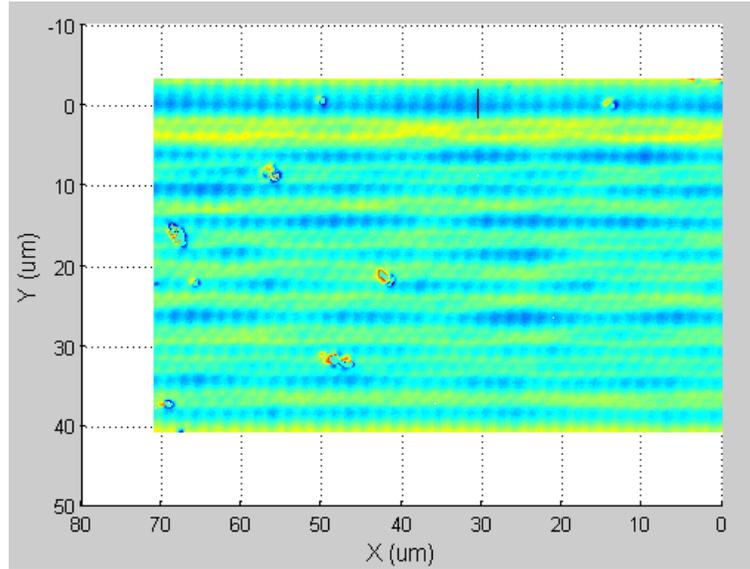
The yaw angle  $\theta$  is equal to the y-direction yaw error  $\sin\theta$  by the small angle theorem. The depth-of-cut direction error is equal to the Abbé offset multiplied by  $(1 - \cos\theta)$ . An evaluation of Ultramill tool tip actual versus desired position yields two important results.

- support of y-axis positioning accuracy as measured at the encoder readhead
- If the y-axis encoder position (as collected during machining) and the Ultramill tool tip (as shown in workpiece features) are both accurate in a given region of the workpiece, this places a limit on y-axis yaw error, and thereby on depth of cut error due to this cause.

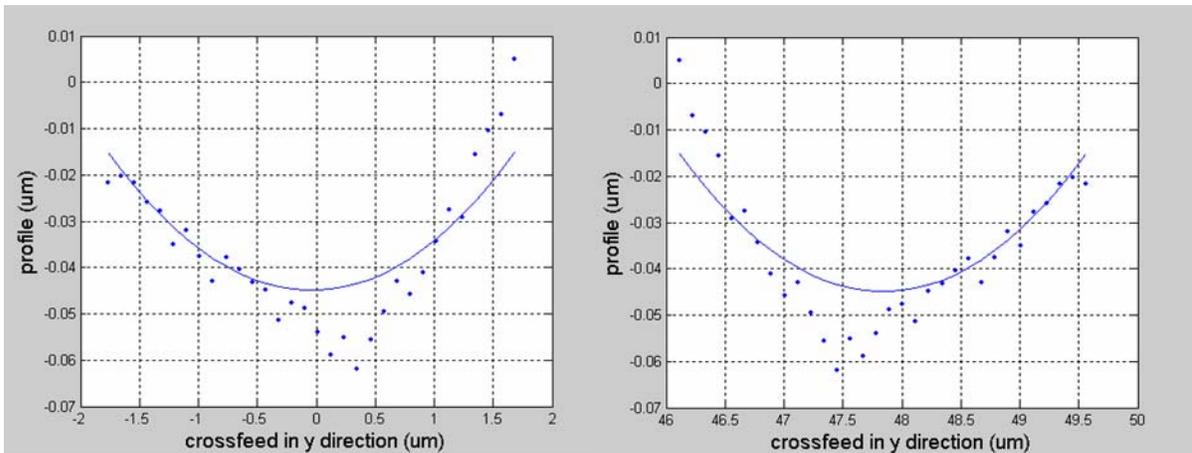
A program was written in Matlab to allow the Ultramill tool radius to be superimposed on surface topology data. A 100x interferogram of a flat is shown in Figure 5.1-44. Figure 5.1-45 and Figure 5.1-46 show the placement of the first crossfeed pass and the surface profile data of that pass.



**Figure 5.1-44.** Crossfeed profile: 2  $\mu\text{m}$  crossfeed, 1.91 mm/s upfeed, 1000 Hz



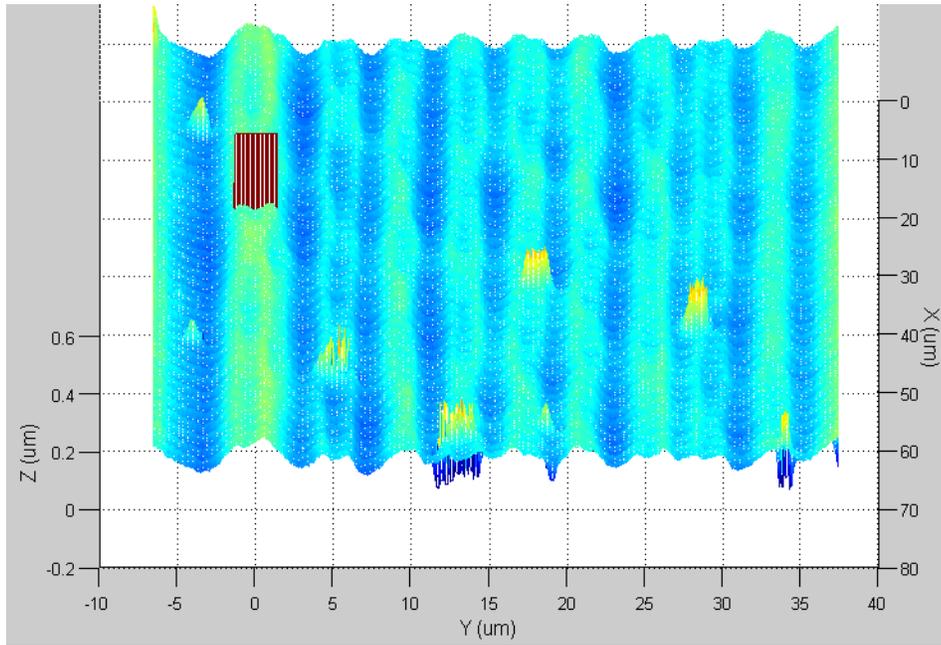
**Figure 5.1-45.** Crossfeed pass #1



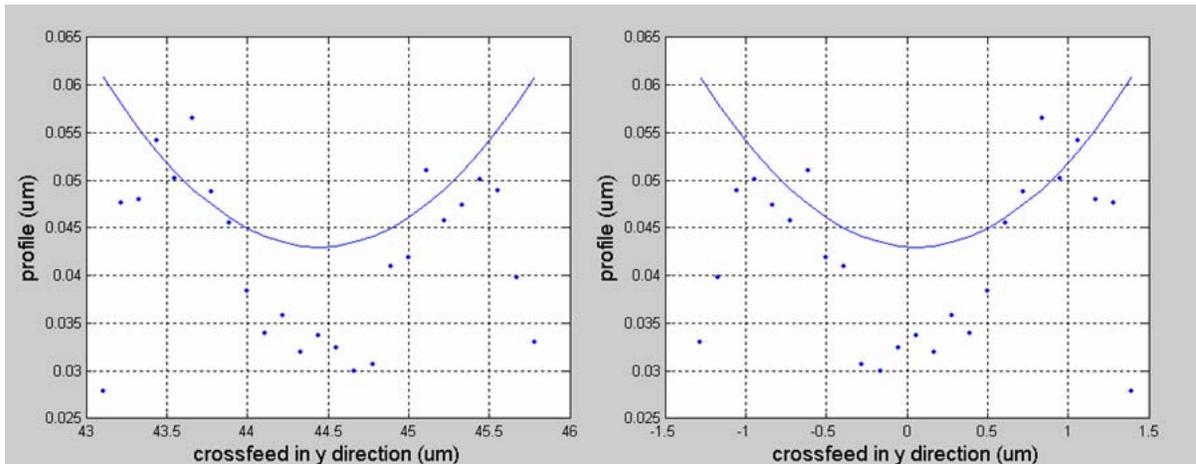
**Figure 5.1-46.** Placing crossfeed pass #1 and location zero. 50  $\mu\text{m}$  radius tool 49.955  $\mu\text{m}$  out of part, Zygo y-coordinate 47.8.

Figure 5.1-47 and Figure 5.1-48 show the same data for pass #2. Table 5.1-4 contains the data for the remaining passes on this flat. In this table, the “programmed y-axis coordinate” is the crossfeed increment of 2  $\mu\text{m}$  multiplied by the crossfeed pass number. The “measured

y coordinate” is the location of the center of the tool radius fit to each crossfeed pass using the *crossfeed.m* Matlab program. The “measured [pass] size” is the difference of two adjacent pass locations.



**Figure 5.1-47.** Crossfeed pass #2 location.



**Figure 5.1-48.** Placing pass #2 at 44.5  $\mu\text{m}$ .

pass #	$\mu\text{m}$				
	programmed y-axis coordinate	@ tool tip			@ encoder
		measured y coordinate	measured size	error	y-axis PV error
1	2	2	no data	no data	0.04
2	4	5.3	3.3	1.3	0.04
3	6	8.3	3	1.0	0.04
4	8	10.8	2.5	0.5	0.04
5	10	12.6	1.8	-0.2	0.04
6	12	15	2.4	0.4	no data
7	14	16.6	1.6	-0.4	0.04
8	16	18.6	2	0.0	0.04
9	18	20.6	2	0.0	0.04
10	20	22.5	1.9	-0.1	0.04
11	22	24.5	2	0.0	no data
12	24	26.5	2	0.0	no data
13	26	28.5	2	0.0	no data
14	28	30.5	2	0.0	no data
15	30	32.55	2.05	0.1	no data
16	32	34.7	2.15	0.1	no data
17	34	36.7	2	0.0	no data
18	36	no data	no data	no data	no data
19	38	40.7	no data	no data	no data
20	40	no data	no data	no data	no data

**Table 5.1-4.** Y-axis accuracy statistics of each pass.

The measured sizes of passes 3 through 16 show good agreement with the 2  $\mu\text{m}$  programmed pass size. Axis-position data was only collected for the first ten passes. The y-axis encoder position confirms that, for all the passes in which this data was collected, the y-axis (at the encoder) moved no more than its resolution of 40 nm. The Abbé offset from the y-axis encoder to the Ultramill tool tip is approximately 250 mm. The  $\pm 500$  nm error of y-direction tool tip location limits the y-axis yaw angle to the microradian range and the cosine error in the depth of cut direction to less than 1 nm.

### 5.1.4 Spindle

The natural frequencies of the spindle rotating mass in both the depth of cut (z) and upfeed (x) directions were found by performing shaker<sup>10</sup> tests. The spindle air bearing is mounted on the x-axis. It was possible to excite the x-axis with the shaker and measure acceleration of the rotating mass of the spindle to determine the spindle natural frequencies. Vibration of the spindle in the crossfeed (y) direction was not examined in this research because neither Ultramill excitation nor x-axis motion exerts significant forces in the y-direction.

#### **Z-direction (depth of cut)**

The experimental setup for the z-direction shaker test is shown in Figure 5.1-49, and the accelerometer signal at the first natural frequency of about 190 Hz is shown in Figure 5.1-50. No resonance with a signal-to-noise ratio of greater than 2:1 was observed at lower excitation frequencies. The acceleration amplitude in Figure 5.1-50 is  $18.3 \text{ mm/s}^2$ , and the predicted displacement amplitude at  $190 \text{ Hz} = 1193 \text{ rad/s}$  is 13 nm (from Equation 9).

---

<sup>10</sup> The shaker test procedure was discussed in more detail in Section 5.1.1. Relations for accelerometer voltage, acceleration, and displacement amplitudes were also provided.

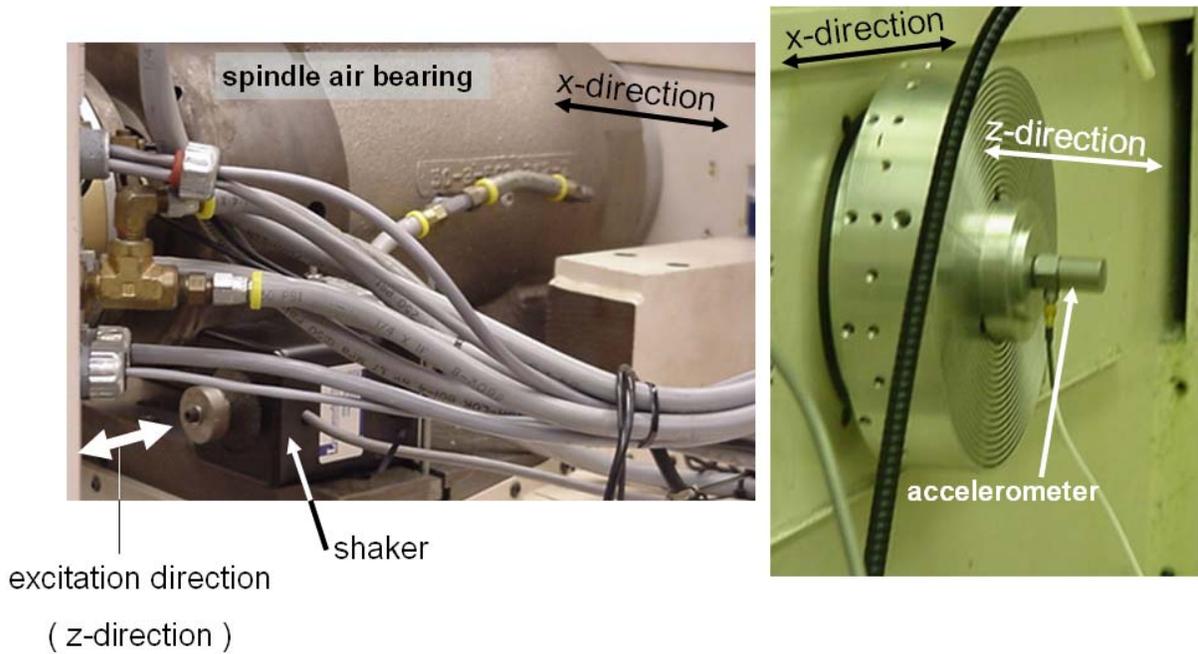


**Figure 5.1-49.** Spindle z-direction shaker test setup.

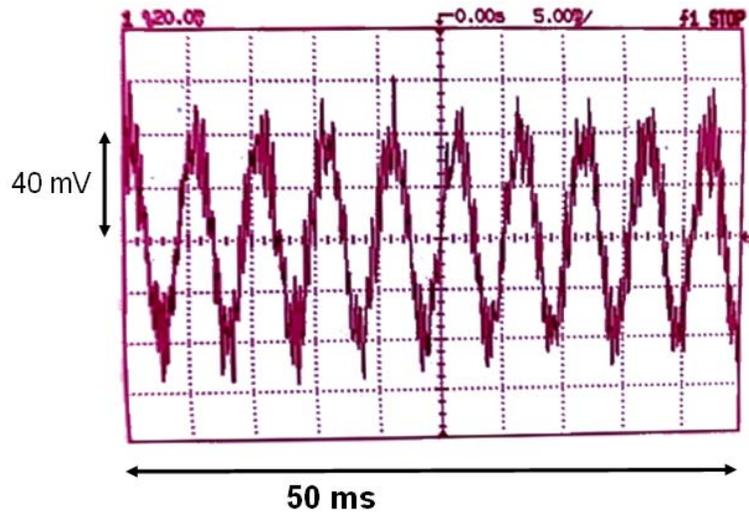


**Figure 5.1-50.** Spindle z-direction accelerometer signal at  $f_1 \sim 190$  Hz.

**X-direction (upfeed)**

The setup for the spindle shaker test in the x-direction is shown in Figure 5.1-51. Vibration of the spindle was examined with the spindle lock installed because the Ultramill is used with

the lock installed. Due to this constraint of vacuum chuck rotation, no convenient mounting point for the accelerometer was available within a few degrees of the x-direction. Spindle vibration was measured with x-axis excitation in the x-direction, but with two different accelerometer positions. These two positions were at about 19° clockwise and 9° counterclockwise from the x-direction.

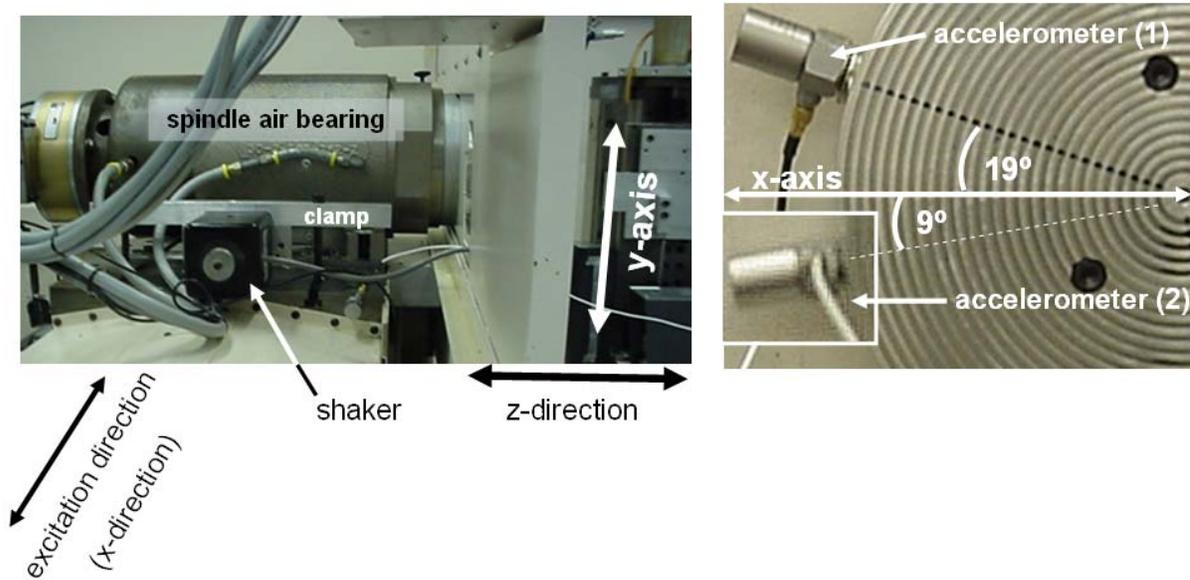


**Figure 5.1-51.** Spindle x-direction shaker test setup with two accelerometer positions.

A resonance was detected at about 120 Hz. However, this frequency matches the natural frequency found for the x-axis in the x-direction. It makes sense that the natural frequency of the spindle in the radial direction would be higher than the natural frequency of the x-axis in its direction of travel, because the spindle air bearing should be stiffer than the x-axis ball screw. Another resonance was detected at 312 Hz on accelerometer (1) and 275 Hz on accelerometer (2). Vibration in this frequency range may reflect either transverse (x-direction) motion or yaw (rotation about the y-direction) of the spindle rotating mass. Either one would affect upfeed motion of the workpiece with respect to the Ultramill. No

resonances with signal-to-noise ratio greater than 2:1 were observed at lower excitation frequencies. The acceleration amplitude shown in Figure 5.1-52 ranges from 270-370 mm/s<sup>2</sup> and the predicted displacement amplitude is 70-140 nm (from Equation 9).

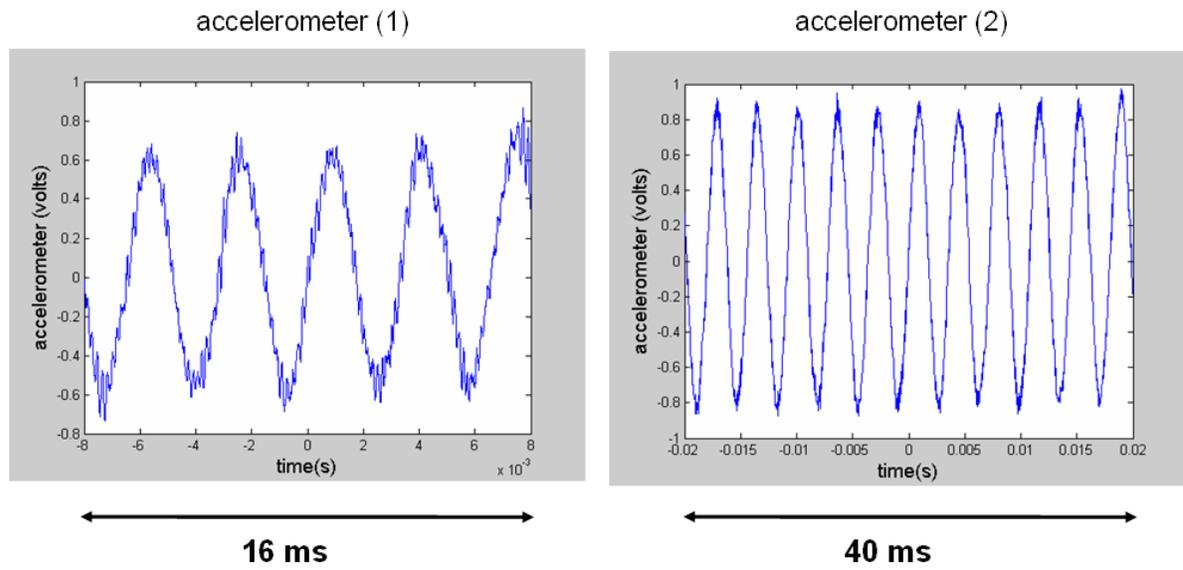


**Figure 5.1-52.** Spindle x-direction accelerometer signal in two positions,  $f_1 \sim 300$  Hz.

## 5.2 TEMPERATURE EFFECTS

Experiments were performed to explore the influence of thermal effects in the Ultramill on the shape of the machined features. These experiments include thermal effect on depth of cut, direct measurement of tool holder position with changing temperature and an assessment of variation in tool holder position after a period of constant operating conditions. Average piezo stack temperature was estimated by application of Negishi's convection model [22, § 2.2.2]. It uses the finite-difference method to model forced convection of the cooling fluid over the piezo stack actuators and predicts temperature as a function of position over the length of the piezo stack. The standard operating conditions for the Ultramill in this research

was 400 Volt peak-peak (Vpp) at 1000 Hz. The input power is given by Equation 13 [22, § 2.2].

$$P = \frac{CV_{pp}^2 f_{UM}}{2} \quad (13)$$

where C is the capacitance of the piezo stack actuators,  $V_{pp}$  is the actuation voltage, and  $f_{UM}$  is the actuation frequency. Negishi determined by experimentation that 22% of this power is lost to heat [22, § 2.2.1]. The measured capacitance of the actuators is 0.15  $\mu$ F. The input power for standard operating conditions is 12 W, and the power lost to heat is 2.6 W. Figure 5.2-1 shows the relationship between piezo stack temperature and position as predicted by this model for standard operating conditions at 20° C coolant temperature and at an elevated coolant temperature of 26° C. Piezo stack length is zero at the steel base of the Ultramill and 22 mm at the interface with the tool holder. In the experiments below, the piezo stack RTD probe was located at approximately 13.5 mm piezo stack length.

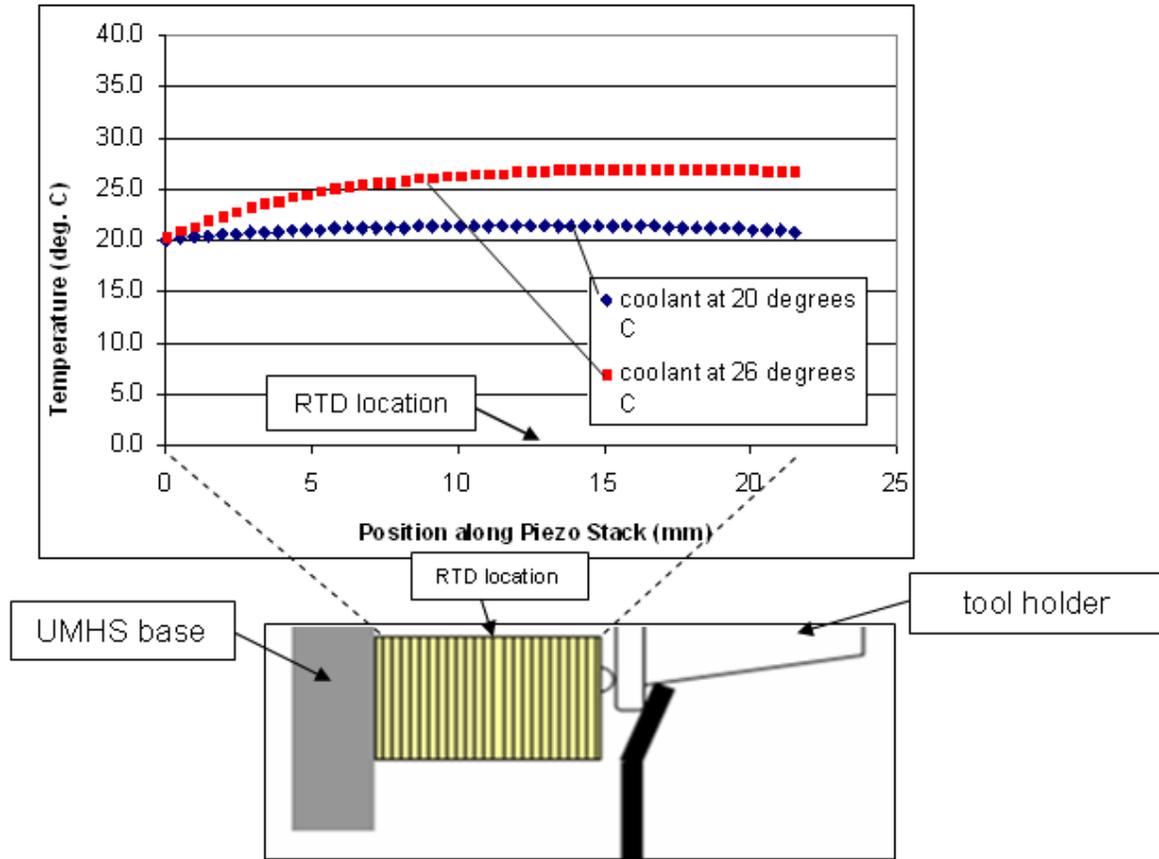


**Figure 5.2-1.** Predicted temperature vs. position in piezo stack length: Ultramill actuation  $400 V_{pp}$  - 1000 Hz.

### 5.2.1 Thermal Effect on Depth of Cut

An experiment was performed to increase understanding of thermal effects on the Ultramill depth of cut. A flat 2 mm in the x (upfeed) direction by 200  $\mu\text{m}$  in the y (crossfeed) direction was machined. The crossfeed increment used was 1  $\mu\text{m}$ . A deliberate temperature excursion was caused just after pass 50. This was accomplished by raising the Thermocube PID controller's target temperature for the return line from the Ultramill to the reservoir from 20

to 25 °C. The target temperature was lowered to the original value of 20° C after the return line temperature reached apparent thermal equilibrium at the elevated value. Figure 5.2-2 shows a plot of temperature excursion vs. crossfeed distance. Piezo stack temperature is measured by an RTD mounted on the surface of one piezo stack. The return temperature is measured by an RTD in the return line from the Ultramill to the Thermocube reservoir.

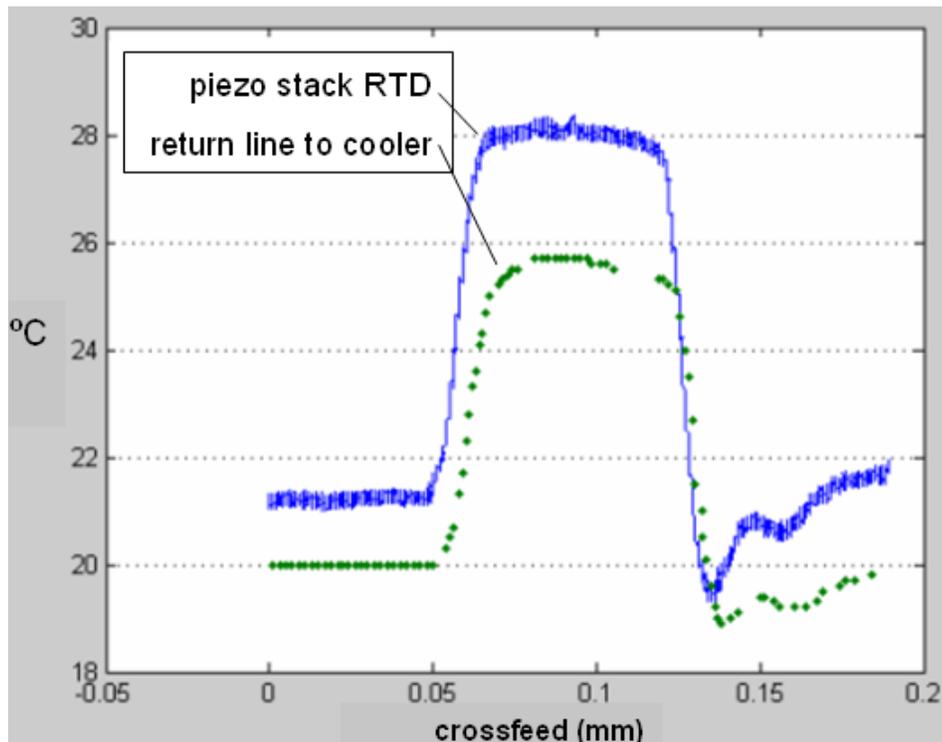


**Figure 5.2-2** Temperature excursion vs. crossfeed.

The 50  $\mu\text{m}$  section of thermal equilibrium provided a baseline against which to measure the effects of the temperature excursion. The flat area also provided a rough fiducial feature to line up (in y) the section of best-case flatness with the section of best-case temperature control. Depth of cut data was collected on the Form Talysurf profilometer. The surface profile is shown in Figure 5.2-3.

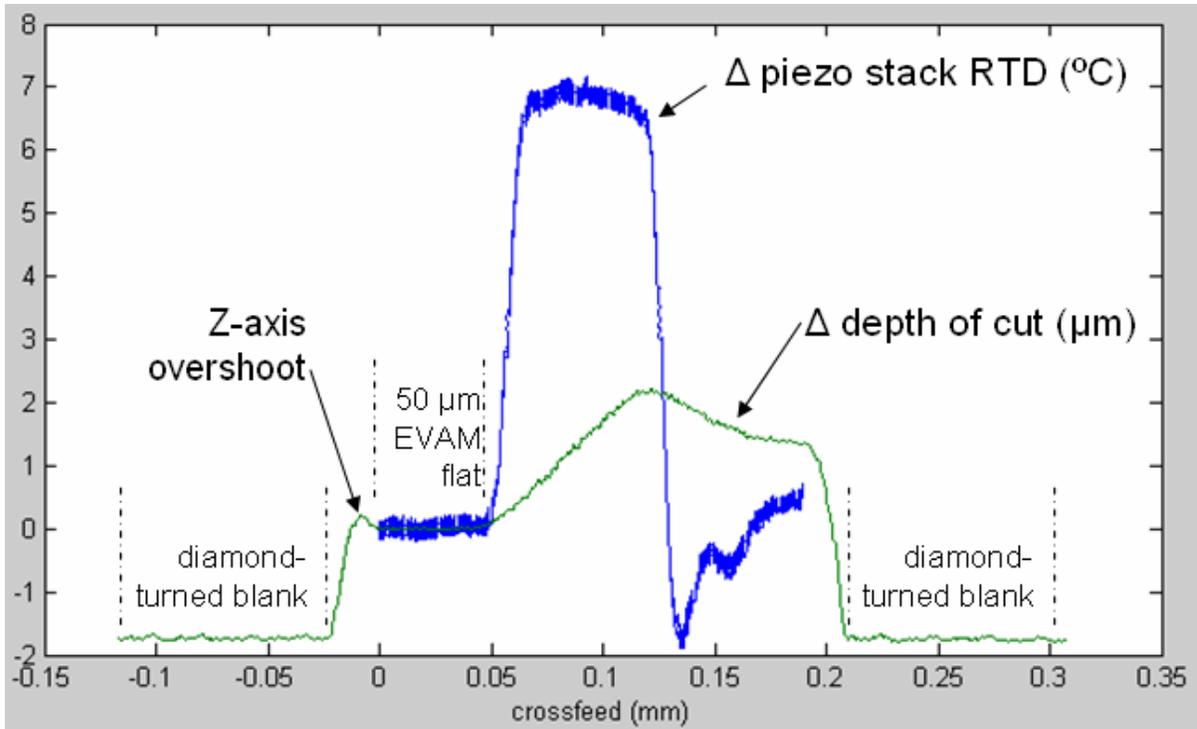


**Figure 5.2-3** Changes in piezo stack temperature and in depth of cut

The depth of the 50  $\mu\text{m}$  EVAM flat section between  $y = 0$  mm and  $y = 0.05$  mm is zeroed so that any deviation is equal to the change in depth of cut. The maximum change in depth of cut is 2.2  $\mu\text{m}$ . The change in piezo stack RTD temperature is also zeroed in this section to indicate thermal equilibrium. The measured piezo stack temperature at the RTD probe, averaged over 50  $\mu\text{m}$  of crossfeed distance, is 21.3  $^{\circ}\text{C}$  at thermal equilibrium and 28.1  $^{\circ}\text{C}$  in the elevated region. Table 5.2-1 shows the results of the application of Negishi's convection model and calculations of the effective coefficient of thermal expansion (CTE). The effective CTE is calculated from Equation 14:

$$CTE, \frac{ppm}{^{\circ}C} = \frac{\Delta L}{(\Delta T, ^{\circ}C)L_0} 1 \times 10^6 \quad (14)$$

where  $\Delta L$  is the change in length and  $L_0$  is the nominal length of the actuator (22 mm). The temperatures in the “piezo average” column are the average along the piezo length direction of the temperature at each node in the finite difference convection model, and are equal to the average of the values of each curve in Figure 5.2-1. The temperatures in the “piezo RTD” columns indicate the measured temperature at the RTD or the predicted temperature at the convection model node in that location. The deviation of measured piezo RTD temperature from predicted temperature at that location is 1.6 °C. One possible explanation for this difference lies in the location of the RTD probe on the exterior of one piezo stack between the two stacks, shown in Figure 5.2-4. This raises several issues:

1. The probe is exposed to heat rejected by both piezo stacks and may measure a higher temperature than that of either stack.
2. The probe fills most of the void between the stacks at its location and causes some interference with convection in this area, causing higher local temperatures than would otherwise occur.
3. The finite-difference convection is one-dimensional along the length of each piezo stack actuator. The skin temperature of a single layer may be different from the average temperature of the layer.

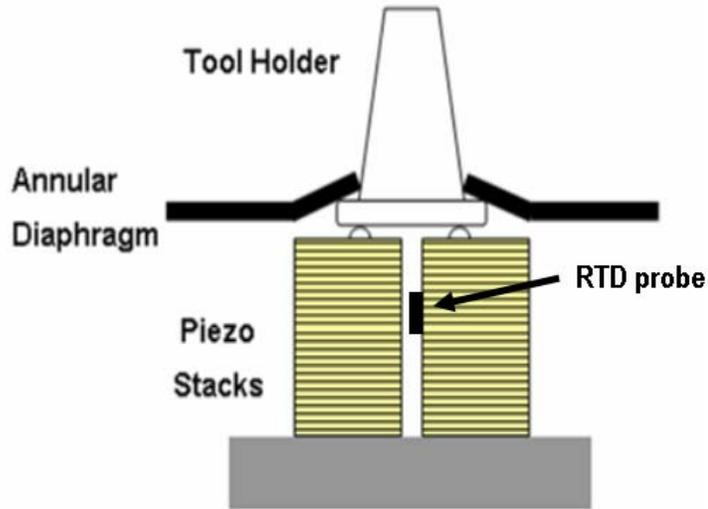


**Figure 5.2-4.** Location of RTD probe

	measured		convection model predicts	
	reservoir RTD	piezo RTD	piezo RTD	piezo average
thermal equilibrium (°C)	20	21.3	21.5	21.1
elevated temperature (°C)	25.7	28.1	26.5	25.3
$\Delta$ temperature (°C)	5.7	6.8	5	4.2
effective CTE (ppm / °C)		14.7	20.0	23.8

**Table 5.2-1.** Temperature changes from Figure 5.2 – 3 (measured and predicted).

A temperature excursion of 4.2 (modeled average) – 6.8 °C (measured at the RTD) in piezo stack resulted in a change in depth of cut of 2.2  $\mu\text{m}$ . These changes in temperature and DOC indicate an effective coefficient of thermal expansion of 14.7 – 23.8 ppm / °C. Published values for the CTE of high-voltage piezoceramic materials range from 1 – 9.6 ppm / °C [28, 29]. Piezomechanik product literature (not Kinetic Ceramics, the manufacturer of the Ultramill stacks) states that high-voltage piezoceramic actuators may exhibit CTE much higher than 1 ppm / °C due to oversized adhesive layers [29]. It is not obvious from these experimental results whether the Ultramill had reached equilibrium at the time that the

setpoint temperature returned to the initial value, about five minutes after the initiation of the temperature excursion. Also, the slope of thermal contraction was neither constant nor equal to the slope of expansion. Due to the questions raised by these results, further experiments were performed to directly measure tool holder position over longer periods of time.

## 5.2.2 Thermal Effects on Tool Holder Position

A brass capacitance gage target was mounted on the Ultramill tool holder. The experiment was performed with the Ultramill dismounted from the Nanoform 600 DTM. The capacitance gage was positioned to measure average tool holder position. Federal gages were used to measure movement of the preload adjustment nut face (shown in Figure 5.2-5). Any expansion of the cooling chamber would be reflected by preload adjustment nut motion. Figure 5.2-6 shows the experimental setup.

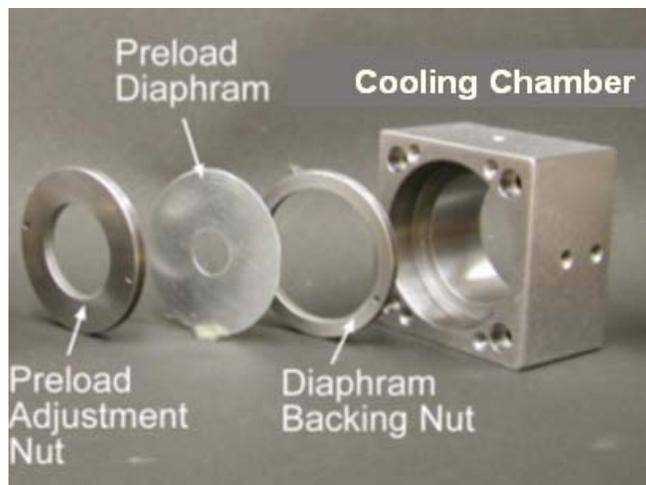


**Figure 5.2-5.** Preload adjustment nut shown with cooling chamber and associated parts [22].

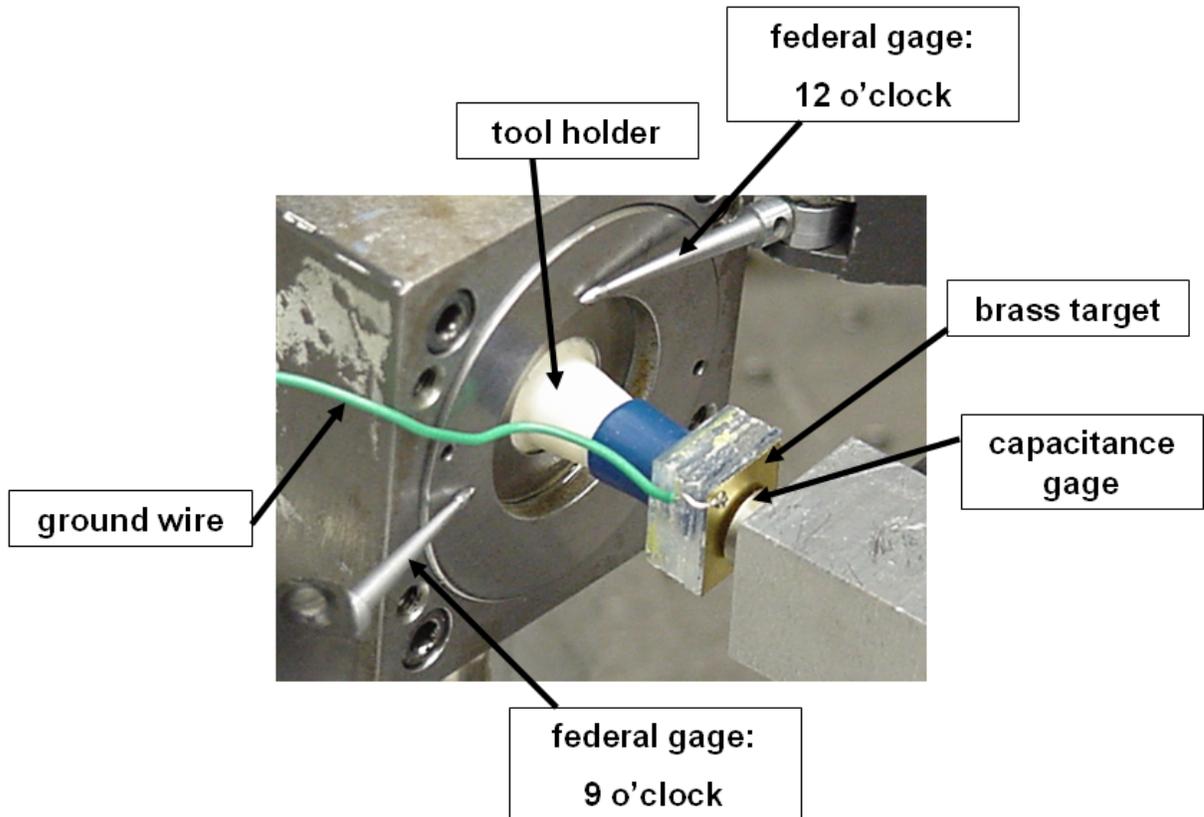


**Figure 5.2-6.** Capacitance and federal gages positioned to measure thermal expansion

This experimental setup had several advantages over the depth-of-cut thermal experiments.

1. No y- or z-axis vibration would be included in the measurement of thermal deformation, as the Ultramill was mounted rigidly on an optical table.
2. Time-synchronization of capacitance gage deformation data and piezo stack RTD temperature data were automatic when collected with a DSpace data acquisition system.
3. Capacitance gage-measured deformation is preserved by data acquisition. This overcame a disadvantage of change-in-depth of cut experiments: profile data on a rastered flat may be obliterated by later crossfeed passes.

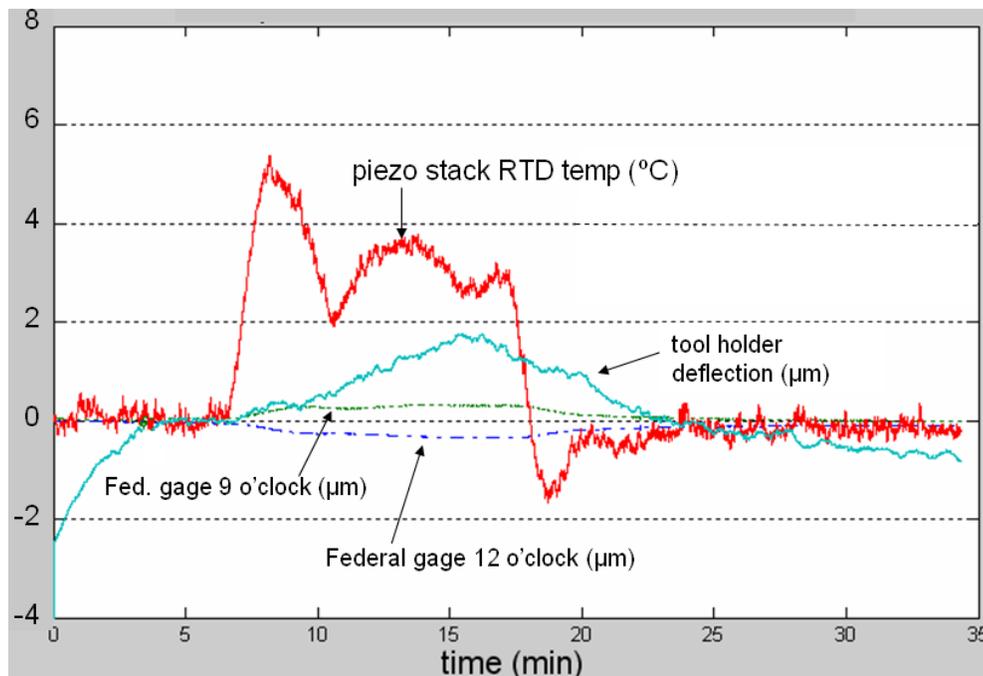
The range of the capacitance gage, and the difficulty of manually centering the tool holder vibration within that range, limited the tool-path size that was used for the test. However, it was possible to operate the Ultramill at an equivalent power level to the DOC test shown previously. The Ultramill was operated at 300Vpp / 1780 Hz<sup>11</sup>.

Figure 5.2-7, Figure 5.2-8, and Figure 5.2-9 show three similar tests with an excursion in the piezo stack skin temperature caused by a change in the coolant-return setpoint temperature. The principal difference between the tests was the location of the Federal gauges used to measure the cooling chamber expansion and the duration of the temperature excursion. The piezo stack RTD temperature, tool holder average total deflection, and Federal gauge deflections for 2 locations on the tool holder preload adjustment nut are plotted as functions of time in minutes. Table 5.2-2 shows a summary of tool holder deflection and CTE results. During the tests, instantaneous position data was acquired for the tool holder total deflection as measured by the capacitance gauge. This instantaneous data included the elliptical motion of the tool driven by the piezo stacks. The overall trend of the tool holder position envelope was assessed visually to estimate when steady state tool holder deflection had been reached. The average position was determined by filtering the instantaneous data to remove the components of tool motion. It can be seen that true steady state was not achieved for the average tool holder deflection. This is most notable in Figure 5.2-7 and Figure 5.2-9.

---

<sup>11</sup> 12W input power, equal power to the 400Vpp / 1000 Hz of the previous test (see Equation 13)

Figure 5.2-7 shows temperature and deformation data for a 3° C change in Thermocube temperature setpoint of about 10 minutes duration. The deflection of the tool holder, following the change in coolant return setpoint, reaches a maximum of 1.8 μm. The expansion and contraction have similar slopes. Deflection of the cooling chamber at the 12 o'clock and 9 o'clock positions on the preload adjustment nut is less than 500nm. This indicates that thermal expansion of the cooling chamber is substantially less than that of other components. Figure 5.2-8 shows an excursion duration of about 20 minutes.



**Figure 5.2-7** Three degree temperature excursion, 10 minutes duration

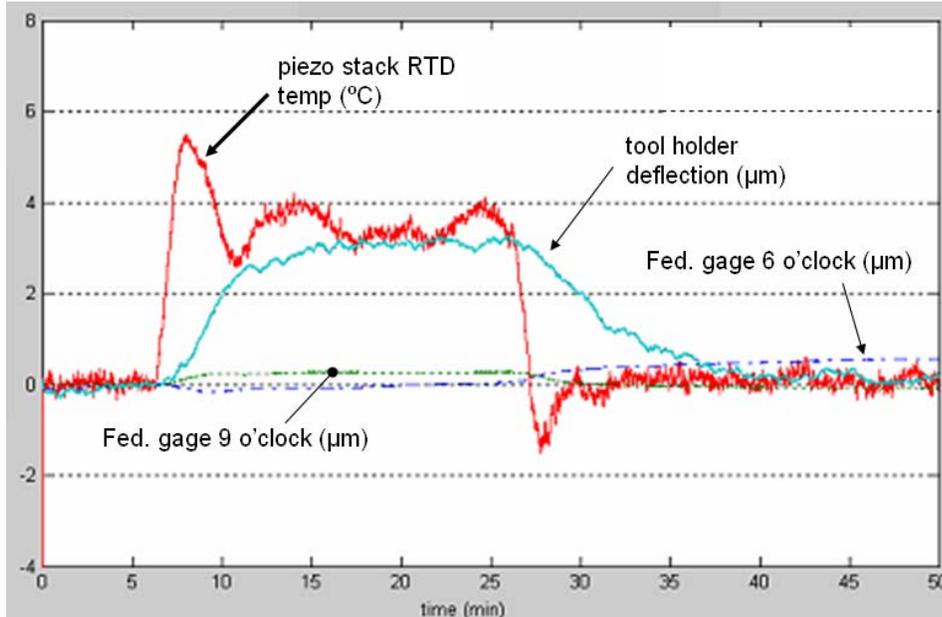


**Figure 5.2-8** Three degree temperature excursion, 20 minutes duration

The maximum tool holder deflection is about 3.2  $\mu\text{m}$  in this case. This experiment would indicate that recovery of thermal equilibrium within  $\pm 500$  nm of thermal expansion after a temperature excursion requires at least 20 minutes. Long-term drift of the preload adjustment nut 6 o'clock position Federal gage approaches 700 nm. Figure 5.2-9 shows an excursion duration of about 25 minutes.

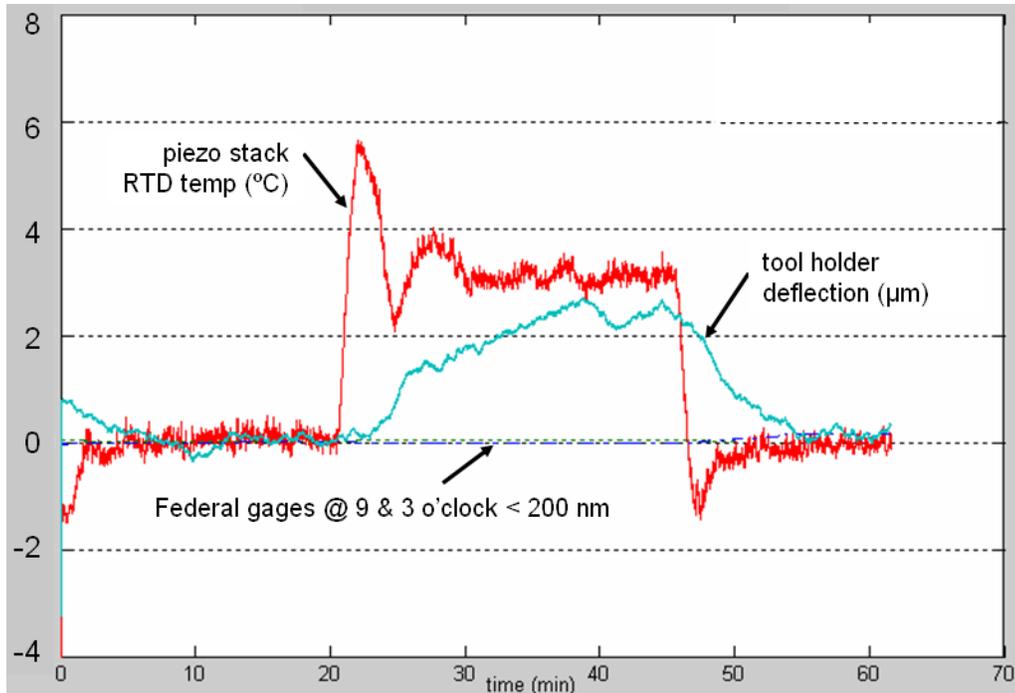


**Figure 5.2-9** Three degree temperature excursion, 25 minutes duration

excursion elapsed time (ET)	reservoir RTD $\Delta T$	tool holder deflection @ ET	(measured)		(modeled)		average CTE
			piezo RTD @ ET $\Delta T$	effective CTE	piezo avg $\Delta T$	effective CTE	
units	minutes	$^{\circ}C$	$\mu m$	$^{\circ}C$	ppm / $^{\circ}C$	$^{\circ}C$	ppm / $^{\circ}C$
	10	3	1.8	2.8	29.2	3.3	24.8
	20	3	3.3	3.4	43.9	3.3	45.2
	25	3	2.4	3.1	35.2	3.3	33.1
					36.1		34.3

**Table 5.2-2.** Changes in temperature and tool holder position, long-term excursions.

The tool holder average expansion deflection, as a function of piezo stack temperature, is significant. The effective coefficient of thermal expansion, based on the convection model average piezo stack temperature, averages 34 ppm /  $^{\circ}C$  over these three tests. This value is 340% of the largest published value found for piezoceramic actuators.

The low ( $< 500$  nm) deflection of the cooling chamber structure during each of the three temperature excursions requires investigation. The cooling chamber is made of 1018 steel, which has a coefficient of thermal expansion of 12.1 ppm / °C, and the length of the chamber exposed to the coolant is about 33 mm. A change in temperature of 3 °C would yield a change in length of 1.2  $\mu$ m. The maximum temperature change through the cooling chamber wall thickness is given by Equation 15.

$$\Delta T_{\max} = \frac{th_{\text{wall}} q_{\max}}{kA_{\text{wall}}} \quad (15)$$

where  $th_{\text{wall}}$  is the wall thickness,  $q_{\max}$  is the maximum heat dissipation by conduction,  $k$  is the thermal conductivity of 1018 steel ( 52 W/(m\*K) [30] ), and  $A_{\text{wall}}$  is the surface area of the wall. Figure 5.2-10 shows an illustration of the wall thickness.

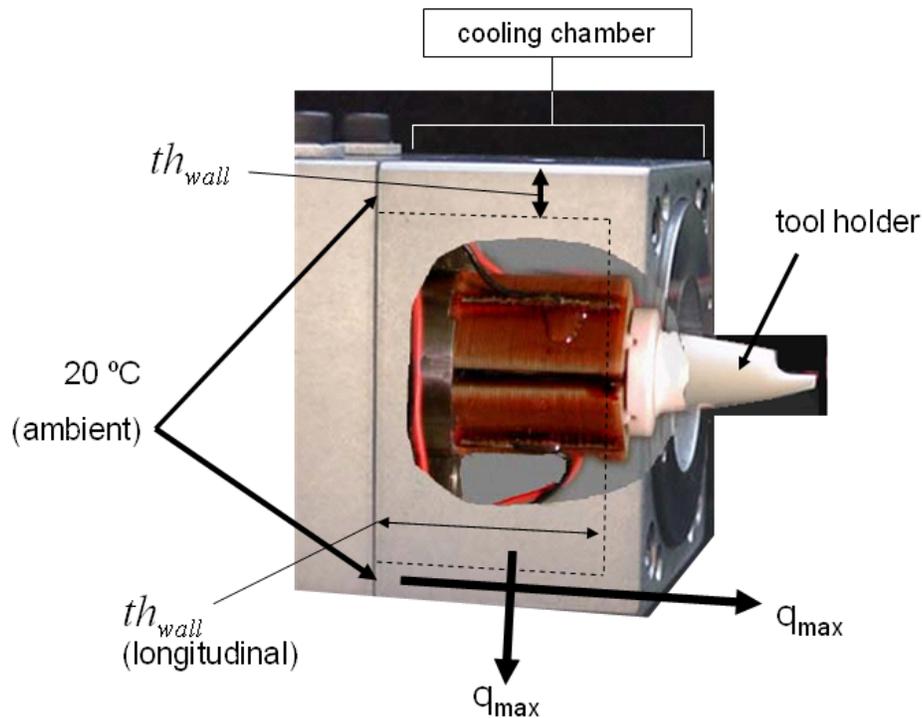


**Figure 5.2-10.** Diagram of cooling chamber wall heat conduction.

The average wall thickness is 16 mm and the surface area is about  $4000 \text{ mm}^2 = 0.004 \text{ m}^2$ . If each of the two piezo stacks is losing 2.6 W to heat and the coolant is assumed to be at lower temperature than the piezo stacks,  $\Delta T_{\text{max}}$  (through the wall thickness) is about 0.4 °C. Equation 15 can also be applied to the longitudinal direction of the cooling chamber. In this case, the length of the cooling chamber is treated as the wall thickness. The cross-sectional area is  $0.0024 \text{ m}^2$ , length of 33 mm and  $q_{\text{max}}$  of 5.2 W yield a  $\Delta T_{\text{max}}$  of 1.4 °C. If the base of the cooling chamber (contacting the 2-Kg steel Ultramill base) is assumed to be at the room temperature of 20 °C, the maximum temperature of the cooling chamber wall is no greater than 21.5 °C. A change in average temperature of the cooling chamber wall from 20 °C to 21.5 °C would yield a thermal deformation of 600 nm. The maximum cooling chamber deflection (during the temperature excursion) seen in Figure 5.2 – 7 is approximately 400 nm. The maximum deflections shown in Figures 5.2 – 8 and 5.2 – 9 are smaller.

The tool holder average expansion, as a function of piezo stack temperature, is not constant. Compare Figure 5.2-7 with both Figure 5.2-8 and Figure 5.2-9. In Figure 5.2-7, the tool holder maximum expansion is approximately 1.8  $\mu\text{m}$  and the expansion relative to stack temperature is about 0.6  $\mu\text{m} / ^\circ\text{C}$ . For the other two cases, maximum expansion is 2.2 to 3  $\mu\text{m}$  and the expansion rate is 0.8 to 1  $\mu\text{m} / ^\circ\text{C}$ . It can take different amounts of time (from the time the coolant return temperature setpoint is changed) to achieve maximum tool holder expansion. The test in Figure 5.2-8 reaches its upper thermal expansion equilibrium about 10 minutes after the setpoint change. The test in Figure 5.2-9 requires about 25 minutes to reach this upper equilibrium.

The thermal expansion of the Ultramill cooling chamber is small compared to that of the tool holder, as noted by the Federal gage results. The direction of cooling chamber expansion is not predictable at this time.

Figure 5.2-11 shows a cyclical temperature variation and the resulting expansion effects. This test demonstrates that Ultramill thermal expansion occurs out of phase with short-duration temperature excursions.

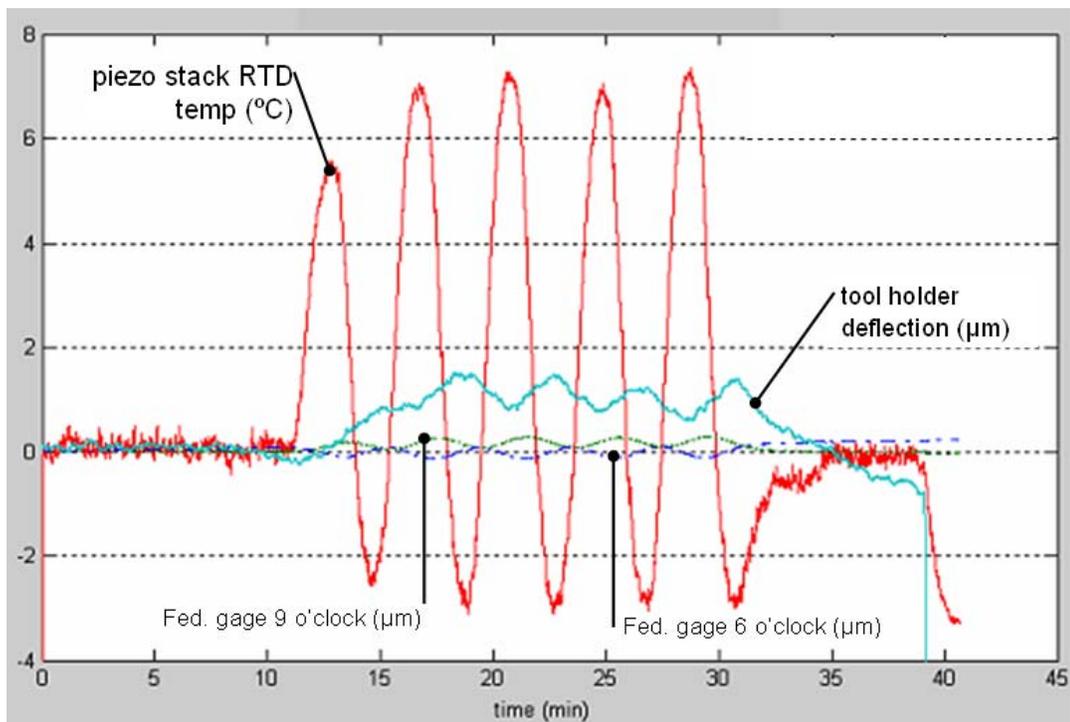


**Figure 5.2-11** Cyclical temperature variations

During a typical machining run, piezo stack temperature variation rarely exceeds 0.2 °C. The temperature excursions seen in these tests are extreme compared to operational situations. The relatively large tool holder displacements which occurred during the test indicate that temperature changes could be a major factor in z-direction deviations from nominal depth of cut.

### **5.2.3 Thermal Effects at Equilibrium**

Figure 5.2-12 shows the average position of the tool holder during 29 minutes of equilibration. This test demonstrated approximately 900nm variation in tool holder average position from 16-29 minutes of equilibration. A thermal equilibration time of this length is generally used before microstructuring with the Ultramill. After 26 minutes of equilibration there are still 100 nm-amplitude swings in tool holder average position. The wavelength of these changes in average position is about 45 seconds. Because the elapsed cutting time of a single upfeed pass on an Ultramilled parts is 1-3 seconds, upfeed pass surface finish errors are not attributable to temperature. Temperature-dependent crossfeed error is possible, and would be included in the low-frequency finish error range defined in Section 4.2.3.

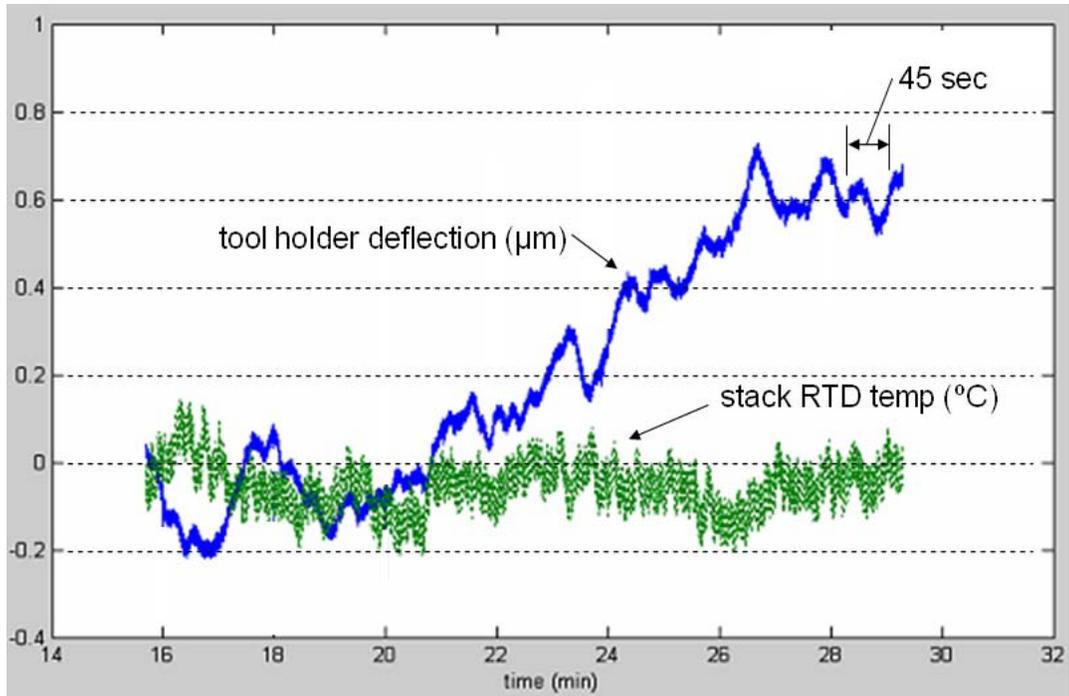


**Figure 5.2-12** Deflection at thermal equilibrium

### 5.3 PIEZOELECTRIC OR AMPLIFIER EFFECTS

Electrical noise in the high-voltage signal used to drive the Ultramill piezoelectric actuators is one possible cause of surface finish errors. Mechanical vibration at 60 or 120 Hz could be attributed to electrical noise. Significant vibration at these frequencies has not been found in vibration data collected with the Ultramill running. This is shown in the frequency data of Figure 5.1-34.

## 5.4 DIAGNOSIS OF SURFACE FEATURES

This section examines various features found on Ultramilled parts and attempts to attribute likely causes among the components characterized.

### 5.4.1 Crossfeed Spatial Frequencies

A number of Ultramilled flats were made with varying crossfeed increments. At crossfeed increments from 0.85 – 2  $\mu\text{m}$ , irregular spatial frequencies in the crossfeed direction were observed. At 2  $\mu\text{m}$  crossfeed increment, a dominant spatial frequency of approximately one cycle per 4  $\mu\text{m}$  (or per two passes) was observed. An example of the topology is shown in Figure 5.4-1 (left), with the marked profile shown on the right. A spatial-domain FFT of this data (after conversion to nanometers) is shown in Figure 5.4-2.

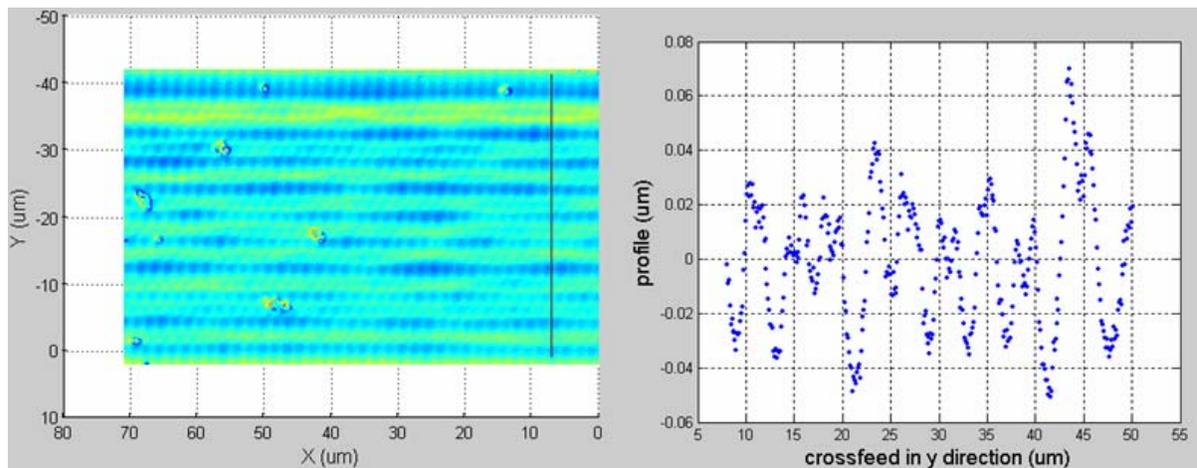


**Figure 5.4-1.** 20 pass, 2  $\mu\text{m}$  crossfeed flat (left), highlighted profile (right).

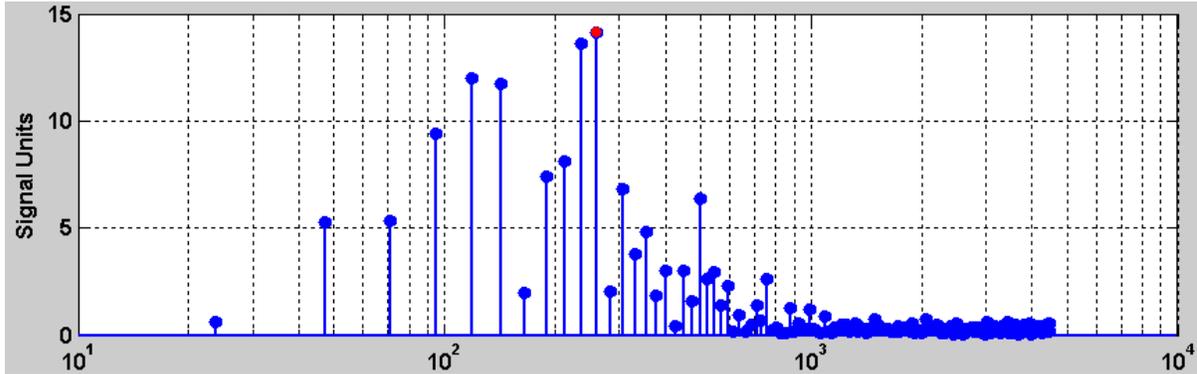


**Figure 5.4-2.** FFT of spatial profile in nanometers amplitude.

This data shows a peak amplitude of 13 nm at 234 and 260 cycles per mm. The elapsed time of an upfeed pass during the machining of this flat, including the time for all 3 axes to their original positions, was eight seconds. The ratio of the 17-second period air bearing vibration to this 8-second period is 2.1. The crossfeed pass size of 2  $\mu\text{m}$  multiplied by this ratio equals 4.3  $\mu\text{m}$  of crossfeed distance for every cycle of the air bearing vibration. The spatial frequency of a 4.3  $\mu\text{m}$  wavelength feature is 233 cycles per mm. This shows agreement with the ratio of air bearing vibration and upfeed pass frequency.

### 5.4.2 Upfeed Spatial Frequencies

An interferogram was taken at 20x and the data was imported into Matlab. The actual depth of cut is 2.2  $\mu\text{m}$ . The Zygo NewView white light interferometer has 560 nm resolution at this magnification. At an upfeed speed of 2 mm/s, each Ultramill cycle is 500 nm long, so Ultramill cycles will not be shown accurately at this resolution. The actual upfeed speed is shown in Figure 5.4-3. The average upfeed speed in the peak-speed region is 1.913 mm/s.

The elapsed time of an upfeed cycle for the 355  $\mu\text{m}$  length of a 20x interferogram is 0.19 seconds.

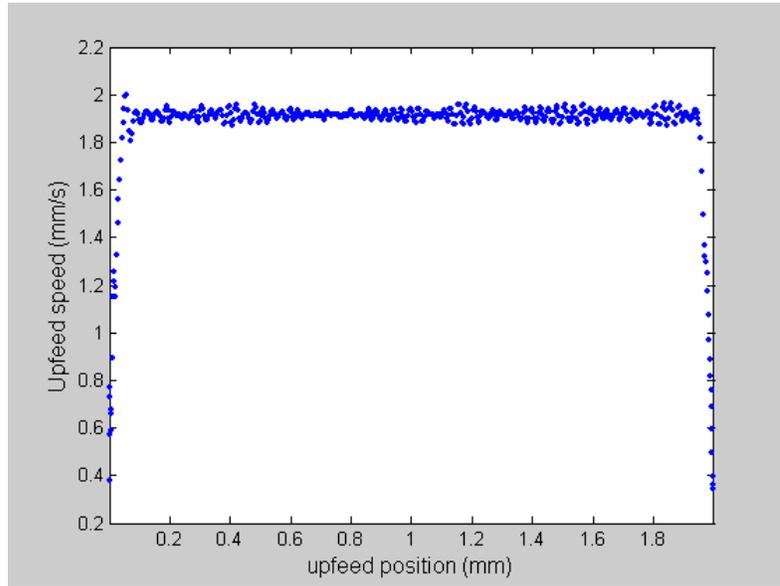


**Figure 5.4-3** Actual upfeed speed vs. position, programmed value 2 mm/s

Figure 5.4-4 shows an upfeed line of interest on this flat, Figure 5.4-5 the spatial profile along that upfeed line, and Figure 5.4-6 shows an FFT with spatial and time-domain frequency data.

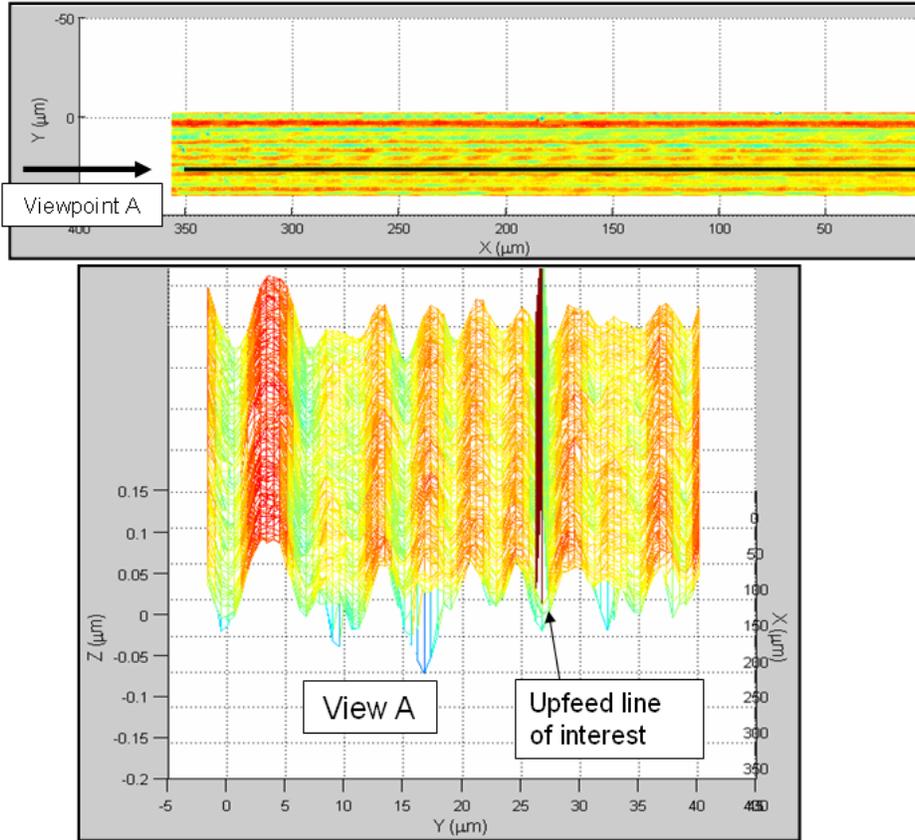


**Figure 5.4-4.** Trough upfeed line

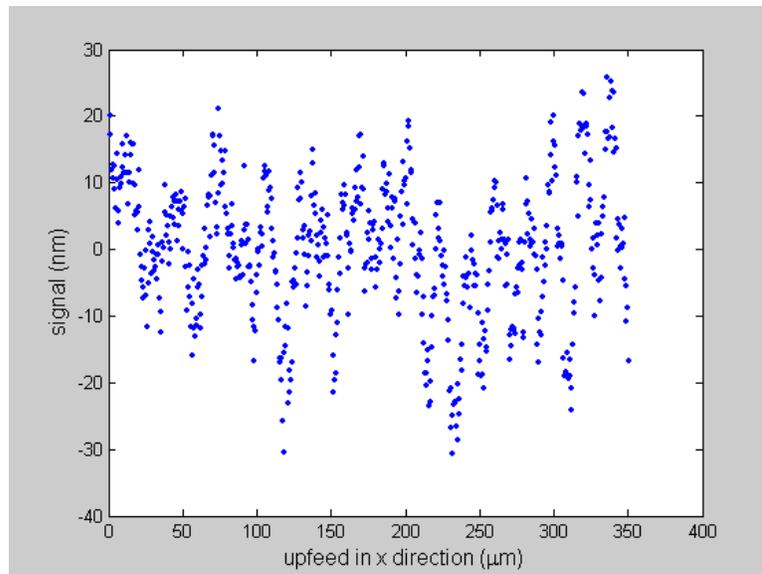


**Figure 5.4-5.** Spatial profile at line of interest

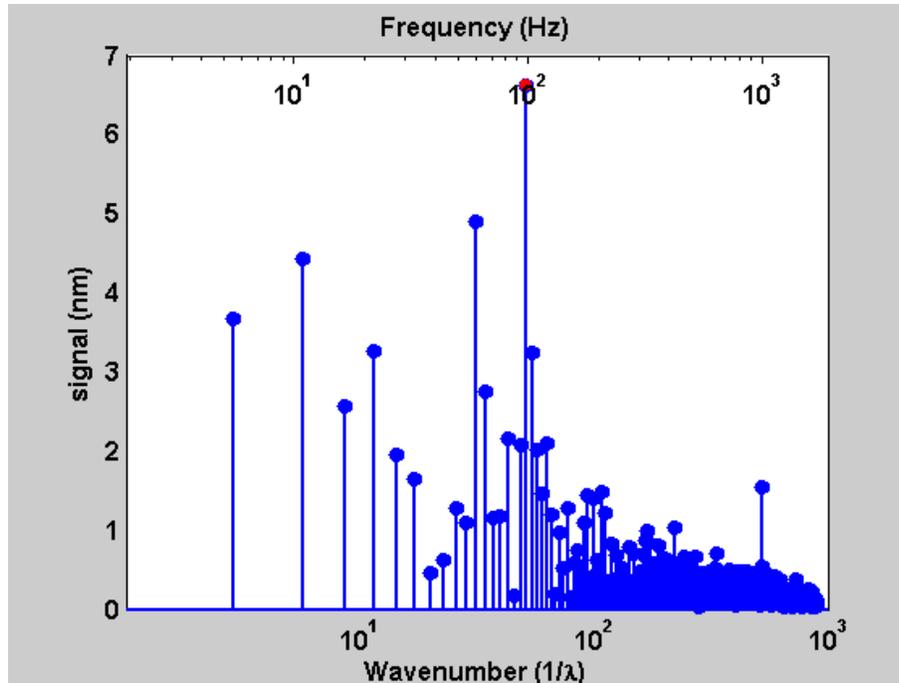


**Figure 5.4-6.** FFT of spatial profile at line of interest

The two largest amplitudes in this FFT are at 100 and 60 Hz. The 100 Hz frequency is consistent with the DOC-direction natural frequencies of both the y- and the z-axis. However, the z-axis vibration amplitude at this frequency during machining (with the Ultramill running) has been shown to be less than 2 nm. The 100 Hz error in upfeed finish may be due to a combination of y- and z-axis vibration. The y-axis was observed to vibrate in the 60-Hz range in shaker testing, shown in Figure 5.1-22. A similar cross-section was taken at one of the peak formations on the part. This data is shown in Figure 5.4-7, Figure 5.4-8, and Figure 5.4-9.

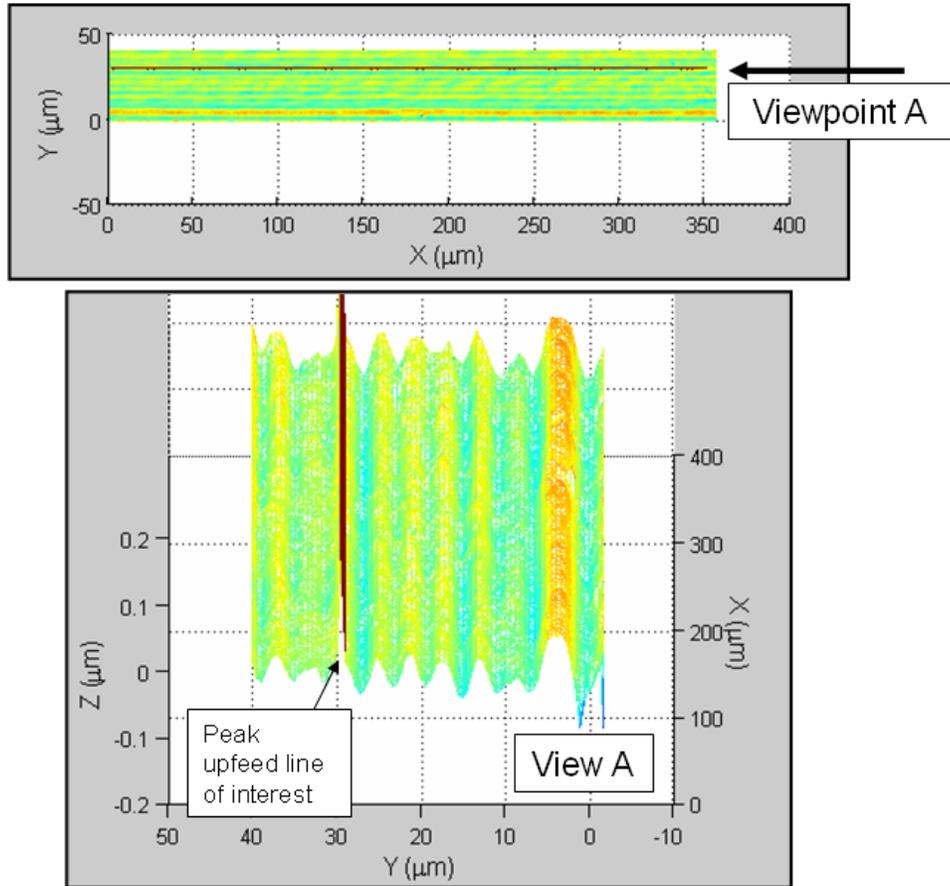


**Figure 5.4-7.** Peak upfeed line

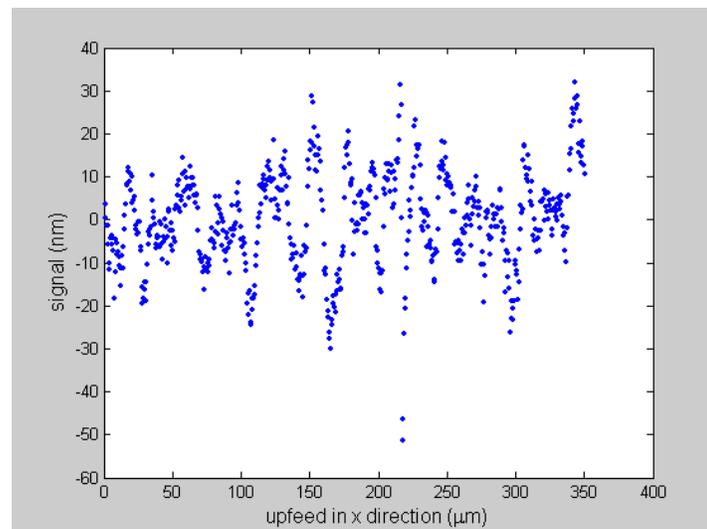


**Figure 5.4-8.** Peak upfeed line spatial profile

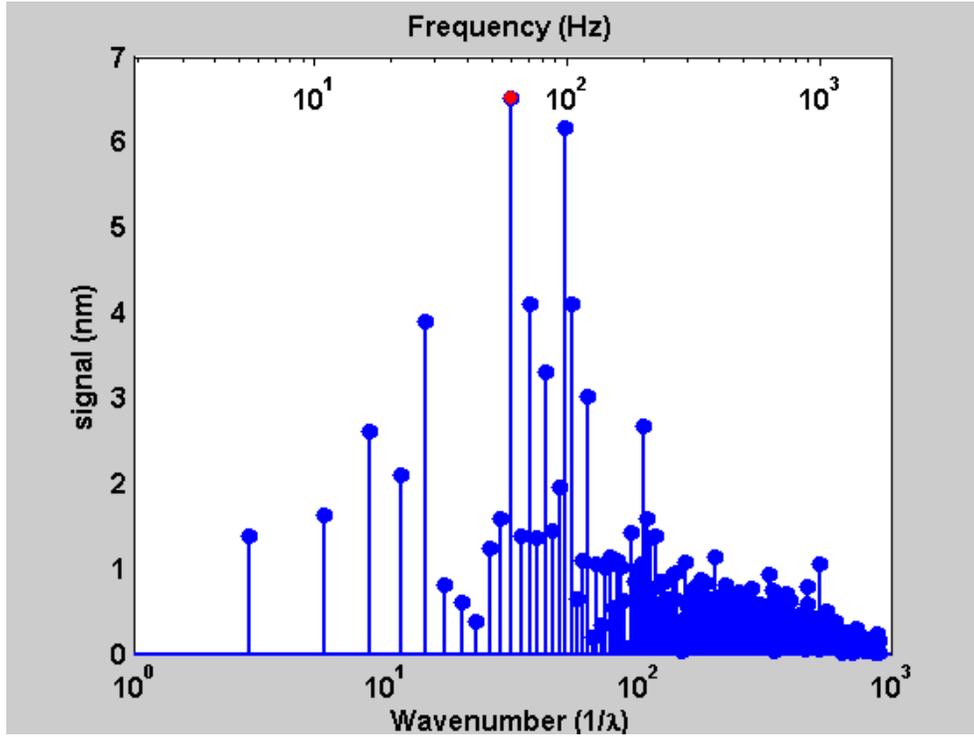


**Figure 5.4-9.** Peak upfeed line FFT

The highest amplitudes in this FFT are again at 60 and 100 Hz.

## 6 CONCLUSIONS

Key questions:

- Is the Ultramill capable of multi-level machining on a micrometer scale?
  - Yes. Microstructures as small as 200  $\mu\text{m}$  square have been fabricated, comprised of binary features with arbitrary geometry as small as 15  $\mu\text{m}$  wide and 0.5  $\mu\text{m}$  high. Surface finishes of 14 nm RMS (40 nm PV) in the upfeed direction and 19 nm RMS (91 nm PV) in the crossfeed direction have been achieved.
- What are the limitations of the 3-axis DTM arrangement?
  - The primary limitation of the experimental setup is the y-axis air bearing.
    - A long-wavelength drift occurring a few times a minute has been identified. This motion creates unintended features in the crossfeed direction on rastered parts.
    - Multiple vibration modes of the y-axis in the 1-500 Hz frequency range have been identified.
  - Other components of the DTM have been found to vibrate in the 1-500 Hz frequency range. However, measured vibration of the other axes is of much smaller amplitude than that of the y-axis.

Machining tests to date in hard-plated copper have demonstrated that EVAM using the Ultramill High Speed and Nanoform 600 combination is capable of sub-millimeter binary microstructuring. Tool geometry and motion programming are important factors in the scale

and shape of binary features which can be achieved on a microstructure. Reducing the diamond tool's nose radius from 1 mm to 50  $\mu\text{m}$  allowed the overall size of a demonstration microstructure (the PEC's angstrom logo) to be reduced from 1 mm to 0.2 mm square. Further work in motion program planning and machining strategy is expected to permit more complex (non-binary) binary geometries to be achieved, and may permit further reduction in feature sizes. Automated motion program generation will facilitate this work, by reducing the turnaround time required to run experiments.

Theoretical surface finishes in both the upfeed and crossfeed directions are less than 10 nm PV, as predicted by the EVAM tool path parameters. This is considerably better than results to date. Among errors of low time-domain frequency, which would show up as crossfeed-direction errors on rastered parts, the y-axis air bearing and temperature control have been identified as major contributors.

## 7 REFERENCES

1. Benevides, G., "Meso-machining Capabilities," M<sup>4</sup>: Workshop on Micro/Meso-Mechanical Manufacturing, Evanston, IL, May 2000.
2. Lawes, Ron. "Microfabrication Cost Models for Micromachining Methods," Materials & Packaging Challenges for Micro and Nano Technologies, Melbourne, Australia, December 10, 2002, < [www.cmf.rl.ac.uk/pdf/aus2002.pdf](http://www.cmf.rl.ac.uk/pdf/aus2002.pdf) >.
3. Bado, Phillipe *et al.* "Handbook of Micromachining," Clark-MXR, Inc. < <http://www.cmxr.com/Industrial/Handbook/Chapter14.htm> >.
4. Fu, Yongqi *et al.* "Focused Ion Beam Direct Fabrication of Micro-optical Elements: Features Compared with Laser Beam and Electron Beam Direct Writing," IMST Technical Programme, Singapore-MIT Alliance (SMA) Symposium, January 19, 2004.
5. Schaller, Th. *et al.*, "Microstructure Grooves with a Width Less than 50  $\mu\text{m}$  Cut with Ground Hard Metal Micro End Mills." *Precision Engineering*, 23, pp 229, 1999.
6. Takeuchi, Yoshimi *et al.*, Computer Aided Ultra-Precision Micro-Machining of Metallic Materials. IEEE International Conference on Robotics and Automation, pp 67, (1995).
7. Kawai, Tomohiko *et al.*, "Ultra-Precision Micro Structuring by Means of Mechanical Machining." MEMS 2001. 14th IEEE International Conference on Micro Electro Mechanical Systems, 2001.
8. Friedrich, Craig. "Microweb," Michigan Technical University <<http://www.me.mtu.edu/~microweb/main.htm>>.
9. Berden, Thomas *et al.* "Debris-reduced laser machining of polymeric waveguides for optoelectronic applications," Laser Applications in Microelectronic and Optoelectronic Manufacturing VI. Proc. SPIE Vol. 4274, p. 432-441, Malcolm C. Gower *et al* (Eds).

10. Semiconductor OneSource. "Semiconductor Glossary,"  
<<http://www.semiconductorglossary.com/default.asp?searchterm=KrF+excimer+laser>>.
11. Pflieger, W. *et al.* "Laser Micromachining of Mold Inserts for Replication Techniques – State of the Art and Applications," Laser Applications in Microelectronic and Optoelectronic Manufacturing VI. Proceedings of SPIE, Volume 4274. Malcolm C. Gower *et al* (Eds).
12. Kentek Corporation, "Laser Glossary," <<http://www.kentek-laser.com/helpers/glossary.htm>>.
13. Koh, Won-Gun and Pishko, Michael. "Photoreaction Injection Molding of Biomaterial Microstructures," Langmuir 2003. American Chemical Society, Vol. 19, pp. 10310-10316.
14. Tamkin, John M. *et al.* "High Speed Gray Scale Laser Direct Write Technology for Micro-optic Fabrication," MicroMachining Technology for Micro-optics and Nano-optics, SPIE proceedings, 28-29 Jan 2003, Eric G Johnson, (Ed).
15. University of Arizona Optical Sciences Center. "High Speed Maskless Grayscale Lithography," White paper. <<http://www.optics.arizona.edu/microoptics/facilities.htm>>.
16. Stock, Michelle *et al.* "'Time-tailored' laser pulses: a new approach for laser micromachining and microfabrication processing," MicroMachining Technology for Micro-optics and Nano-optics, SPIE proceedings, 28-29 Jan 2003, Eric G Johnson, (Ed).
17. Narasimhan, Jayakumar *et al.* "Tool Wear Compensation and Path Generation in Micro and Macro EDM," Transactions of NAMRI/SME, Vol. 32, 2004.

18. Frese, Ines. "Microoptics Using the LIGA Technology," Microoptics - From Technology to Applications, Springer Series in Optical Sciences, Vol. 97 (2004), J. Jahns, K.-H. Brenner (Eds.).
19. Klocke, F., Rubenach, O.; "Ultrasonic Assisted Diamond Turning of Steel and Glass", American Society of Precision Engineers Conference Proceedings, Vol. 19, pp. 179-190, 1998.
20. Jung-Hwan, A., Han-Seok, L., Seong-Min, S.; "Improvement of Micro-machining Accuracy by 2-Dimensional Vibration Cutting", American Society of Precision Engineers Conference Proceedings, Vol. 20, pp. 150-153, 1999.
21. Moriwaki, T., Shamoto, E.; "Ultra-precision Diamond Turning of Stainless Steel by Applying Ultrasonic Vibration", Annals of the CIRP, Vol. 40, pp. 559-562, 1991.
22. Negishi, N., "Elliptical Vibration Assisted Machining with Single Crystal Diamond Tools", MS Thesis, North Carolina State University, 2003.
23. Cerniway, M., "Elliptical Diamond Milling: Kinematics, Force, and Tool Wear", MS Thesis, NC State University, 2001.
24. Wyant, James C. "White Light Interferometry", AeroSense Conference, April 2002  
<[http://www.optics.arizona.edu/jcwyant/pdf/Meeting\\_papers/WhiteLightInterferometry.pdf](http://www.optics.arizona.edu/jcwyant/pdf/Meeting_papers/WhiteLightInterferometry.pdf)>.
25. Zygo Corporation, "Metro Pro Reference Guide OMP-0347D," Manual, 1998.
26. Vibrationandshock.com, "Glossary of terms,"  
<<http://www.vibrationandshock.com/glossary.htm>>
27. Dow, Thomas and Sohn, Alex. "MAE 545: Precision Metrology," text book, North Carolina State University.

28. Piezo Technologies, “Kézite K600: Navy VI Equivalent Lead Zirconate Titanate Piezoelectric Ceramic with High Coupling Coefficient and High Dielectric Constant”, product literature, <<http://www.piezotechnologies.com/k600.htm>>.
29. Piezomechanik, “Comments on [Product] datasheets”, <<http://www.piezomechanik.com/hp030530/introduction/intro300.htm>>.
30. Matweb.com, “AISI 1018 Steel, cold drawn,” <<http://www.matweb.com/search/SpecificMaterial.asp?bassnum=M1018A>>

## 7.1 APPENDIX A: DATA-GATHERING METHODS

### 7.1.1 Method for Importing Zygo NewView Surface Topology Data to Matlab

This method replaces the value “No Data” in a Zygo NewView .xyz file with a value “NaN” which can be interpreted by Matlab. The Matlab data-import functions in Appendix B require a consistent number of columns on each row and the value “NaN” in column 3 for any missing data point. The following procedure has advantages over two other methods tried. The JMP statistics package method shown here is preferable to a similar method using Microsoft Excel because Excel has a limited number of rows in a spreadsheet, which is insufficient for 640x480 pixels of data. The “Find and Replace” function of the Matlab text editor or another text editor may require many minutes to execute. This method is complex, but relatively quick and dependable.

1. Save a \*.dat data file on the Zygo NewView and move it to a computer with Matlab
2. At a DOS command line, in a directory containing the Zygo utility dat\_to\_xyz.exe (note: if dat\_to\_xyz was not included with your version of MetroPro, it is available from Zygo tech support)
  - o dat\_to\_xyz Zygofilename.dat xyzfilename.xyz
3. Open this .xyz file in Windows Notepad or another ANSI text editor
4. Note the number highlighted in Figure 8.1 – 1. This is the pixel scaling in meters per pixel. It must be entered in a Matlab xyzread.m file.

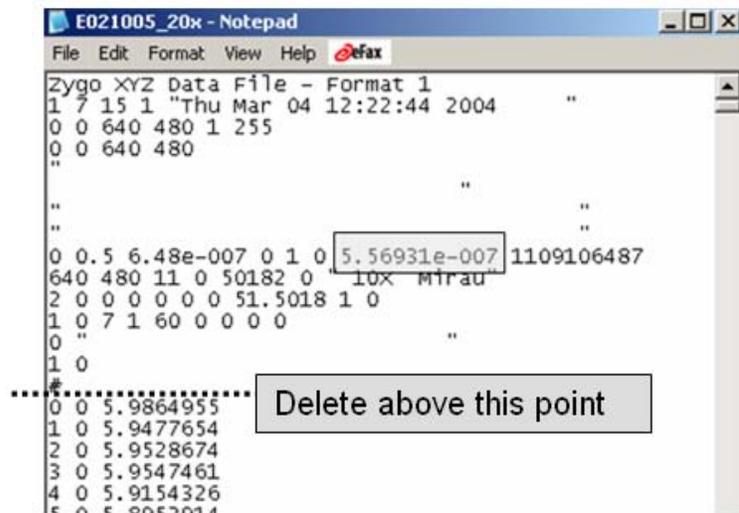
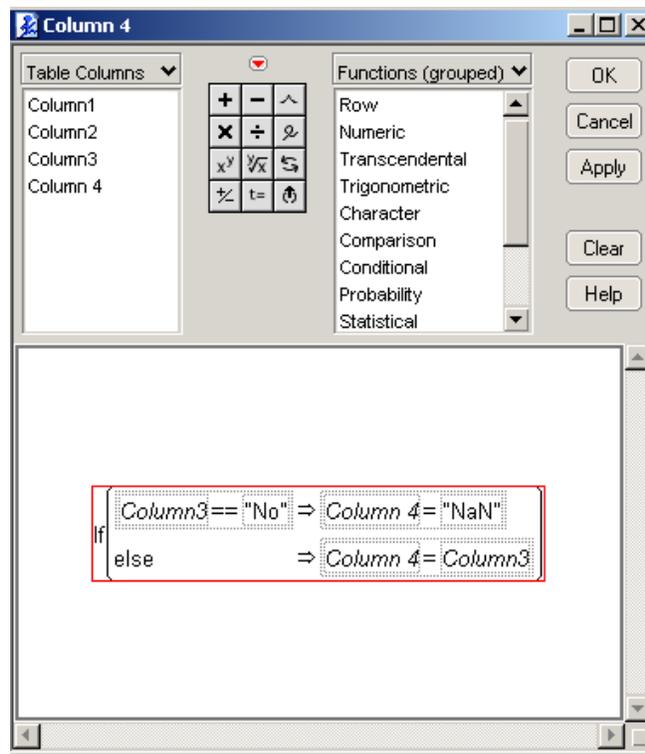


Figure 7.1-1. Pixel scaling in meters per pixel

5. Delete the header before the first row of x-y-z coordinates, including the # character.

6. Delete the # character at the end of the file.
7. Save the file with an appropriate name.
8. Open the file in the JMP statistics package.
  - Choose “Open Data Table”
  - select “All Files” in the **Files of Type** drop-down box
  - select “Text Import Preview” in the Get File Type dialog box
  - select “Delimited” in the **How Should This Text File Be Imported?** dialog box.
  - Change the **Data Type** of Column 3 to “Character” in the Text **Import Preview – Delimited** dialog box.
    - (the file takes a minute to load)
  - Hit **OK** when the caution dialog box appears.
  - Column 4 will contain the word “Data” on any row that had “No Data” in the .xyz file. Delete this column.
  - Add a new Column 4.
  - Right-click on the heading of column 4 and pick “Formula...” from the menu.
  - The formula shown in Figure 8.1 – 2 will convert Column 3 values of “No” to the value “NaN”, which will be read by Matlab as *not a number*. Column 4 will be equal either to “NaN” or to the floating-point z value of Column 3



**Figure 7.1-2.** JMP formula converting text “No” to text “NaN” while preserving floating point values.

9. Select Columns 1, 2, and 4 of the JMP data table, and choose **Copy** from the **Edit** menu.
10. Paste this data into an empty text file.

11. Save it as a \*.xyz file with an appropriate file name.
12. In Matlab, after selecting the current directory with the .xyz file containing NaN's, run the xyzread.m file specific to this data set or to the Zygo magnification and attendant pixel resolution.

## 7.1.2 Method for Gathering High-Frequency Axis-Position Data In Delta Tau PEWinPro32

PMAC PlotPro32 is highly prone to hang-ups. The maximum data rate at the PEC's current settings is 2262 Hz (PMAC gather period = 1). At this rate, if even 1.5 sec of four data items are gathered, the program may crash when the "Upload" button is pressed. At 40 Hz (PMAC gather period = 60), a user may be able to gather 10-15 minutes of real-time data on three axes positions (about 100000 data words), but there is a good chance of losing this data during the upload operation. The method described below has been successful for 10 raster passes on three axes' actual positions at 452 Hz (PMAC gather period = 5). That is about 5 minutes of real time, but only around 80 seconds of data points are used. Data is only gathered while the tool is very near or actually cutting the part (not during backfeed, etc), so it is used very efficiently. That efficiency is one of the two advantages of using this method. The other is the fact that, even after a PEWin hang-up, the operator may still restart PEWin and retrieve the data. This is not true when using PlotPro32. One disadvantage of using the method described here is a loss of real elapsed time reference. The time difference in contiguous data points can be reproduced by multiplying the index of each data point by inverse of the data rate. However, this time difference is not valid for any two data points separated by the "endg" (end gather) command.

The method described here is not convenient. Saving 10 raster passes of data may require 10 or more minutes of the operator's time after a part program is run. Hang-ups of PEWinPro32 (not PlotPro32) are possible during this operation, but data is retained in the PMAC gather buffer, and is still available upon restart of PEWin after a hang-up. To use this method, a part program should be modified with commands like those shown in the program at the end of this section. After the program is run, make sure that the following two quantities are in the PEWinPro32 Watch Window:

- rx:\$3120
- ry:\$3120

The difference between these two quantities is the size of the gathered data in the buffer in words, with each word being one data point of one of your chosen data gathering variables. If this difference is greater than 150000 words, there may be problems uploading the data, and the operator may consider issuing a "delete gather", starting a new motion program, and gathering less data (fewer passes or a lower data rate) before uploading. To upload the data, right-click in the Terminal Window, select "clear terminal window," then type in the following command.

- list gather 0,15000

The first data point of your first variable gathered is at memory location 0 in the buffer. The command will output 15000 words of data starting at location 0. If you gathered 3 variables, this is 5000 data points of three variables. The 15000-word listing size is a good compromise between being large enough to be a significant fraction of the total buffer, but small enough

so that hanging up PEWinPro32 is less likely. This command will take about 5 seconds to execute. If it takes longer than 15 seconds, PEWinPro32 should be shut down and restarted. After the data appears in the terminal window, right-click in the terminal window, pick “Copy Terminal to Notepad.” After the data appears in Windows Notepad, trim any unwanted characters (like the list gather command at the beginning), being careful to preserve all the data, and save it with a name such as “*axisdata\_0\_15000.txt*”. After this file is saved, repeat the procedure with commands such as:

- list gather 15001,15000
- list gather 30001,15000

until the first number plus the second is about equal to the buffer size of ( ry:\$3120 - rx:\$3120 ). A total of about 110000 words is the largest data set the author has saved. The gather buffer size was observed to stop growing at approximately 157000 words of data, and that may be the maximum possible size. The author knows of no reason that this quantity of data cannot be saved, given importance of that data and the patience to endure several PEWin hang-ups while uploading it. After collecting a data set in several text files, a variant of the *process\_flat.m* Matlab function (Appendix C) should be run to import this data into Matlab.

A sample program of a 20-pass rastered flat with high-frequency data gathering commands is shown below.

```
A          // abort any current programs
#1j/
#2j/
#3j/
p820=999
p400=0
&1
#1->809076.5X
#2->25000Y
#3->809076.5Z
i5198 = 450    // #1 motor feedrate limit, mm/min
OPEN PROG 10
CLEAR
LINEAR
ABS
FRAX(X,Y,Z)

//data gathering stuff
I5000=0        //use regular RAM, do not wrap around
i5050=$7       // i5001-i5024 selection mask: i5001, i5002, i5003 to be gathered
I5051=$0       //i5025-i5048 data gathering selection mask: none to be gathered
I5049=5        // data gather period: data rate in Hz = ( 1/( i5049 * .000442sec ) )
I5001=$80008B  // x actual position
I5002=$80010B  // Y actual position
```

```

I5003=$80018B // z actual position
cmd"i5004..5048=$0" //clear out other gathering locations
p857 = 0 // pass after which to start gathering
p858 = 11 // pass before which to stop gathering
//

p808 = 0
p809 = 0
p810 = 0
p811 = 0
p812 = 0
p813 = 0

P803 = 1 // PASS number COUNTER
P804 = 0 // STARTING Y (CROSSFEED) COORDINATE (mm)
P805 = 0 // CURRENT Y COORDINATE (mm)
P806 = .0015 // CROSSFEED INCREMENT (mm)
P814 = 0.001 // BACKGROUND DOC (mm)
p856 = .0005 // Z initial approach
P802 = 0.0005 // DOC DELTA down(mm)
p854 = 1.5*p814 // DOC DELTA up (mm)
P820 = 999 // COMMAND-CHECK VARIABLE INITIALIZED
i15 = 0 // trig calcs operate on degrees

p851 = 90 // x cutting feedrate
p861 = 150 // x backfeedrate
p852 = 0.5 // y crossfeed increment feedrate
p853 = 2 // z approach feedrate
p855 = 0.05 // z final plunge feedrate

cmd"delete gather"
dly3000 //cautionary 3 sec pause
cmd"define gather"

// BOTTOM BLANK SECTION OF SYMBOL
p801 = 20 // #PASSES STARTING WITH NO DOC CHANGE
f(p853)
z.005
dly0
WHILE (p803 !> p801)
    p805 = p804 + p803*p806
    f(p851)
    x2
    dly100
    p820=p803+105

```

```

f(p852)
Y(p805)
dly1000
f(p853)
z.002
IF (P803 > p857 and p803 < p858) cmd"gather"
f(p853)
z(p856)           // stop just about surface for final plunge
f(p855)
Z(-p814) // x MICRONS INTO THE PART FOR THE BACKGROUND
dly500
f(p851)
x0
dly250
f(p855)
Z(p856) // SLOW RISE TO JUST ABOVE ZERO
DLY0
cmd"endg" // doesn't matter if you issue this when you're not gathering
f(p853)
Z(-p814+p854) // BACK OUT OF PART 1 DOC DELTA FOR BACKFEED
p803 = p803 + 1 // INCREMENT PASS number
ENDWHILE
f(p853)
Z(-p814+p854) // ENSURE OUT OF PART 1 DOC DELTA
dly1500
Z0.1 // ENSURE OUT OF PART 100UM
dly0

```

## 7.2 APPENDIX B: MATLAB FUNCTIONS

### 7.2.1 Loading Zygo Surface Topology Data into Matlab: xyzread.m

```
% written by Brett C. Brocato
% master's candidate, NC State University Precision Engineering Center, 2005

%insert a file name for a Zygo .xyz format file that has been modified
% to replace "No Data" with "NaN"

A = load('E021005_13x_trim2.xyz');

% insert the .xyz file resolution from the file header, then delete the header

res = 8.33411e-007;           %13X res is 8.33411e-007 m per pixel
res_mm = res*1000;           %resolution in mm

% Zigo is used instead of Zygo to avoid conflicts on Search and Replace
% with "y"
for count = 1:size(A,1)
    zZigo( (A(count,1)+1), (A(count,2)+1) ) = A(count,3);
end

a = 1;
b = 1;

xZigo = zeros(size(zZigo,1),size(zZigo,2));
yZigo = zeros(size(zZigo,1),size(zZigo,2));

for a = 1:size(zZigo,1)
    xZigo(a,:) = res_mm*a;
end
for b = 1:size(zZigo,2)
    yZigo(:,b) = res_mm*b;
end
```

### 7.2.2 Analyzing Rastered Crossfeed Features: crossfeed.m

```
% written by Brett C. Brocato
% master's candidate, NC State University Precision Engineering Center, 2005

% run this program only after xyzread.m has been run

% Zigo is used instead of Zygo to avoid conflicts on Search and Replace
```

```

% with "y"

xZigorange = max(max(xZigo(:, :))) - min(min(xZigo(:, :))); %mm x length of flat
yZigorange = max(max(yZigo(:, :))) - min(min(yZigo(:, :))); %mm y length of flat

% this variable should be true if you want a tool radius
% superimposed on a crossfeed feature
drawtool = false;
spikesize = 0.15; % mm; data farther off the surface than this will be eliminated

% the following "yzero" should probably start at zero. The plot "zZigoflatline"
% will be plotted with y=zero (in this program's coordinate system) placed at this
% location (in the Zygo coordinate system). The value of this location should be
% chosen by examining the plot "flat/trimmed", which has the unchanged Zigo
% coordinate system.

yzero = 9.1; % um Zigo coordinate system of 1st pass or pass of interest;

%these variables are the range of the data you want to look at, in mm
%Choose this range by issuing [ mesh(xZigo,yZigo,zZigo) ] after loading
%data with xyzread.m and before running crossfeed.m, or just run
%crossfeed.m with this range set to the total size of the data range,
%look at the plot "flat/trimmed" to choose the range of interest,
%modify these quantities, and run crossfeed.m again.

xZigolo = 0;
xZigolo_pixel = round( (xZigolo/xZigorange)*size(xZigo,1) ) + 1;

xZigohi = 0.071;
xZigohi_pixel = round( (xZigohi/xZigorange)*size(xZigo,1) ) - 1;

yZigolo = 0.007;
yZigolo_pixel = round( (yZigolo/yZigorange)*size(xZigo,2) ) + 1;

yZigohi = 0.051;
yZigohi_pixel = round( (yZigohi/yZigorange)*size(xZigo,2) ) - 1;

% this is the location in the x or upfeed direction that you will section
% the part for examination
upfeedxZigocoord = .007; %mm, location of radius of interest

%pixel column of interest
Zigoup_pixel = round( (upfeedxZigocoord/xZigorange)*size(xZigo,1) );

% if the tool radius is drawn, a 3-um range around yzero is included in the

```

```

% spatial profile. Otherwise, the profile range is set manually.

if drawtool == true
    startyZigocoord = yzero/1000 - .0015;
    endyZigocoord = yzero/1000 + .0015;
else
    startyZigocoord = .008 ; %mm, start of line of interest
    endyZigocoord = .050 ; %mm, start of line of interest
end

%starting pixel row of interest
startyZigo = round( (startyZigocoord/yZigorange)*size(xZigo,2) );

%ending pixel row of interest
endyZigo = round( (endyZigocoord/yZigorange)*size(xZigo,2) );

zZigoavg = mean(zZigo(Zigoup_pixel,:,:)); %only averages the xfeed line of interest
% um x positions of pixels
xZigopos(1:size(xZigo,1)) = res_mm*(1:size(xZigo,1))*1e3;
yZigopos(1:size(xZigo,2)) = res_mm*(1:size(xZigo,2))*1e3; %um y positions of pixels

%mean of tilted flat z, disregarding non-numbers
zZigoavg_all = nanmean(nanmean(zZigo(xZigolo_pixel:xZigohi_pixel,...
    yZigolo_pixel:yZigohi_pixel)));

for a = 1:size(A(:,3)) % make A(:,3) NaNs into A(:,3) averages
    if isnan(A(a,3))
        A(a,3) = zZigoavg_all;
    end
end

%This next section flattens the data within the range of interest

Axcoll = A(:,1);
Aycoll = A(:,2);
Azcoll = A(:,3);
trimAxcoll = Axcoll(find(and ( and (Axcoll > xZigolo_pixel, Axcoll < xZigohi_pixel), and
(Aycoll > yZigolo_pixel, Aycoll < yZigohi_pixel) )));
trimAycoll = Aycoll(find(and ( and (Axcoll > xZigolo_pixel, Axcoll < xZigohi_pixel), and
(Aycoll > yZigolo_pixel, Aycoll < yZigohi_pixel) )));
trimAzcoll = Azcoll(find(and ( and (Axcoll > xZigolo_pixel, Axcoll < xZigohi_pixel), and
(Aycoll > yZigolo_pixel, Aycoll < yZigohi_pixel) )));

trimA = [trimAxcoll,trimAycoll,trimAzcoll];

% calculate best-fit plane of unflattened data

```

```

% thanks to www.mathworks.co.uk Solution Number: 1-1AVW5

Const = ones(size(trimA(:,1)));
Coefficients = [trimA(:,1) trimA(:,2) Const]\trimA(:,3); % Find the coefficients
XCoeff = Coefficients(1); % X coefficient
YCoeff = Coefficients(2); % Y coefficient
CCoeff = Coefficients(3); % constant term

% Using the above variables, z = XCoeff * x + YCoeff * y + CCoeff
[xZigoflat, yZigoflat]=meshgrid(1:1:size(xZigo,1),1:1:size(xZigo,2)); % Generating a
regular grid for plotting
zZigoflatten = XCoeff * xZigoflat + YCoeff * yZigoflat + CCoeff;
zZigoflatten = zZigoflatten';
xZigoflat = xZigoflat';
yZigoflat = yZigoflat';
zZigoflat = zZigo(:, :) - zZigoflatten;

%mean of flattened flat z disregarding non-numbers

zZigoavg_all_flat = nanmean(nanmean(zZigoflat (xZigolo_pixel+1:xZigohi_pixel-
1,yZigolo_pixel+1:yZigohi_pixel-1)));

%mean of zflat over line of interest
zZigoavg_line = nanmean(nanmean(zZigoflat(Zigoup_pixel,startyZigo:endyZigo)));
%move the mean of zflat to ~0
zZigoflat = zZigoflat - zZigoavg_all_flat;

% get rid of corrosion spikes -> better color resolution for meshing
for q = 1:size(xZigo,1)
    for r = 1:size(xZigo,2)
        if zZigoflat(q,r) > spikesize
            zZigoflat(q,r) = 0;
        end
        if zZigoflat(q,r) < -spikesize
            zZigoflat(q,r) = 0;
        end
    end
end
end

%mean of zflat over line of interest, after spike removal
zZigoavg_line = nanmean(nanmean(zZigoflat(Zigoup_pixel,startyZigo:endyZigo)));

% this will be the flattened flat with the line of interest superimposed
zZigoflatline = zZigoflat;

% superimpose the line of interest. If it's not obvious on plot "zflatline",

```

```

% make the number bigger.

for t = startyZigo:endyZigo
    zZigoflatline(Zigoup_pixel,t) = zZigoavg_line + .25;
end

% plot the data as flattened and trimmed down to range of interest, but in
% the original Zigo coordinates
figure;mesh(xZigo(xZigolo_pixel:xZigohi_pixel,yZigolo_pixel:yZigohi_pixel)*1000,...
    yZigo(xZigolo_pixel:xZigohi_pixel,yZigolo_pixel:yZigohi_pixel)*1000,...
    zZigoflat(xZigolo_pixel:xZigohi_pixel,yZigolo_pixel:yZigohi_pixel) )
xlabel('X (\mum)','FontSize',12)
ylabel('Y (\mum)','FontSize',12)
zlabel('Z (\mum)','FontSize',12)
view([-10.5 88]);
daspect([20 20 1]);
set(gcf,'Name','flat/trimmed')

% plot it flattened, trimmed, with the xfeed line of interest marked, and
% crossfeed zero at the coordinate in yzero
figure;mesh(xZigo(xZigolo_pixel:xZigohi_pixel,yZigolo_pixel:yZigohi_pixel)*1000,...
    -( yZigo(xZigolo_pixel:xZigohi_pixel,yZigolo_pixel:yZigohi_pixel)*1000 - yzero),...
    zZigoflatline(xZigolo_pixel:xZigohi_pixel,yZigolo_pixel:yZigohi_pixel) )
xlabel('X (\mum)','FontSize',12)
ylabel('Y (\mum)','FontSize',12)
zlabel('Z (\mum)','FontSize',12)
view([-180 90]);
daspect([20 20 1]);
set(gcf,'Name','zZigoflatline')

circumf = 0; %initialize the tool circumference
toolcrossbias = 0; % um, move the tool off of yzero this much
tool = 50; % um radius
tooloff = 49.955+.03; %um tool radius center distance from part
avgy = nanmean(yZigopos(startyZigo:endyZigo)) + toolcrossbias; %um mid y range

centerZigoy = yZigopos(startyZigo:endyZigo) - avgy; % centered on mid range

for r = 1:size(centerZigoy,2)
    circumf(r) = tooloff - ( -centerZigoy(r)^2 + tool^2)^(1/2);
end

avgcirc = mean(circumf);

%plot the xfeed spatial profile and tool radius, with Zigo coord system
% y coordinates.

```

```

if drawtool == true
    figure;plot((yZigopos(startyZigo:endyZigo) ),...
                ( zZigoflat(Zigoup_pixel,startyZigo:endyZigo) ),'b.',...
                (yZigopos(startyZigo:endyZigo)),circumf)
else
    figure;plot((yZigopos(startyZigo:endyZigo)),...
                ( zZigoflat(Zigoup_pixel,startyZigo:endyZigo) ),'b.')
end
xlabel('crossfeed in y direction (\mum)','FontSize',14)
ylabel('profile (\mum)','FontSize',14)
set(gcf,'Name','spatial profile raw y')
grid

%plot the xfeed spatial profile and tool radius, with zeroed
% y coordinates.

if drawtool == true
    figure;plot(-(yZigopos(startyZigo:endyZigo) - yzero),...
                ( zZigoflat(Zigoup_pixel,startyZigo:endyZigo) ),'b.',...
                -(yZigopos(startyZigo:endyZigo) - yzero),circumf)
else
    figure;plot(-(yZigopos(startyZigo:endyZigo) - yzero),...
                ( zZigoflat(Zigoup_pixel,startyZigo:endyZigo) ),'b.')
end
xlabel('crossfeed in y direction (\mum)','FontSize',14)
ylabel('profile (\mum)','FontSize',14)
set(gcf,'Name','spatial profile y zeroed')
grid

```

### 7.2.3 Analyzing Rastered Upfeed Features: upfeed\_line.m

```
% written by Brett Brocato, Precision Engineering Center, NC State

% run this program only after xyzread.m has been run

% Zigo is used instead of Zygo to avoid conflicts on Search and Replace
% with "y"

xZigorange = max(max(xZigo(:,:))) - min(min(xZigo(:,:))); %mm x length of flat
yZigorange = max(max(yZigo(:,:))) - min(min(yZigo(:,:))); %mm y length of flat

% the following "yzero" should probably start at zero. The plot "zZigoflatline"
% will be plotted with y=zero (in this program's coordinate system) placed at this
% location (in the Zygo coordinate system). The value of this location should be
% chosen by examining the plot "flat/trimmed", which has the unchanged Zigo
% coordinate system.

%these variables are the range of the data you want to look at, in mm
%Choose this range by issuing [ mesh(xZigo,yZigo,zZigo) ] after loading
%data with xyzread.m and before running upfeed_line.m, or just run
%upfeed_line.m with this range set to the total size of the data range,
%look at the plot "flat/trimmed" to choose the range of interest,
%modify these quantities, and run upfeed_line.m again.

yzero = 42; %um Zigo coordinate system of first pass; plot zflatline at zero here

xZigolo = 0.001;
xZigolo_pixel = round( (xZigolo/xZigorange)*size(xZigo,1) ) + 1;

xZigohi = 0.071;
xZigohi_pixel = round( (xZigohi/xZigorange)*size(xZigo,1) ) - 1;

yZigolo = 0.013;
yZigolo_pixel = round( (yZigolo/yZigorange)*size(xZigo,2) ) + 1;

yZigohi = 0.045;
yZigohi_pixel = round( (yZigohi/yZigorange)*size(xZigo,2) ) - 1;

% this is the location in the y or crossfeed direction that you will section
% the part for examination

crossfeedyZigocoord = .030; %mm, location of line of interest
```

```

Zigopass_pixel = round( (crossfeedyZigocoord/yZigorange)*size(xZigo,2) ); %pixel
row of interest

startxZigocoord = .001; %mm, start of line of interest

startxZigo = round( (startxZigocoord/xZigorange)*size(xZigo,1) ); %starting pixel
column of interest

endxZigocoord = .07; %mm, end of line of interest
endxZigo = round( (endxZigocoord/xZigorange)*size(xZigo,1) ); %ending pixel
column of interest

zZigoavg = mean(zZigo(:,Zigopass_pixel,:)); %only averages the upfeed line of
interest
xZigopos(1:size(xZigo,1)) = res*(1:size(xZigo,1))*1e6; % um x positions of pixels
yZigopos(1:size(xZigo,2)) = res*(1:size(xZigo,2))*1e6; %um y positions of pixels
% pixels per mm, upfeed direction
spacerate = round( 1/ ((max(max(xZigo))-min(min(xZigo)))/size(xZigo,1) ) );
%mean of tilted flat x disregarding non-numbers
zZigoavg_all =
nanmean(nanmean(zZigo(xZigolo_pixel:xZigohi_pixel,yZigolo_pixel:yZigohi_pixel)));

for a = 1:size(A(:,3)) % make A(:,3) NaNs into A(:,3) averages
    if isnan(A(a,3))
        A(a,3) = zZigoavg_all;
    end
end

Axcoll = A(:,1);
Aycoll = A(:,2);
Azcoll = A(:,3);
trimAxcoll = Axcoll(find(and ( and (Axcoll > xZigolo_pixel, Axcoll < xZigohi_pixel),...
    and (Aycoll > yZigolo_pixel, Aycoll < yZigohi_pixel) )));
trimAycoll = Aycoll(find(and ( and (Axcoll > xZigolo_pixel, Axcoll < xZigohi_pixel),...
    and (Aycoll > yZigolo_pixel, Aycoll < yZigohi_pixel) )));
trimAzcoll = Azcoll(find(and ( and (Axcoll > xZigolo_pixel, Axcoll < xZigohi_pixel),...
    and (Aycoll > yZigolo_pixel, Aycoll < yZigohi_pixel) )));

trimA = [trimAxcoll,trimAycoll,trimAzcoll];

%zflatten
% calculate best-fit plane of unflattened data
% thanks to www.mathworks.co.uk Solution Number: 1-1AVW5

Const = ones(size(trimA(:,1)));
Coefficients = [trimA(:,1) trimA(:,2) Const]\trimA(:,3); % Find the coefficients

```

```

XCoeff = Coefficients(1); % X coefficient
YCcoeff = Coefficients(2); % X coefficient
CCcoeff = Coefficients(3); % constant term
% Using the above variables, z = XCoeff * x + YCcoeff * y + CCcoeff

% Generating a regular grid for plotting
[xZigoflat, yZigoflat]=meshgrid(1:1:size(xZigo,1),1:1:size(xZigo,2));
zZigoflatten = XCoeff * xZigoflat + YCcoeff * yZigoflat + CCcoeff;
zZigoflatten = zZigoflatten';
xZigoflat = xZigoflat';
yZigoflat = yZigoflat';
zZigoflat = zZigo(:, :) - zZigoflatten;

%mean of flattened flat x disregarding non-numbers
zZigoavg_all_flat = nanmean(nanmean(zZigoflat (xZigolo_pixel+1:xZigohi_pixel-1,...
    yZigolo_pixel+1:yZigohi_pixel-1)));

%mean of zflat over line of interest
zZigoavg_line = nanmean(nanmean(zZigoflat(startxZigo:endxZigo,Zigopass_pixel)));
zZigoflat = zZigoflat - zZigoavg_all_flat; %move the mean of zflat to ~0

for a = 1:size(xZigo,1) % get rid of corrosion spikes -> better color resolution for
meshing
    for b = 1:size(xZigo,2)
        if zZigoflat(a,b)> 0.5
            zZigoflat(a,b) = 0;
        end
        if zZigoflat(a,b)< -0.5
            zZigoflat(a,b) = 0;
        end
    end
end
end

%mean of zflat over line of interest
zZigoavg_line = nanmean(nanmean(zZigoflat(startxZigo:endxZigo,Zigopass_pixel)));

zZigoflatline = zZigoflat; % this will be the flattened flat with the line of interest
superimposed

for t = startxZigo:endxZigo % superimpose the line of interest
    zZigoflatline(t,Zigopass_pixel) = zZigoavg_line + .15;
end

figure;mesh(xZigo(xZigolo_pixel:xZigohi_pixel,yZigolo_pixel:yZigohi_pixel)*1000,...

```

```

    yZigo(xZigolo_pixel:xZigohi_pixel,yZigolo_pixel:yZigohi_pixel)*1000,...
    zZigoflat(xZigolo_pixel:xZigohi_pixel,yZigolo_pixel:yZigohi_pixel) )
%xlabel('X (', 'Font', 'Symbol', 'u', 'Font', 'Arial', 'm)', 'FontSize', 12)
xlabel('X (\mum)', 'FontSize', 12, 'Interpreter', 'tex')
ylabel('Y (\mum)', 'FontSize', 12, 'Interpreter', 'tex')
zlabel('Z (\mum)', 'FontSize', 12, 'Interpreter', 'tex')
view([-10.5 88]);
daspect([80 80 1]);
set(gcf, 'Name', 'flat/trimmed')

figure; mesh(xZigo(xZigolo_pixel:xZigohi_pixel,yZigolo_pixel:yZigohi_pixel)*1000,...
    -( yZigo(xZigolo_pixel:xZigohi_pixel,yZigolo_pixel:yZigohi_pixel)*1000 - yzero),...
    zZigoflatline(xZigolo_pixel:xZigohi_pixel,yZigolo_pixel:yZigohi_pixel) )
xlabel('X (\mum)', 'FontSize', 12, 'Interpreter', 'tex')
ylabel('Y (\mum)', 'FontSize', 12, 'Interpreter', 'tex')
zlabel('Z (\mum)', 'FontSize', 12, 'Interpreter', 'tex')
view([-180 90]);
daspect([80 80 1]);
set(gcf, 'Name', 'zflatline')

%spatial frequency

signal = (zZigoflat(startxZigo:endxZigo,Zigopass_pixel) ) * 1000 - zZigoavg_line * 1000;
%signal in nm

[f, mag, phase, fq, h] = freq_nm( signal, spacerate, 1e-10, 1.0001, 502);
set(gcf, 'Name', 'Bode')
%xlabel('string')
figure; plot(fq, mag, 'b. ');
xlabel('frequency (1/mm)', 'FontSize', 12)
ylabel('amplitude (nm)', 'FontSize', 12)
xlim([0 1500]);
set(gcf, 'Name', 'Magnitude vs. Frequency')
%figure; plot((xpos), z(:, pass_pixel, :) - zavg)
figure; plot((xZigopos(startxZigo:endxZigo)), signal, 'b. ');
xlabel('upfeed in x direction (\mum)', 'FontSize', 12, 'Interpreter', 'tex')
ylabel('signal (nm)', 'FontSize', 12)
set(gcf, 'Name', 'spatial profile')
%set(gcf, 'Marker', '.')
%set(gcf, 'LineStyle', 'none')

```

## 7.2.4 Analyzing nanometer spatial frequency signals: `freq_nm.m`, `plot_freq_nm.m`

*Note: `plot_freq_nm.m` and `magphase.m` are called by `freq_nm.m`*

### `freq_nm.m`

% written by Ken Garrard, Precision Engineering Center, NC State

% Perform FFT of a signal and plot magnitude and phase  
% [f,mag,phase,fq,h] = freq(X,rate,threshold,scale,nstyle)

% Input

% X        signal vector

% rate     sample rate in Hz            (default = 100)

% threshold cutoff value for trim filter    (default = 1e-10)

% scale    scale factor for spatial data    (default = 1)

% nstyle   maximum vector length for stem plots (default = 502)

% Output

% f        FFT of X after application of trim filter, complex

% mag     absolute magnitude of FFT(X), signal units

% phase   unwrapped phase    of FFT(X), degrees

% fq      frequency values for mag and phase, dc to Nyquist

% h        figure object handle for magnitude and phase plots

function [f,mag,phase,fq,h] = freq\_nm(X,rate,threshold,scale,nstyle)

if nargin < 2, rate = 100; end

if nargin < 3, threshold = 1e-10; end

if nargin < 4, scale = 1; end

if nargin < 5, nstyle = 502; end

% calculate fft of signal vector

f = fft(X);

% set NaNs and values below threshold to zero

f = cplxfilt(f,threshold);

% calculate magnitude and phase

[mag,phase,fq] = magphase(f,rate,scale);

% plot magnitude and phase vs frequency

h = plotfreq\_nm(fq,mag,phase,scale,nstyle);

### **plot\_freq\_nm.m**

*please note: the time-domain frequency on the upper x-axis of the frequency plot should not be used unless the XLim property has been set correctly for the upfeed speed. See the comment paragraph near the end of this code. The user should always confirm that the range of time-domain and spatial frequencies in a given plot makes sense given the programmed upfeed speed.*

```
% written by Ken Garrard, Precision Engineering Center, NC State
% modified for time and spatial frequency domains by Brett Brocato
```

```
% Plot magnitude and phase vs frequency
% h = plotfreq(fq,mag,phase,scale,nstyle)
% Input
% fq      frequency values for mag and phase, dc to Nyquist
% mag     absolute magnitude of FFT(X), signal units
% phase   unwrapped phase   of FFT(X), radians
% scale   scale factor for spatial data      (default = 1)
% nstyle  maximum vector length for stem plots (default = 502)
% Output
% h      figure object handle for magnitude and phase plots
%
% A single figure containing two subplots is produced. The upper
% subplot is linear magnitude and the lower subplot is phase angle.
% Angles are plotted in degree units on the phase subplot. The
% horizontal axis for both subplots is frequency (or wavenumber).
% Logarithmic scaling is used, hence the DC component is not shown.
% The maximum magnitude is indicated as well as the phase angle at
% that frequency.
```

```
function h = plotfreq_nm(fq,mag,phase,scale,nstyle)
```

```
if nargin < 4, scale = 1; end
if nargin < 5, nstyle = 502; end
```

```
% 2D line plot or 2D stem plot ?
plotfun = @plot;
if length(fq) <= nstyle, plotfun = @stem; end
```

```
% convert phase angles to degrees
phase = phase * 180/pi;
```

```
% find maximum magnitude
if max(mag) < Inf, mxidx = find(mag/max(mag)>0.99);
else          mxidx = find(mag==max(mag));
end
mxfq = fq(mxidx(1));    % lowest frequency at max magnitude
```

```

mxmag = mag(mxidx(1)); % maximum magnitude
mxphase = phase(mxidx(1)); % phase at 1st maximum

% exclude DC value for log plots
if (fq(1)==0)
    fq = fq(2:end);
    mag = mag(2:end);
    phase = phase(2:end);
    % refill maximum magnitude index vector
    if max(mag) < Inf, mxidx = find(mag/max(mag)>0.99);
    else
        mxidx = find(mag==max(mag));
    end
end

% create new figure, subplot for magnitude and phase
h = figure;

% plot magnitude
%subplot(2,1,1);
m = feval(plotfun,fq,mag);
set(m,'Color','b','LineWidth',2,'MarkerFaceColor','b');
set(gca,'XScale','log','FontName','Arial','FontSize',12,'FontWeight','Bold');
ylabel('signal (nm)','FontName','Arial','FontSize',12,'FontWeight','Bold');

title(['Frequency (Hz)'],...
      'FontName','Arial','FontSize',12,'FontWeight','Bold','color','k');

hold on;

% mark maximums on magnitude plot
plot(fq(mxidx),mag(mxidx),'r.','MarkerSize',20);
grid off;
% horizontal axis is frequency or wavenumber ?
if scale == 1,
    xlabel('Frequency (Hz)','FontName','Arial','FontSize',12,'FontWeight','Bold');
else
    xlabel('Wavenumber
(1/lambda)','FontName','Arial','FontSize',12,'FontWeight','Bold','Interpreter','tex');
    set(gca,'TickLength',[0 0]);
end

% this next statement sets up a second x-axis on the top of the FFT plot with a
% time-domain scale in Hz. The quantities in brackets after 'XLim' should be
% equal to:
% [ ( 1/mm * upfeed speed in mm/s ) ( 1000/mm * upfeed speed in mm/s ) ]

```

```
% Please note: if this graph is zoomed, the time-domain axis will no longer  
% be accurate. I would have preferred to set this quantity dynamically by  
% an upfeed speed input, but Matlab does not allow dynamic calculation of  
% these limits in an axes statement.
```

```
axes('position',[0.13 .923 .7750 0.001],'XScale','log','XLim',[1.913 1913],...  
     'Layer','Top','TickDir','out','FontWeight','bold','FontSize',12,'XGrid','off','Layer','Top')
```

## magphase.m

%written by Ken Garrard, Precision Engineering Center, NC State

% Extract magnitude and phase from a complex vector

% [mag,phase,fq] = magphase(f,rate,fscale,mscale)

% Input

% f        FFT of signal vector

% rate    sample rate in Hz    (default = 100)

% fscale   frequency scale factor (default = 1)

% mscale   magnitude scale factor (default = 2/length(f))

% Output

% mag     absolute magnitude of FFT(X), signal units

% phase   unwrapped phase   of FFT(X), radians

% fq     frequency values for mag and phase, dc to Nyquist

function [mag,phase,fq] = magphase(f,rate,fscale,mscale)

% find the number of unique frequencies in result

% even length -> dc, delta, 2\*delta, ... (rate/2-delta), rate/2

% odd length -> dc, delta, 2\*delta, ... (rate/2-delta)

N = length(f);        % length of fft

len = ceil((N+1)/2);    % no Nyquist value for odd length vectors

if nargin < 2, rate = 100; end

if nargin < 3, fscale = 1; end

if nargin < 4, mscale = 2/N; end

% calculate linear magnitude

mag = abs(f)\*mscale;

% calculate unwrapped phase angles

phase = unwrap(angle(f));

% calculate frequency (or wavenumber) range

fq = (0:len-1)\*(rate)/length(f)\*fscale;

% delete conjugate

mag = mag(1:len);

phase = phase(1:len);

% DC and Nyquist values are unique, rescale them by 1/2

mag(1) = mag(1)/2;

if ~rem(N,2)        % no Nyquist value for odd length vectors

mag(end) = mag(end)/2;

end

## 7.2.5 Loading Nanoform Axis Position Data into Matlab: process\_flat.m, processxyz.m, read\_umac\_data.m

*Note: processxyz.m and read\_umac\_data.m are called by process\_flat.m*

### **process\_flat.m**

% written by Brett Brocato, Precision Engineering Center, NC State

```
xaxislo = 0; %mm
xaxishi = 2; %mm
yaxislo = 0; %mm
yaxishi = .5; %mm
zaxislo = -.05; %mm
zaxishi = -.0005; %mm
```

% The file names below should match those of a set of data gathered in PEWin.  
% The second argument should change to 2 or 3 if the first data word in the file is  
% not an x-axis value. Add a fifth command (or more) for five or more text files.

```
[x1,y1,z1] = processxyz('Flat_E_0_18000.txt',1);
[x2,y2,z2] = processxyz('Flat_E_18000_24000.txt',1);
[x3,y3,z3] = processxyz('Flat_E_42000_18000.txt',1);
[x4,y4,z4] = processxyz('Flat_E_60000_15180.txt',1);
```

% add x5, y5, and z5 to these concatenation statements for a fifth text file.

```
xaxis = [x1;x2;x3;x4];
yaxis = [y1;y2;y3;y4];
zaxis = [z1;z2;z3;z4];
```

```
xaxis_trim = xaxis(find( and( and ( and (xaxis > xaxislo, xaxis < xaxishi),
and (yaxis > yaxislo, yaxis < yaxishi) ) ,...
and (zaxis > zaxislo, zaxis < zaxishi) ) ) );
```

```
yaxis_trim = yaxis(find( and( and ( and (xaxis > xaxislo, xaxis < xaxishi),
and (yaxis > yaxislo, yaxis < yaxishi) ) ,...
and (zaxis > zaxislo, zaxis < zaxishi) ) ) );
```

```
zaxis_trim = zaxis(find( and( and ( and (xaxis > xaxislo, xaxis < xaxishi),
and (yaxis > yaxislo, yaxis < yaxishi) ) ,...
and (zaxis > zaxislo, zaxis < zaxishi) ) ) );
```

```
xaxis_trim = xaxis_trim';
yaxis_trim = yaxis_trim';
```

```
zaxis_trim = zaxis_trim';  
  
xaxis_zeroed = xaxis_trim - xaxislo;  
  
figure;plot3( (xaxis_zeroed)*1e3,yaxis_trim*1e3,zaxis_trim*1e3,'.b','MarkerSize',.5)  
xlabel('X (\mum)','FontSize',12)  
ylabel('Y (\mum)','FontSize',12)  
zlabel('Z (\mum)','FontSize',12)  
zaxis_trim_avg = nanmean(zaxis_trim);  
set(gcf,'Name','axes positions')
```

## processxyz.m

```
% written by Brett Brocato, Precision Engineering Center, NC State

function [x,y,z] = processxyz(file,coordfirst)

% coordfirst specifies which axis (x, y, or z) is first in a file. If you run
% it with "1" and get data that looks like y, put "2" in coordfirst and rerun.
% If run it with "1" and get z-looking data, put "3" and rerun.

xcounts = 809076.48; %interferometer counts per mm
ycounts = 25000;% encoder counts per mm
zcounts = 809076.48;% interferometer counts per mm

read_umac_data(file,6);
dataset = ans;

if coordfirst == 1
    a = 1; b = 2; c = 3; d = 4; e = 5; f = 6;
elseif coordfirst == 2
    a = 5; b = 6; c = 1; d = 2; e = 3; f = 4;
elseif coordfirst == 3
    a = 3; b = 4; c = 5; d = 6; e = 1; f = 2;
end

for count = 1:size(dataset,1)
% if the first column of the two is not huge, the number is positive

    if dataset(count,a) < hex2dec('7FFFFFFF')
        x(count) = ( ( dataset(count,a)*(2^24))+dataset(count,b) )/3072)/xcounts;

% if the first column is huge, like FFFFFFFF, the number is negative.

    else
        x(count) = - ( ( hex2dec('1000000000000') - (dataset(count,...
            a)*(2^24)+dataset(count,b) ) )/3072)/xcounts;
    end
    if dataset(count,c) < hex2dec('7FFFFFFF')
        y(count) = (( dataset(count,c)*(2^24))+dataset(count,d) )/3072)/ycounts;
    else
        y(count) = - ( ( hex2dec('1000000000000') - ( dataset(count,...
            c)*(2^24)+dataset(count,d) ) )/3072)/ycounts;
    end
    if dataset(count,e) < hex2dec('7FFFFFFF')
        z(count) = ( ( dataset(count,e)*(2^24))+dataset(count,f) )/3072)/zcounts;
    else
```

```
z(count) = - ( ( hex2dec('1000000000000') - (
dataset(count,e)*(2^24)+dataset(count,f) ) )/3072)/zcounts;
end
end
```

```
x = x';
y = y';
z = z';
```

## **read\_umac\_data.m**

%written by Ken Garrard, Precision Engineering Center, NC State

% Read UMAC format data capture file into a matrix

% [ud,nrows] = read\_umac\_data(fn,ncols,nhdr)

% Input

% fn input text file, ascii hex format

% ncols number of data columns, default = 1

% nhdr number of header lines to ignore, default = 0

% Output

% ud output data matrix, [nrows x ncols]

% nrows number of rows

function [ud,nrows] = read\_umac\_data(fn,ncols,nhdr)

error(nargchk(1,3,nargin));

if nargin < 2, ncols = 1; end % One columns

if nargin < 3, nhdr = 0; end % No header lines

fid = fopen(fn,'rt'); % Open text input file

% Abort if file does not exist or cannot be opened

if fid < 0, error('cannot open file %s',fn); end

finfo = dir(fn); % Get file info for input file

if isempty(finfo), % Error if info not available

error('unable to retrieve system info for input file %s',fn);

end

% Read past header lines

for k = 1:nhdr

s = fgetl(fid);

end

% Estimate number of rows in data matrix

nrows = ceil(finfo.bytes / (ceil(ncols/2) \* 13) );

% Preallocate space for output matrix

ud = zeros(nrows\*ncols,1);

% Read remainder of file into a vector

ud = fscanf(fid,'%6x'); % Use 6 digit hex conversion format

fclose(fid); % Close input file

% Find actual number of rows

```
lud = length(ud);  
nrows = ceil(lud/ncols);  
  
% Pad incomplete last row with zeros  
ud = [ud; zeros(nrows*ncols-lud,1)];  
  
% Reshape vector into a matrix, [nrows x ncols]  
ud = reshape(ud,ncols,nrows).';
```

## 7.2.6 Analyzing Nanoform Axis Upfeed Data: axis\_upfeed\_pickline.m

```
% written by Brett Brocato, Precision Engineering Center, NC State

format long;
linecount = 1;
lineOK = false;
% gp :. PMAC gather period
gp = 5;
axisdatarate = 1/(gp*.000442); % Hz = 1/(gp*.000442 seconds)
DOC = 1; % um programmed depth of cut
DOCcutoff = .98; % this percentage of program DOC is kept in the data
%data within 85% of it is kept in mean peak speed calculation
%also in the yPV calculation
progspeed = 2; % programmed upfeed mm/s;

upfeedzero = 2; % mm position of Nanoform x axis at zero upfeed
upfeedoffset = 0 % mm of upfeed distance to cut off
approxcrossfeed = .0015; % mm position of upfeed of interest within xinterval
xinterval = 0.5; %um basket for crossfeed

lowerxf = approxcrossfeed*1000 - xinterval; %um lower limit xfeed
higherxf = approxcrossfeed*1000 + xinterval; %um higher limit xfeed

xaxis_line = xaxis_zeroed( find( xaxis_zeroed ( and ( yaxis_trim*1000 < higherxf,...
    yaxis_trim*1000 > lowerxf ) )));
yaxis_line = yaxis_trim(find( yaxis_trim ( and ( yaxis_trim*1000 < higherxf,...
    yaxis_trim*1000 > lowerxf ) )));
zaxis_line = zaxis_trim( find( zaxis_trim ( and ( yaxis_trim*1000 < higherxf,...
    yaxis_trim*1000 > lowerxf ) )));

xaxis_line = xaxis_line( find( xaxis_line < (upfeedzero - upfeedoffset) ) ) ;
yaxis_line = yaxis_line( find( xaxis_line < (upfeedzero - upfeedoffset) ) ) ;
zaxis_line = zaxis_line( find( xaxis_line < (upfeedzero - upfeedoffset) ) ) ;

xaxis_line = xaxis_line( find( zaxis_line < -( DOC*1e-3*DOCcutoff) ) ) ;
yaxis_line = yaxis_line( find( zaxis_line < -( DOC*1e-3*DOCcutoff) ) ) ;
zaxis_line = zaxis_line( find( zaxis_line < -( DOC*1e-3*DOCcutoff) ) ) ;

xaxis_line = xaxis_line';
yaxis_line = yaxis_line';
zaxis_line = zaxis_line';

zaxis_avg_line = mean(zaxis_line)

figure;plot((upfeedzero - xaxis_line),(zaxis_line)*1e6,'b.-')
```

```

xlabel('upfeed position (mm)','FontSize',12)
ylabel('Z (nm)','FontSize',12)
set(gcf,'Name','z vs upfeed position')

%diff x is in distance units per data point, not per second
diffx = diff(xaxis_line);

%axisspeed is in distance units per second.
axisspeed = diffx*axisdatarate;
meanaxisspeed = mean(axisspeed);

%normspeed includes speeds within 85% of the programmed upfeed
normspeed = mean(axisspeed(find(axisspeed < -0.85*progspeed)));
ynorm = yaxis_line(1:size(axisspeed,1));

%Y-axis peak-to-valley calculates maximum change in y encoder when
% the x-axis is at at least 85% programmed upfeed speed.

ypeak = max(ynorm(find(axisspeed < -0.85*progspeed)));
yvalley = min(ynorm(find(axisspeed < -0.85*progspeed)));
yPV = (ypeak - yvalley)*1000 %microns
figure;plot(upfeedzero - xaxis_line( 1:size(diffx,1) ),- axisspeed,'b.-')
xlabel('upfeed position (mm)','FontSize',12)
ylabel('Upfeed speed (mm/s)','FontSize',12)
set(gcf,'Name','upfeed speed')
xlim( [ min(xaxis_line) max(xaxis_zeroed) ] );

diff2x = diff(diff(xaxis_line)); % speed per data point
axisaccel = diff2x*axisdatarate; % speed per second
figure;plot(upfeedzero - xaxis_line( 1:size(diff2x,1) ),- axisaccel,'b.-')
xlabel('upfeed position (mm)','FontSize',12)
ylabel('Upfeed acceleration (mm/s^2)','FontSize',12)
set(gcf,'Name','upfeed acceleration')
xlim( [ min(xaxis_line) max(xaxis_zeroed) ] );

axistime = gp*.000442*(1:size(xaxis_line,1));
figure;plot( axistime(1:(size(xaxis_line,1)-1) ) ,- axisspeed,'b.' );
xlabel('upfeed time (s)','FontSize',12)
ylabel('Upfeed speed (mm/s)','FontSize',12)
set(gcf,'Name','upfeed speed vs time')

figure;plot(axistime, (zaxis_line)*1e6);
xlabel('upfeed time (sec)','FontSize',12)
ylabel('Z (nm)','FontSize',12)
set(gcf,'Name','z vs time')

```

```
signal = (zaxis_line - zaxis_avg_line)*1e6;  
  
[f,mag,phase,fq,h] = freq_nm(signal,axisdatarate,1e-10,1.0001,502);  
set(gcf,'Name','Bode')  
xlabel('Frequency')  
figure;plot(fq,mag,'b.');
```

xlabel('frequency (Hz)','FontSize',12)  
ylabel('amplitude (nm)','FontSize',12)  
set(gcf,'Name','Frequency')

### 7.3 APPENDIX C: ULTRAMILL PMAC SAMPLE PART PROGRAM

Angstrom symbol: 200  $\mu\text{m}$  x 200  $\mu\text{m}$

```
a                // abort any other programs
#1j/             // jog-stop motor #1
#2j/
#3j/

p820=999        // initialize debugging variable
p400=0

// all distance units in this program are in millimeters
&1              // select coordinate system 1
#1->809076.5X    //motor #1 interferometer cts per mm
#2->26666.67Y    //motor #2 encoder cts per mm
#3->809076.5Z    //motor #3 interferometer cts per mm
i5198 = 450      // #1 motor feedrate limit mm/min

OPEN PROG 10
CLEAR
LINEAR
ABS              // absolute positioning (not incremental)
FRAX(X,Y,Z)     // all three are feedrate axes

p808 = 0
p809 = 0
p810 = 0
p811 = 0
p812 = 0
p813 = 0

P802 = 0.0005   // DOC DELTA down(mm)
p854 = 0.001    // DOC DELTA up (mm)
P803 = 1        // PASS number COUNTER
P804 = .0063    // STARTING Y (CROSSFEED) COORDINATE (mm)
P805 = .0063    // CURRENT Y COORDINATE (mm)
P806 = .001     // CROSSFEED INCREMENT (mm)
P814 = .002     // BACKGROUND DOC (mm)
P820 = 999     // COMMAND-CHECK VARIABLE INITIALIZED
i15 = 0        // trigonometry calculations operate on degrees

p851 = 50       // x cutting feedrate mm/min
p861 = 50       // x backfeedrate mm/min
p852 = 0.5      // y crossfeed increment rate
p853 = 2        // z depth change feedrate
```

```
// BOTTOM BLANK SECTION OF SYMBOL
```

```
p801 = 8    // #PASSES STARTING AT BOTTOM WITH NO DOC CHANGE
```

```
f(p853)    // set feedrate for depth change
```

```
z.002
```

```
dly0
```

```
WHILE (p803 !> p801)
```

```
    // INCREMENT CROSSFEED LOCATION IN Y
```

```
    p805 = p804 + p803*p806
```

```
    f(p851)
```

```
    x0.2
```

```
    dly250
```

```
    f(p852)
```

```
    Y(p805)
```

```
    dly1500
```

```
    P820 = 110 + P803
```

```
    f(p853)
```

```
    //x MICRONS INTO THE PART FOR THE BACKGROUND
```

```
    Z(-p814)
```

```
    dly750
```

```
    P820 = 120 + P803
```

```
    f(p851)
```

```
    x0
```

```
    dly250
```

```
    P820 = 130 + P803
```

```
    f(p853)
```

```
    // BACK OUT OF PART 1 DOC DELTA FOR BACKFEED
```

```
    Z(-p814+p854)
```

```
    dly250
```

```
    P820 = 140 + P803
```

```
    f(p861)
```

```
    x0.2
```

```
    dly250
```

```
    P820 = 150 + P803
```

```
    p803 = p803 + 1 // INCREMENT PASS number
```

```
ENDWHILE
```

```
f(p853)
```

```
Z(-p814+p854)    // ENSURE OUT OF PART 1 DOC DELTA
```

```
dly250
```

```
// OPEN BOTTOM SECTION OF A, WITH ELLIPTICAL APPROACH TO BOTTOM  
LEFT POINT OF A
```

```

p801 = 20          //PASS number TO jump TO NEXT SECTION

WHILE (p803!>p801)

    //ELLIPTICAL APPROACH FOR BOTTOM LEFT POINT
    p811 = 32.04*p805*p805 - 1.3491*p805 + .0343

        // OPEN BOTTOM END START
        // all numbers “/5” are transferred from the 1-mm angstrom, but divided by 5
    p810 = (.241469/5 + p805/TAN(65))

    // OPEN BOTTOM END END
        p809 = 0.2 - p810

    //ELLIPTICAL END FOR B.RIGHT POINT
    p808 = 0.2 - p811

        // INCREMENT CROSSFEED LOCATION IN Y
    p805 = p804 + p803*p806

    f(p851)
    x0.2
    f(p852)
    Y(p805)
    dly1500
    P820 = 210 + P803
    f(p853)
    Z(-p814)          // BACKGROUD DOC
    dly750
    P820 = 220 + P803
    f(p851)
    X(p808)
    dly250
    P820 = 230 + P803
    f(p853)
        //+Z BY ONE DOC DELTA FOR THE LEFT RAISED SECTION
    Z(-p814+p802)
    dly750
    P820 = 240 + P803
    f(p851)
    X(p809)
    dly250
    P820 = 260 + P803
    f(p853)

```

```

Z(-p814) //BACKGROUND DOC FOR SUNKEN BOTTOM END
dly750
P820 = 270 + P803
f(p851)
X(p810)
dly250
P820 = 280 + P803
f(p853)
//+Z BY ONE DOC DELTA FOR THE RIGHT RAISED SECTION
Z(-p814+p802)
dly750
P820 = 290 + P803
f(p851)
X(p811)
dly250
p820 = 291 + p803
f(p853)
Z(-p814) //BACK TO BACKGROUND DOC
dly750
p820 = 292 + p803
f(p851)
x0
dly250
p820 = 293 + p803
f(p853)
Z(-p814+p854) // 1 DOC DELTA OUT OF PART
dly250
p820 = 294+p803
f(p861)
x0.2 // BACKFEED TO X=0
dly250
p820 = 295 + p803

p803 = p803 + 1 // INCREMENT PASS number

ENDWHILE

f(p853)
Z(-p814+p854) // ENSURE OUT OF PART 1 DOC DELTA
dly250

// HORIZONTAL CROSSBAR SECTION

p801 = 53 //PASS number TO jump TO NEXT SECTION

WHILE (p803!>p801)

```

```

p813 = .04355/5 + p805/TAN(65) //LEFT LONG DIAGONAL
p812 = 0.2 - p813 //RIGHT LONG DIAGONAL
p805 = p804 + p803*p806 // INCREMENT CROSSFEED LOCATION IN
Y

```

```

f(p851)
x0.2
f(p852)
Y(p805)
dly1500
f(p853)
Z(-p814) // BACKGROUND DOC
dly750
f(p851)
X(p812)
dly250
f(p853)
Z(-p814+p802) // RAISED PART THROUGH HORIZ CROSS BAR
dly750
f(p851)
X(p813)
dly250
f(p853)
Z(-p814) //BACKGROUND DOC
dly750
f(p851)
x0
dly250
f(p853)
Z(-p814+p854) // 1 DOC DELTA OUT OF PART
dly250
f(p861)
x0.2 // BACKFEED TO X=0
dly250

```

```

p803 = p803 + 1 // INCREMENT PASS number

```

```

ENDWHILE

```

```

f(p853)
Z(-p814+p854) // ENSURE OUT OF PART 1 DOC DELTA
dly250

```

```

// SMALL SUNKEN CENTER TRIANGLE SECTION

```

```

p801 = 88 //PASS number TO jump TO NEXT SECTION

```

```

WHILE (p803!>p801)
  //LEFT LONG DIAGONAL
  p811 = .04355/5 + p805/TAN(65)

  //SMALL CENTER TRIANGLE LEFT LEG
  p810 = .241469/5 + p805 / TAN(65)

  //SMALL CENTER TRIANGLE RIGHT LEG
  p809 = 0.2 - p810

  //ELLIPTICAL END FOR B.RIGHT POINT
  p808 = 0.2 - p811

  // INCREMENT CROSSFEED LOCATION IN Y
  p805 = p804 + p803*p806

  f(p851)
  x0.2
  f(p852)
  Y(p805)
  dly1500
  f(p853)
  Z(-p814)           // BACKGROUD DOC
  dly750
  f(p851)
  X(p808)
  dly250
  f(p853)
  //+Z BY ONE DOC DELTA FOR THE LEFT RAISED SECTION
  Z(-p814+p802)
  dly750
  f(p851)
  X(p809)
  dly250
  f(p853)
  //BACKGROUND DOC FOR SUNKEN SMALL CENTER TRIANGLE
  Z(-p814)
  dly750
  f(p851)
  X(p810)
  dly250
  f(p853)
  //+Z BY ONE DOC DELTA FOR THE RIGHT RAISED SECTION
  Z(-p814+p802)
  dly750

```

```

f(p851)
X(p811)
dly250
f(p853)
Z(-p814)          //BACK TO BACKGROUND DOC
dly750
f(p851)
x0
dly250
f(p853)
Z(-p814+p854)    // 1 DOC DELTA OUT OF PART
dly250
f(p861)
x0.2             // BACKFEED TO X=0
dly250

p803 = p803 + 1   // INCREMENT PASS number

ENDWHILE

f(p853)
Z(-p814+p854)    // ENSURE OUT OF PART 1 DOC DELTA
dly250

// TOP POINT OF "A" SECTION

p801 = 128        //PASS number TO jump TO NEXT SECTION

WHILE (p803!>p801)
  p813 = .04355/5 + p805/TAN(65)    //LEFT LONG DIAGONAL
  p812 = 0.2 - p813                //RIGHT LONG DIAGONAL
  p805 = p804 + p803*p806          // INCREMENT CROSSFEED LOCATION IN
Y

f(p851)
x0.2
f(p852)
Y(p805)
dly1500
f(p853)
Z(-p814)          // BACKGROUND DOC
dly750
f(p851)
X(p812)
dly250
f(p853)

```

```

        // RAISED PART THROUGH TOPMOST SECTION OF "A"
Z(-p814+p802)
dly750
f(p851)
X(p813)
dly250
f(p853)
Z(-p814)           // BACKGROUND DOC
dly750
f(p851)
x0
dly250
f(p853)
Z(-p814+p854)     // 1 DOC DELTA OUT OF PART
dly750
f(p861)
x0.2              // BACKFEED TO X=0
dly250
p803 = p803 + 1   // INCREMENT PASS number

ENDWHILE

f(p853)
Z(-p814+p854)     // ENSURE OUT OF PART 1 DOC DELTA
dly250

// one blank pass between
// #PASSES STARTING WITH NO DOC CHANGE
p801 = 135
WHILE (p803 !> p801)
    // INCREMENT CROSSFEED LOCATION IN Y
    p805 = p804 + p803*p806
    f(p861)
    x0.2
    f(p852)
    Y(p805)
    dly1500
    P820 = 110 + P803
    f(p853)
    // x MICRONS INTO THE PART FOR THE BACKGROUND
    Z(-p814)
    dly750
    P820 = 120 + P803
    f(p851)
    x0
    dly250

```

```

P820 = 130 + P803
f(p853)
  // BACK OUT OF PART 1 DOC DELTA FOR BACKFEED
Z(-p814+p854)
dly750
P820 = 140 + P803
f(p861)
x0.2
dly250
P820 = 150 + P803

  p803 = p803 + 1 // INCREMENT PASS number
ENDWHILE

f(p853)
Z(-p814+p854) // ENSURE OUT OF PART 1 DOC DELTA
dly250

// bottom 1/3rd of topknot

p801 = 140 //PASS number TO jump TO NEXT SECTION

WHILE (p803!>p801)

  p812 = -34.334*p805*p805 + 10.117*p805 - 0.6158
  p813 = 0.2 - p812
  // INCREMENT CROSSFEED LOCATION IN Y
  p805 = p804 + p803*p806
  f(p861)
  x0.2
  f(p852)
  Y(p805)
  dly1500
  f(p853)
  Z(-p814) // BACKGROUND DOC
  dly750
  f(p851)
  X(p812)
  dly250
  f(p853)
  // RAISED PART THROUGH TOPMOST SECTION OF "A"
  Z(-p814+p802)
  dly750
  f(p851)
  X(p813)

```

```

dly250
f(p853)
Z(-p814)           // BACKGROUND DOC
dly750
f(p851)
x0
dly250
f(p853)
Z(-p814+p854)     // 1 DOC DELTA OUT OF PART
dly250
f(p861)
x0.2              // BACKFEED TO X=0
dly250

p803 = p803 + 1   // INCREMENT PASS number

ENDWHILE

f(p853)
Z(-p814+p854)     // ENSURE OUT OF PART 1 DOC DELTA
dly250

// 13 passes the same before hole

p801 = 153        //PASS number TO jump TO NEXT SECTION

WHILE (p803!>p801)

    p812 = .647/5
    p813 = .353/5
    // INCREMENT CROSSFEED LOCATION IN Y
    p805 = p804 + p803*p806
    f(p861)
    x0.2
    f(p852)
    Y(p805)
    dly1500
    f(p853)
    Z(-p814)       // BACKGROUND DOC
    dly750
    f(p851)
    X(p812)
    dly250
    f(p853)
    Z(-p814+p802) // RAISED PART
    dly750

```

```

f(p851)
X(p813)
dly250
f(p853)
Z(-p814)           // BACKGROUND DOC
dly750
f(p851)
x0
dly250
f(p853)
Z(-p814+p854)     // 1 DOC DELTA OUT OF PART
dly250
f(p861)
x0.2              // BACKFEED
dly250

p803 = p803 + 1   // INCREMENT PASS number

ENDWHILE

f(p853)
Z(-p814+p854)     // ENSURE OUT OF PART 1 DOC DELTA
dly250

// mid-topknot hole

p801 = 162        //PASS number TO jump TO NEXT SECTION

WHILE (p803!>p801)
  p808 = 0.647/5
  p809 = 0.565/5
  p810 = 0.435/5
  p811 = 0.353/5
  // INCREMENT CROSSFEED LOCATION IN Y
  p805 = p804 + p803*p806
  f(p861)
  x0.2
  f(p852)
  Y(p805)
  dly1500
  f(p853)
  Z(-p814)         // BACKGROUD DOC
  dly750
  f(p851)
  X(p808)
  dly250

```

```

f(p853)
    //+Z BY ONE DOC DELTA FOR THE LEFT RAISED SECTION
Z(-p814+p802)
dly750
f(p851)
X(p809)
dly250
f(p853)
    //BACKGROUND DOC FOR SUNKEN SMALL CENTER TRIANGLE
Z(-p814)
dly750
f(p851)
X(p810)
dly250
f(p853)
    //+Z BY ONE DOC DELTA FOR THE RIGHT RAISED SECTION
Z(-p814+p802)
dly750
f(p851)
X(p811)
dly250
f(p853)
Z(-p814)                //BACK TO BACKGROUND DOC
dly750
f(p851)
x0
dly250
f(p853)
Z(-p814+p854)          // 1 DOC DELTA OUT OF PART
dly250
f(p861)
x0.2                    // BACKFEED TO X=0
dly250
p803 = p803 + 1        // INCREMENT PASS number

ENDWHILE

f(p853)
Z(-p814+p854)          // ENSURE OUT OF PART 1 DOC DELTA
dly250

// 13 passes the same after hole

p801 = 175              //PASS number TO jump TO NEXT SECTION
WHILE (p803!>p801)

```

```

p812 = .647/5
p813 = .353/5
    // INCREMENT CROSSFEED LOCATION IN Y
p805 = p804 + p803*p806
f(p861)
x0.2
f(p852)
Y(p805)
dly1500
f(p853)
Z(-p814)                // BACKGROUND DOC
dly750
f(p851)
X(p812)
dly250
f(p853)
Z(-p814+p802)          // RAISED PART
dly750
f(p851)
X(p813)
dly250
f(p853)
Z(-p814)                // BACKGROUND DOC
dly750
f(p851)
x0
dly250
f(p853)
Z(-p814+p854)          // 1 DOC DELTA OUT OF PART
dly250
f(p861)
x0.2                    // BACKFEED TO X=0
dly250

p803 = p803 + 1        // INCREMENT PASS number

ENDWHILE

f(p853)
Z(-p814+p854)          // ENSURE OUT OF PART 1 DOC DELTA
dly250

// top 1/3rd of topknot

p801 = 180              //PASS number TO jump TO NEXT SECTION

```

```

WHILE (p803!>p801)

    p812 = -37.628*p805*p805 + 13.701*p805 - 1.1177
    p813 = 0.2 -p812
    p805 = p804 + p803*p806
    f(p861)
    x0.2
    f(p852)
    Y(p805)
    dly1500
    f(p853)
    Z(-p814)                // BACKGROUND DOC
    dly750
    f(p851)
    X(p812)
    dly250
    f(p853)
    Z(-p814+p802) // RAISED PART THROUGH TOPMOST SECTION OF "A"
    dly750
    f(p851)
    X(p813)
    dly250
    f(p853)
    Z(-p814)                // BACKGROUND DOC
    dly750
    f(p851)
    x0
    dly250
    f(p853)
    Z(-p814+p854)          // 1 DOC DELTA OUT OF PART
    dly250
    f(p861)
    x0.2                    // BACKFEED TO X=0
    dly250
    p803 = p803 + 1        // INCREMENT PASS number

ENDWHILE

f(p853)
Z(-p814+p854)            // ENSURE OUT OF PART 1 DOC DELTA
dly250

// top BLANK SECTION OF symbol

p801 = 188 // #PASSES STARTING AT BOTTOM WITH NO DOC CHANGE

```

```

WHILE (p803 !> p801)
  p805 = p804 + p803*p806
  f(p861)
  x0.2
  dly250
  f(p852)
  Y(p805)
  dly1500
  P820 = 110 + P803
  f(p853)
  Z(-p814) //x MICRONS INTO THE PART FOR THE BACKGROUND
  dly750
  P820 = 120 + P803
  f(p851)
  x0
  dly250
  P820 = 130 + P803
  f(p853)
  Z(-p814+p854) // BACK OUT OF PART 1 DOC DELTA FOR BACKFEED
  dly250
  P820 = 140 + P803
  f(p861)
  x0.2
  dly250
  P820 = 150 + P803

  p803 = p803 + 1 // INCREMENT PASS number
ENDWHILE

f(p853)
Z(-p814+p854) // ENSURE OUT OF PART 1 DOC DELTA
dly250

Z0.1 // ENSURE OUT OF PART 100µM

```

## 7.4 APPENDIX D: Y-AXIS REGAP PROCEDURE

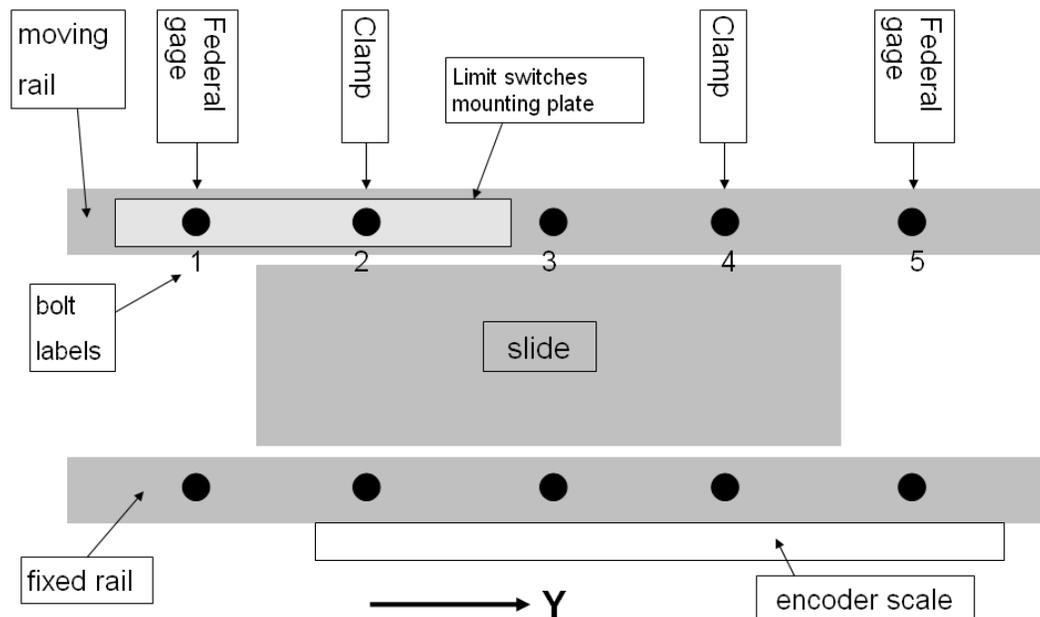


**Figure 7.4-1.** Bolt labels, gage and clamp locations.

- *do not loosen screws on the fixed rail*
- If the encoder scale is removed from the axis, both it and the readhead will need to be realigned. The axis can be regapped with the encoder scale in place.
- If the encoder scale is still attached to the axis, cover it with a Kem-wipe, optical wipe, or both. Otherwise, speaking and working over it will get it dirty.
- fix axis base as well as possible to optical table with a minimum 3 screws and/or clamps
- place Federal gage stands on axis base and probes on outside of bolt #1 and bolt #5
  - stands are magnetized to the side of the y-axis so that any motion of the entire axis with respect to the optical table is not included (see Figure 8.4-2)
  - avoid placing the magnet stand bases under either bolt #2 or bolt #4
  - check for any interference between gage stands and table or between gage stands and stationary components of the y-axis (Figures 8.4-4, 8.4-5)
  - clamps and gages are placed at bolt locations so that elastic deformation of the bearing rail (and its effect on gap measurement) is minimized.

- clamp loosely on bolt #2 & bolt #4 locations (Figure 8.4-3)
- NOTE PRESSURE CHANGE: using a regulator, adjust bearing air pressure to 20 psi
- loosen all five screws (on the moving rail) in 2 torque stages, leaving them all just looser than “first bite”
- ensure that the limit switch target affixed to the side of the slide is not over any of the screw heads
- clamp down with slide uncoupled from the ball screw and resting between the rails
- After clamping, ensure that zero may be reached on both Federal gage scales. Measuring from greater than zero on a  $\pm 25 \mu\text{m}$  gage scale is not a good idea. Starting at zero leaves you at least  $6\mu\text{m}$  of excess travel at the top end (beyond the desired gap) before going off the scale.
  - If not, adjust the gage stands.
- tighten bolt 1 & bolt 5 to 3-4 ft#
- tighten bolt 2 & bolt 4 to 1-2 ft#
- leave bolt 3 loose
- loosen clamps, expecting  $< 1 \mu\text{m}$  movement (due to elastic deformation) in either federal gage when releasing
- flip clamp fingers (by removing thumb screws highlighted in Figure 8.4–3),
- remove orange pads
- place clamps as spreaders between each end of rails and pump just enough to keep in place.
  - expect 1-2  $\mu\text{m}$  deflection of Federal gages
- loosen bolt 2 & bolt 4 to minimal torque.
- rezero the Federal gages

**begin loop**

- Loosen either 1 or 5 very slightly

- aim for 4-5  $\mu\text{m}$  deflection in the Federal gage at that bolt location
  - this may be achievable by very slowly loosening the bolt
  - if a  $\sim 50\%$  torque reduction does not achieve the 4-5  $\mu\text{m}$  target, turn the air up very slowly to hit 4-5  $\mu\text{m}$
  - if air pressure is insufficient, pump the spreader to achieve this target
  - retighten the bolt after achieving some deflection greater than 4  $\mu\text{m}$  but less than 19  $\mu\text{m}$  (if aiming for 17  $\mu\text{m}$  total bearing gap)
  - note this deflection as the next target for the other Federal gage location
- aim for the same deflection at the other bolt
- Repeat, alternating location #1 and #5, increasing the gap 2-5  $\mu\text{m}$  at a time on each side.
- If deflection at either bolt location exceeds 25  $\mu\text{m}$ , go back to the clamping procedure and start over.
- loop until each gage reads 1-2  $\mu\text{m}$  beyond (larger gap than) desired gap. For a 17  $\mu\text{m}$  desired total bearing gap, stop at 18-19  $\mu\text{m}$ .

**repeat loop**

- tighten 1 and 5.
- expect 1-2  $\mu\text{m}$  gap reduction between tightening that screw and releasing the spreading compression.
- examine float and travel of slide. If one end of travel demonstrates excessive friction, increase the gap on that end by 1-2  $\mu\text{m}$ .

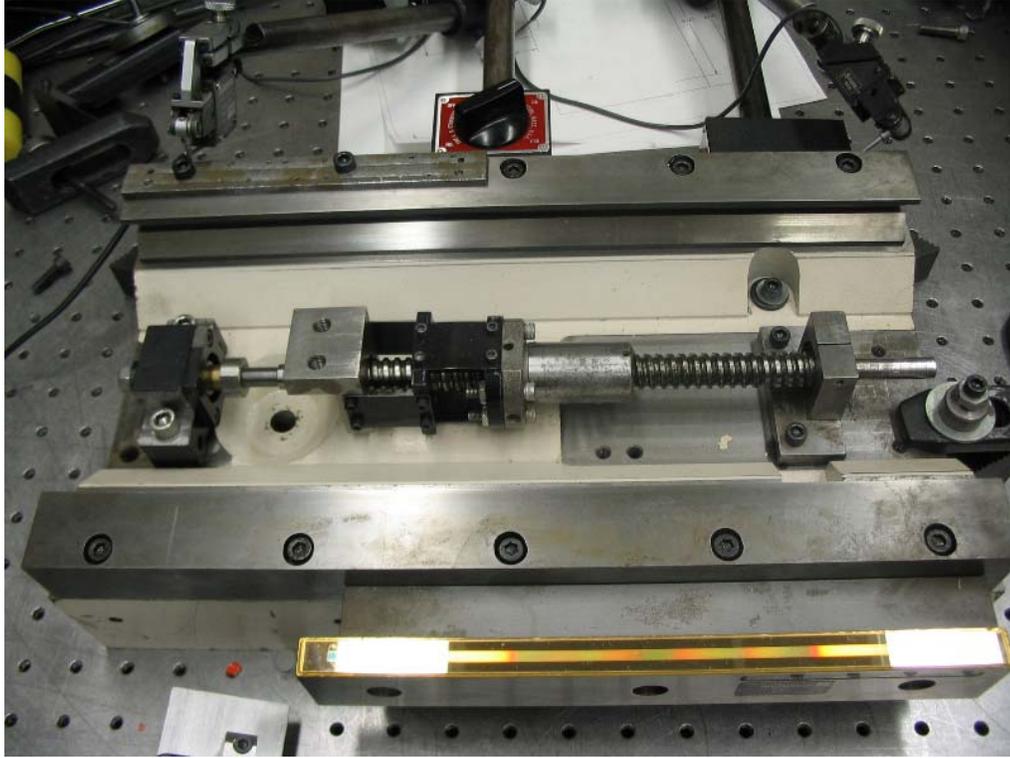


**Figure 7.4-2.** Proper Federal gage locations (not necessary to demount slide from axis)

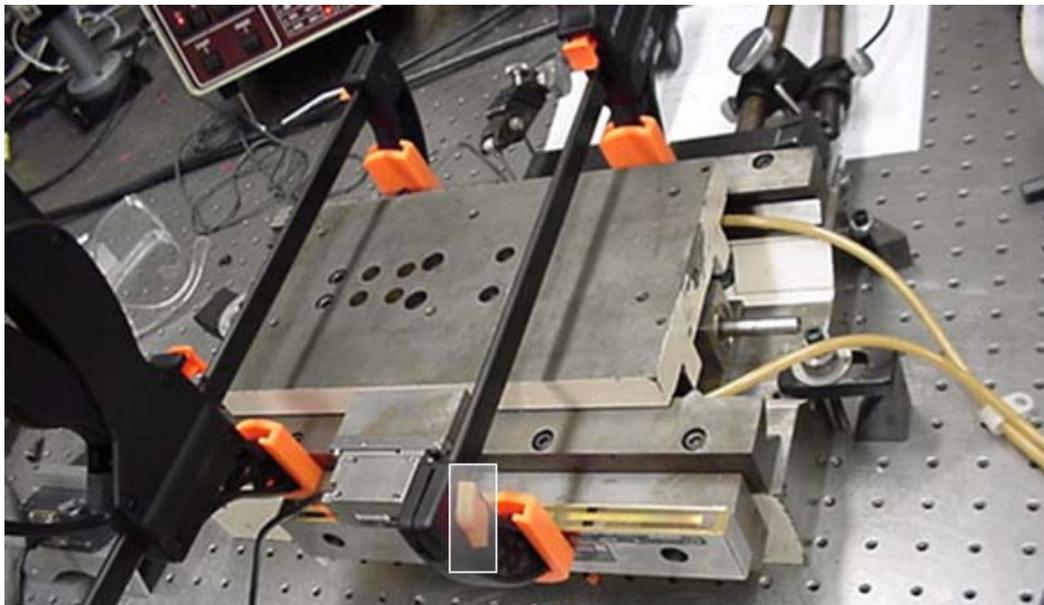


**Figure 7.4-3.** Proper clamp locations shown, clamp finger thumbscrew highlighted (ignore Federal gage at bolt #3)

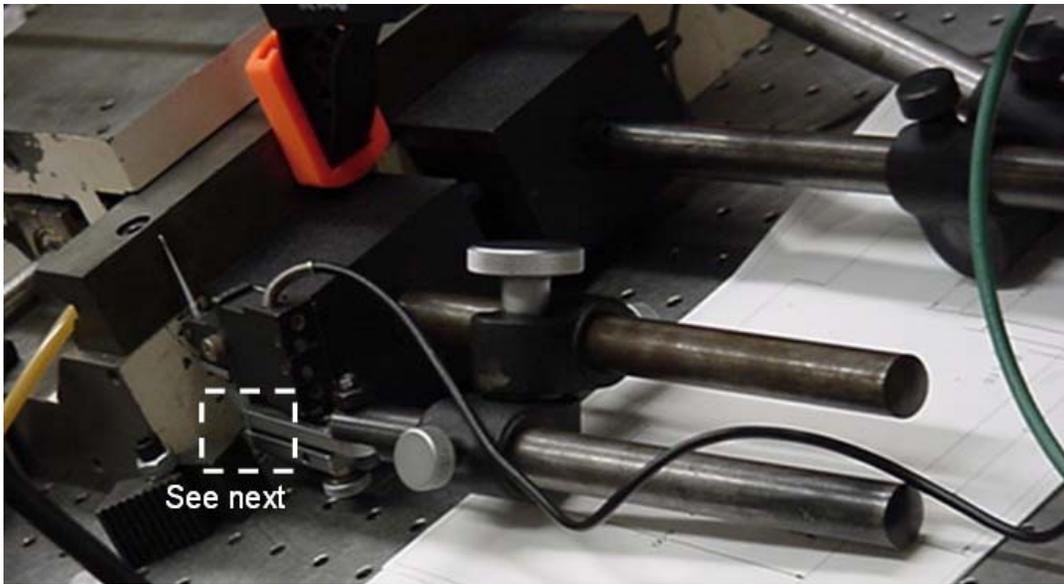


**Figure 7.4-4.** Gage stand: check interference with table. Paper on table should move freely.



**Figure 7.4-5.** Y-axis base clamping should not interfere with gage heads.

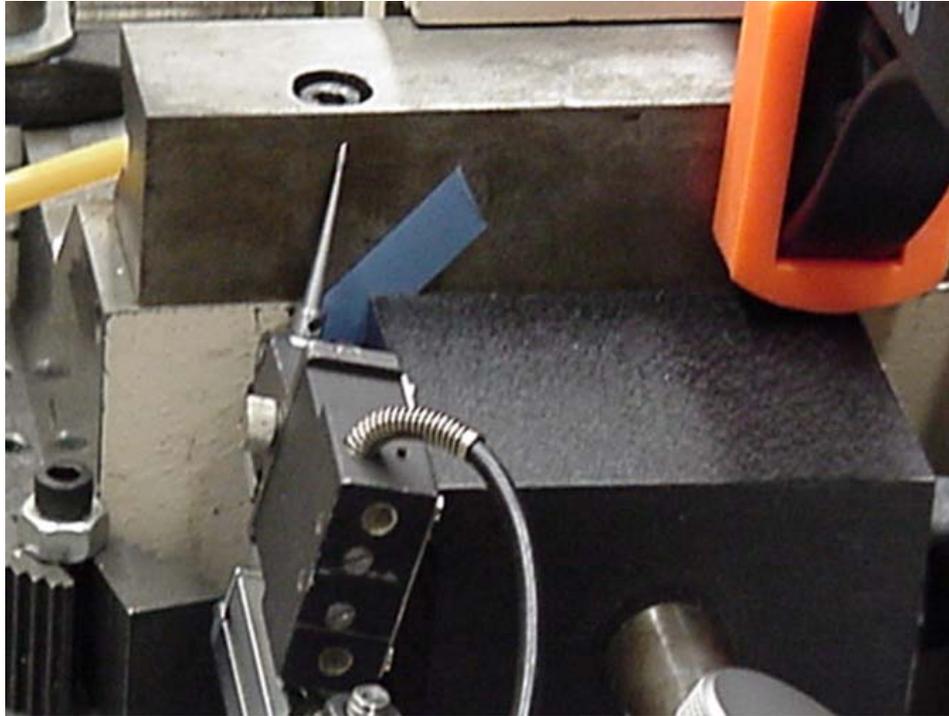


**Figure 7.4-6.** If either Federal gage base wobbles, shim the loose corner.

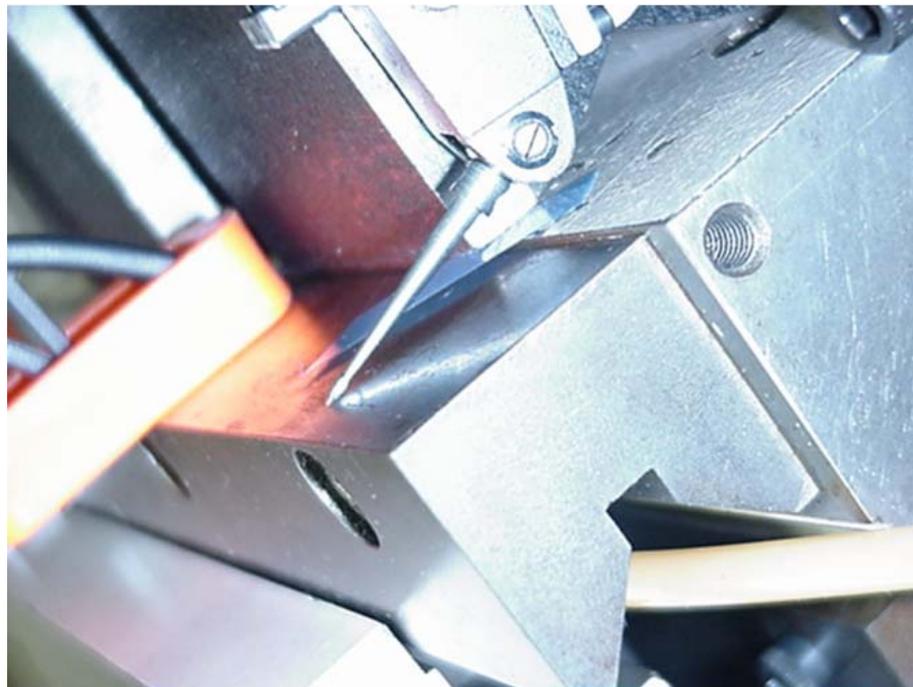


**Figure 7.4-7.** Ensure that Federal gage involute tip contacts in the curved section.

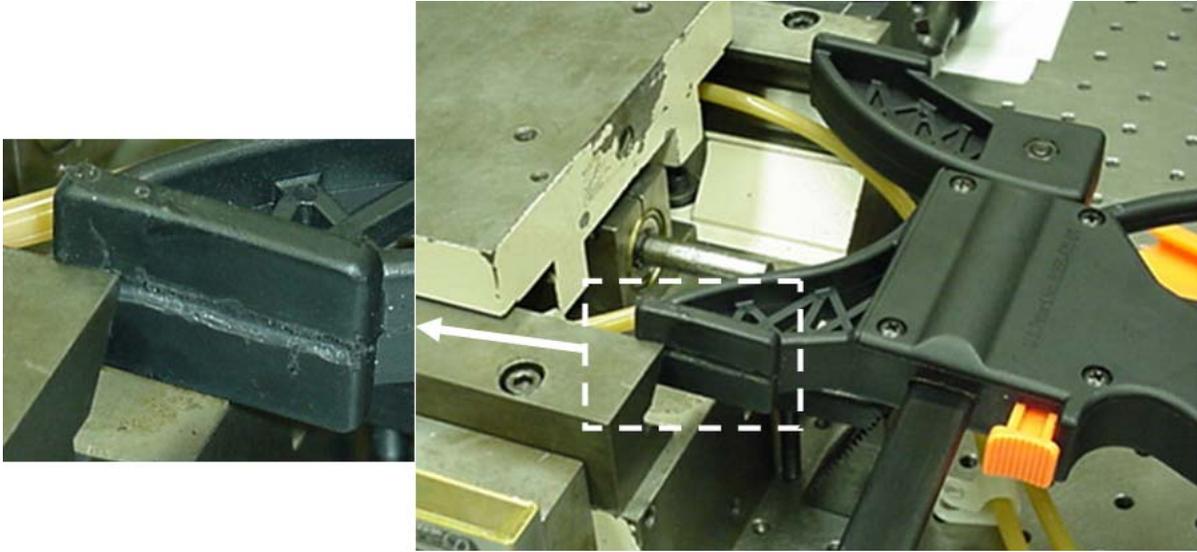


**Figure 7.4-8.** Clamps reversed as spreaders, grooved finger shown in inset.